THE UNIVERSITY of EDINBURGH

Title	Constraining the dark energy equation of state using three dimensional weak lensing
Author	Kitching, Thomas D
Qualification	PhD
Year	2006

Constraining the Dark Energy Equation of State using Three Dimensional Weak Lensing

THOMAS D. KITCHING

Institute for Astronomy

School of Physics

University of Edinburgh

Doctor of Philosophy

October 2006

Abstract

The determination of the nature of the Universe has always been one of the major goals of cosmology. Until now (circa 2006) this determination has been one of accounting for the relative abundances of known constituents of the Universe. However it is now known, with a convincing degree of accuracy, that the vast majority of the Universe is composed of two components, dark matter and dark energy accounting for approximately 30% and 70% of the current mass-energy budget respectively (Spergel et al., 2003; Spergel et al., 2006), and the nature of these components is entirely unknown. This thesis will present two new methods which could, given data from future surveys, determine the nature of dark energy through its equation of state $w = p_{\rm de}/\rho_{\rm de}c^2$ and its evolution in cosmologies with arbitrary spatial curvature.

Both methods presented use shear and redshift information from weakly lensed galaxies: 3D weak lensing. Dark energy affects both the geometry of the Universe, manifest in the redshift-distance relation, and the growth of structure which affects the power spectrum of matter over-densities. 3D weak lensing can probe both these effects. As well as presenting the methods formally, this thesis will present parameter forecasts for future weak lensing surveys using the Fisher matrix framework. I use the parameterization (Chevallier and Polarski, 2001; Linder, 2003) of the redshift evolution of the equation of state $w(a) = w_0 + w_a(1-a)$ where a is the scale factor.

The shear-ratio geometric test, an adaption and refinement of the Jain–Taylor test (Jain & Taylor, 2003), uses the weakly sheared galaxies around galaxy clusters. By taking the ratio of the shear signal generated by the cluster at differing redshift any mass-dependence of the shear signal on the mass or shape of the cluster cancels. One is left with a statistic that depends purely on the geometry of the Universe, and how it varies with redshift. The full shear-ratio covariance matrix is calculated for lensed sources, including the intervening large-scale structure and

photometric redshift errors as additional sources of noise, and a maximum likelihood method for applying the test is presented. Decomposing the lensing matter distribution into dark matter haloes I calculate the parameter covariance matrix for an arbitrary experiment. Combining with the expected results from the CMB I design an optimal survey for probing dark energy and investigate different observing strategies. For highest accuracy a large-scale photometric redshift survey is required, where the largest gain in signal arises from the numerous $\approx 10^{14}\mathrm{M}_{\odot}$ haloes corresponding to medium-sized galaxy clusters. Combined with expected CMB results, a near-future 5-band survey covering 10,000 square degrees to $z_m = 0.7$ could achieve 1-σ statistical errors of $\Delta w_0 = 0.075$ and $\Delta w_a = 0.326$. A stronger combined constraint is put on $w(z)$ measured at the pivot redshift $z_p = 0.27$ of $\Delta w(z_p) = 0.0298$. I compare and combine the geometric test with the cosmological and dark energy parameters measured from planned Baryon Acoustic Oscillation (BAO) and supernova Type Ia (SNIa) experiments, and find that the geometric test results combine with a significant reduction in errors due to different degeneracies.

The 3D cosmic shear spectral test uses the shear and redshift information from every galaxy within a survey, this work represents a refinement of the statistic presented in Heavens (2003). I treat the weakly lensed galaxies as estimators of an underlying 3D shear field. This 3D shear field can be decomposed using spherical harmonics and the spherical harmonic coefficients used to extract cosmological information. I demonstrate in particular that, in conjunction with expected results from CMB experiments, the properties of dark energy can be estimated with very high precision with large-scale, fully 3D weak lensing surveys employing the spectral test. In particular, a 5-band, 10,000 square degree ground-based survey of galaxies to a median redshift of $z_m = 0.7$ could achieve 1-σ marginal statistical errors, in combination with the constraints expected from the CMB, of $\Delta w_0 = 0.108$ and $\Delta w_a = 0.099$. The error on the value of $w(z)$ at an intermediate pivot redshift of $z_p = 0.368$ is constrained to $\Delta w(z_p) = 0.0175$. Again, I compare and combine the 3D weak lensing constraints with the cosmological and dark energy parameters measured from planned BAO and SNIa experiments, and find that the spectral test significantly improves the marginalized errors on w_0 and w_a in combination, and provides constraints on $w(z)$ at a unique redshift through the lensing effect.

Both of these methods have been applied to the COMBO-17 data set. The spectral test has been used to analyse galaxies with redshift estimates from the CDFS and S11 fields. The spectral test analysis was used to constrain the (σ_8, Ω_m) plane as well as provide a conditional constraint on w_0. The (σ_8, Ω_m) plane analysis constrained the relation between σ_8 and Ω_m

to be $\sigma_8(\Omega_m/0.3)^{0.57\pm0.19} = 1.06^{+0.17}_{-0.16}$. The spectral tests conditional constraint on w_0 using the CDFS and S11 fields is $w_0 = -1.27^{+0.64}_{-0.70}$. The geometric test has been applied to the A901/2 field, which contains three clusters of galaxies. This application yields a conditional error on w_0 of $w_0 = -0.11^{+1.05}_{-1.29}$ from only three small clusters. Combining the analysis from the A901/2 field, using the geometric test, and the CDFS and S11 fields, using the spectral test, w_0 is conditionally constrained to $w_0 = -1.08^{+0.63}_{-0.58}$. These impressive results, for such a small survey area, are shown to agree with the Fisher matrix predictions made in this thesis.

I also make predictions for future of dark energy surveys using the methods described in this thesis. Different stages of survey development are considered and the implications of the constraints that they could yield discussed. I present a dark energy timeline using the methods presented here and show that, given proposed future dark energy surveys, the dark energy question has the potential to be convincing answered using 3D weak lensing.

Declaration

I declare that this thesis is not substantially the same as any that I have submitted for a degree or diploma or other qualification at any other University. I further state that no part of my thesis has already been or is being concurrently submitted for any such degree, diploma or other qualification.

Parts of the work contained in this thesis have been published in refereed scientific journals, or will be published soon.

Chapter 3 is based on work presented in the paper "Probing dark energy with the shear-ratio geometric test", A.N. Taylor, T.D. Kitching, D.J. Bacon, A.F. Heavens, accepted to MNRAS (astro-ph/0606416). The formalism (pages 80 to 96) was developed in partnership with Andy Taylor. The photometric redshift error discussion, Section 3.6.2, was done with help from Chris Wolf. The parameter bias investigation, Section 3.6.3, was done in partnership with Andy Taylor and Alan Heavens.

Chapter 4 is based on work presented in the paper "Measuring dark energy properties with 3D cosmic shear", A. F. Heavens, T. D. Kitching, A. N. Taylor (2006) MNRAS, 373, 105-120 (astro-ph/0606568). In particular the formalism (pages 151 to 161) was developed in partnership with Alan Heavens.

Chapter 5 is based on work presented in the paper "Cosmological constraints from COMBO-17 using 3D weak lensing", T. D. Kitching, A. F. Heavens, A. N. Taylor, M. L. Brown, K. Meisenheimer, C. Wolf, M. E. Gray, D. J. Bacon, submitted to MNRAS (astro-ph/0610284). Section 5.3 was done in partnership with Alan Heavens, Section 5.4 was done in partnership with Andy Taylor.

This thesis is the outcome of my own work except where specifically indicated in the text.

Thomas D. Kitching
Edinburgh,
October 2006.

Acknowledgements

Firstly I would like to thank Alan and Andy. Thank you both for introducing me to the wonderful world of weak lensing. A student really couldn't ask for better supervisors.

I would also like to thank the other lensing people who were at Edinburgh during my time there. David, Patricia, Micheal and Barney thank you all for the help and encouragement in all aspects of my work. I would also like to thank John and Alexandre for their interesting and enjoyable examination!

I owe much to all of the fellow PhD students who were in Edinburgh whilst I was doing my PhD. Thank you to all the astronomy PhD's, knowing that someone else is going through the same experience is invaluable. Thank you in particular to my office mates. Also thank you to all my 'non-astronomy' friends in Edinburgh, some of my best memories from my PhD will be the times I spent with you talking about everything apart from work.

I wouldn't have been able to do a PhD without my undergraduate degree so I would like to say thanks to all my Imperial mates, without good friends it would have been impossible.

To all my friends from the Island. I can't imagine not knowing all of you, your always there and always great friends. Thank you to Kyle in particular, my longest and best friend. Thanks for everything dude.

Thanks to all my family for their love and support. I cannot express how much I owe to my Mum and Dad and my sister Amy, I love you all. You are the best family in the Universe and I am thankful everyday to be part of such a wonderful family.

Lastly, and most importantly of all, I would like to thank Brooke. In the infinity of time and space I feel privileged to be with you, I love you.

"For small creatures such as we the vastness is bearable only through love." Carl Sagan

Contents

List of Figures

List of Tables

Chapter 1

Introduction

Here is a outline of standard cosmology. This Introduction aims to familiarise the reader with the background upon which this work is based. The subject of Cosmology in its entirety is too vast to be completely covered here so discretion, with a bias towards this work, has been exercised.

Firstly a review of standard cosmology will outline its basis in General Relativity and the modelling of cosmological models based on various potential components of the Universe. Observable parameters and physically observable phenomenon will be discussed. The history of the Universe as it is currently understood, and the major epochs will be reviewed. The matter-dominated Universe will be extensively reviewed, as this is the component that allows for weak lensing, resulting in a discussion on dark matter.

Dark energy, will be introduced. Evidence for the remarkable claim that $\sim 70\%$ of our Universe is comprised of an unknown negative pressure component that is causing an acceleration of the expansion, will be reviewed. Possible candidates for dark energy, and how the nature of dark energy can be deduced from observations will be reviewed.

1.1 Standard Cosmology

Standard cosmology began with the formulation of General Relativity (GR) in 1915 (Einstein, 1916). GR allowed four-dimensional manifolds consisting of the three spatial dimensions plus one time dimension, spacetime, to be described mathematically for the first time. Through rigorous observational tests[1] it soon became evident that GR was a powerfully predictive theory. The reality that GR implicitly suggests for the Universe[2] is one in which the three spatial dimensions and time are features of a fundamental four-dimensional spacetime. In GR the gravitational force is caused by the curvature of spacetime; locally the Earth's mass distorts spacetime causing its gravitational field, cosmologically spacetime on the largest scales can be curved. Here is reviewed some basic GR, leading to an outline of standard Cosmology.

1.1.1 Essential General Relativity

For comprehensive reviews of cosmological general relativity see Peacock (1999), Peebles (1993) or Keyton (1990). In GR the notion of distance between two spacetime points is encoded in the *metric tensor* (commonly 'the metric'), $g_{\mu\nu}$. The separation, ds, between two points being

$$ds^2 = c^2 d\tau^2 = g_{\mu\nu} dx^\mu dx^\nu. \tag{1.1}$$

Central to GR is the principle of equivalence, which states that: the laws of physics take the same form in a freely-falling frame as in a frame in the absence of gravity[3]. The equivalence principle allows one to construct both the metric and the equation of motion for GR from the equations governing Special Relativity (SR), by generally transforming from the frame of a freely falling observer to an accelerating frame (see Peacock, 1999). The GR equation of motion is given by:

$$\frac{d^2 x^\mu}{d\tau^2} + \Gamma^\mu_{\alpha\beta} \frac{dx^\alpha}{d\tau} \frac{dx^\beta}{d\tau} = 0, \tag{1.2}$$

where x^μ is some set of coordinates. $\Gamma^\mu_{\alpha\beta}$ are known as components of the *affine connection* (or metric connection) or as *Christoffel symbols*. It can be shown that the Γ's can be expressed

[1] For example the advance of the perihelion of Mercury, and deviation in the position of stars caused by the Sun.

[2] The question of whether mathematics, and physical models are representative of reality at all or merely convenient predictive tools is an interesting one, and is often raised in the study of the foundations of quantum theory, see Isham 1995.

[3] Actual the *strong* equivalence principle, the *weak* equivalence principle only requiring that a freely falling observer experience no gravitational field.

entirely by the metric,

$$\Gamma^{\alpha}_{\lambda\nu} = \frac{1}{2} g^{\alpha\nu}(g_{\mu\nu,\lambda} + g_{\lambda\nu,\mu} - g_{\mu\lambda,\nu}), \tag{1.3}$$

where a comma, $g_{\mu\nu,\lambda} = \frac{\partial g_{\mu\nu}}{\partial x^{\lambda}}$ denotes a derivative. This expression is called the **fundamental theorem** of Riemannian geometry. Once the metric is known both the structure of spacetime and the motion of particles within it can be deduced.

To construct an example of an invariant quantity in GR (i.e. one that is the same for all observers) the **covariant** A_{μ} and **contravariant** A^{μ} components of a vector (or tensor) need to be contracted (not all invariants are like this, for example B^{μ}_{μ}). For example, the contraction $A^{\mu}A_{\mu}$ of the vector A^{μ} would be constant but $A^{\mu}A^{\mu}$ would not be. The metric is used to 'raise' or 'lower' indices, for example: $A_{\mu} = g_{\mu\nu}A^{\nu}$. Tensor equations that have the same relative positions for all the indices are said to be **generally covariant**, that is the equations have the same form for all observers. It is worth noting that the metric is not invariant but $\delta^{\mu}_{\nu} = g_{\nu\alpha}g^{\alpha\mu}$ is (this actually defines $g^{\alpha\mu}$).

Revisiting the equation of motion, equation (1.2), it is not manifestly covariant in this form as it is not an equality of tensors. The Γ has made the equation **gauge invariant**. More generally the equation of motion of a gravitational field can be expressed as a *covariant derivative* of 4-velocity, $U^{\mu} = \gamma(c, \mathbf{v})$, a generalisation of velocity to four dimensions:

$$\frac{D_{\mu}U^{\mu}}{d\tau} = 0, \tag{1.4}$$

where D_{μ} is the covariant derivative defined as:

$$D_{\mu}A^{\mu} = dA^{\mu} + \Gamma^{\mu}_{\alpha\beta}A^{\alpha}dx^{\beta}. \tag{1.5}$$

In general the equations of SR can be converted into GR equivalent forms by mapping the Minkowski metric (the metric used in SR), $\eta \rightarrow g$, and by mapping $\partial \rightarrow D$.

A **geodesic** is, geometrically, the shortest path between two spacetime events; physically they are the path that a free-falling body would take. Geodesics are stationary paths: that is, any small deviation from the path produces no change in the length, to first order, $\delta S = 0$. Where the integrated path length is given by (see equation 1.1):

$$S = \int (g_{\mu\nu}dx^{\mu}dx^{\nu})^{1/2}. \tag{1.6}$$

The general problem is one of the calculus of variations, where the path integral:

$$I = \int \mathcal{L}d\tau, \tag{1.7}$$

is stationary. $\mathcal{L}$ is the *Lagrangian* and is a function of the coordinates x^μ and their derivatives U^μ, $\mathcal{L} = \sqrt{g_{\mu\nu}U^\mu U^\nu}$. So that in its most general form the geodesic equation can be expressed:

$$\delta \int (g_{\mu\nu}U^\mu U^\nu)^{1/2} d\tau = 0. \tag{1.8}$$

The geodesic equation can be used to derive the previous equation of motion, see equation (1.2). The geodesic path that a body takes depends on its starting velocity. Massive particles ($v < c$) follow *time-like* geodesics with $\int ds^2 > 0$. Photons ($v = c$) follow *null* geodesics with $\int ds^2 = 0$. Finally *space-like* geodesics which have $\int ds^2 < 0$ would correspond to $v > c$ (neither photons or massive particles can follow space-like geodesics, however they can be used in order to set up coordinate frames that span spacetime).

The **energy-momentum** tensor (or stress-energy tensor) $T^{\mu\nu}$ succinctly describes the energy and momentum of spacetime, in the presence of any 'perfect fluid' (an inviscid fluid with isotropic pressure). It can be expressed as:

$$T^{\mu\nu} = (\rho + p/c^2)U^\mu U^\nu - pg^{\mu\nu}. \tag{1.9}$$

Where ρ is the density of the fluid and p its pressure. There exist four conservation laws, generalisations of the classical energy and momentum conservation laws, that are expressed as:

$$D_\mu T^{\mu\nu} = 0, \tag{1.10}$$

that is the $T^{\mu\nu}$ divergences vanish. Note that in the absence of a component exhibiting a pressure and/or density, the energy-momentum tensor also vanishes.

The **Riemann curvature tensor** provides a full description of the curvature of spacetime at each point. For a full derivation of this tensor see Keyton (1990). What distinguishes a flat space from a curved one is that in curved space a frame in free-fall at x differs a the frame in free fall at an event a small distance away $x+\Delta x$. By considering a parallel transport argument, that is considering the change dv^α that occurs to a vector v^α when it is moved around a closed, rectangular, loop of sides da and db, the following can be derived:

$$dv^\alpha = da^\delta db^\gamma v^\beta R^\alpha_{\beta\gamma\delta}. \tag{1.11}$$

Where any change is caused by the curvature of the space, encapsulated in the rank-4 Riemann tensor, which can be written in terms of the connection and its derivatives:

$$R^\alpha_{\beta\gamma\delta} = \Gamma^\alpha_{\beta\delta,\gamma} - \Gamma^\alpha_{\beta\gamma,\delta} + \Gamma^\alpha_{\sigma\gamma}\Gamma^\sigma_{\beta\delta} - \Gamma^\alpha_{\sigma\delta}\Gamma^\sigma_{\beta\gamma}. \tag{1.12}$$

This can also be expressed solely in terms of second derivatives of the metric, see equation (1.3). $R^{\alpha}_{\beta\gamma\delta}$ can be contracted to the **Ricci tensor** $R_{\beta\gamma} = R^{\alpha}_{\beta\gamma\alpha}$ or further to the **curvature scalar** $R = R^{\mu}_{\mu} = g^{\mu\nu}R_{\mu\nu}$.

Einstein identified the energy-momentum of spacetime as the *source* of its curvature. This can be summarised in the following equation, GR's field equation:

$$G^{\mu\nu} = -\frac{8\pi G}{c^4}T^{\mu\nu}. \tag{1.13}$$

The **Einstein tensor** $G^{\mu\nu}$ encapsulates all curvature information and is defined as:

$$G^{\mu\nu} = R^{\mu\nu} - \frac{1}{2}g^{\mu\nu}R. \tag{1.14}$$

GR can make predictions in 'normal' conditions in which Newtonian gravity is almost always valid via the *weak field limit* (or weak field régime). In the weak field limit the full GR metric is assumed to be nearly that of a flat, Minkowski spacetime. Using a perturbative approach the metric can be written as:

$$g^{\mu\nu} = \eta^{\mu\nu} + h^{\mu\nu}, \tag{1.15}$$

where $\eta_{\mu\nu}$ is the standard SR Minkowski metric and the $h_{\mu\nu}$ is a small perturbation:

$$|h^{\mu\nu}| \ll 1. \tag{1.16}$$

The weak field regime applies to those scenarios in which the gravitational field is weak and slowly varying in time i.e. slowly varying in spacetime. In fact, the majority of cosmological applications of GR can use the weak field limit, as on the largest scales the weak field limit conditions are met.

With the tool of GR a mathematical description of the Cosmos on the largest scales, and in its entirety, is possible. GR allowed the bulk properties of spacetime and their evolution to be studied within a sound mathematical framework for the first time.

1.1.2 Cosmological General Relativity

The Cosmological Principle is an extension of the Copernican Principle (that we are not privileged observers). It states that the Universe is both *isotropic* and *homogenous*, on the largest scales[4]. The original motivation for these assumption was one of simplicity, an isotropic and

[4]The Cosmological Principle extends the observation of isotropy by implying homogeneity. Also, on other scales, for example the scale of humans, it is obviously *not* isotropic or homogenous.

homogenous mass distribution is the simplest possible in much the same way that GR is the simplest relativistic gravitational formulation possible[5].

Observational evidence confirmed that the Universe on the largest scales was indeed isotropic and homogenous; and every basic observation since is consistent with large scale homogeneity and isotropy. The Cosmic Microwave Background (CMB) (see Section 1.4.1) is observed to be the same in every direction to within 1 part in 10^{-5}, and number counts of Quasars are approximately the same in all directions: implying isotropy. The direct proportionality of the recessional velocity of galaxies with their distance implies homogeneity (if the power law were not directly proportional for us then for another observer the power of proportionality would be different than ours). This suggests that any other observer would observe the same directly proportional velocity-distance relation we observe, implying homogeneity. Large scale redshift surveys, for example SDSS (e.g. Tegmark et al., 2003) and 2DFRGS (e.g. Sanchez et al., 2005), have begun to observationally confirm homogeneity[6].

The cosmological metric, then, needs to be one which describes a time varying universe but one that is, at each time, homogenous and isotropic. The cosmological metric, known as the **Robertson-Walker metric** (RW metric), describes a homogenous, isotropic universe with matter uniformly distributed, as a perfect fluid, at the mean density of the universe and is written as:

$$-ds^2 = c^2 d\tau^2 = c^2 dt^2 - R^2(t)[dr^2 + \mathrm{S}^{0}{}_{k}^{2}(r)(d\theta^2 + \sin^2\theta d\phi^2)], \tag{1.17}$$

where r is a time independent **comoving distance** (a distance defined to remain constant between a source and an observer), θ and ϕ are the usual traverse polar coordinates. t is the **cosmic time**: the proper time measured by an observer at rest to the local matter distribution (or 'substratum'). $R(t)$ is the scale factor of the Universe. The function $\mathrm{S}^{0}{}_{k}(r)$ is defined as:

$$\mathrm{S}^{0}{}_{k}(r) = \begin{cases} \sin(r) & (k = +1) \\ r & (k = 0) \\ \sinh(r) & (k = -1), \end{cases} \tag{1.18}$$

where k encodes the geometric curvature of spacetime: $k = 0$ being a flat spacetime, $k = +1$ describes a positively curved hyperspherical spacetime, $k = -1$ describes a negatively curved

[5]The goal of simplification in science is common. Occam's Razor is a commonly cited example: in which the simplest explanation is usually the correct one. More recently the goal of grand unification of the four fundamental forces is motivated by a unifying scientific philosophy.

[6]In actuality, since one can only observe along a past light cone, the observation of spatial homogeneity over large distances is impossible. However observations within narrow redshift ranges are homogenous on large scales.

hyperbolic spacetime. Another common form of the RW metric uses a different definition of the comoving distance where $S^0{}_k(r) \rightarrow r$ so that:

$$-ds^2 = c^2dt^2 - R^2(t)\left[\frac{dr^2}{1-kr^2} + r^2(d\theta^2 + \sin^2\theta d\phi^2)\right]. \tag{1.19}$$

A dimensionless scale factor $a(t)$ can be defined:

$$a(t) \equiv \frac{R(t)}{R_0}, \tag{1.20}$$

where R_0 is the present day scale factor; $a = 1$ at the present day. From here on the time dependence of $a(t)$ will be implicit; unless included for clarity $a(t)$ will be abbreviated to a. The metric can then be rewritten in this dimensionless form as:

$$-ds^2 = c^2d\tau^2 = c^2dt^2 - a^2[dr^2 + S_k^2(r)(d\theta^2 + \sin^2\theta d\phi^2)] \tag{1.21}$$

$$-ds^2 = c^2dt^2 - a^2\left[\frac{dr^2}{1-k(r/R_0)^2} + r^2(d\theta^2 + \sin^2\theta d\phi^2)\right],$$

where $S_k(r)$ can be redefined as:

$$S_k(r) = \begin{cases} R_0\sin(r/R_0) & (k=+1) \\ r & (k=0) \\ R_0\sinh(r/R_0) & (k=-1). \end{cases} \tag{1.22}$$

This is the form of the metric, and $S_k(r)$, that will be used from hereon.

1.1.3 Cosmological Redshift

The Universe is expanding[7]. Consider a light signal emitted by a source, e, at time t_e, which is then observed at a time t_0 at the coordinate origin. Since this is a radial photon, and photons travel along null geodesics it can immediately be seen from the metric (equation 1.21) that the comoving distance, defined to be a constant, between the source and observer can be written:

$$r = \int_0^e ds = \int_{t_e}^{t_0} \frac{cdt}{a(t)} = \text{constant}. \tag{1.23}$$

[7]It is incorrect to state that space or spacetime is expanding, since spacetime can be locally described by a (static and flat) Minkowskian spacetime. The redshift of galaxies can be attributed solely to the Doppler effect. 'Expanding Universe' here refers to the fact that all galaxies are moving away from each other, the global coordinate frame used by a fundamental observer is expanding. The expansion is due to initial conditions (and recently dark energy). For discussions regarding the 'expanding space misconception' see Barnes et al. (2006) and Chodorowski (2006).

Differentiating this with respect to t_e it can be shown that:

$$\frac{dt_0}{dt_e} = \frac{a(t_0)}{a(t_e)}, \tag{1.24}$$

and the 'inverse time interval' can be equated with the frequency of the emitted light i.e. $\frac{dt_0}{dt_e} = \frac{\nu_e}{\nu_0} = \frac{\lambda_0}{\lambda_e}$. The **redshift** z of a light signal is defined as the relative change in wavelength between emission and observation:

$$z = \frac{\lambda_0 - \lambda_e}{\lambda_e}. \tag{1.25}$$

So that the redshift can be related to the scale factor in the following way:

$$\frac{a(t_0)}{a(t_e)} = 1 + z, \tag{1.26}$$

and since we have defined $a(t_0) = 1$ the redshift is usually related to the scale factor simply by $a = (1 + z)^{-1}$.

The redshift is related, via the Doppler effect, to the apparent recessional velocity of a source:

$$1 + z \approx 1 + \frac{v}{c}. \tag{1.27}$$

Hubble (1929) observed that the redshift of a galaxy was proportional to its distance and arrived at Hubble's law, $v = H_0 r$, where H_0 is a constant of proportionality known as the **Hubble constant**. More generally the time varying **Hubble parameter** can be related to the dimensionless scale factor by:

$$H(t) = \frac{\dot{a}(t)}{a(t)}, \tag{1.28}$$

where the value at the present epoch is H_0, a constant in space not time. The Hubble constant is usually expressed in the following way:

$$H_0 = 100h \ \text{kms}^{-1}\text{Mpc}^{-1}. \tag{1.29}$$

Here the Megaparsec distance measure has been introduced, this is the standard distance measure used in Cosmology for convenience 1Mpc$= 3.08568025 \times 10^{22}$metres.

1.2 Dynamics of the Expansion

The result of combining equations (1.13) and (1.21) is two independent Einstein equations:

$$\left(\frac{\dot{a}}{a}\right)^2 + \frac{kc^2}{a^2} = \frac{8\pi G}{3}\rho, \tag{1.30}$$

$$2\left(\frac{\ddot{a}}{a}\right)+\left(\frac{\dot{a}}{a}\right)^2+\frac{kc^2}{a^2}=-\frac{8\pi G}{c^2}p. \tag{1.31}$$

Equation (1.30) is known as the **Friedmann equation** and relates the density ρ of the Universe (including all contributions i.e. matter, vacuum, radiation, relativistic particles etc.) to its global geometry. It can immediately be seen from (1.30) that there will exist a **critical density** ρ_c for which $k=0$, using equation (1.28) this can be written as:

$$\rho_c(t)=\frac{3H^2(t)}{8\pi G}. \tag{1.32}$$

It is then clear that a universe whose density is above this critical value will have a positive curvature, that is be **spatially closed** (k=+1), one whose density is equal to or less than this value will be **spatially open** ($k=0$ or $k=-1$). Cosmological models which can be described by both the RW metric and the Friedmann equation are known as FRW models. A dimensionless **density parameter** for any given fluid can then be defined as:

$$\Omega(t)=\frac{\rho(t)}{\rho_c(t)}=\frac{8\pi G\rho(t)}{3H^2(t)}. \tag{1.33}$$

A current value of the density parameter is denoted Ω_0, also the time dependence is usually exchanged for a redshift dependence $\Omega(z)$, or $\Omega(a)$. Note that in general the density can be an arbitrary function of the scale factor $\rho=\rho(a)$, so that using equations (1.28) and (1.32) the Friedmann equation can be rewritten in the following way:

$$H(t)a^2=\frac{k^2c^2}{\Omega(t)-1}, \tag{1.34}$$

where $\Omega(t)$ is the total dimensionless density, at time t.

Subtracting equation (1.30) from (1.31) yields the **acceleration equation**:

$$\frac{\ddot{a}}{a}=-4\pi G\left(\frac{\rho}{3}+\frac{p}{c^2}\right). \tag{1.35}$$

Equations (1.30) and (1.31) can also be used to construct the **fluid**, or continuity equation:

$$\dot{\rho}+3\frac{\dot{a}}{a}\left(\rho+\frac{p}{c^2}\right)=0 \tag{1.36}$$

this describes how the density and pressure are related to one another, and how they will evolve for any given component of the Universe (i.e. matter, radiation etc.). It is worth noting that this equation can also be derived from the 1^{st} law of thermodynamics for an adiabatic perfect fluid. If the dependence of the density on the scale factor is known then using the fluid equation an **equation of state**, a relation between a fluids density and its pressure, can be derived. The

Friedmann equation can also be derived using Newtonian gravity, as the weak field regime is applicable on the cosmological scale this should not be surprising.

It is a useful approximation to divide the components of the Universe into distinct parts, each one of which is assumed to evolve independently, and differently. The motivation for the division is both physical, in that they represent physically different phenomenon, and mathematical in that the density evolutions are distinct, which suggests a logical splitting. Also, as will be discussed later, the components should be decoupled for all late cosmological times.

1.2.1 Dust Dominated Models

'Dust', in this context, refers to pressureless matter. Galaxies can be conceptualised as particles in a pressureless fluid, as they rarely interact. Since the pressure is zero $p_m = 0$ the density scales with the 'volume' of the universe:

$$\rho_m(a) = \frac{\rho_{m,0}}{a^3}, \tag{1.37}$$

where $\rho_{m,0}$ is the current density, and $a(t_0) = 1$. Substituting into equation (1.30), and assuming 'flatness' (k=0), the time evolution of the scale factor can be derived:

$$a(t) = \left(\frac{t}{t_0}\right)^{2/3}. \tag{1.38}$$

Using equation (1.28) the evolution of the Hubble parameter in this case is:

$$H(t) = \frac{2}{3t}. \tag{1.39}$$

This is same solution as the well known **Einstein-de Sitter** (EdS) solution.

1.2.2 Radiation Dominated Models

A 'radiation' dominated universe is one in which the majority of energy in the universe is in the form of relativistic particles, most commonly photons and relativistic neutrinos. Such a scenario is thought to have existed in the early Universe see Section 1.4. Heuristically it can be argued that the density of radiation has a $\rho_{rad} \propto a^{-4}$ behaviour: not only does any expansion dilute the radiation fluid, in a similar way to matter, but the wavelength of any radiation is increased by the expansion so that its energy decreases $E_{rad} \propto a^{-1}$ and from thermodynamics

$E_{rad} = \rho_{rad}c^2 = \alpha T^4$, where T is the temperature of the radiation and α is the Stefan-Boltzmann constant. Using this relation, and the fluid equation (1.36), the equation of state for radiation can be derived:

$$\rho_{rad}(a) = \frac{\rho_{rad,0}}{a^4} \; ; \; p_{rad} = \frac{\rho_{rad}c^2}{3}. \tag{1.40}$$

Combining this with the Friedmann equations, and assuming flatness (k=0), the time dependence of the scale factor and Hubble parameter can be obtained, in this case:

$$a(t) = \left(\frac{t}{t_0}\right)^{1/2} \; ; \; H(t) = \frac{1}{2t}. \tag{1.41}$$

1.2.3 Dark Energy Dominated Models

In an effort to remain consist dark energy will be briefly introduced here as a further cosmological component, although for a justification of the equations and further explanation see Section 1.8. Here it will merely be considered as a further fluid component with a distinct equation of state.

Dark energy is a 'negative pressure' component of the Universe, whose equation of state can be written, in its most general form as:

$$p_{de} = wc^2\rho_{de}, \tag{1.42}$$

where w can be some arbitrary function of redshift, scale factor or cosmic time with the constraint that $w \leq 0$ i.e. negative pressure. Using the fluid equation (1.36) and assuming that w is some arbitrary function of a, $w = w(a)$ the following density-scale factor relation can be derived:

$$\rho_{de}(a) = \rho_{de,0}\mathrm{e}^{-3\int_a^1[1+w(a')]d(\ln a')}. \tag{1.43}$$

Detailing a general time dependence for the scale factor and Hubble parameter would not be instructive in this case. Although it can be seen that in a *special case* of constant $w(a) = -1$, the fluid equation (1.36) implies that the density is constant: $\rho_{de}(a)$ =constant. Using the Friedmann equation (1.30) it can be seen that in this case, as the scale factor increases, the $\frac{kc^2}{a^2}$ term will eventually become negligible compared to the others. The scale factor then has the functional form:

$$a(t) = a(t_0)\mathrm{e}^{\left(\frac{8\pi G\rho_{de}}{3}\right)^{1/2}t} = a(t_0)\mathrm{e}^{\left(\frac{\Lambda c^2}{3}\right)^{1/2}t}, \tag{1.44}$$

where $\Lambda = \frac{8\pi G\rho_{de}}{c^2}$. This is same solution as the well known **de Sitter** solution. The de Sitter solution helped to inspire Inflationary arguments see Section 1.4.5.

1.3 Observational Quantities

To study of the global properties of the Universe, Cosmology, one usually has to make inferences from objects within it, usually galaxies[8]. In this Section the classic observables of galaxies (redshift, apparent size and luminosity), will be related to their redshift.

1.3.1 The Hubble Parameter

The total density of the Universe, in terms of its constituent components can be written as the sum of the densities of those components, $\rho = \rho_m + \rho_{rad} + \rho_{de}$ at any given cosmic time (or corresponding scale factor). The total dimensionless density can then be written $\Omega = \Omega_m + \Omega_{rad} + \Omega_{de}$. Where the subscript 0 has been dropped for clarity; from here on $\Omega_{m,o} \rightarrow \Omega_m$, $\rho_{m,o} \rightarrow \rho_m$ etc. The Friedmann equation (1.30) can now be rewritten using equations (1.37), (1.40) and (1.43):

$$H^2(a) = \frac{8\pi G}{3}(\rho_m a^{-3} + \rho_{rad} a^{-4} + \rho_{de} \mathrm{e}^{-3\int_a^1 [1+w(a')]d(\ln a')}) - \frac{kc^2}{a^2}. \tag{1.45}$$

This can further be rearranged using equations (1.33) and (1.34) so that:

$$H^2(a) = H_0^2[\Omega_m a^{-3} + \Omega_{rad} a^{-4} + \Omega_{de} \mathrm{e}^{-3\int_a^1 [1+w(a')]d(\ln a')} + (1-\Omega)a^{-2}], \tag{1.46}$$

or, in terms of redshift:

$$H^2(z) = H_0^2[\Omega_m(1+z)^3 + \Omega_{rad}(1+z)^4 + \Omega_{de}\mathrm{e}^{3\int_0^z [1+w(z')]/(1+z')dz'} + (1-\Omega)(1+z)^2]. \tag{1.47}$$

Occasionally $(1-\Omega)$ is replaced by Ω_k: the density due to the intrinsic geometry of spacetime. Equation (1.46) is of central importance to cosmology as it allows the distance of an object to be calculated from its redshift, and relates this distance to the global density components, and geometry, of the Universe.

The deceleration parameter is defined as:

$$q = -\frac{a\ddot{a}}{\dot{a}^2}, \tag{1.48}$$

and parameterises the deceleration of the Universe's expansion at a given time. This however is largely a defunct parameter since the discovery of dark energy in which the current expansion is accelerating; it is included here for completion.

[8] Indeed GR only formally describes the motion of test particles, the use of GR in cosmology to describe the Universe in general is an extension and inference of the conclusions of GR. Also note that the temperature can be measured directly.

1.3.2 Distances in Cosmology

When dealing with a generally curved spacetime the meaning of 'distance' is no longer unique. That is, the separation measured between any two events (e.g. between a given source and an observer) depends on the definition of distance being employed. Here is described the four most common distance measures utilised in cosmology.

Proper Distance. The proper distance between two events at redshifts z_1 and z_2 is defined as the light travel time between them $dD_{prop} = cdt$, rearranging this becomes $dD_{prop} = c\frac{da}{\dot{a}} = c\frac{da}{aH(a)}$ so that:

$$D_{prop}(z_1, z_2) = \int_{a_1(z_2)}^{a_2(z_1)} \frac{cda}{aH(a)},$$
$$D_{prop}(z_1, z_2) = \int_{z_1}^{z_2} \frac{cdz}{H(z)(1+z)}. \tag{1.49}$$

For an observer at $z_1 = 0$ the proper distance to an object with redshift z is:

$$D_{prop}(z) = \int_0^{z_2} \frac{cdz'}{H(z')(1+z')}. \tag{1.50}$$

This distance measure is rarely used and is included here for completeness.

Comoving Distance. Has been defined previously in equation (1.23). It is the distance on the spatial hypersurface at $t = t_0$ between the worldlines of two events. From equation (1.23) it can be seen that $dr = dD_{com} = a^{-1}cdt$ rearranging this becomes $dr = dD_{com} = c\frac{da}{a\dot{a}} = c\frac{da}{a^2H(a)}$ so that:

$$D_{com}(z_1, z_2) = \int_{a_1(z_2)}^{a_2(z_1)} \frac{cda}{a^2H(a)},$$
$$D_{com}(z_1, z_2) = \int_{z_1}^{z_2} \frac{cdz}{H(z)}. \tag{1.51}$$

For an observer at $z_1 = 0$ the comoving distance to an object with redshift z is:

$$D_{com}(z) = \int_0^{z} \frac{cdz'}{H(z')}. \tag{1.52}$$

Note that $r = D_{com}$.

Angular Diameter Distance. The angular diameter distance relates the apparent angular size of an object to its redshift. In analogy with Euclidean geometry the angular diameter distance relates the cross-sectional area of an object dA to the solid angle the object subtends, as measured by an observer, $d\Omega$:

$$dA = D_{ang}^2(z_1, z_2)d\Omega. \tag{1.53}$$

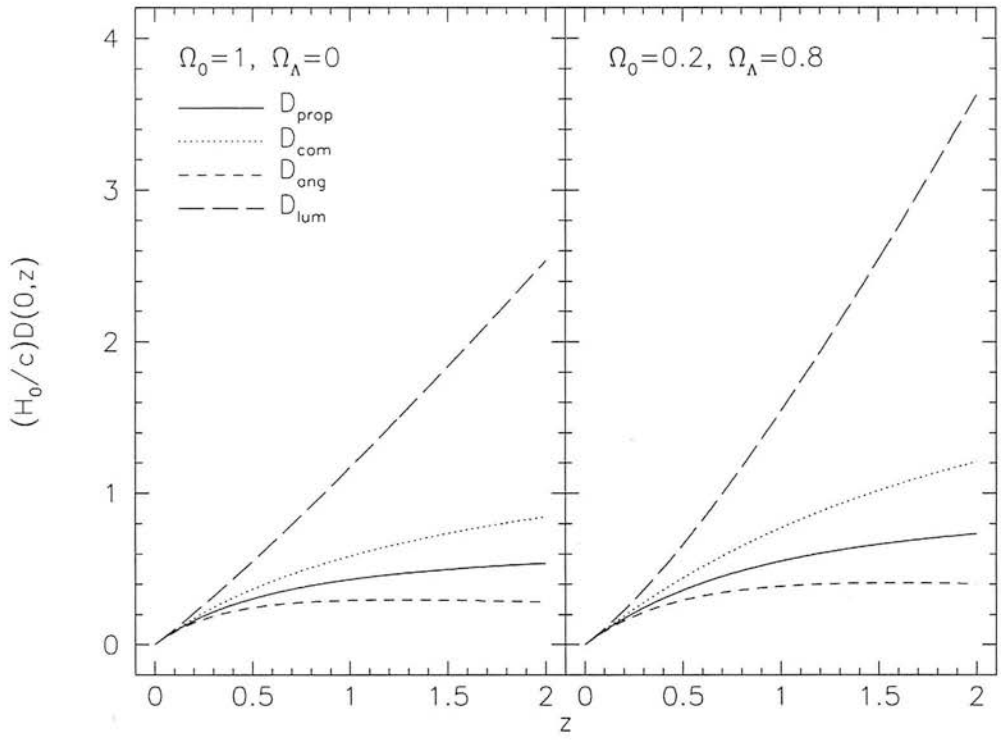

Figure 1.1: Dependence of the distance measures on redshift for two alternative cosmologies, an $\Omega_m = 1$ EdS universe and a dark energy dominated (for the special $w = -1$ case) $\Omega_m = 0.2$, $\Omega_\Lambda = \Omega_{de} = 0.8$. Figure from Bartelmann and Schneider (2001).

For an object at redshift z_2 the surface area of a sphere of radius $\mathcal{R} = a(z_2)S_k[D_{com}(z_1, z_2)]$ centred on the object will be $A = 4\pi\mathcal{R}^2 = 4\pi a^2(z_2)S_k^2[D_{com}(z_1, z_2)]$ and the angle subtended would be 4π so that:

$$\frac{dA}{4\pi a^2(z_2)S_k^2[D_{com}(z_1, z_2)]} = \frac{d\Omega}{4\pi}. \tag{1.54}$$

The angular diameter distance can then be defined as:

$$D_{ang}(z_1, z_2) = a(z_2)S_k[D_{com}(z_1, z_2)]. \tag{1.55}$$

Commonly written, for an observer at $z_1 = 0$, an object with redshift z will have:

$$D_{ang}(z) = (1 + z)^{-1}S_k[D_{com}(z)]. \tag{1.56}$$

Luminosity Distance. In a similar way to the angular diameter distance the luminosity distance can be defined in terms of a Euclidean analogy. The luminosity distance can be conceptualised as the distance that a source *would* be at *if* the inverse-square law always held, and is related

to the observed flux S and luminosity L of a source by:

$$D_{lum} = \left(\frac{L}{4\pi S}\right)^{1/2}. \tag{1.57}$$

In terms of D_{ang} and D_{com} the luminosity distance is given by:

$$D_{lum}(z_1, z_2) = \left[\frac{a(z_1)}{a(z_2)}\right]^2 D_{ang}(z_1, z_2) = \frac{a(z_1)^2}{a(z_2)} S_k[D_{com}(z_1, z_2]. \tag{1.58}$$

Commonly written, for an observer at $z_1 = 0$, an object with redshift z will have:

$$D_{lum}(z) = (1 + z) S_k[D_{com}(z)]. \tag{1.59}$$

Equation (1.58) can be understood in terms of three factors. Firstly the photons are cosmologically redshifted by a factor $a(z_1)a(z_2)^{-1}$, secondly there is a shift in frequency due to time dilation that contributes a further $a(z_1)a(z_2)^{-1}$. Finally the size of a sphere, centred on an observer, on which photons arrive will increases in area between z_1 and z_2 by a factor of $[a(z_1)a(z_2)^{-1}]^2$. Combining these effects yields a total factor of $[a(z_1)a(z_2)^{-1}]^4$ in flux, hence $[a(z_1)a(z_2)^{-1}]^2$ in equation (1.58). An alternative, heuristic, explanation of equation (1.59) in relation to equation (1.56), states that there is both a relativistic redshift *and* a Doppler shift of emission, each of which contributes an attenuation factor of $(1 + z)$ in luminosity.

All these distance measure depend on cosmology and each of them differ in their functional redshift dependence, although locally they all approximate Hubble's law to first order. Expanding any one in z using a Taylor expansion yields: $D(z) = \frac{cz}{H_0} + O(z^2)$. For a diagram of how each of these distance measures depend on redshift and Cosmology see Figure 1.1.

1.4 The Early Universe

This Section will review the early Universe. Unfortunately in order to explain some aspects of the very early Universe some later (chronologically) phenomenon first need to be explained. The order of explanation, then, is logical (and approximately chronological in terms of the history of cosmology) though not cosmologically chronological. The initial singularity[9] is not discussed, however it should be noted that there are quantum-gravity proposals (dealing with Planck scale physics), for example superstring and braneworld theories, that either negate the need for a singularity or attempt to explain it.

[9]Penrose and Hawking showed that the initial singularity is extremely generic if the strong energy condition $\rho c^2 + 3p > 0$ is satisfied; it should be noted that in some dark energy scenarios this is not the case.

1.4.1 Cosmic Microwave Background

The Cosmic Microwave Background (CMB) is an extremely isotropic source of microwave radiation. Its spectrum corresponds to a perfect blackbody, at a temperature of $T_0 = 2.728 \pm 0.004K$, as measured by *WMAP* (Spergel et al., 2003). Using the current temperature and $E_{rad} = \rho_{rad}c^2 = \alpha T^4$, the density of radiation (photons) can be calculated:

$$\Omega_{rad} = 2.47 \times 10^{-5} h^{-2}. \tag{1.60}$$

Since $\rho_{rad} \propto a^{-4}$ the temperature evolution of the Universe can be seen to be:

$$T = \frac{T_0}{a}; \tag{1.61}$$

the Universe cools as it expands. Or, at very early times the temperature was very high, hence the 'Hot Big Bang' theory. The CMB, therefore, is the expansion-cooled radiation left from the early, hot, epoch of the Universe. The CMB's discovery by Penzias & Wilson (1965) was the first direct observational evidence for the Hot Big Bang.

By deduction there must have existed, then, an epoch at which the Universe's ambient radiation temperature corresponded to an energy equal to the ionisation potential of Hydrogen, 13.6 eV. At this stage the Universe was a very energetic 'sea'[10] of particles and radiation (and dark matter and dark energy): a hot ionised plasma. The particles were mainly electrons and protons; at earlier times more 'fundamental' particles freely existed (i.e. quarks) when the ambient energy corresponded to those particles rest mass energies. The radiation and free electrons were coupled via Thompson scattering, and due to high density of electrons the mean free path of the photons was very short i.e. the Universe was 'opaque'. Furthermore any Hydrogen atoms that formed were readily ionised by the ambient photons.

As the Universe expanded and cooled, see equation (1.61), and the ambient photons' energy decreased there came a point where the energy of the photons was no longer sufficient to ionise Hydrogen. At this point, and within a relatively small amount of time, all of the electrons and protons combined to form neutral Hydrogen (and some other isotopes see Section 1.4.3), the photons were then free to move unimpeded through the Universe. This process is known as **decoupling** and occurred at a temperature of $\sim$ 2500K, when the Universe was approximately 379 ± 8 thousand years old (Spergel et al., 2003). The decoupled photons are the photons that constitute the CMB. The highly thermal state from which they originate explains the CMB's

[10] Meant to describe a uniform, continuous fluid that filled all of space in this context.

blackbody spectrum. The celestial surface from which the CMB's photons arrive, essentially unimpeded since the time of decoupling, is known as the **surface of last scattering**[11].

1.4.2 Matter-Radiation Equality

At early times the Universe was dominated by radiation, and at the present epoch it is dominated, *neglecting dark energy*, by matter. This can be explained be considering their respective density evolutions $\rho_m \propto a^{-3}$ and $\rho_{rad} \propto a^{-4}$. Including relativistic neutrinos the total relativistic density is $\Omega_{rel} = 4.2 \times 10^{-5} h^{-2}$, so that the total contribution from non-relativistic matter sources is $\Omega_{non-rel} \approx \Omega_m \approx \Omega$. So that the ratio of the contribution of the components is:

$$\frac{\Omega_{rel}}{\Omega_{non-rel}} = \frac{4.2 \times 10^{-5} h^{-2}}{a\Omega}. \tag{1.62}$$

From this equation it can immediately be seen that there will exist a scale factor (or corresponding time) when the contributions from matter and radiation were equal:

$$a_{equal} = \frac{1}{24000 \Omega h^2}, \tag{1.63}$$

the so called epoch of **matter-radiation equality**. Using equation (1.61) it can be seen that at decoupling $a_{dec} \approx \frac{1}{1000}$.

1.4.3 Nucleosynthesis

By considering equation (1.61) the deduction can be made that at some point the temperature of the Universe was equal to that of the interior of the Sun, where nuclear reactions occur. Primordial nucleosynthesis describes the production of the light elements during this epoch, here briefly reviewed. In a similar way to the process of decoupling, before $\sim$ 400 seconds the energy of the ambient photons ($\sim 0.1\text{MeV}$) was such that any nuclei that formed would be disassociated as the photon energy was greater than the binding energy of the nuclei. When the temperature fell nucleosynthesis became possible, this occurred at a temperature which was low enough that the nucleons, protons and neutrons, were non relativistic, $kT \ll m_{nucleon} c^2$. The relative population numbers of the nucleons is described by a Maxwell-Boltzmann distribution:

$$\frac{N_n}{N_p} = \left(\frac{m_n}{m_p}\right)^{3/2} \mathrm{e}^{-(m_n - m_p)c^2/kT} \tag{1.64}$$

[11] The photons were initially at a visible wavelength of 0.5 microns. Note this due to the evolutionary advantage of being able to see photons that have decoupled from a plasma (the Sun's photosphere).

where subscripts n and p refer to neutrons and protons respectively, and $m_p = 938.3\text{MeV}$ and $m_n = 939.6\text{MeV}$. While the temperature remained high enough i.e $kT \gg (m_n - m_p)c^2 = 1.3\text{MeV}$ the protons and neutrons will be in thermal equilibrium, and the population numbers will be nearly equal. The decay of a neutron to a proton occurs via β^- decay:

$$n \rightleftharpoons p + e^- + \bar{\nu}_e + 0.8\text{MeV}. \tag{1.65}$$

Free neutrons decay via the rightward reaction with a half life of 940 seconds. The nucleon plasma remains in thermal equilibrium, via equation (1.65), whilst the temperature remains 0.8MeV or higher. Once the temperature drops below 0.8MeV the leftward reaction in equation (1.65) becomes harder, this process is known as **freeze-out** i.e. the neutrons 'froze out' of the plasma at this point. At this stage, using equation (1.64), the relative populations were $N_n/N_p \approx 0.2$. The production of light elements then proceeds through a series of two-body reactions like:

$$\begin{aligned} n + p &\leftrightarrow \text{D} + \gamma \\ \text{D} + \text{D} &\leftrightarrow {}^3\text{He} + n \\ {}^3\text{He} + n &\leftrightarrow {}^3\text{H} + p \\ {}^3\text{H} + \text{D} &\leftrightarrow {}^4\text{He} + n. \end{aligned} \tag{1.66}$$

The crucial step in this process is the production of Deuterium. The binding energy of Deuterium is low, 2.2MeV, and it is readily disassociated until the temperature drops to 0.1MeV, the corresponding age of the Universe at this point is 400 seconds. By this time a portion of the neutrons would have decayed via the rightward reaction in equation (1.65) so that the actual nucleon ratio is, via a standard decay rate equation:

$$\frac{N_n}{N_p} = 0.2 \times \text{e}^{(-400\text{s})/(\ln 2\ 940\text{s})} \approx \frac{1}{7}, \tag{1.67}$$

where the $\ln 2$ factor converts the half-life to an exponential decay time.

Almost all of the neutrons end up in Helium-4 nuclei, see equation (1.66), as this is the most stable light nucleus. So that the relative primordial Helium abundance Y_4 can be calculated:

$$Y_4 = \frac{2N_n}{N_n + N_p} = \frac{2}{1 + (N_n/N_p)} \approx 0.25, \tag{1.68}$$

where the factor of two arises because there are an equal number of protons and neutrons in the Helium-4 nucleus. So, 25% of baryonic matter is predicted to be Helium-4. The abundances of the other light elements (Deuterium, Helium-3, Lithium-7 and Beryllium-7) can also be

calculated. Observations have confirmed the predicted cosmological relative abundances of the lightest elements; which is further evidence is support of the Hot Big Bang theory.

The primordial abundance of the light elements depends on the amount of photons and baryons in the Universe. Heuristically because this affects the 'destruction rate' of Deuterium, more rigorously because it depends on the reciprocal of the entropy per baryon η which is related to the density of baryons, Ω_b, see Peacock (1999):

$$\eta \equiv \frac{n_p + n_n}{n_\gamma} = 2.74 \times 10^{-8} (T_{CMB}/2.73K) \Omega_b h^2. \tag{1.69}$$

Observational evidence from absorption lines in the line of sight to high redshift quasars (e.g. Yahata et al., 2005) and from CMB observations (Spergel et al., 2003) has constrained the baryon density to be $\Omega_b h^2 = 0.024 \pm 0.001$.

1.4.4 Baryogenesis

So far it has been assumed that photons outnumber baryons by a large fraction. Given that antimatter has been created in high energy particle physics experiments (see for example Krasnikov & Matveev, 1997) it is reasonable to assume that such naturally occurring reactions in the early Universe would also have created antimatter. It is theorised that matter and antimatter would have frozen-out in an analogous way the neutron freeze-out in nucleosynthesis, the mutual annihilation of which produced the primordial photons. Given the self-evident observation that matter exists, there exists then an **matter-antimatter asymmetry** in the Universe, the outstanding question then is: why were matter and antimatter created in unequal amounts? The observed photon to baryon ratio, see equation (1.69), suggests that there were $1 + O(10^{-9})$ protons for every antiproton.

In is generally assumed that such an asymmetry must arise via some reaction at high energy when $kT \gg m_p c^2$ ($\sim 10^{15}$GeV) when a nucleon anti-nucleon plasma existed:

$$\begin{aligned} \gamma + \gamma &\rightleftharpoons p + \bar{p} \\ \gamma + \gamma &\rightleftharpoons n + \bar{n} \end{aligned} \tag{1.70}$$

The asymmetry producing reaction must satisfy the **Sakharov conditions**:

- $\Delta B \neq 0$;

- Charge-Parity (CP) violation;
- non-equilibrium conditions.

The first condition, that baryon number not be conserved, is in some sense self evident as baryons have to be produced some how. Such non-baryon number conserving reactions have been proposed by some Grand Unified Theories (GUT's) using supersymmetry[12]. The second condition requires that there exist a necessary asymmetry between matter and antimatter. The CP operation relates a particle to its antiparticle equivalent, a CP-violating process produces matter and antimatter in unequal quantities. One such process, the decay of kaons K_0 and anti-kaons $\bar{K}_0$ has been observed in particle physics experiments. The third condition is naturally provided by the expanding Universe whose ambient energy decreases with time, providing the potential for previously thermally equilibrated leftward reactions (i.e. photons to particles) to become frozen-out. There are a number of theories that attempt to explain baryogenesis (for a recent, circa 2006, and extensive pedagogical review see Cline, 2006), the two main alternatives are GUT and Electroweak baryogenesis.

1.4.5 Inflation

The idea of Inflation was first created by Guth (see Guth, 1997) from investigations in particle physics relating to the supercooling of scalar Higgs fields in the early Universe[13]. It was realised that if such a supercooled[14] field had ever existed the it would have caused an exponential expansion of the Universe. It was realised that if such an exponential expansion had occurred in the early Universe then a number of outstanding cosmological problems, that were not addressed by standard Cosmology, at the time, could be solved. The most commonly cited problems are outlined here, for a full description of all the problems see Guth (1997) or Peacock (1999).

The Horizon Problem. This can be summarised in the expression that the Universe is, naively, *too* isotropic. As Section 1.4.1 discussed the CMB is extremely isotropic, however in FRW cosmology there is no way in which different parts of the CMB, at opposite points on the sky, could

[12] In which for every baryon there exists a supersymmetric leptonic partner and vice versa.

[13] Starobinsky did propose an alternative Inflationary mechanism, involving modifications to the geometric part of the Einstein equation, slightly earlier than Guth. However it did not highlight the potential solutions to the horizon, flatness and monopole problems that were explicitly pointed out by Guth.

[14] Existing in a 'false vacuum' state. 'False' in this context means temporary.

have been in causal connection. The very fact that CMB photons from opposite parts of the sky are only reaching us now implies that no signal (faster than light) could have been exchanged between them. The problem is exacerbated when we consider that a thermal equilibrium must have been established before the time of decoupling, by which time a given photon could have travelled even less distance. In fact, regions on the surface of last scattering separated by more than 1 or 2 degrees could not have been in causal contact. The horizon problem is then: how did regions of the CMB, apparently causally disconnected, become thermally equilibrated?

The Flatness Problem. Rearranging equation (1.34) the following can be obtained:

$$|\Omega(t) - 1| = \frac{|k|c^2}{a^2 H^2}, \tag{1.71}$$

so that if $\Omega = 1$ initially then its evolution will be negligible and it will remain at this value indefinitely. Using the solutions for a and H for radiation and dust the evolution of Ω for each fluid can be written:

$$\begin{aligned} |\Omega(t) - 1|_{rad} &\propto t \\ |\Omega(t) - 1|_{m} &\propto t^{2/3}, \end{aligned} \tag{1.72}$$

ignoring dark energy for demonstrative effect (although for $t \to 0$ dark energy effects are negligible). In either model $|\Omega - 1|$ is amplified with time. If initially $\Omega < 1$ then it will become increasing small with time, if initially $\Omega > 1$ then it will likewise increases with time. Alternatively if there existed *any* initial geometric curvature then the curvature should become more pronounced with time, only a 'perfectly' flat initial geometry is stable over long time scales. Observations have constrained the current total density to be $0.99 < \Omega < 1.01$, using this value and equation (1.71) retrospective constraints on earlier allowable values of Ω can be calculated (that would result in the observation we see today). At decoupling $|\Omega - 1| \leq 10^{-3}$, at nucleosynthesis $|\Omega - 1| \leq 10^{-16}$, and at the epoch of electro-weak symmetry breaking[15] $|\Omega - 1| \leq 10^{-28}$. Observational constraints suggest, then, that the geometry was initially *very* flat. The flatness problem is then: why is the global geometry of the Universe so flat?

The Monopoles Problem. This problem arose when reconciliations between proposed GUT's and standard Cosmology were attempted. Phase transitions occurred in the early Universe when the temperature cooled to a point where the local value of any scalar field became frozen at a particular (non unique) minimum energy value[16]. During very early phase transitions

[15]When photons and the weak force bosons froze out of a unifying electro-weak bosonic field.

[16]The state of a material changes at a phase transition e.g. water undergoes a phase transition at 0°C and 100°C.

symmetry breaking events are thought to have occurred; that is the vacuum energy value of particular scalar fields at different points in space freeze-out at different values (the value of the scalar field can be conceptualised as an arrow pointing in a particular direction in a particular phase space). Before the transition the scalar field values were essentially random in space, however this random variation from place to place requires energy and as the Universe cooled the scalar field values became smoothed out, with the values in neighbouring regions becoming aligned. At some points in the initially random state the scalar field values would have been zero, and the 'maximum amount of alignment' about such points is a state in which surrounding alignments all point away from the centrally zero value. These topological features are known as **monopoles** and are remnants of the previously chaotic nature of the field. Monopoles have very large energy densities, due to the central zero-value of the scalar field, so that any surviving monopoles should dominate the energy density of the Universe, Preskill (1979) showed that they would outweigh everything else in the Universe by a factor of 10^{12}. No such monopoles have been found so that the monopole problem is: given that GUT theories predict a large production rate of monopoles, why are none observed?

1.4.6 Inflationary Theory

The basic theory of inflation is: before approximately 10^{-37} seconds after the initial singularity there existed a highly energetic set of scalar fields. The energy density of these fields was in the form of a 'Mexican hat' (see Figure 1.2) in standard Inflation[17], and as the Universe cooled the field in at least one place became frozen at the elevated position in the 'centre' of the Mexican hat. This is the false vacuum state. As the Universe cooled the energy density could not change further (it was stuck in the false vacuum position); the field is said to have become 'supercooled'. As we previously saw in equation (1.44) a constant energy density implies a negative pressure component and an accelerated phase of expansion. The scale factor during Inflation has the de Sitter form:

$$a(t) = \mathrm{e}^{\left(\frac{\Lambda_I}{3}\right)^{1/2} t}, \tag{1.73}$$

where Λ_I approximately represents energy density of the Inflationary field, the 'Inflaton'. Indeed the Inflaton, has many of the same characteristics as some proposed fields used to explain dark energy. This accelerated phase of expansion lasted until the field rolled down to a min-

[17] Or as a smooth slope in chaotic Inflation, I will deal only with standard Inflation here as a pedagogical example. Note that chaotic Inflation, in which a there is a simple power law potential with a slowly varying field, is more favourable at the present time (circa 2006).

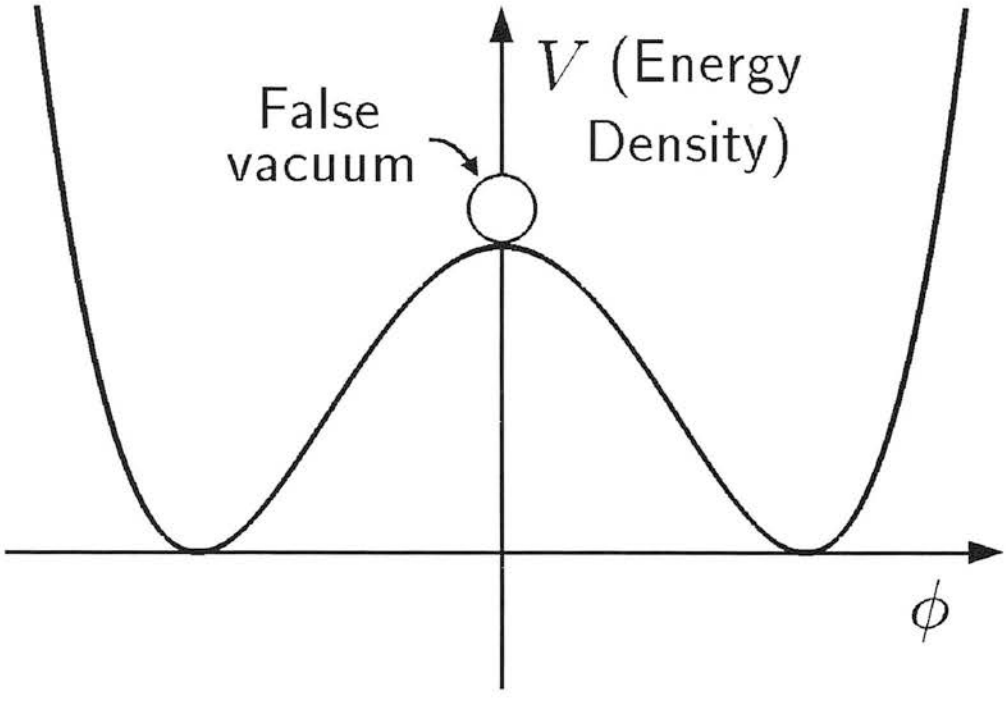

Figure 1.2: A schematic of the standard Inflationary energy potential, shown as a one-dimensional cross-section. Figure from Guth, 1997.

imum value (the 'dip' of the Mexican hat), this occurred in approximately 10^{-34} seconds in typical Inflationary models. The energy density of the Inflaton field would have been very high, characterised by the energy of the GUT scale ($\sim 2 \times 10^{16}$GeV), so that the associated magnitude of the negative pressure would have been very large. The scale factor is thought to have increased during Inflation by $a_{\text{after}} \sim \mathrm{e}^{65} a_{\text{before}}$. Furthermore *any* point which found itself in a false vacuum state would have undergone this increase[18]. Once Inflation ends the Inflaton field then decays into the familiar fundamental particles, and the standard FRW description then becomes apt.

Inflation solves the standard problems in the following ways:

The Horizon Problem. This is solved in the fact that during Inflation a very small part of the initial Universe is inflated to span the entire observable Universe. The initial, inflated, patch was small enough that it would have reached thermal equilibrium before the onset of Inflation.

[18]Motivation for some 'multiverse' theories. There are also string/brane motivated Inflationary scenarios, so called Ekpyrotic models, in which Inflation is caused by the collision of two branes within a higher-dimensional bulk.

The Flatness Problem. Since during Inflation the scale factor scales as in equation (1.73) the Ω evolution during this time can be written, using equation (1.71) as:

$$|\Omega(t) - 1| \propto \mathrm{e}^{-\left(\frac{4\Lambda_I}{3}\right)^{1/2} t}. \tag{1.74}$$

So that $|\Omega - 1|$ is driven *very* close to 0, so close that even all the subsequent expansion has not driven the value significantly away from its initial value.

The Monopoles Problem. Most Inflationary models predict monopole production before, or during, the Inflationary epoch. Therefore, even though monopoles are still within the spectrum of possible particles, the monopole density is diluted by the exponential expansion to such a degree that none exist within the observable Universe.

A further attractive feature of the Inflationary scenario is that it provides a natural explanation for the origin of structure. The gravitational collapse of an initially smooth background needs 'seed' fluctuations/perturbations about which structure can form. The Inflationary scenario attributes the origin of these fluctuations to random quantum fluctuations in the Inflaton field potential. A key prediction of Inflation is that the initial metric fluctuations are nearly scale invariant. This can be understood heuristically by considering that different parts of the Universe will have slightly different potentials at a given time (with a difference $\delta\phi$) due to random quantum processes, but that they are all part of the same rolling potential field. Different parts of the Universe will therefore exit Inflation at different times with $\delta t = \delta\phi/\dot{\phi}$. The density amplitude on the horizon scale is given by the different amounts that the separate parts of the Universe have expanded by i.e. $\delta_H = H\delta t = H^2/2\pi\dot{\phi}$ =constant. For a more detailed derivation see Peacock (1999).

1.5 The Matter Dominated Universe

After the epoch of matter-radiation equality the Universe became dominated by matter (until the onset of dark energy). Since it is self-evident that the Universe is not homogenous on *all* scales, a theory is needed in which structure can arise in the matter component of the Universe from an initially very smooth distribution (as observed by CMB measurements). Structure has been observed on the scale of individual galaxies, as well as **Large Scale Structure** (LSS) on scales of up to 100Mpc and more.

1.5.1 Structure Formation

The underlying mechanism for structure formation is that of self-gravitational collapse. Matter is thought to have begun to collapse around initial 'seed' fluctuations in the initially homogenous distribution[19]. The collapsed matter increasing the relative density of the region causing further collapse of yet more matter in an amplifying effect. The relative density (how dense an volume is relative to the mean density $\bar{\rho}$) at particular point in space, $\mathbf{x}$, can be expressed as a density contrast:

$$\delta(\mathbf{x}) = \frac{\rho(\mathbf{x}) - \bar{\rho}}{\bar{\rho}}. \tag{1.75}$$

$\delta(\mathbf{x})$ is a dimensionless density perturbation of the underlying matter distribution. Within a matter-radiation fluid there are two different types of density perturbation that can occur. **Adiabatic** perturbations can be conceptualised as what would occur if one could adiabatically compress the fluid in space, since the energy density of the radiation $\propto T^4$ and the number density is $\propto T^3$ the energy densities of matter and radiation are related by: $\delta_r = 4\delta_m/3$. **Isocurvature** perturbations within a fluid would occur when the entropy density is perturbed, but not the energy density, heuristically it can be imagined that energy that a spatial density increase creates is transferred to the radiation energy density, the respective density fields are in anti-phase. Since the total energy density remains constant there is no change in spatial curvature and: $\rho_r\delta_r = -\rho_m\delta_m$.

Fourier analysis helps to analyse the amount of perturbation on different scales, a particular 'mode' corresponding to a particular scale. The Fourier transform pair of $\delta(\mathbf{x})$ being:

$$\begin{aligned} \hat{\delta}(\mathbf{k}) &= \int d^3x \delta(\mathbf{x}) \mathrm{e}^{i\mathbf{k}.\mathbf{x}}; \\ \delta(\mathbf{x}) &= \int \frac{d^3k}{(2\pi)^3} \hat{\delta}(\mathbf{k}) \mathrm{e}^{-i\mathbf{k}.\mathbf{x}}, \end{aligned} \tag{1.76}$$

each mode is assumed to evolve independently. In general the evolution of any perturbations need to be done in a fully relativistic manner, as at early times the scale of some perturbations could have been equivalent to the curvature scale of spacetime. Structure evolution is affected by self-gravitation as well as dissipative effects and pressure. For details of the theory see Lifshitz (1946) and Bardeen (1980). The general results are that for adiabatic perturbations in

[19]There are various theoretical explanations for the initial seeds; for example quantum fluctuations amplified by Inflation, or the effect of topological defects before or during the Inflationary epoch.

the EdS régime and for $\delta \ll 1$ for a particular mode:

$$\delta \propto \begin{cases} a(t)^2 & (a < a_{eq}); \\ a(t) & (a > a_{eq}), \end{cases} \tag{1.77}$$

i.e. any initial mode perturbation grows with time through gravity. For isocurvature perturbations any expansion acts to preserve the initial uniform density:

$$\delta \propto \begin{cases} \text{constant} & (a < a_{eq}); \\ a(t)^{-1} & (a > a_{eq}). \end{cases} \tag{1.78}$$

For both cases the overall shape of the spectrum (over all modes) of the perturbations is preserved, whilst the amplitude of the spectrum changes. A number of processes affect the growth evolution.

Suppression of Growth. During the radiation dominated epoch the growth of certain modes is suppressed. These can be characterised in terms of the **horizon scale** $\lambda_H(a)$ which is the distance light could have travelled since the initial singularity ct, a comoving horizon size. A mode 'enters the horizon' when $\lambda = \lambda_H(a)$ (where $\lambda = (2\pi)/k$). If $\lambda < \lambda_H(a_{eq})$ then a mode enters the horizon during the radiation dominated epoch. The time scale for collapse of matter is larger during this epoch than the typical expansion time scale ($t \sim 1/H[a]$), due to the relatively rapid expansion $\rho_{rad} \propto a^{-4}$, so that the growth of these modes is suppressed. After the epoch of matter-radiation equality $a = a_{eq}$ these perturbations can then collapse. A suppression factor can be defined for a particular mode as the factor by which the amplitude is suppressed by had it not entered the horizon:

$$f_{sup} = \left(\frac{a_{enter}}{a_{eq}}\right)^2 = \left(\frac{k_0}{k}\right)^2, \tag{1.79}$$

where the mode evolves as $\propto a^2$ until it enters the horizon at a_{enter} and is suppressed until a_{eq} when its evolution resumes as $\propto a$; the second equality comes from applying an EdS approximation where $k_0 = 1/\lambda_H(a_{eq})$, for a full explanation see Bartelmann and Schneider (2001).

Pressure. The suppression of growth can be understood in terms of pressure. Pressure opposes gravitational collapse, for modes with a wavelength less than the Jeans length:

$$\lambda_j = c_s \sqrt{\frac{\pi}{G\rho}}. \tag{1.80}$$

During the radiation dominated epoch the sound speed $c_s = c/\sqrt{3}$ and the Jeans length is always close to the horizon scale. The Jeans length then reaches a maximum at $a = a_{eq}$ and then begins to decrease as the sound speed declines. So that on scales larger than the comoving horizon size at $z_{eq} \approx \frac{16.0}{\Omega h^2}\mathrm{Mpc}$ modes are only affected by gravity, and a change in the spectrum should appear where the effects of pressure begin to dominate, allowing for a determination of Ω.

Silk Damping. Silk damping has the affect of 'smearing out' observed perturbations on very small scales. This is due to photon diffusion in the matter-radiation fluid, the distance travelled by a photon in a random walk by the time of last scattering is $\lambda_s = 2.6(\Omega\Omega_b^2 h^6)^{-1/4}\mathrm{Mpc}$.

Non-Linear Processes. All of the processes outlined so far have a linear effect on the growth of perturbations. Non-linear evolution occurs on small scales where the local density is very much larger than the mean and gravitational collapse begins to form complex structures i.e. galaxies and galaxy clusters, see Section 1.6.1.

1.5.2 Growth Evolution with Dark Energy

The previous examples were for the specific case of an EdS universe. In general the matter perturbation field evolves according to the following equation:

$$\begin{aligned} \ddot{\delta} + 2H\dot{\delta} - (3/2)H^2\Omega_m\delta &= 0 \\ \delta'' + (2-q)a^{-1}\delta' - (3/2)\Omega_m a^{-2}\delta &= 0, \end{aligned} \tag{1.81}$$

where a dot denotes a time derivative and a dash denotes a derivative with respect to a and q is defined in equation (1.48). The physical interpretation of this equation is simple in that the perturbations grow according to a source term which involves the amount of matter but that growth is suppressed by the friction, or Hubble drag, term due to the expansion of the Universe. Note that the Hubble drag term is a pseudo-force in that no actual force is being applied to the galaxies.

Defining *growth* as the ratio of a perturbations amplitude relative to some initial amplitude $D(a) = \delta(a)/\delta(a_i)$ the equation becomes, see Linder & Jenkins (2003), in a general dark energy scenario where $w = w(a)$:

$$D'' + \frac{3}{2}\left[1 - \frac{w(a)}{1+X(a)}\right]\frac{D'}{a} - \frac{3}{2}\frac{X(a)}{1+X(a)}\frac{D}{a^2} = 0, \tag{1.82}$$

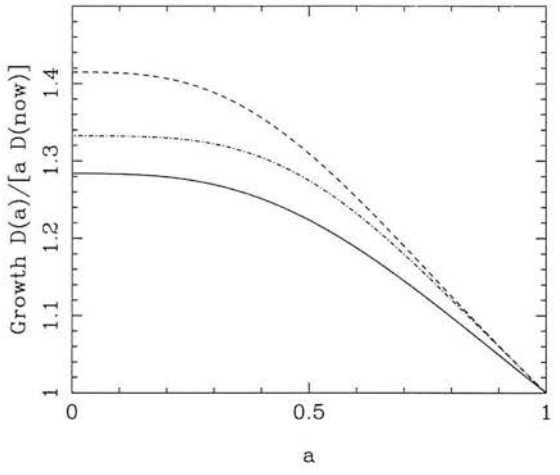

Figure 1.3: The functional form of the normalised growth factor, equation (1.84). The solid line is for $\Omega_m = 0.3$ and $w(a) = -1.0$, the dot-dashed line is $\Omega_m = 0.2$ and $w(a) = -1.0$, the dashed line is for $\Omega_m = 0.2$ and $w(a) = -1.2$

where

$$X(a) = \frac{\Omega_m}{1-\Omega_m} \mathrm{e}^{-3\int_a^1 d\ln a' w(a')} \tag{1.83}$$

is the ratio of the matter density to the dark energy density. For large X the matter dominated ($\Omega_m = 1$) $D \sim a$ behaviour is recovered. As a result a normalised growth factor $G = D/a$ can be defined see Linder & Jenkins (2003), that divides out the EdS behaviour[20]:

$$G'' + \left[\frac{7}{2} - \frac{3}{2}\frac{w(a)}{1+X(a)}\right]\frac{G'}{a} - \frac{3}{2}\frac{1-w(a)}{1+X(a)}\frac{G}{a^2} = 0. \tag{1.84}$$

In the presence of dark energy the Hubble drag term is increased, so that growth is suppressed in an accelerating universe; this is similar to the previous suppression due to the rapid expansion due to radiation dominance. For an example of the functional form of the normalised growth factor, G, in various dark energy scenarios see Figure 1.84.

1.6 The Matter Power Spectrum

Since the density field describes a homogenous and isotropic universe its statistical properties should also be homogenous. The amplitudes of the individual Fourier modes of the matter perturbation field are assumed to be uncorrelated due to homogeneity. Also, the mode amplitudes

[20]Coupling between matter and dark energy is ignored, and dark energy is treated as a smooth, non-clustering fluid.

are often assumed to be Gaussian distributed. The motivation for this assumption comes from the theoretical source of the initial seed fluctuations (quantum fluctuations), or from the central limit theorem. Such a field, with uncorrelated modes, and a Gaussian distribution of mode amplitudes, is called a **Gaussian random field** and can be *entirely* described by its two-point correlation function:

$$\langle \delta(\mathbf{x})\delta^*(\mathbf{y})\rangle = C_{\delta\delta}(|\mathbf{x}-\mathbf{y}|). \tag{1.85}$$

The angled brackets represent an *ensemble average* (over a multitude of realisations). The value of δ at a given point in the Universe will have a different value in each realisation with a variance $\langle\delta^2\rangle$. Given that we can only observe one realisation of our Universe we need to apply the principle of ergodicity. The **ergodic** condition attests that the average over a sufficiently large volume is equal to the ensemble average. The cosmological matter density field is assumed to be ergodic.

In Fourier space the correlation function can be written as:

$$\langle \hat{\delta}(\mathbf{k})\hat{\delta}^*(\mathbf{k}')\rangle = \int d^3x \mathrm{e}^{i\mathbf{k}.\mathbf{x}} \int d^3x' \mathrm{e}^{-i\mathbf{k}'.\mathbf{x}'} \langle \delta(\mathbf{x})\delta^*(\mathbf{x}')\rangle, \tag{1.86}$$

substituting equation (1.85) and replacing $\mathbf{x}' = \mathbf{x} + \mathbf{y}$ this can be rewritten as:

$$\begin{aligned} \langle \hat{\delta}(\mathbf{k})\hat{\delta}^*(\mathbf{k}')\rangle &= \int d^3x \mathrm{e}^{i\mathbf{k}.\mathbf{x}} \int d^3y \mathrm{e}^{-i\mathbf{k}'.(\mathbf{x}+\mathbf{y})} C_{\delta\delta}(|\mathbf{y}|) \\ &= (2\pi)^3\delta_D(\mathbf{k}-\mathbf{k}') \int d^3y \mathrm{e}^{-i\mathbf{k}.(\mathbf{y})} C_{\delta\delta}(|\mathbf{y}|) \\ &= (2\pi)^3\delta_D(\mathbf{k}-\mathbf{k}')P_\delta(|\mathbf{k}|), \end{aligned} \tag{1.87}$$

where the **Power Spectrum** has been defined as the Fourier transform of the correlation function:

$$P_\delta(|\mathbf{k}|) = \int d^3y \mathrm{e}^{-i\mathbf{k}.(\mathbf{y})} C_{\delta\delta}(|\mathbf{y}|), \tag{1.88}$$

$P_\delta(|\mathbf{k}|)$ is usually abbreviated to $P(k)$ where $k = |\mathbf{k}|$. The power spectrum is often quoted in a dimensionless form, as the variance per $\ln k$ so that:

$$\Delta^2(k) = \frac{k^3P(k)}{2\pi^2}. \tag{1.89}$$

A key type of power spectrum in Cosmology is the **scale invariant** power spectrum (or Harrison-Peebles-Zel'dovich spectrum). The defining characteristic of this type of spectrum is that it describes a fractal metric, where the degree of spacetime fluctuation is the same on all scales. The form of the scale invariant spectrum is $P(k) \propto k$ or $\Delta^2(k) \propto k^4$ (for a derivation of this result see Peacock, 1999). It is normally assumed that the power spectrum on large

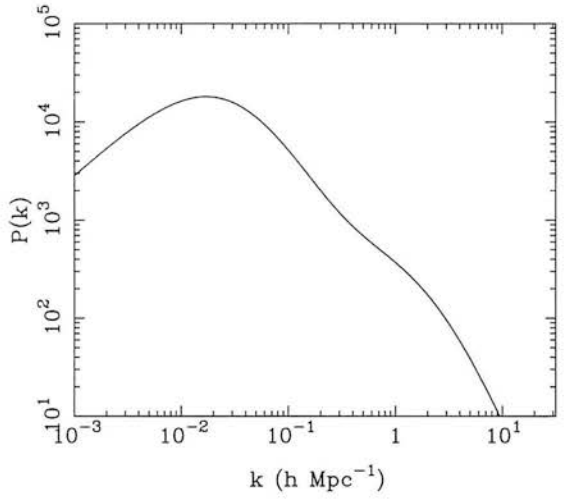

Figure 1.4: The matter power spectrum at $z = 0$ for $\Omega_m = 0.27$, $\Omega_{de} = 0.73$, $\Omega_b = 0.04$, $w(z) = -1$, $\sigma_8 = 0.8$ created using the `halofit` code.

scales should be scale invariant which implies that, combining with equation (1.79), that the general expected overall shape the power spectrum should be, in an EdS scenario:

$$P(k) \propto \begin{cases} k & (\text{for } k \ll k_0) \\ k^{-3} & (\text{for } k \gg k_0). \end{cases} \tag{1.90}$$

The general form can be seen in Figure 1.4. The actual shape of the power spectrum depends in non-trivial ways upon a variety of cosmological parameters including Ω_m, Ω_{de}, Ω_b, $w(z)$, σ_8 (see Section 1.6.2) and n_s. n_s describes the 'slope' of the linear power spectrum, $P(k) \propto k^{n_s}$, its fiducial value is taken to be 1.0 as this implies a scale invariant spectra in the linear régime.

1.6.1 The Non-Linear Power Spectrum

On small scales the linear evolution of the power spectrum breaks down. This breakdown occurs on scales at which complex structures begin to form. In this régime perturbations begin to grow non-linearly. The most influential attempt was made by Hamilton et. al (1991) (commonly referred to as HKLM), who developed the spherical collapse model. HKLM assumed that a non-linear collapsed object would form an isolated, virialised, system that had 'decoupled' from the expansion of the Universe: the 'stable clustering' hypothesis. Jain, Mo & White (1995) and Peacock & Dodds (1996) expanded on the HKLM procedure and took the approach that the non-linear power spectrum could be described by an 'scaling Ansatz'.

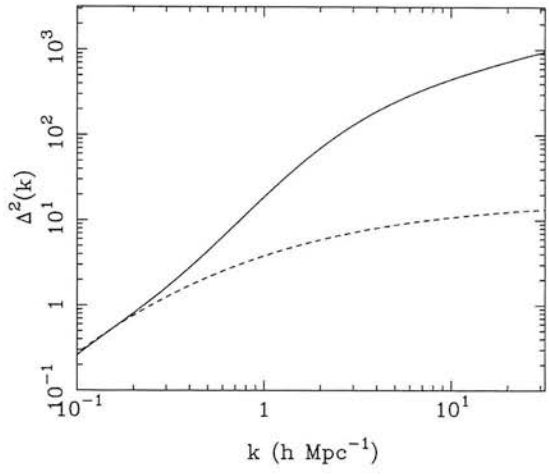

Figure 1.5: The dimensionless matter power spectrum at $z = 0$ for $\Omega_m = 0.27$, $\Omega_{de} = 0.73$, $\Omega_b = 0.04$, $w(z) = -1$, $\sigma_8 = 0.8$ created using the `halofit` code. The dashed line is the linear power spectrum the solid line is the full non-linear power spectrum.

That is an analytic function that describes the non-linear spectrum as an function of the linear spectrum:

$$\Delta_{NL}(k_{NL}) = f_{NL}[\Delta_L(k_L)], \tag{1.91}$$

where L denotes linear and NL non-linear and $k_{NL} = [1+\Delta_{NL}(k_{NL})]^{1/3}k_L$. Such functional scaling relations need to be calibrated by large N-body simulations.

Smith et al. (2003) took a different approach known as the 'halo model' (see Seljak, 2000 and Peacock & Smith, 2000). In the halo model the density field is decomposed into clumps of matter with some density profile and varying mass; the question posed is how many clumps of matter of a certain mass exist within a given volume? In this model structure arises through correlations between 'halos' of varying mass. In a similar way to the scaling Ansatz approach a functional relation between the linear and non-linear spectra was derived and calibrated using large N-body simulations. The `halofit` code is the result of Smith et al. (2003) which produces accurate power spectra which are reliable well into the non-linear régime. Figure 1.5 shows the standard linear power spectrum and how it is modified by a non-linear approach.

1.6.2 Normalisation

As well as the shape of the power spectrum, the overall normalisation of the power spectrum needs to be considered. Usually (and the approach taken here) this is done by defining the

quantity σ_8 as the rms variation of the density field when smoothed with a top-hat filter (a sphere of uniform weight) of radius $8h^{-1}$Mpc. This can be written

$$\sigma^2(R,z) = \int_0^\infty \frac{dk}{k}\Delta^2(k,z)W^2(kR) \tag{1.92}$$

where the weighting function is defined in this case as the Fourier transform of a spherical top-hot filter

$$W(k,R) = \frac{3j_1(kR)}{kR} \tag{1.93}$$

$j_1(x)$ is a spherical Bessel function of order 1, so that $\sigma_8 \equiv \sigma(8h^{-1}\mathrm{Mpc})$. Note this is the linear σ_8, describing the linear clustering of matter. This is done as the observed value of σ_8 is close to unity. There are a number of methods that have been employed in attempting to measure σ_8, not least weak lensing (see Chapter 5). For a full exposé see Brown et al. (2003).

1.7 Dark Matter

Up until this Section the identity of the 'matter' in the Universe has been alluded to but not explicitly stated. There is compelling evidence that dark matter is *non-baryonic* in nature. In Section 1.4.3 the quantity of baryonic matter in the Universe was stated as being observed to be $\Omega_b h^2 = 0.024 \pm 0.001$, but the observed value of $\Omega_m \approx 0.3$. What, then, constitutes the 'missing mass' in the Universe? The fluid component that accounts for the majority of the matter in the Universe is referred to as **dark matter**[21]. The baryons then, that which constitute all the galaxies and fine structure we observe, are a separate component with certain individual characteristics which are reviewed here. The matter power spectrum, of Section 1.6 is, in fact, dominated by dark matter clustering on large scales, the halos referred to in the halo model are in fact dark matter halos. The evidence for the extraordinary claim that over 90% of matter in the Universe is dark and non-baryonic is reviewed here.

1.7.1 Evidence for Dark Matter

Here is reviewed the evidence for dark matter.

Galaxies and the Sachs-Wolfe effect. As reviewed in Section 1.4.1 the level of anisotropies in the CMB is of the order 10^{-5} on large scales. These anisotropies are mainly due to an ef-

[21] An allusion to the fact that it does not, apparently, emit light. Also to its unknown nature.

fect known as the Sachs-Wolfe effect in which anisotropies in the CMB photons are related to anisotropies in the baryonic density field. If at decoupling a CMB photon is at the bottom of a baryonic potential well it will become gravitationally redshifted as is propagates out. This redshift is manifested as a temperature variation. Observation the of amplitude of the CMB anisotropy leads, by inference to the conclusion that the baryon density field had a similar variation at the time of decoupling. Using equation (1.77) the amplitude of the density fluctuations should have reached $\sim 10^{-2}$ by the present time. Clearly structures with $\delta \gg 1$ exist in the Universe at the present time (galaxies and galaxy clusters), the discrepancy then is how did these structures arises so swiftly. A solution is that there already existed potential wells for the baryons to fall into after the decoupling of photons and baryons. These potential wells could have been formed by a *weakly interacting* fluid that decoupled well before baryons and began to cluster much earlier: dark matter (this fluid would have the property that it only interacts via the gravitational force and possibly the weak nuclear force). The baryons then fall into the dark matter potential wells, enabling $\delta \gg 1$ structure by the present day.

Rotation Curves. The rotation curve of a galaxy relates the tangential velocity of its constituent stars (or gas etc.) about its centre to the radius of the stars from the centre. Using a simple Newtonian argument (valid since the gravitational field is weak) the expected shape is:

$$v(r) = \sqrt{\frac{GM(<r)}{r}}, \tag{1.94}$$

where the velocity $v(r)$ is related to the radius of an objects orbit r, $M(<r)$ is the mass contained within the orbit. So that at large radii, when the majority of the galaxy is within the orbit, the velocity should decrease as $v \propto r^{-1/2}$. However observations of the velocities of globular clusters about galaxies show that at large radii the velocities are approximately constant, this implies that $M \propto r$ and that the amount of mass in galaxies is much larger than the visible component. The difference being attributed to some non-emitting component: dark matter. The total mass-to-luminosity ratio ('mass to light' ratio, M/L) shows how much more mass than purely visible mass exists, in galaxies $M/L \sim 30hM_\odot/L_\odot$ for galaxy clusters $M/L \sim 200hM_\odot/L_\odot$. The missing mass could, in this case, be comprised of MAssive Compact Halo Objects ('MACHOs') (e.g. brown dwarfs or black holes[22]) but recent observations of microlensing events around the Milky Way have concluded that the density of such objects cannot account for the majority of the missing mass see Alcock et al. (2000), Lasserre et al. (2000), Zebrun et al. (2001). Less that $\sim 10\%$ of the halo mass of the Milky Way is comprised

[22]One candidate for such black holes, primordial black holes, are predicted by some theories to be created before Nucleosynthesis.

of MACHOs.

Nucleosynthesis. As seen in Section 1.4.3 the density of baryons is restricted by the observed elemental abundances to $\Omega_b h^2 = 0.024 \pm 0.001$. From Section 1.4.5 it is also theoretically, and observational well motivated to assume that the Universe has close to critical mass. The majority of the Universe, then, must be non-baryonic in nature, at least some of which may be dark matter (in fact most is dark energy at the present epoch).

Peculiar Velocities. The peculiar velocity of a galaxy is that motion it has relative to the Milky Way, which is not due to the Hubble flow, assumed to be due to gravitational attraction. Observed motions of galaxies and the velocity field of the local Universe imply that $\Omega_m \geq 0.3$ see Hawkins (2001). This, coupled with the Nucleosynthesis constraints, imply a non-baryonic massive fluid component: dark matter.

Gravitational Lensing. See Chapter 2 for a detailed description of gravitational lensing. Observations of lensed galaxies about galaxy clusters show that the amount of lensing (dependant on the amount of mass in the cluster) is larger than that which can be accounted for by the visible matter in the cluster (observations in X-rays can discount the possibility that such missing mass is due to a large gas component). Both strong lensing (e.g. Hamana, 2005) and weak lensing (e.g. Taylor et al., 2004) results have observed evidence for dark matter in galaxy clusters.

Acoustic Oscillations. Before the surface of last scattering when the baryonic matter began to fall into the already formed dark matter potential wells pressure would have built up as baryons accumulated. As the baryons constitute an incompressible fluid eventually the in-falling baryons 'bounced' out of the potential well. Oscillations in the in-fall of baryons (as they collapsed then bounced etc.) are known as baryonic oscillations. Since the temperature of baryons is related to their pressure (and the photons were coupled to the baryons) there should exist features in the CMB temperature power spectrum corresponding to the baryonic oscillations; so called acoustic oscillations see Meisken, White & Peacock (1998). Such features have now been observed in the CMB power spectrum implying the existence of dark matter (Spergel, 2003). Remnants of the baryonic oscillations are also present in the matter power spectrum, see Section 1.8.2 and Eisenstein (2005).

1.7.2 Dark Matter Candidates

There are a number of dark matter candidates. The consensus (circa 2006) is that dark matter is a fluid which only interacts with normal matter via the gravitational force and is itself weakly self-interacting. Such a fluid is usually assumed to be comprised of a sea of Weakly Interacting Massive Particles (WIMPs)[23]. Particle physics provides a number of potential candidates including heavy neutrinos or some kind of stable supersymmetric particle; the lightest supersymmetric particles are thought to be stable (due to R-parity). Since by definition the cross-section of such particles must be small they are very difficult to directly detect, attempts such as DAMA (see Bernabei et al., 2003) and the Cryogenic Dark Matter Search (CDMS, 2005) have placed bounds on the mass of the dark matter particle to be $10\text{GeV} \leq M_{WIMP} \leq 100\text{GeV}$. 'Cold' dark matter refers to non-relativistic particles, the most promising candidate being the supersymmetric neutralino (a superposition of the gravitino, photino and wino). 'Hot' dark matter refers to relativistic particles the most promising candidate being a massive neutrino, however if dark matter were entirely hot then structure could not have formed as formation would have been damped by the relativistically moving particles. Indeed Berezinsky et al. (2002) have attempted to measure the density of primordial neutrinos and concluded that $\Omega_\nu \ll \Omega_M$ implying that hot dark matter cannot account for the dark matter density.

The cosmological paradigm, then, is that the majority of the mass in the Universe is comprised of Cold Dark Matter (CDM), whose presence is likely but whose identity is still unknown. However, given that Inflation predicts $\Omega \approx 1$, which has been confirmed by observations to within 1%, and that even with CDM $\Omega_m \approx 0.3$ there must be *another* non-baryonic component of the Universe, accounting for $\Omega \approx 0.7$: dark energy.

1.8 Dark Energy

From the introductory review of Cosmology thus far it should be clear that there exists a discrepancy between the inference of flatness ($\Omega \approx 1$) and of the matter density of the Universe ($\Omega_m \approx 0.3$). The must exist another component, alluded to in Section 1.2.3 with $\Omega_{de} \approx 0.7$, which has been observed to be causing an isotropic acceleration of the Universe. This is the so

[23] A once on-going cosmological debate was whether dark matter could be explained by MACHOs or WIMPs.

called 'dark energy'[24] component of the Universe, and is the dominant form of energy during the present epoch. The negative pressure nature of dark energy has the effect that the present epoch's expansion rate is *accelerating*. In this Section the formulation of dark energy within standard Cosmology, evidence for dark energy, and some possible candidates will be reviewed.

1.8.1 Historical Remarks

The history of the idea of dark energy is long and insightful. For a comprehensive review see Peebles and Ratra (2003), I will briefly mention some of the highlights here. The first incarnation of dark energy was as a correction to GR (a correction to the geometric part of the field equation): the cosmological constant, Λ. At the time the formalism predicted an non-static Universe which Einstein felt to be in opposition to his belief in a static Universe[25]. Slipher's measurements of the spectra of the 'spiral nebulae' subsequently showed that most were shifted towards the red, and Hubble later published the linear redshift-distance relation. In light of these observations, and others, Einstein later withdrew his support for the cosmological constant.

As early as 1934 Lemaitre and Eddington make the point of associating Λ with the vacuum or dark energy density – energies measured in laboratories are energy *differences* whereas it is the *net* energy density which matters in cosmology. Complementary, as early as 1916 Nerst addressed the problem of the zero-point energy field in statistical mechanics, this idea was refined by Pauli in the 1920's as part of quantum physics. Zel'dovich (1967) was the first to convincingly suggest a connection between the zero-point energy density in quantum physics and Einstein's cosmological constant. If the vacuum properties are observed to be same by any inertial observer then the vacuums contribution to the stress-energy tensor, in GR's field equation, is the same as Einstein's cosmological constant.

Observations in the 1980's and 1990's precipitated a number of problems with the cosmological view at the time – that of a purely matter dominated, expanding Universe with a present day Hubble constant of $H_0 \simeq 70$ kms^{-1} Mpc^{-1}. The 'age problem' was that certain stars seemed to have ages that were older than the predicted age of the Universe. The CDM power spectrum could not be made to fit observations in detail. Whereas the Inflationary scenario, which has

[24] Some authors refer to 'vacuum energy', 'quintessence' or the cosmological constant explicitly – I will use 'dark energy' as it retains the most ambiguity.

[25] Born from evidence available at the time.

considerable observational and theoretical motivation, predicted a $\Omega_{total} = 1$, flat, Universe. Two models were considered to hold a possible resolution to these problems: one was ΛCDM in which the Universe has a contribution to the energy density from a cosmological constant-like term, and a ν+CDM model in which the 'missing' mass came from a massive neutrino ($m_\nu \simeq 7eV$).

In 1998 observations of the luminosities of Type-Ia supernovae indicated that, in fact, the isotropic expansion of the Universe appears to be accelerating – one effect of dark energy. Since then further observations[26] of the CMB, X-Ray clusters and simulations of large scale structure all indicate a ΛCDM Universe with a dark energy density of $\Omega_{de} \simeq 0.7$.

1.8.2 Evidence for Dark Energy

The evidence that the present epochs expansion rate is accelerating is now compelling. Here the primary, current (circa 2006), results that provide evidence for the existence of dark energy are summarised. All these techniques also have the ability to constrain the dark energy equation of state, given more data from future experiments.

Apart from cosmological observations the theoretical expectation that some form of dark energy should exist, as either a cosmological constant or as a vacuum energy is strong. As already discussed particle physics predicts that some form of zero-point energy should exist, and evidence for Inflation suggests that scalar fields may have existed in nature during the early Universe. So the existence of a dark energy scalar field now would not be a departure from already proposed physics[27]. Also, see Ishak (2005), the equations of GR in their most general form suggest a cosmological constant (of some magnitude) in their own right. The only tensor of rank two that can be constructed from $g^{\mu\nu}$ and its first two derivatives (linear in the second derivative), is divergent-free and symmetric is: $A^{\mu\nu} = c_1 G^{\mu\nu} + c_2 g^{\mu\nu}$ where c_1 and c_2 are constants, this should be compared with equation (1.95). This could be used as an argument for identifying some dark energy with a cosmological constant of some magnitude on theoretical grounds. It should be stressed that a vacuum energy with an equation of state the same as a cosmological constant is not a cosmological constant and vice versa.

[26] Including observations of neutrino mass which indicate $m_\nu \ll 7eV$, thus discounting the ν+CDM model. Observations have been direct (e.g. SuperKamiokand; Beacom & Vogul, 1999) and indirect (e.g. WMAP 3-year data; Spergel et al. , 2006).

[27] Also mesons (quark–antiquark pairs) can be described using a scalar field.

Type-Ia Supernovae. In 1998 the first convincing evidence for dark energy came from Type-Ia supernovae (SNIa) (see Riess et al., 1998 and Perlmutter, et al., 1999). SNIa are used as 'standard candles' to effectively place constraints on the luminosity distance relation see equation (1.59). This can be done since the intrinsic luminosity of a SNIa is constant and relies on relatively simple nuclear physics. SNIa occur in white dwarf–main sequence binaries, where a flow of material accretes from the main star onto the dwarf, when the mass of the dwarf approaches the Chandrasekhar limit ($1.4M_{\odot}$) a Carbon fusion is initiated, emitting a large, specific, amount of energy that is observed as a SNIa, although the details of the theory are not well understood. Crucially SNIa distances can be calibrated to within 7%, and their luminosity is bright enough that they can be distinguished from the host galaxies over cosmological distances. Using this technique, and effectively constraining the Hubble diagram, both Riess (1998) and Perlmutter (1999) found evidence for a present acceleration. Further SNIa results, for example Knop et al. (2003), have found the same result.

Cosmic Microwave Background. By measuring the temperature anisotropies in the CMB power spectrum tight constraints can be placed on a variety of cosmological parameters, see Verde (2003) and Hinshaw (2003). Particularly, the geometry of the Universe can be measured to a high degree of accuracy. The *WMAP* experiment, see Spergel et al. (2003), observed the CMB power spectrum to an unprecedented resolution and constrained the combination $\Omega_{de}+\Omega_m$ to be $\Omega_{total} = 1.02 \pm 0.02$, as well as the baryon density $\Omega_b h^2 = 0.024 \pm 0.001$ and the matter density $\Omega_m h^2 = 0.14 \pm 0.02$. This, independently, constrains the dark energy density to non-zero, and when combined with other cosmological tests (see Figure 1.6) constrains the dark energy density to a high degree of accuracy. CMB photons should also be affected by large scale structure, as a CMB photon enters the potential well of a galaxy cluster it should be blue shifted, as it leaves the well it should be redshifted. Any evolution of the potential well, due to dark energy for example, will result in a discrepancy between the amount of blue shifting and red shifting. This is known as the Integrated Sachs-Wolfe (ISW) effect and occurs on large angular scales in the CMB. Also, by correlating LSS and ISW measurements the equation of state of dark energy can be constrained.

Large Scale Structure. Observations of the Large Scale Structure (LSS) in the local Universe, for example SDSS (e.g. Tegmark et al., 2003) and 2DFRGS (e.g. Sanchez et al., 2005), have allowed the matter power spectrum see Section 1.6 to be observed. These surveys spectroscopically observe a large number of galaxies (approximately a million), covering a large areas of the sky, so that the redshift to each galaxy can be deduced. By assuming that the galaxies trace

the underlying dark matter structure, constraints can be placed upon the form of the matter power spectrum, at various redshifts; or equivalently the full three-dimensional matter power spectrum see Percival (2002). These techniques are particularly useful for placing constraints on Ω_m, as this affects the growth of the matter power spectrum. When constraints of Ω_m are combined with flatness constraints the dark energy density can be constrained, see Figure 1.6.

Acoustic Oscillations. As outlined in Section 1.7.1 remnants of the baryonic acoustic oscillations (BAO) should be present in the matter power spectrum. If such oscillations can be observed (see Eisenstein, 2005), then these will be an excellent measure of the angular diameter distance (as they should occur on characteristic length scales) see equation (1.55), and the growth function of the matter power spectrum equation (1.84). Both these effects depend on the density and nature of dark energy allowing constraints of $w(z)$ and Ω_{de}. The CMB provides the size of the oscillations as a standard length scale that can then be measured in the clustering of galaxies. Such oscillations have not yet been conclusively observed but future experiments, for example WFMOS (Bassett et al., 2005), should constrain the matter power spectrum to a sufficient accuracy.

Currently accepted constraints on Ω_{de} are: $\Omega_{de} = 0.72 \pm 0.04$, so that the *existence* of dark energy is likely. However the *nature* of the dark energy, parameterised by w_0 and w_a (see Section 1.8.5) is poorly constrained: see Wang and Tegmark (2004) and Jassal et al. (2005). Even assuming a constant $w(z)$ (which hides potentially important physical information) the current combined constraint (from CMB, LSS and SNIa; Spergel et al., 2006) is: $w(\text{constant}) = -1.06^{+0.13}_{-0.08}$.

1.8.3 The Cosmological Constant

The cosmological constant is a particular example, and a distinct possible explanation for, dark energy. The cosmological constant enters the GR field equations (1.13) simply as an additive term:

$$G^{\mu\nu} + \Lambda g^{\mu\nu} = -\frac{8\pi G}{c^4} T^{\mu\nu}, \tag{1.95}$$

where Λ is a new gravitational constant, the **cosmological constant**. It is this modification that allowed Einstein to reconcile GR with a static Universe, by providing a negative pressure which can act to counter the self-gravitation between matter acting to collapse the Universe (in the static case). In the form of equation (1.95) the dark energy, a cosmological constant, is a

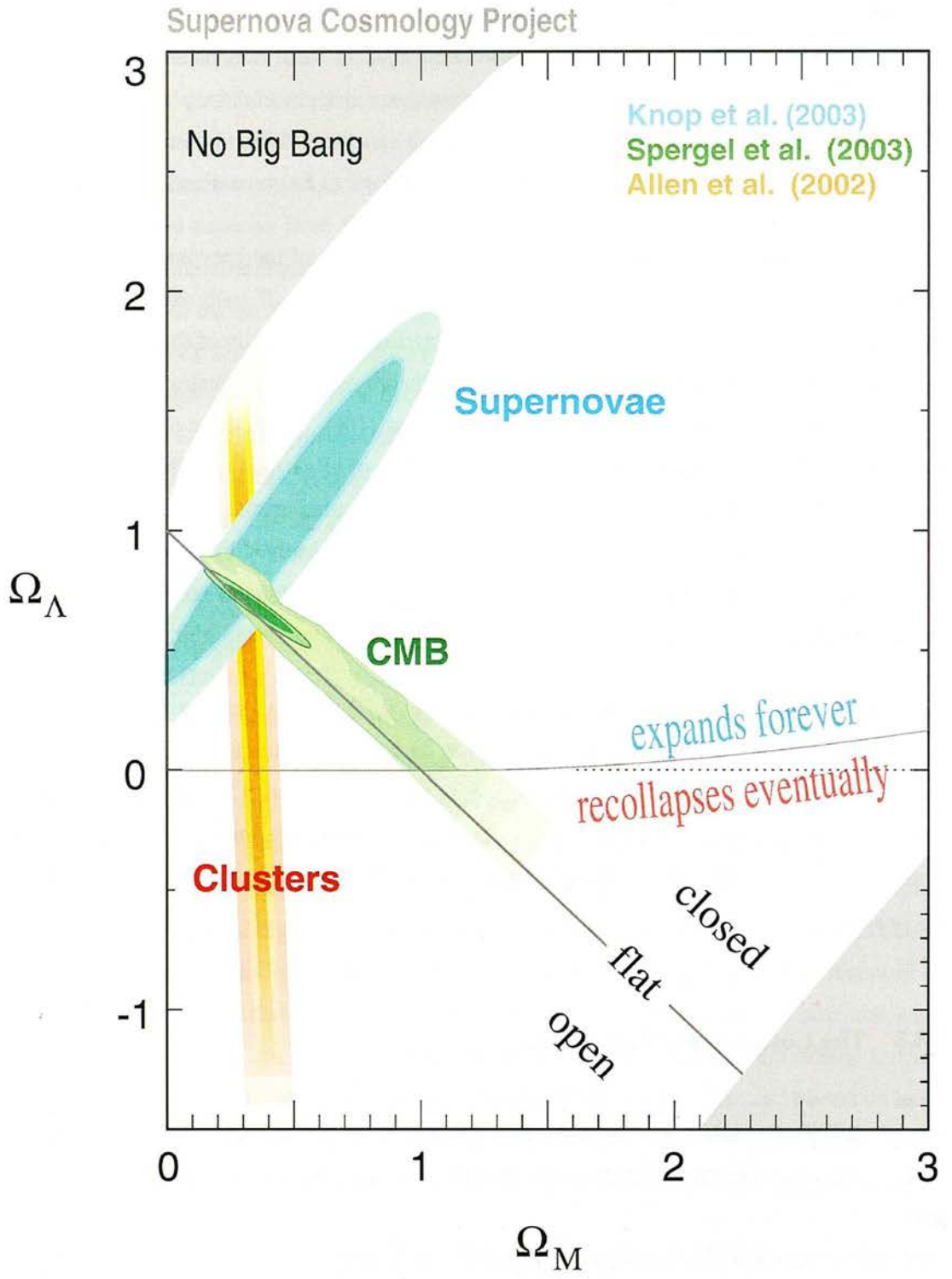

Figure 1.6: Confidence regions for Ω_m vs. Ω_{de} for a variety of experiments, highlighting the different degeneracies and how the combination of the different techniques allows for the constraint of the dark energy density. Note here $\Omega_\Lambda = \Omega_{de}$. The darker colours represent 98% confidence regions, the lighter colours represent the 68% confidence regions. Figure from Knop et al. (2003).

feature of gravity. However, an equivalent, and equally valid, form for the field equations is:

$$G^{\mu\nu} = -\frac{8\pi G}{c^4}T^{\mu\nu} - \Lambda g^{\mu\nu}, \tag{1.96}$$

where dark energy is now expressed as a feature of the energy-momentum of empty space so that it can be conceptualised as the **vacuum energy density**:

$$T^{\mu\nu}_{vac} = \Lambda\frac{c^4}{8\pi G}g^{\mu\nu}. \tag{1.97}$$

Since Special Relativity is apt for all inertial observers $T^{\mu\nu}_{vac}$ must be the same for all these observers, an inertial observer can locally describe spacetime using the Minkowski metric: $\eta_{\mu\nu} = (1, -1, -1, -1)$. Under a general coordinate transform the only requirement for covariance is that $T^{\mu\nu}_{vac}$ is proportional to the metric (as in equation 1.97), so that for SR the vacuum has a negative equation of state:

$$p_{vac} = -\rho_{vac}c^2, \tag{1.98}$$

where ρ_{vac} is proportional to the cosmological constant. In the terms of equation (1.42): $w(z) \equiv -1$. This is a constant, time independent value, so that the energy density of a cosmological constant will remain the same despite any expansion. This is an artifact of its equation of state; the work done by the negative pressure is just sufficient to maintain the energy density.

There lies a subtlety in the expressions used to describe the effect of a cosmological constant. Within a relativistic fluid there are two measures of gravitational interaction. The passive gravitational mass density refers to how the streaming velocity of the fluid is affected by the gravitational field of another object. The active gravitational mass is the gravitational field caused by the fluid itself. The passive interaction is represented by the first term on the right hand side of equation (1.9), which can be seen to vanish in the cosmological constant case, so that the active gravitational mass is negative if ρ_{vac} is positive. The active gravitational mass interaction can be quantified by considering the acceleration equation (1.35), it can be seen that a homogenous fluid with $p = -\rho/3$ will produce no gravitational field. If ρ_{vac} is dominant, $\rho c^2 + 3p < 0$ (i.e. $w < -1/3$), then $\ddot{a}$ will be positive, and the Universe will accelerate. So that the effect of a cosmological constant is that of the negative active gravitational mass, not a new force law.

The effect of dark energy on the Hubble parameter has already been shown in Section 1.3.1, and on the growth of structure in Section 1.5.2. However a dark energy term (expressed as an example by Λ here) also has an effect on the Friedmann equations:

$$\left(\frac{\dot{a}}{a}\right)^2 + \frac{kc^2}{a^2} = \frac{8\pi G}{3}\rho + \frac{\Lambda}{3}, \tag{1.99}$$

where

$$\Omega_{de} = \frac{\Lambda}{3H^2}. \tag{1.100}$$

1.8.4 Dark Energy Candidates

There is a plethora of dark energy theories and candidates. I will briefly describe the main contenders here and explicitly highlight how each theory predicts a different equation of state. For an extensive and recent (circa 2006) review see Copeland et al. (2006).

Explanations for Λ and the Fine Tuning Problem

Particle physics predicts that the value of ρ_{vac} (vacuum energy density), calculated by summing the energy contributions from the zero-point energies of each fundamental field should be,

$$\rho_{vac} = \frac{1}{2}\sum \hbar\omega. \tag{1.101}$$

If a cut off at 100GeV energies is imposed (and $\hbar = c = 1$) then $\rho_{vac} \sim (100\text{GeV})^4$, of the order of 10^{120} orders of magnitude larger than observed values (made even worse by considering GUT and Planck-scale particles). A vacuum energy explanation of dark energy relies on the fact that 'some how' the vacuum energy is cancelled by approximately 10^{199} orders of magnitude (but not the final one). One explanation of this is super-symmetry, that is each fermionic field's zero-point energy would be cancelled by its corresponding superpartners (bosonic field's) zero-point energy; although this would naively predict a complete cancellation.

Λ from Strings. It is beyond the scope of this thesis to discuss the details of string theoretical approaches to dark energy. It is sufficient to highlight the fact that within M-theory there are many possible solutions that can create de Sitter-like vacua. Indeed there may be upto 10^{100} different solutions within string theory that could account for a vacuum energy density. As discussed by Susskind (2003) within this 'string landscape' one can provide an anthropic explanation for dark energy in that of the many allowed vacua only a biophillic one would allow for our existence (the others exist in some sense as part of a larger ensemble or 'multiverse').

Causal Sets. Distinct from string theoretic explanations for a cosmological constant is an alternative quantum theory of gravity: casual sets. The causal set approach posits a spacetime

discreteness, where the total volume $\mathcal{V}$ is produced of N elements. Sorkin (1997) predicted that a fluctuating cosmological constant could be reproduced by the causal set structure. The fluctuations arise from Poisson fluctuations in N where Λ is a conjugate of $\mathcal{V}$. Since these fluctuations are small this could explain why the value of Λ is so small during the present epoch.

Anthropic Arguments. As alluded to earlier in this Section one can resort to biophillic selection effects within the context of a larger ensemble of universes[28], to explain the existence of dark energy. If the values of the Universe's constant were not within the ranges that would allow for intelligent life then we would not exist to observe the Universe. The basic argument is that if Λ was too large then matter would have been rarefied so quickly that there would not have been time for structure to form. However the probability that we observe any given value of Λ is given by (e.g. Starkman & Trotta, 2006)

$$P_{\rm obs}(\Lambda) = P(\Lambda)P_{\rm sel}(\Lambda). \tag{1.102}$$

The probability of the observation depends on the prior probability of any given value being such, $P(\Lambda)$, presumably from some fundamental theory, and the probability of the observation taking place $P_{\rm sel}(\Lambda)$. $P_{\rm sel}(\Lambda)$ encapsulates the probability of galaxies forming, life evolving and indeed observations being made. Since both these probabilities are currently ill-defined it is difficult to assign much credence to anthropic arguments. They are however tempting to evoke since the observation that we do exist is self-evident; the Universe is biophillic and the value of Λ is such that it allows for observations. The theoretical task then is either to explain the values of the physical constants, which coincidentally allow for life, or provide a compelling reason to believe that an ensemble of universes exists[29].

Scalar Fields and Dark Energy

The motivation of including a discussion of scalar fields in the case of dark energy is that it has already been shown that the Inflaton field could have caused an acceleration (albeit a larger one) in the early Universe. The acceleration due to dark energy, then, could be due to a similar

[28] Either physical separate regions of the same spacetime manifold, separate and distinct inflating manifolds (predicted by some chaotic Inflationary scenarios) or quantum-superposed universes (needed for some many-world quantum mechanical interpretations).

[29] Note that all these arguments assume an extension of the cosmological principle to encompass the reasoning that our Universe has no preferred place amongst a wider ensemble.

scalar field effect. Also, from a definitional stand point, a homogenous, isotropic uniform energy field, is indistinguishable from a non-zero vacuum energy density. There are a number of scalar field proposals, I will review the main candidates here.

Quintessence. Out of the theories that explain the dark energy by a homogenous, isotropic scalar field, ϕ, the dominant theory proposes a field known as 'quintessence'[30]. Different theories choose potentials $V(\phi)$ *ad hoc* so that a realistic scenario can be reproduced, although analogies can be adduced within supergravity, superstring/M-theory and brane theory. Each theory (and hence potential potential) predicts a different $w(z)$ dependence. The Lagrangian of a general quintessence scalar field can be written (where $c = 1$):

$$\mathcal{L}_\phi = -\frac{1}{2} g^{\mu\nu} \partial_\mu \phi \partial_\nu \phi - V(\phi), \tag{1.103}$$

where $V(\phi)$ is the (self-interaction) potential energy density of the field[31]. When the ϕ field is spatially homogenous (and curvature terms are neglected) the field equation, see Peebles & Ratra (2003), can be written:

$$\ddot{\phi} + 3\frac{\dot{a}}{a}\dot{\phi} + \frac{dV}{d\phi} = 0 \tag{1.104}$$

the stress-energy tensor (which is diagonal in the rest frame of a comoving observer) of this homogenous field has components:

$$\begin{aligned} \rho_\phi &= \frac{1}{2}\dot{\phi}^2 + V(\phi) \\ p_\phi &= \frac{1}{2}\dot{\phi}^2 - V(\phi). \end{aligned} \tag{1.105}$$

So, in the *slow roll* case (slowly time varying), $\dot{\phi}^2 \ll V(\phi)$, the scalar fields equation of state approximates that of a cosmological constant $p_\phi \approx -\rho_\phi$.

K-essence. 'K-essence' is similar to quintessence, though in this case the Lagrangian is not a simple linear function of the kinetic part of the scalar field ($[\nabla\phi]^2 = g^{\mu\nu}\partial_\mu\phi\partial_\nu\phi$). Usually K-essence Lagrangians are restricted to the form

$$\mathcal{L}_\phi = f(\phi)\hat{p}(X) \tag{1.106}$$

where $X \equiv -(1/2)(\nabla\phi)^2$. There are various string theoretical motivations for considering Lagrangians of this type. One such Lagrangian that can be deduced from string theory (see

[30] It is interesting to note that ideas such as quintessence propose a field with properties akin to the 'ether' formally proposed as an all-pervading massless medium for the electromagnetic field.

[31] Note: writing a Lagrangian density that includes gravitational and quantum field terms leads to the temptation to combine such terms, this should presently be avoided as a unified theory does not yet exist.

Copeland et al, 2006) is

$$\mathcal{L}_\phi = p(\phi, X) = f(\phi)(-X + X^2) \quad \text{and} \quad \rho(\phi, X) = f(\phi)(-X + 3X^2). \tag{1.107}$$

The equation of state is then

$$w = \frac{1 - X}{1 - 3X} \tag{1.108}$$

which for a constant value of $X = 1/2$ will mimic a cosmological constant, and will produce accelerated expansion for $1/2 \leq X \leq 2/3$. This is only one example of K-essence, there exists other Lagrangians that satisfy the K-essence conditions with varying X dependence and varying $X(t)$ as well as different forms for $f(\phi)$ which effects the K-essence density and how it may couple to matter.

Phantom (Ghost) Field. In general models where $w(a) < 1$ for some (or all a) are termed 'phantom energy' models, and describe dark energy scenarios where the energy density of the dark energy increases with time, potentially leading to a 'Big Rip', see Caldwell et al. (2003), where the energy density becomes larger than the Planck energy scale. The scalar fields discussed so far produce $w \geq -1$. Motivations for phantom fields have come from Brans-Dicke scalar-tensor gravity and string theory, recently 'quintom' models posit a coupled two field scenario with quintessence and phantom fields (e.g. Guo et al., 2006). The simplest phantom field is given by using a negative kinetic term in a standard Lagrangian

$$\mathcal{L}_\phi = \frac{1}{2} g^{\mu\nu} \partial_\mu \phi \partial_\nu \phi - V(\phi), \tag{1.109}$$

which can be compared to equation (1.104). In a similar way to the quintessence case this results in an equation of state given by

$$w = \frac{\frac{1}{2}\dot{\phi}^2 + V(\phi)}{\frac{1}{2}\dot{\phi}^2 - V(\phi)} \tag{1.110}$$

which again reproduces dark energy behaviour $w < -1$ in the slow roll case. Phantom fields suffer from ultra-violet instabilities as the energy density of the vacuum increases with time, ghost (negative energy) fields and normal (positive energy) fields can be produced resulting in an overproduction of cosmic gamma-rays via phantom$\rightarrow$ 2ghosts $+2\gamma$.

Chaplygin Gas. A more exotic theory is that there is exists a fluid known as a Chaplygin gas (Bento et al., 2002) which has an equation of state:

$$p = -\frac{A}{\rho^\alpha} \tag{1.111}$$

where A and $0 < \alpha < 1$ are constants. The attraction of this theory is that it posits that *both* dark matter and dark energy are in fact different manifestations of the same fluid: at early times the gas looks like dark matter and at late times (as the scale factor approaches infinity) it looks like dark energy. The origin of this hypothetical fluid is theorised to be either an effect from string theory or another quantum gravity effect. Of particular interest is that the equation of state (with $\alpha = 1$) can be reproduced geometrically from the Dirac-Born-Infield Lagrangian in string theory which describes the universe as a 3D+1 'brane' moving within an a 4D+1 'bulk'. A similar equation of state (with $\alpha = 1$) can be reproduced by Tachyon fields (see Copeland et al., 2006) and certain scalar fields.

Modifications to Gravity

Dark energy could be a manifestation of some correction to general relativity either as simply a cosmological constant or as something more complicated, for example effects arising from extra dimensions or from quantum or higher order corrections. A pure cosmological constant (a straightforward correction to general relativity) has a $w = -1$.

DGP Dark Energy. The model of Dvali-Gabadadze-Porrati (DGP; Dvali et al., 2000) considers the Universe as a 4D brane within a 5D Minkowskian bulk. In this scenario (and other brane-bulk scenarios) the weakness of gravity relative to the other forces is explained by gravity 'leaking' into the higher dimensions as it acts through the bulk, whereas the other forces act within the brane. The ratio of the energy scales of the brane and bulk can be written as $r_c = M_{pl}^2/2M_5^3$ where M_{pl} is the Planck mass in the brane and M_5 the Planck mass in the bulk. For length scales less than r_c gravity acts as the usual 4D gravity but on much larger than r_c higher-dimensional effects begin to dominate. The interesting case is when the cross over between the 4D and 5D gravity models occurs at the present epoch i.e. $r_c \approx H_0^{-1}$. It can be shown that in this case (for a flat geometry) the Hubble parameter can be written (see Copeland et al., 2006)

$$H^2 - \frac{\epsilon}{r_c} H = \frac{\rho}{3M_{pl}} \tag{1.112}$$

where $\epsilon = \pm 1$. When $H^{-1} \ll r_c$ the second term on the lefthand side in negligible and a matter-like (EdS) scenario is produced. When $H^{-1} \geq r_c$ and $\epsilon = +1$ then for $r_c \gg 1$ a de Sitter solution is reproduced: creating an accelerated expansion without dark energy. The acceleration is not due to a negative pressure fluid but a weakening of gravity on the brane as it leaks into the bulk. For $\epsilon = -1$ a negative pressure fluid is still needed to produce an

acceleration.

f(R) Dark Energy. It may be possible to arrive at an accelerated expansion using corrections to the geometric part of the Einstein equation only (e.g. Capozziello et al., 2006). There are many varieties of gravitational Lagrangian $f(R)$ (cf equation 1.7) that can reproduce an accelerated phase, for a review is Copeland et al. (2006), in which the Einstein tensor depends on higher order powers of the Ricci scalar.

Backreaction. It has recently been proposed (e.g. Kolb et al., 2005) that the observed acceleration could be due to the effect of backreaction from either super or sub-horizon perturbations, instead of a negative pressure fluid or modifications to gravity. In this case the acceleration is due to large inhomogeneities that occur beyond the observable horizon, that on even larger scales the Universe has $\Omega_m = 1$ and that the small matter content in our local patch results in the effect of acceleration, much as in the frame of a void in normal large scale structure. This is attractive in that it does not need to evoke any 'new' physics. However there are many arguments against such back reactions existing, for example Ishibashi & Wald (2006) show that since the Universe can be described so well by a Newtonianly perturbed FRW metric then the effect of backreactions must be negligible.

There exists a menagerie of other proposals, for example modifications to the Friedmann equation (e.g. Dvali & Turner, 2003) and holographic dark energy (Li, 2004).

The outstanding question is, then, what constitutes the majority (70% of the present day mass-energy content) of our Universe: **what is dark energy?**

1.8.5 The Dark Energy Equation of State

It is the dark energy equation of state parameter $w(z)$ that has the potential to distinguish between dark energy candidates and illuminate the nature of dark energy.

The are a number of different parameterisations for $w(a)$, for a full explanation see Linder (2003) and Wang & Freese (2005). Here the most common parameterisation is used, which characterises any evolution of the equation of state by the derivative of w with respect to the logarithm of the scale factor:

$$w(a) = w_0 + w_a(1 - a) \tag{1.113}$$

or $w(z) = w_0 + w_a z/(1+z)$, where

$$w_a = -\frac{dw}{d\ln a}. \tag{1.114}$$

It can immediately be seen that at the present time ($a = 1$) $w(a) = w_0$. The integral in the Hubble parameter, equation (1.46), expression now changes so that:

$$H^2(a) = H_0^2[\Omega_m a^{-3} + \Omega_{rad} a^{-4} + \Omega_{de} a^{-3(1+w_0+w_a)} \mathrm{e}^{-3w_a(1-a)}]. \tag{1.115}$$

It has been shown that this parameterisation is both stable over large redshift ranges and is robust. It is also flexible enough so that any physically motivated functional form for $w(a)$ can be parameterised by the w_0–w_a combination see Chevallier & Polarski (2001) and Linder (2003).

The parameterisation of $w(z)$ into w_0 and w_a is arbitrary and, although it can represent a large class of dark energy models, there are some dark energy models which it cannot reproduce. There have been a number of papers discussing the relative merit of different equation of state parameterisations for example Linder (2003), Linder (2004), Linder (2006), Linder & Huterer (2005), Jassal et al. (2004), Wang & Freese (2005). However, it is clear that in the absence of any compelling theory the w_0–w_a parameterisation allows for a simple comparison between models and provides a pivot redshift, see Section 3.9.6, at which a given method maximally constrains the equation of state – valuable in determining whether dark energy is a cosmological constant.

The need for such a parameterisation of the evolution has also been shown, see Linder (2004). Since if a constant $w(a)$ is assumed then scenarios can be imagined in which a time varying $w(a)$ could mimic, in measurement, a constant $w(a)$, thereby disguising underlying physics. Moreover there are many models which asymptotically approach a cosmological constant $w(a) = -1$ behaviour at late times for example the linear potential model (Linde, 1987) and the cyclic model (Steinhardt & Turok, 2004).

1.9 Summary

In this Chapter the standard cosmological framework has been reviewed. From the underlying GR prescription to the adaption of GR to Cosmology resulting, via the RW metric, to the standard FRW cosmological formalisms. The observable parameters that result from FRW

cosmology through their relation to the redshift of objects was outlined. The various cosmological components, matter, radiation and dark energy, and how they affect the evolution of the Universe and its expansion rate were reviewed. This resulted in the familiar cosmological parameters that describe our Universe and how various distance measures depend upon their values. The history and physics of the Universe were reviewed from the Inflationary epoch, Baryogenesis, Nucleosynthesis to the matter-radiation equality. The principle observable features of the Universe, including the CMB and LSS were explained in detail. Dark matter and dark energy were introduced as the components that dominate the present epoch, evidence for them, and potential candidates reviewed. The cosmological paradigm (circa 2006) can be summarised as:

- The Universe is homogenous and isotropic on large scales, and its geometry is very nearly flat. The Universe is large and is approximately 13.6 billion years old.
- The Universe is expanding, and has been throughout its history, and at the present epoch this expansion is accelerating. The current rate of expansion is parameterised by a Hubble constant of $H_0 \sim 71$ kms^{-1} Mpc^{-1}. The acceleration is due to a negative pressure component, dark energy, that accounts for $\sim 70\%$ of the mass-energy of the Universe but whose identity is unknown.
- Of the remaining $\sim 30\%$ most, $\sim 26\%$ is a cold, collisionless, weakly interacting massive fluid known as dark matter whose identity is also unknown.
- The remaining $\sim 4\%$ of the Universe is made of baryonic matter, which constitutes all the visible matter (galaxies, stars, gas, dust etc.).
- Structure formation was seeded by small perturbations during an Inflationary epoch, which have evolved via linear gravitational collapse (and non-linear effects on small scales) to form the structure we see during the present epoch.

The problem with which this thesis is concerned has been introduced: what is dark energy? How can we measure its equation of state? One way, which will be proved to be extremely powerful, is gravitational lensing, which will be introduced in Chapter 2.

Chapter 2

Gravitational Lensing

As photons propagate through an inhomogeneous gravitational field the path that the light takes is deflected. This phenomenon is known as **gravitational lensing**. The basic concept is that light follows geodesics in spacetime, and these geodesics are distorted from the 'straight', Euclidean, paths in a generally curved spacetime. The path that a photon takes in the vicinity of a massive body becomes curved by the local gravitational field. The use of gravitational lensing in cosmology can be heuristically understood by considering the following. Given a single intervening mass, an image of a distant galaxy should be distorted as the light from the galaxy travels through the gravitational field caused by the mass. The amount of distortion depends on the distances of the mass creating the intervening gravitational field and the distance of the source galaxy. The determination of these distances then provides a way to constrain cosmological parameters. Furthermore since the large scale, inhomogeneous, structure of the Universe will lens background galaxies – and the exact statistical distribution of the LSS depends on cosmological parameters – gravitational lensing should also constrain cosmological parameters by indirectly determining the statistical properties of the LSS.

The elegance of gravitational lensing in its use to constrain cosmological parameters lies in its simple underpinning in extremely well-understood physics, namely GR, and its simple relation to Cosmology. The subtlety of gravitational lensing lies in the fact that a relatively small statistical phenomenon (in weak lensing) can reveal so much about the nature of our Universe when the information is used in an optimal way. The beauty of gravitational lensing lies, not only in its elegance and subtlety but also in the fantastic images that it can create.

In this Chapter the basic formalism of gravitational lensing will be reviewed. The different types of lensing will be introduced and the potential for gravitational lensing to constrain cosmological parameters (particularly dark energy) will be explicitly highlighted. For a full exposé of gravitational lensing see Bartelmann & Schneider (2001) and Narayan & Bartelmann (1999).

2.1 Gravitational Lensing Background

As a pedagogical example this Section will be concerned with the simplest and most explanatory gravitational lens configuration, I will refer to galaxies being lensed although it should be remembered that the positions and luminosities of stars can also be gravitationally lensed.

Consider Figure 2.1, the source plane represents the plane in which the source galaxy lies (the galaxy whose image is distorted), the lensing plane is the effective plane in which the lensing mass lies (the creating the gravitational field which is distorting the path of light emitted by the source galaxy); hereafter referred to as the 'source' and the 'lens'. The impact parameter ξ is the distance between the light path and the lensing mass at closest approach.

There are generally three assumptions that are implicit in gravitational lensing. The first being that the gravitational lens potential is small, and can be effectively described by a Newtonian potential, $|\Phi| \ll c^2$. The second that the lenses are slowly moving, $v_{lens} \ll c$. Thirdly individual lenses are assumed to be thin, $L \ll c/H_0$ where L is the length of the lens and c/H_0 is the present day Hubble radius. Under these assumptions lensing galaxies or galaxy clusters can be treated as lenses embedded within a locally flat, Minkowskian, spacetime. The third assumption implies that large scale curvature effects become important only on scales much larger than the lens. So light rays propagating past a lens can be approximated by three sections: from the source to close to the lens as background geodesics of the FRW metric, from close to the lens to the observer again as geodesics of the background FRW metric, with a connecting metric close to the lens which is weakly perturbed.

2.1.1 Deflection Angle

In an analogy to an imperfect optical lens, see Schneider et al. (1992), a refractive index for a gravitational lens can be defined,

$$n = 1 - \frac{2}{c^2}\Phi, \tag{2.1}$$

where Φ is the gravitational potential of the lens. The potential is normalised so that it approaches zero at infinity, and is negative, so that the refractive index is positive. By using Fermats principle, in analogy to an optical lens, and integrating n perpendicular to the light path a deflection angle can be defined, see Figure 2.1:

$$\hat{\alpha} = \frac{2}{c^2}\int \overrightarrow{\nabla}_{\perp}\Phi dz \tag{2.2}$$

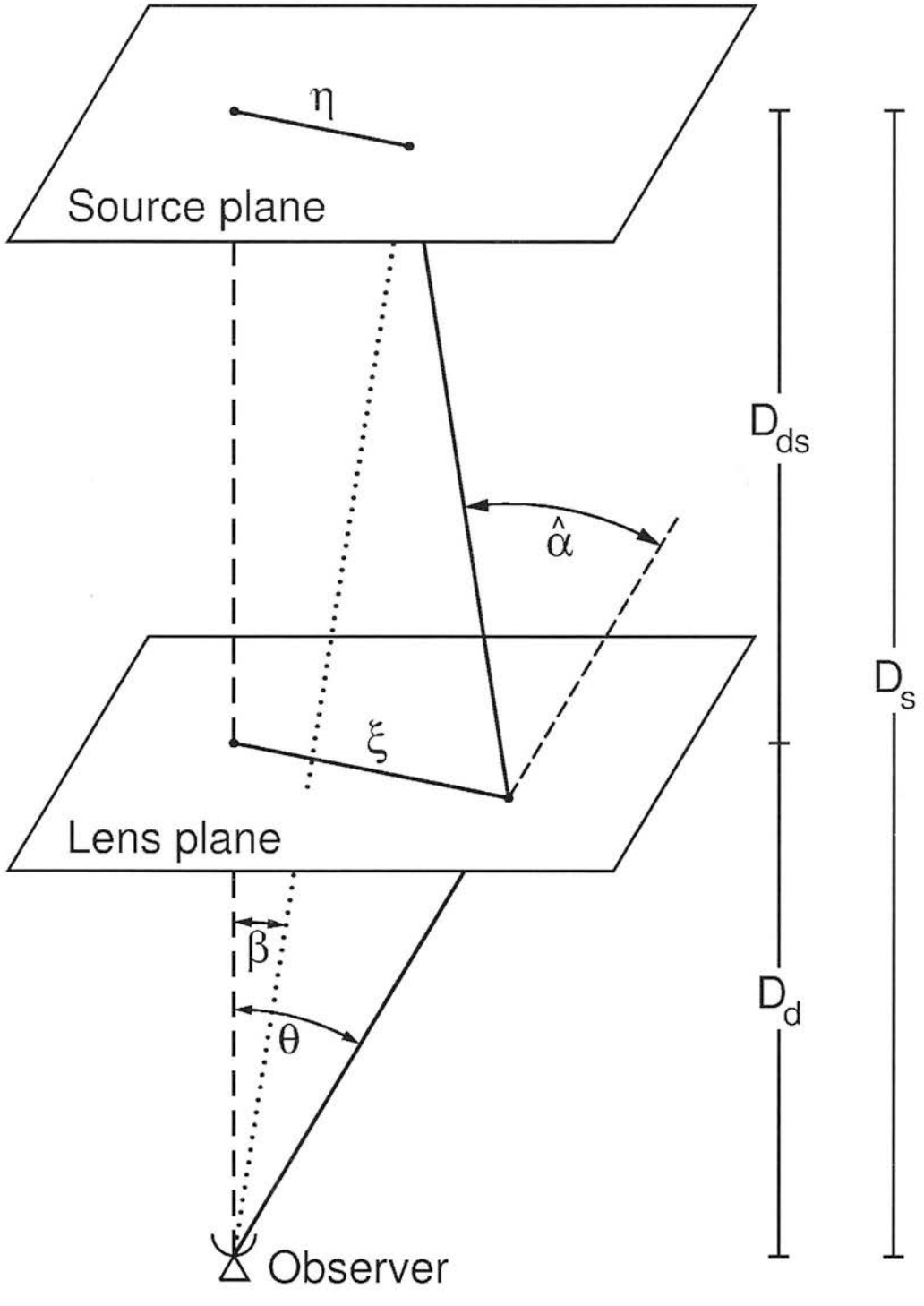

Figure 2.1: Gravitational lens schematic showing source and lens planes. The distances are angular diameter distances. From Bartelmann and Schneider (2001).

where the integration formally proceeds along the whole light path with gradient taken perpendicular to it. This can also be simply derived from GR using a weak field Newtonian metric and the equation of motion. However from the assumption that lenses are weak, any deflection angle is small, so the integral can proceed along the unperturbed light path (a straight line tangential to the incoming light path) see Bartelmann & Schneider (2002). This is known as the **Born approximation**, originally coined in atomic and nuclear physics.

Consider a point mass, of mass $M_{\rm point}$, with a Newtonian potential:

$$\Phi(\xi, z) = -\frac{GM_{\rm point}}{\sqrt{\xi^2 + z^2}}, \tag{2.3}$$

where ξ is the impact parameter and z is the distance along the unperturbed light path. The deflection angle in this case is

$$\hat{\alpha} = \frac{4}{c^2}\frac{GM_{\rm point}}{\xi}. \tag{2.4}$$

This is often compared to the **Schwarzchild radius** $R_S = 2GM/c^2$ so that for a point mass $\hat{\alpha} = 2R_S/\xi$[1].

2.1.2 The Thin Lens Approximation

The previous implication that the lens can be approximated by a plane is known at the **thin lens approximation**. This assumes that any deflection caused by the lens to the light path occurs within a narrow range in redshift $\Delta z \sim \pm\xi$. Using this approximation the mass distribution of the lens can be projected onto the lens plane, and is therefore characterised by its surface mass density Σ:

$$\Sigma(\boldsymbol{\xi}) = \int \rho(\boldsymbol{\xi}, z) dz \tag{2.5}$$

where the impact parameter is generalised to a vector $\boldsymbol{\xi}$ in the lens plane. The deflection angle is then the sum of the deflections from all the mass elements in the plane,

$$\hat{\boldsymbol{\alpha}} = \frac{4G}{c^2}\int \frac{(\boldsymbol{\xi} - \boldsymbol{\xi}')\Sigma(\boldsymbol{\xi}')}{|\boldsymbol{\xi} - \boldsymbol{\xi}'|^2} d^2\boldsymbol{\xi}'. \tag{2.6}$$

For a circularly symmetric lens this reduces to:

$$\hat{\alpha} = \frac{4GM(<\xi)}{c^2\xi} \tag{2.7}$$

where $M(<\xi)$ is the mass enclosed within the radius ξ.

[1] Using a purely Newtonian argument one arrives at $\hat{\alpha} = R_S/\xi$. This difference of a factor of two was a prediction of GR that allowed it to be tested against Newtonian gravity, and was proved correct during the 1919 solar eclipse, Einstein (1920).

2.1.3 The Lensing Equation

The scenario presented in Figure 2.1 represents a typical source-lens-observer configuration. The distances are related to redshifts e.g. $D_d = D_{ang}(z_d)$. The **reduced deflection angle** can be defined as

$$\boldsymbol{\alpha} = \frac{D_{ds}}{D_d}\hat{\boldsymbol{\alpha}}. \tag{2.8}$$

Note that the angular diameter distances should read terms of comoving distances as $S_k(D_d)$ where S_k is defined in equation (1.22), in this case $D_{ds} = S_k(D_d - D_s)$. From here on, for the sake of clarity the S_k's will be implicitly assumed in all instances of D.

The angles of interest in Figure 2.1 are $\boldsymbol{\beta}$, the angular position of the galaxy had it not been lensed, and $\boldsymbol{\theta}$ the actual (lensed) position of the galaxy. These can be related via the deflection angle in the **lensing equation**:

$$\boldsymbol{\theta} D_s = \boldsymbol{\beta} D_s + \hat{\boldsymbol{\alpha}} D_{ds},$$

or

$$\begin{aligned} \boldsymbol{\beta} &= \boldsymbol{\theta} - \hat{\boldsymbol{\alpha}}\frac{D_{ds}}{D_s} \\ \boldsymbol{\beta} &= \boldsymbol{\theta} - \boldsymbol{\alpha}. \end{aligned} \tag{2.9}$$

This equation is central in the formalism of gravitational lensing. It relates the observed position of a galaxy $\boldsymbol{\theta}$ to its true position $\boldsymbol{\beta}$ via the deflection angle $\hat{\boldsymbol{\alpha}}$. If the equation for $\boldsymbol{\theta}$ has more than one solution then *multiple* images of the same galaxy will be observed. This only occurs when the lens is **strong**. A strong lens is one for which the dimensionless surface mass density $\kappa(\boldsymbol{\theta}) \geq 1$ in at least one place where

$$\kappa(\boldsymbol{\theta}) = \frac{\Sigma(\boldsymbol{\theta})}{\Sigma_{\rm cr}}. \tag{2.10}$$

Σ_{cr} is the **critical surface mass density** defined as:

$$\Sigma_{\rm cr} = \frac{c^2}{4\pi G}\frac{D_s}{D_d D_{ds}}. \tag{2.11}$$

κ is known as the **convergence**, and distinguishes a strong lens from a weak lens, see Section 2.2. Where $\Sigma > \Sigma_{\rm cr}$ then $\kappa(\boldsymbol{\theta}) > 1$ and the lens is said to be 'supercritical'.

2.1.4 Effective Lensing Potential

An **effective lensing potential** can be defined as the scaled, projected, Newtonian potential of the lens

$$\psi(\boldsymbol{\theta}) = \frac{D_{ds}}{D_d D_s}\frac{2}{c^2}\int \Phi(\boldsymbol{\xi}, z)dz. \tag{2.12}$$

Taking the gradient of ψ we have

$$\begin{aligned} \vec{\nabla}_\theta\psi &= D_d\vec{\nabla}_\xi\psi \\ \vec{\nabla}_\theta\psi &= \frac{D_{ds}}{D_s}\frac{2}{c^2}\int \vec{\nabla}_\perp\Phi dz, \end{aligned} \tag{2.13}$$

comparing this with equation (2.2) it is clear that the reduced deflection angle is related to the effective lensing potential by

$$\vec{\nabla}_\theta\psi = \boldsymbol{\alpha}. \tag{2.14}$$

The mass density of a lens can be related to its potential by Poisson's equation $\vec{\nabla}^2_\xi\Phi = 4\pi G\rho(\boldsymbol{\xi}, z)$. It is clear then from equation (2.12) that taking the Laplacian of ψ will relate the effective lensing potential to the mass distribution. Here the 3D Laplacian is used, although the radial part of this Laplacian is small (see Hirata & Seljak, 2003) so it can be approximated by a 2D Laplacian.

$$\begin{aligned} \vec{\nabla}^2_\theta\psi &= \frac{2}{c^2}\frac{D_d D_{ds}}{D_s}\int \vec{\nabla}^2_\xi\Phi dz \\ \vec{\nabla}^2_\theta\psi &= \frac{2}{c^2}\frac{D_d D_{ds}}{D_s}4\pi G\Sigma(\boldsymbol{\theta}) = 2\frac{\Sigma(\boldsymbol{\theta})}{\Sigma_{\rm cr}}. \end{aligned} \tag{2.15}$$

So that the effective lensing potential is simply related to the convergence:

$$\vec{\nabla}^2_\theta\psi = 2\kappa(\boldsymbol{\theta}). \tag{2.16}$$

In terms of the κ the reduced deflection angle can be written, by substituting $D_d\boldsymbol{\theta}$ for $\boldsymbol{\xi}$ in equation (2.6):

$$\boldsymbol{\alpha} = \frac{1}{\pi}\int \kappa(\boldsymbol{\theta}')\frac{\boldsymbol{\theta}-\boldsymbol{\theta}'}{|\boldsymbol{\theta}-\boldsymbol{\theta}'|^2}d^2\boldsymbol{\theta}', \tag{2.17}$$

so that using equation (2.16) the effective lensing potential can be related to the convergence by:

$$\psi(\boldsymbol{\theta}) = \frac{1}{\pi}\int \kappa(\boldsymbol{\theta})\ln(\boldsymbol{\theta}-\boldsymbol{\theta}')d^2\boldsymbol{\theta}'. \tag{2.18}$$

2.1.5 Convergence, Shear and Magnification

Liouville's theorem[2] and the absence of absorption or emission of photons during GL imply that the surface brightness of a lensed galaxy must be conserved. The surface brightness in the source plane is related to the observed surface brightness by

$$I(\boldsymbol{\theta}) = I^s[\boldsymbol{\beta}(\boldsymbol{\theta})]. \tag{2.19}$$

If the source is much smaller than the angular size upon which the properties of the lens change then the local distortion of a galaxies image can be described by a linear mapping between the source and image planes. Expressed by considering the Jacobian matrix of the lens, defined by:

$$A_{ij} = \frac{\partial \boldsymbol{\beta}_i}{\partial \boldsymbol{\theta}_j} = \frac{\partial}{\partial \boldsymbol{\theta}_j}(\boldsymbol{\theta}_i - \boldsymbol{\alpha}_i) \tag{2.20}$$

or related to the Hessian matrix ψ_{ij} of ψ using equation (2.14)

$$A_{ij} = \delta_{ij} - \frac{\partial \boldsymbol{\alpha}_i}{\partial \boldsymbol{\theta}_j} = \delta_{ij} - \frac{\partial^2 \psi(\boldsymbol{\theta})}{\partial \boldsymbol{\theta}_i \partial \boldsymbol{\theta}_j} = \delta_{ij} - \psi_{ij} \equiv M_{ij}^{-1}, \tag{2.21}$$

where M_{ij} is the **magnification matrix**. So that the Hessian matrix ψ_{ij} represents the deviation of the lens mapping from the identity mapping (that which describes no distortion). Equation (2.16) can now be written as:

$$\kappa = \frac{1}{2}(\psi_{11} + \psi_{22}). \tag{2.22}$$

There is another combination of the derivatives of ψ_{ij} of central importance. The **complex shear** (or shear) is defined by:

$$\gamma = \gamma_1 + i\gamma_2 = |\gamma| \mathrm{e}^{2i\phi} \tag{2.23}$$

where γ is the distortion of the image and ϕ is the orientation of the distortion. γ_1 represents a distortion in the axes directions, relative to an arbitrary Cartesian coordinate system in the image plane ($\gamma_1 > 0$ along the x-axis, $\gamma_1 < 0$ along the y-axis), and γ_2 represents distortions at $\pi/4$ radians to the axis ($\gamma_2 > 0$ along the $\pi/4$ – $5\pi/4$ radian line, $\gamma_2 < 0$ along the $3\pi/4$ – $7\pi/4$ radian line). The shear is related to ψ by:

$$\gamma_1(\boldsymbol{\theta}) = \frac{1}{2}(\psi_{11} - \psi_{22}) \equiv \gamma(\boldsymbol{\theta})\cos[2\phi(\boldsymbol{\theta})] \tag{2.24}$$

$$\gamma_2(\boldsymbol{\theta}) = \psi_{21} = \psi_{12} \equiv \gamma(\boldsymbol{\theta})\sin[2\phi(\boldsymbol{\theta})]. \tag{2.25}$$

[2]Liouville's theorem states that an entire bounded function is constant e.g. the flux within a given set of geodesics.

The matrix A can now be written in terms of shear and convergence:

$$A = \begin{pmatrix} 1-\kappa-\gamma_1 & -\gamma_2 \\ -\gamma_2 & 1-\kappa+\gamma_1 \end{pmatrix} \tag{2.26}$$

$$A = (1-\kappa)\begin{pmatrix} 1 & 0 \\ 0 & 1 \end{pmatrix} - \gamma \begin{pmatrix} \cos(2\phi) & \sin(2\phi) \\ \sin(2\phi) & -\cos(2\phi) \end{pmatrix}, \tag{2.27}$$

occasionally this is written in terms of **reduced shear** $g(\boldsymbol{\theta}) = \gamma(\boldsymbol{\theta})/[1-\kappa(\boldsymbol{\theta})]$ so that:

$$A = (1-\kappa)\begin{pmatrix} 1-g_1 & -g_2 \\ -g_2 & 1+g_1 \end{pmatrix}. \tag{2.28}$$

From equation (2.27) it is now clear that

- The convergence, κ, causes an isotropic focusing of light rays and an isotropic magnification of the source. Convergence alone does not alter the shape of the source galaxy.
- The shear, γ, introduces an anisotropic mapping from the source to the image plane causing the image to become stretched. γ is the magnitude of the distortion and ϕ is the direction of the distortion.

From equation (2.19), for a point $\boldsymbol{\theta}_0$ in the image plane corresponding to a point in the source plane $\boldsymbol{\beta}_0 = \boldsymbol{\beta}(\boldsymbol{\theta}_0)$, we now have:

$$I(\boldsymbol{\theta}) = I^s[\boldsymbol{\beta}_0 + A(\boldsymbol{\theta}_0)(\boldsymbol{\theta}-\boldsymbol{\theta}_0)]. \tag{2.29}$$

The equations above describe the mapping of a circular source to an elliptic image with the ratio of the semi-major axes of the ellipse to the radius of the original, circular source being $1-\kappa\pm\gamma$. The flux observed from the image and the unlensed source are integrals over the respective surface brightness. The ratio of the image and source flux is the **magnification**; since the surface brightness is conserved the magnification is also simply the ratio of the area of the unlensed galaxy to the lensed image. The magnification is given by:

$$\mu(\boldsymbol{\theta}) = \det M = \frac{1}{\det A} = \frac{1}{(1-\kappa)^2-\gamma^2}, \tag{2.30}$$

for a circularly symmetric lens the ratio of the surface areas $d\theta^2$ to $d\beta^2$ is simply $\mu = \frac{\theta}{\beta}\frac{d\theta}{d\beta}$. Note that the magnification observable is the magnitude of the magnification $|\mu|$.

2.1.6 The Einstein Radius, Critical Curves and Caustics

The Einstein radius is an important length scale in gravitational lensing. As a pedagogical example consider a circularly symmetric lens, so that using equations (2.7) and (2.9)

$$\beta(\theta) = \theta - \frac{D_{ds}}{D_d D_s}\frac{4GM(\theta)}{c^2\theta}. \tag{2.31}$$

So that a source lying directly behind the lens on the optical axis, $\beta = 0$, is imaged as a complete circular arc – known as an 'Einstein ring' – around the lens, if the lens is supercritical. The radius of the circular image given by

$$\theta_E = \left[\frac{4GM(\theta)}{c^2}\frac{D_{ds}}{D_d D_s}\right]^{1/2} \tag{2.32}$$

where θ_E is the **Einstein radius**. So that equation (2.31) can be rewritten as

$$\beta\theta = \theta^2 - \theta_E^2, \tag{2.33}$$

which, being quadratic in θ has two possible solutions $\theta_\pm = (1/2)(\beta \pm \sqrt{\beta^2 + 4\theta_E^2})$. So, for a point lensing mass any source is imaged twice, one image inside θ_E the other outside. For a circularly symmetric lens the magnification is simply $\mu = \frac{\theta}{\beta}\frac{d\theta}{d\beta}$ so substituting β from equation (2.33) this becomes

$$\mu_\pm = \left[1 - \left(\frac{\theta_E}{\theta_\pm}\right)^4\right]. \tag{2.34}$$

So that since $\theta_- < \theta_E$ the magnification of the image inside the Einstein radius is negative. This is interpreted as the parity of the image being reversed. The net magnification is $\mu = |\mu_+| + |\mu_-|$.

Since the mean surface density within an Einstein radius for a point mass is Σ_{cr} the Einstein radius separates regions of strong and weak lensing. Also the typical separation of multiple images is $\sim 2\theta_E$. In fact the Einstein radius is a particular example of a feature of every gravitational lens, the **critical curve**. Critical curves, for any general lens mass distribution are closed curves in the lens plane where the determinant of the Jacobian matrix for the lens is singular ($\det A = 0$). **Caustics** are the corresponding curves in the image plane. According to equation (2.30) the magnification should then become infinite at a critical curve. This does not occur in reality due to the extended nature of the sources; and even for point sources the magnification remains finite, as for a point source the geometric approximation fails near critical curves and a full wave optics description leads to finite magnifications. Even so images become strongly magnified and highly distorted near, or on, caustics. Caustics also represent

Figure 2.2: An image taken using the *Hubble Space Telescope's* ACS instrument of the galaxy cluster Abell 1689. Strongly lensed galaxies, distorted arcs, can be seen as well as tangentially aligned, weakly lensed, galaxies at larger radii from the cluster centre. From the NASA HST Archive.

the boundary between the singular and multiple imaging or sources. If a source moves in the source plane such that its image moves across a caustic in the image plane the number of images of the source will change by ± 2. Only sources inside a caustic are multiply imaged.

2.1.7 Singular Isothermal Sphere

The Singular Isothermal Sphere (SIS) is a useful and commonly used mass distribution since it accurately describes the density profile of a wide range astrophysical bodies including dark matter haloes, and virialised galaxy clusters. It can also reproduce the observed flat-rotation curves, see Section 1.7.1. The density profile of an SIS is (see Schneider, 2006):

$$\rho(r) = \frac{\sigma_\nu^2}{2\pi G}\frac{1}{r^2} \tag{2.35}$$

where r is the radius from the centre of the cluster and σ_ν is the one-dimensional velocity dispersion of stars (or galaxies) in the lensing galaxy (or galaxy cluster). The surface mass density is calculated by projecting the density along the line-of-sight:

$$\Sigma(\xi) = \frac{\sigma_\nu^2}{2G}\frac{1}{\xi}. \tag{2.36}$$

The SIS is of particular interest in gravitational lensing due to the coincidental property that the shear induced at a particular position is equal to the convergence at that position i.e. $|\gamma(\xi)| = \kappa(\xi)$. For an SIS this is simply

$$\kappa(\theta) = \frac{\theta_E}{2\theta}, \text{ where } \theta_E = 4\pi \left(\frac{\sigma_\nu}{c}\right)^2 \frac{D_{ds}}{D_s}. \tag{2.37}$$

From equation (2.17) the scaled deflection angle is constant for a SIS $|\boldsymbol{\alpha}| = \theta_E$ and similarly the effective lensing potential is $\psi = \theta_E|\boldsymbol{\theta}|$. The shear can then be deduced from equations (2.24):

$$\gamma(\boldsymbol{\theta}) = -\frac{\theta_E}{2|\boldsymbol{\theta}|} \mathrm{e}^{2i\phi}. \tag{2.38}$$

Since the SIS is circularly symmetric it defines a critical curve at $|\boldsymbol{\theta}| = \theta_E$, similar to the point mass in Section 2.1.6. The SIS mass distribution is apt in many circumstances but is only an approximation, breaking down in two obvious ways. Firstly the mass distribution is infinite, and secondly the density diverges for $\xi = 0$. The distribution is often curtailed at small and large radii, in order to retain realism. Another widely used profile is the NFW profile, see Navarro et al. (1997), who found that in numerical simulations the density profiles of many dark matter halos could be fitted by the formula:

$$\rho(s) = \rho_c^0 \frac{\nu c^2 g(c)}{3s(1+cs)^2}. \tag{2.39}$$

s is the radius in units of the virial radius $s = r/r_v$, c is the 'concentration parameter' which is related to the density of the halo and $g(c) = 1/[\ln(1+c) - c/(1+c)]$. Typical values for c range from $c = 5$ for clusters of galaxies to $c = 10$ for large bright galaxies, however there is no universal agreement, the exact value depending on the mass of the object and the initial matter power spectrum. The profile diverges from the SIS in that at small radii it is shallower with a $\propto r^{-1}$ dependence steepening to $\propto r^{-3}$ at large radii; at intermediate radii the SIS is a good approximation to the NFW profile.

2.1.8 Lensing Categorisation

In an effort of clarification the four broad categories of gravitational lensing will be explicitly mentioned here. As previously defined **strong** lensing occurs when an image appears within or near a caustic, due to the light path in the lens plane passing within a critical curve; strong lensing can produce distorted, magnified and multiple images. **Weak lensing** occurs when the image appears far outside a caustic, singular images occur and magnification is weak (see Section 2.2 for details). **Micro lensing** and **macro lensing** allude to the size of the lensing

mass. Macro lensing is caused by extended, massive, objects i.e. galaxies, galaxy clusters or dark matter halos etc.

Micro lensing is lensing by relatively small, point-like, objects i.e. stars or planets etc. Micro lensing observations usually measure the increase in the brightness of an object due to the magnification effect. This is usually done over time; the flux from a star (or planet) will increase in a characteristic way if a massive object passes through the line of sight to the source object, or if the source object moves behind a massive object. The measurable increase in flux is due to a caustic crossings so micro lensing is an example of strong lensing. Such microlensing events have been used to place bounds on the number of compact halo objects around the Milky Way see Alcock et al. (2000), Lasserre et al. (2000), Zebrun et al. (2001) and Section 1.7.2.

From here the remainder of this thesis will be concerned soley with macro weak lensing.

2.2 Weak Lensing

As we have seen in Section 2.1 gravitational lensing effects can be separated into two distinct categories: strong and weak lensing. **Weak lensing** produces weakly distorted, single, images of sources outside of caustics. For weak lensing both $|\kappa| \ll 1$ and $|\gamma| \ll 1$, equivalently $|g| \ll 1$.

There are two ways in which weak lensing can produce a measurable effect. Firstly background galaxies will be weakly lensed by foreground structure, either by LSS or by foreground galaxy clusters (see Villumsen, 1996). Secondly the weak magnification effect can change the observed number density of source background galaxies or change the size of images of a given surface brightness (see Schneider, 2006 for a review). This thesis will concentrate only on the first effect, that of foreground structure inducing a *weak shear* on the images of background galaxies.

2.2.1 Ellipticity

The affect of foreground structure is to weakly distort the shape of a background galaxy by changing its apparent shape through the gravitational lensing shear effect: weak shear. In an image this is manifested as a change in the shape of the galaxy. Since galaxies are generally

non-circular in shape the shear effect induces an extra, *additional ellipticity*. It is this additional ellipticity that is induced by lensing foreground structure. Consider a galaxy for with the surface brightness profile $I(\boldsymbol{\theta})$ is well defined for all angular separations from the centre $\bar{\boldsymbol{\theta}}$ of the image, so that:

$$\bar{\boldsymbol{\theta}} \equiv \frac{\int d^2\boldsymbol{\theta} w[I(\boldsymbol{\theta})]\boldsymbol{\theta}}{\int d^2\boldsymbol{\theta} w[I(\boldsymbol{\theta})]} \tag{2.40}$$

where $w[I(\boldsymbol{\theta})]$ is a suitably chosen weight function such that the integrals converge. The tensor of second brightness moments is now:

$$Q_{ij} = \frac{\int d^2\boldsymbol{\theta} w[I(\boldsymbol{\theta})](\theta_i - \bar{\theta}_i)(\theta_j - \bar{\theta}_j)}{\int d^2\boldsymbol{\theta} w[I(\boldsymbol{\theta})]} \;\; ; \;\; i,j \in \{1,2\}. \tag{2.41}$$

The trace part of Q contains the size information whilst the traceless part contains ellipticity information; for a circular image $Q_{11} = Q_{22}$ and $Q_{12} = Q_{21} = 0$. From the definition of Q_{ij} a **complex ellipticity** can be defined (in direct analogy with complex shear):

$$\epsilon = \epsilon_1 + i\epsilon_2 = |\epsilon| \mathrm{e}^{2i\phi} \tag{2.42}$$

where

$$\epsilon = \frac{Q_{11} - Q_{22} + 2iQ_{12}}{Q_{11} + Q_{22}} \tag{2.43}$$

or

$$\epsilon = \frac{Q_{11} - Q_{22} + 2iQ_{12}}{Q_{11} + Q_{22} + 2(Q_{11}Q_{22} - Q_{12}^2)^{1/2}}. \tag{2.44}$$

Both these equally valid definitions have the same phase but different amplitudes. Here the definition from equation (2.44) will be used. Note for a circular image $\epsilon_1 = \epsilon_2 = 0$. Bartelmann & Schneider (2001) and Schneider (2006) show that the original ellipticity ϵ^S of a galaxy is transformed under lensing, using equation (2.44) like:

$$\epsilon^S = \begin{cases} \dfrac{\epsilon - g}{1 - g^*\epsilon} & \text{for} \quad |g| \leq 1 \\ \\ \dfrac{1 - g\epsilon^*}{\epsilon^* - g^*} & \text{for} \quad |g| > 1 \end{cases} \tag{2.45}$$

the inverse transformation is obtained by interchanging ϵ with ϵ^* and replacing g with $-g$. In the weak lensing case $|g| \ll 1$ the inverse of equation (2.45) reduces to:

$$\epsilon \approx \epsilon^S + g. \tag{2.46}$$

Since the ellipticity of any individual source is unknown the above expressions are of little use when applied to individual galaxies. However, the key realisation in weak lensing is that when

a large statistical sample of galaxies is used the *average intrinsic ellipticity* should be zero i.e. since there should be no preferred orientation of galaxies in the Universe:

$$\langle \epsilon^S \rangle = 0. \tag{2.47}$$

So average additional ellipticity in the weak lensing régime is:

$$\langle \epsilon \rangle = 0 + \langle g \rangle. \tag{2.48}$$

By assuming that a galaxy sample covers a small angular patch on the sky, so that the light from each part of the galaxy experiences approximately the same gravitational field an estimator for the shear can be deduced

$$\gamma \approx g \approx \langle g \rangle = \langle \epsilon \rangle. \tag{2.49}$$

The result here is actually for sources all at a fixed redshift, however Bartelmann & Schneider (2001) show that this result is in fact general for a redshift distributed source population. Equation (2.49) also implies that the variance in the shear is related to the variance in the ellipticity by $\sigma^2_\gamma = \sigma^2_\epsilon$, or for the individual components γ_1 and γ_2, $\sigma^2_{\gamma_\alpha} = \sigma^2_\epsilon/2$. It is worth noting that if the definition of complex ellipticity in equation (2.43) is used then $\langle \epsilon \rangle = 0 + 2\langle g \rangle$, $\gamma \approx \langle \epsilon \rangle/2$ and $\sigma^2_{\gamma_\alpha} = \sigma^2_\epsilon/4$.

To measure the ellipticity of a galaxy a number of complementary techniques have been developed. The first to be developed, and most commonly used is known as the KSB test after Kaiser, Squires & Broadhurst (1995), which allows for the accurate removal of the smearing of a galaxies image due to an anisotropic point spread function (PSF) on an instrument. Shapelets, see Réfrégier & Bacon (2003), is the main contender where a galaxy's image is decomposed into spherical polar harmonics, the shear signal corresponding to particular 'quantum numbers' in the devolution.

2.2.2 Tangential Shear

The components of complex shear γ_1 and γ_2 are defined relative to a local Cartesian coordinate frame. Is is often apt to consider the projected shear components in a rotated frame, particularly in the case of galaxy clusters where the centre of the polar coordinate frame can be defined as the centre of the cluster. For a lensing cluster the image distortions are aligned tangentially about the cluster as can be seen in Figure 2.2. If ϕ_c specifies the angular position about the centre of the coordinate frame the the tangential and cross-component shears (aligned respectively

perpendicular and parallel to the radius vector) are:

$$\gamma_t = -\mathbb{R}\mathrm{e}[\gamma \mathrm{e}^{-2i\phi_c}] \text{ and } \gamma_\times = \mathbb{I}\mathrm{m}[\gamma \mathrm{e}^{-2i\phi_c}], \tag{2.50}$$

or using the definition for complex shear in equation (2.23)

$$\gamma_t = -[\gamma_1 \cos(2\phi_c) + \gamma_2 \sin(2\phi_c)] \text{ and } \gamma_\times = -\gamma_1 \sin(2\phi_c) + \gamma_2 \cos(2\phi_c). \tag{2.51}$$

A perfect lensing cluster should only produce a tangential signal in the shear so the cross-component shear (which should be $\gamma_\times = 0$) can be used to estimate the noise on the measurement of the tangential shear. For a SIS, see Section 2.1.7, the tangential and cross-component shear becomes $\gamma_t = \theta_E/2|\boldsymbol{\theta}|$ and $\gamma_\times = 0$, so that any measured, residual $\gamma_\times$ can be used to estimate the noise in the measured γ_t.

2.2.3 Cosmic Shear

As well as galaxy clusters inducing shear in the images of background galaxies, there should be a lensing effect from the intervening LSS for any background galaxy; even in an apparently 'empty' field background galaxies should exhibit some amount of shear. This lensing by LSS is known as **cosmic shear**, the measurement of cosmic shear has been one of the major goals of weak lensing, and has been successfully measured many times (see for example Brown et al., 2003), and used to place constraints on various cosmological parameters by constraining the lensing power spectrum.

This Section is written as an introduction to the notion of cosmic shear and the cases represented are for the three-dimensional (3D) case. The 2D case is recovered by replacing r with the horizon comoving distance r_H, so that the convergence and shear fields (or maps) are projected onto the sky (2D), in equations (2.52) and (2.55).

Recasting equation (2.12) in a more general form, the effective cosmological lensing potential $\phi(r, \boldsymbol{\theta})$ can be related to the 3D comoving gravitational potential of the lens $\Phi(r, \boldsymbol{\theta})$, see Bartelmann & Schneider (2001):

$$\phi(r, \boldsymbol{\theta}) = \frac{2}{c^2} \int_0^r dr' \left[\frac{S_k(r - r')}{S_k(r) S_k(r')} \right] \Phi(r', \boldsymbol{\theta}), \tag{2.52}$$

where r is the comoving distance and S_k is defined in equation (1.22). From here, in the rest of this Section the S_k's will be implicit in any instance of r: $r = S_k(r)$, $r_1 - r_2 = S_k(r_1 - r_2)$. Since equation (2.16) can be generalised for the cosmic lensing potential, $\nabla^2 \phi = 2\kappa$, the

convergence field, the value of κ at a position on the sky $\boldsymbol{\theta}$ for source galaxies at a distance r, can be written as

$$\kappa(r,\boldsymbol{\theta}) = \frac{1}{c^2}\int_0^r dr' \left[\frac{r-r'}{rr'}\right] r'^2 \frac{\partial^2\Phi(r',\boldsymbol{\theta})}{\partial r'^2}, \tag{2.53}$$

this is also known as the **effective convergence**. Applying Poisson's equation to the 3D potential, $\nabla^2\Phi(r) = 4\pi G\rho_m a^2\delta$, where ρ_m is the cosmological matter density, a is the scale factor and δ the relative matter density contrast, equation (2.53) can be rewritten

$$\kappa(r,\boldsymbol{\theta}) = \frac{3}{2}\left(\frac{H_0}{c}\right)^2 \Omega_m \int_0^r dr' \left[\frac{r-r'}{r}\right] r' \frac{\delta(r'\boldsymbol{\theta},r')}{a(r')}, \tag{2.54}$$

since $\nabla^2\Phi(r) = 4\pi G\rho_m a^2\delta = \frac{3}{2}H_0^2\Omega_m a^{-1}\delta$. Where $\delta(r\boldsymbol{\theta},r)$ is the fractional matter overdensity at comoving distance r and position $\boldsymbol{\theta}$. Including a normalised redshift distribution for the source galaxies $p(z)dz = G(r)dr$, and integrating over the redshift distribution the convergence field can be generalised further to:

$$\kappa(r,\boldsymbol{\theta}) = \frac{3}{2}\left(\frac{H_0}{c}\right)^2 \Omega_m \int_0^r r'dr'\overline{W}(r,\tilde{r}) \frac{\delta(r'\boldsymbol{\theta},r')}{a(r')}, \tag{2.55}$$

where

$$\overline{W}(r,r') = \int_{r'}^r d\tilde{r} G(\tilde{r}) \left[\frac{\tilde{r}-r'}{\tilde{r}}\right]. \tag{2.56}$$

Equations (2.22) and (2.24) can, in a similar way as before, be generalised by replacing $\psi \rightarrow \phi$

$$\begin{aligned} \kappa(r,\boldsymbol{\theta}) &= \frac{1}{2}(\phi_{11}+\phi_{22}) \\ \gamma_1(r,\boldsymbol{\theta}) &= \frac{1}{2}(\phi_{11}-\phi_{22}) \\ \gamma_2(r,\boldsymbol{\theta}) &= \phi_{12} = \phi_{21}. \end{aligned} \tag{2.57}$$

2.2.4 2D Weak Lensing Power Spectrum

A full power spectrum analysis in 2D is not performed here as this thesis is conserned with the 3D weak lensing measures, however as a basic example the 2D convergence power spectra will be explicitly highlighted here to introduce concepts used later. Since in Section 2.2.3 the idea of the convergence and shear being represented by continously varying fields (or maps) on the sky (2D) has been introduced it is natural to ascribe a Fourier transform to these fields i.e. $\kappa(\boldsymbol{\ell})$. The Fourier transform of $\kappa(\boldsymbol{\theta})$ is

$$\kappa(\boldsymbol{\theta}) = \int \frac{d^2\boldsymbol{\ell}}{2\pi}\kappa(\boldsymbol{\ell})e^{i\boldsymbol{\ell}.\boldsymbol{\theta}}. \tag{2.58}$$

The 2D **effective convergence power spectrum**, $C_\ell^{\kappa\kappa}$ can then be defined as:

$$\langle \kappa(\boldsymbol{\ell})\kappa^*(\boldsymbol{\ell}')\rangle = (2\pi)^2 C_\ell^{\kappa\kappa}\delta_D(\boldsymbol{\ell}-\boldsymbol{\ell}'), \tag{2.59}$$

where δ_D is the Dirac delta function. Applying Limbers equation in Fourier space Kaiser (1998) showed that the 2D effective convergence power spectrum can be related to the 3D matter power spectrum, defined in Section 1.6, by

$$C_\ell^{\kappa\kappa} = \frac{9}{4}\left(\frac{H_0}{c}\right)^4 \Omega_m^2 \int_0^{r_H} dr P_\delta(\frac{\ell}{r}, r)\left[\frac{\overline{W}(r)}{a(r)}\right]^2. \tag{2.60}$$

This key expression, used in many applications of weak lensing, relates a measureable quantity – the convergence – to cosmological parameters.

2.2.5 The $\eth$ Formalism

Equation (2.57) can be rewritten in a more succinct form, where the shear components are expressed in terms of a shear tensor $[\gamma(\mathbf{r})]_{ij}$ which reprents the cosmic shear field at a 3D position $\mathbf{r}$. Here I will assume a flat sky for convience (the metric of the sky surface locally being $g = diag[1,1]$) for a full exposé see Castro et al. (2005). In this case the shear tensor is:

$$[\gamma(\mathbf{r})]_{ij} = \begin{bmatrix} \gamma_1(\mathbf{r}) & \gamma_2(\mathbf{r}) \\ \gamma_2(\mathbf{r}) & -\gamma_1(\mathbf{r}) \end{bmatrix} = (\partial_i\partial_j - \frac{1}{2}\delta_{ij}\nabla^2)\phi(\mathbf{r}) \tag{2.61}$$

which reproduces the familiar equation (2.57) by

$$\begin{aligned} \gamma_1(\mathbf{r}) &= \frac{1}{2}(\partial_x^2 - \partial_y^2)\phi(\mathbf{r}) \\ \gamma_2(\mathbf{r}) &= \partial_x\partial_y\phi(\mathbf{r}) \end{aligned} \tag{2.62}$$

where $\nabla^2 = \partial_i\partial_i$. The convergence field can be written in a similar way such that $\kappa(\mathbf{r}) = \frac{1}{2}\nabla^2\phi(\mathbf{r}) = \frac{1}{2}(\partial_x^2 + \partial_y^2)\phi(\mathbf{r})$.

Mathematically the complex shear is a spin-weight, $s = 2$ object, similar to the Q and U components of polarisation in electromagnetism. The spin weight of an object is related to its properties under a rotation of the frame where it is defined (e.g. a scalar is an $s = 0$ object). The complex shear transforms under a rotation of the fixed coordinate system as $\gamma \rightarrow \gamma e^{si\phi}$ where $s = 2$ is its *spin-weight*. This dependence arises simply from the fact that the complex shear is invariant under a rotation of π radians. Also the two shear components are related by a $\pi/4$ radians rotation so that $\gamma_1' = -\gamma_2$ and $\gamma_2' = \gamma_1$ where prime denotes the transformed field.

The shear field, then, can be mathematically described as a spin-weight $s = 2$ function defined on a 2D Riemannian manifold (a 2D manifold with a metric); the sky, in this case taken to be flat. I will here introduce the *edth* operator, $\eth$ (and its conjugate $\bar{\eth}$), which acts as a raising (or lowering) operator on the 'quantum number' of a spin weight object s. $\eth$ effectively acts to relate quantities with different spin-weights which are not invariant under coordinate frame transformations to scalar quantitites that are invariant under rotations. A spin-weight s field, η, is said to be 'even' if $\eta = \eth^s f$ and odd if $\eta = i\bar{\eth}^s f$ for some scalar ($s = 0$) real function f.

Newman & Penrose (1966) showed that any spin-weight s function defined on on a 2D Riemannian manifold can be uniquely decomposed into a scalar gradient (electric/even) E-component and a scalar curl (magnetic/odd) B-component. So in this case two real scalar functions $\phi_E(\mathbf{r})$ and $\phi_B(\mathbf{r})$, for the even and odd parts can be related to the complex spin-weight $s = 2$ shear field

$$\gamma(\mathbf{r}) \equiv \gamma_1(\mathbf{r}) + i\gamma_2(\mathbf{r}) = \frac{1}{2}\eth\eth[\phi_E(\mathbf{r}) + i\phi_B(\mathbf{r})] \tag{2.63}$$

$$\gamma^*(\mathbf{r}) \equiv \gamma_1(\mathbf{r}) - i\gamma_2(\mathbf{r}) = \frac{1}{2}\bar{\eth}\bar{\eth}[\phi_E(\mathbf{r}) - i\phi_B(\mathbf{r})]. \tag{2.64}$$

Of central importance is that weak cosmic shear is derivable from a real (lensing) potential $\phi_E(\mathbf{r})$ requiring that $\phi_B(\mathbf{r}) = 0$, see Castro et al. (2005). So that the cosmic shear field induced by a gravitional tidal field only produces an E-pattern in shear maps. This is of importance in that any non-gravitational noise may contribute to both E and B modes equally, so the magnitude of any noise terms can be estimated by measuring the B mode signal in shear maps[3]. Equation (2.61) can now be written simply as

$$\gamma(\mathbf{r}) = \frac{1}{2}\eth\eth\phi(\mathbf{r}), \tag{2.65}$$

or for γ_1 and γ_2

$$\gamma_1(\mathbf{r}) = \frac{1}{4}(\eth\eth + \bar{\eth}\bar{\eth})\phi(\mathbf{r}) \tag{2.66}$$

$$\gamma_2(\mathbf{r}) = -\frac{i}{4}(\eth\eth - \bar{\eth}\bar{\eth})\phi(\mathbf{r}). \tag{2.67}$$

Since the convergence field is a spin-weight $s = 0$ object one would expect one raising and one lowering operator in the equivalent expression and indeed, see Castro et al. (2005), $\kappa(\mathbf{r}) = \frac{1}{4}(\eth\bar{\eth} + \bar{\eth}\eth)\phi(\mathbf{r})$.

[3]Gravitational waves (Stebbins et al., 1996) and multiple light lensing (Schneider et al., 2002) may also produce B modes, but their effect is thought to be small.

Flexion describes the 'arcness' of galaxies around halos see Bacon et al. (2006) and is simply specified by the spin-weight $s = 1$ first flexion $\mathcal{F}(\mathbf{r}) = \frac{1}{2}\eth\eth\bar{\eth}\phi(\mathbf{r})$ and the spin-weight $s = 3$ second flexion $\mathcal{G}(\mathbf{r}) = \frac{1}{2}\eth\eth\eth\phi(\mathbf{r})$.

2.3 Three Dimensional Weak Lensing

Three dimensional weak lensing (3D weak lensing) will be introduced, in a qualitative sense, here. The remainder of this thesis will be conserned soley with 3D weak lensing. Various mathematical formalisms will be inroduced in Chapters 3 and 4. The basic principle is simply extending the 2D, projected shear, and convergence fields, in standard weak lensing to 3D where both angular and any redshift information can be used. This has the intuitive *a priori* advantage that the 3D effects can directly probe both the angular diameter distances involved in weak lensing and the 3D power spectrum by directly probing the 3D LSS distribution.

As dark energy is a evolving effect, an acceleration, measurements of how the expansion rate and matter growth change with time is vital in constraining its nature. A truely 3D probe, therefore, has an obvious advantage in measuring dark energy, since it naturally uses time (redshift) varing information.

2.4 Summary

This Chapter has outlined the basic conceptual and mathematical formalisms of gravitational lensing. The varied aspects of gravitational lensing have been explicitly stated and outlined; strong, weak, macro and micro lensing, as well as potential cosmological dependence. Weak lensing was clarified and 3D weak lensing alluded to.

It has only been in the last five years or so that the first measurements of cosmic shear have appeared (Bacon, Réfrégier and Ellis, 2000; Kaiser, Wilson and Luppino, 2000; van Waerbeke et al., 2000; Wittman et al., 2000). Weak lensing measurements to date have concentrated on obtaining the matter density parameter Ω_m and the amplitude of mass density fluctuations σ_8 (Hoekstra, Yee and Gladders, 2002; Jarvis et al., 2003; Rhodes et al., 2004; Heymans et al., 2004; Hoekstra et al., 2006; Semboloni et al., 2006). More ambitiously, weak lensing observations have started to put constraints on the equation of state of dark energy (Jarvis et al., 2005;

Semboloni at al., 2006). Theoretically, the prospects for determining dark energy properties (specifically its equation of state w) using weak lensing have been explored in a number of papers (e.g. Taylor et al., 2006; Hu and Tegmark, 1999; Huterer, 2002; Heavens, 2003; Heavens et al., 2006; Réfrégier, 2003; Simon, King and Schneider, 2004; Takada and Jain, 2004; Song and Knox, 2004; Ishak et al., 2004; Ishak, 2005). The prospects for determining w as a function of redshift z are markedly improved when 3D information on the individual lensed sources is available. Source distances could come from spectroscopic redshifts, but given the depth and the sky area required, they are more likely to be estimated from photometric redshifts. With 3D information, the lensing pattern can be analyzed in shells or bins at different distances (e.g. Hu, 1999; Hu and Jain, 2004; Ishak, 2005), or by analyzing the shear pattern as a fully three-dimensional field (Heavens, 2003).

The remainder of this thesis will be concerned with two ways in which shear and redshift information can be combined, 3D weak lensing, in such a way that cosmological information – specifically information on $w(z)$ – can be extracted.

The cosmological dependence of the two methods will be analysed using the Fisher Matrix approach which will be outlined in the Chapter 3. The two methods themselves will be described in detail in Chapters 3 and 4. An application of these methods using the COMBO-17 survey will be presented in Chapter 5.

Chapter 3

The Shear-Ratio Geometric Test

Here I present the shear-ratio geometric test[1] (geometric test). The method presented here, and in Taylor et al. (2006), is an adaption and extension of the Jain & Taylor (2003) shear-ratio test. This Chapter will formally present the method and derive the full shear-ratio covariance matrix, including intervening large scale structure and photometric redshift errors as additional sources of noise. The photometric redshift error is accurately modelled by integrating a redshift and magnitude dependent redshift error formula over a measured luminosity function. A maximum likelihood technique for applying the geometric test will then be presented. The geometric test is a technique that uses shear information from around galaxy clusters. To accurately model the distribution of clusters in mass and redshift the lensing matter distribution is decomposed into dark matter haloes. The Fisher Matrix and its application to the geometric test will be outlined in detail.

An optimisation of both the median redshift and photometric redshift error of an arbitrary experiment using the geometric test to measure the dark energy equation of state is presented.

This Chapter also presents the Fisher matrix analysis for three further dark energy probes with which the geometric test will be combined. These are a Cosmic Microwave Background (CMB) experiment, a Baryon Acoustic Oscillation (BAO) experiment and a supernovae Type-Ia (SNIa) experiment. All combinations of the experiments will be considered.

[1]The techniques presented in this thesis are named as 'tests' (of dark energy/cosmology) and will be referred to as 'methods'.

The layout of this Chapter is as follows. Sections 3.1 and 3.2 will outline the central mathematical formalism used in parameter error forecasts, with which the remainder of this Chapter and Chapter 4 will be concerned. Sections 3.3 and 3.4 will introduce both the concept and mathematics of the geometric test; the statistical properties are outlined in Section 3.5. A method for modelling an arbitrary survey design is introduced in Section 3.6 and various survey strategies are investigated in Section 3.7. Section 3.8 introduces three alternative dark energy probes with which the geometric test will be combined. Sections 3.9 and 3.10 present the optimisation and parameter error predictions for a wide field lensing survey, and any additional systematic effects are discussed in Section 3.11.

Before an introduction to the geometric test I will introduce the main probabilistic tools used throughout the remainder of this thesis.

3.1 Bayesian Statistics

The notion of probability is central in cosmology. It allows us to apply logical reasoning to data so that we can deduce, with a particular – and calculable – degree of accuracy, properties of that data. By modelling the properties of the data with particular cosmological models these deductions allow us constrain cosmological model parameters to a certain degree of accuracy.

We want to apply the *deductive* reasoning of everyday experience, and pure maths (Boolean logic), to problems which require *inductive* reasoning: that is going from general principles to particulars (or effects/observations to possible causes). This is an example of what is known as the 'epistemic' philosophical stance on probability:

- *Aleatory* is the concept of probability used for example in games of chance. It deals with predicting the future outcome of random physical processes. It can further be subdivided into phenomenon which are in principle predictable and those which are inherently unpredictable.
- *Epistemic* is the concept of probability used to describe the property or effect of a system when the causative circumstances for that property are unknown or uncertain.

There are a number of interpretations that one can use when dealing with the notion of probability. These can be categorised under the following, broad, headings:

- *Propensity*. Here probabilities are objective properties of a system.
- *Relative Frequency*. The relative frequency (probability) of an event arises from the number of times this event would occur defined relative to an infinite ensemble of 'identical' experiments.
- *Bayesian Probability*. Takes probability theory as a 'logic of inference', probabilities are the 'likelihood' of an event being such given all available information (data).

The propensity interpretation[2] is moot in cosmology as no theories have been proposed, and indeed can realistically be imagined, in which the probability of a cosmological parameter being

[2]Within quantum theory the propensity interpretation does have some credence, in that the probability of a particle being in a given state can be interpreted as an objective property of the particle, indeed this is the philosophical stance taken by the Heisenberg formalism, see Isham (1995).

measured as a certain value is an objective property of the Universe. The frequentist interpretation can be used within cosmology, if blindly believed it will yield sensible uncertainties on a measurement, although the underlying philosophy of such an approach contains manifest assumptions. A cosmological frequentist interpretation would posit that the uncertainty in a measurement of Ω_{de} (for example) came from that fact that if an identical experiment was performed then the value measured would be slightly, and randomly, different; the spread of measured values after an infinite number of experiments would yield the probability inferred. Since we do not perform experiments on the Universe, we passively observe the outcome of its evolution, the frequentist approach should be dismissed. Apart from this, the notions both of infinity and randomness are both ill-defined when make probabilistic assertions.

Therefore the Bayesian approach is the only logically consistent way to make assertions within cosmology. The central notion is that probability is a 'logic of inference', not an objective property of things[3] or ensembles. Probabilistic statements are interpreted as assertions about the 'degree of belief' given the data available i.e. "the probability of $\Omega_{de} = 0.7$ is 0.5" is interpreted as "it is 50% certain that $\Omega_{de} = 0.7$ given the data available". A criticism of the Bayesian approach is that it is subjective in that any assertion made depends on a given data set, but in actuality it retains the objective in that if the data sets and the priors are the same then there will be agreement. Given that all data in cosmology is derived from one source (the Universe) there should be objective agreement in results using Bayesian approaches. Bayesian probability therefore relates directly to the data, and requires no ensembles or propensities.

In general the desired value is the probability of a given set of parameters $\{\theta\}$, defined within a hypothesis H, given a data set D: $p(\{\theta\}|D, H)$. Usually this is not readily calculable, however the transposition, $p(D|\{\theta\}, H)$, usually is given a certain assumed model. For example if a Gaussian probability, with a mean μ and a variance σ, $\{\theta\} = (\mu, \sigma)$, is assumed as the model for a one-dimensional data set, $D = x$, then

$$p(D|\{\theta\}, H) = \frac{1}{\sqrt{2\pi}\sigma} \exp\left[-\frac{(x-\mu)^2}{2\sigma^2}\right]. \tag{3.1}$$

Bayes' theorem allows the the desired probability $p(\{\theta\}|D, H)$ to be related to the calculable probability $p(D|\{\theta\}, H)$ and is written as

$$p(\{\theta\}|D, H) = \frac{p(D|\{\theta\}, H)p(\{\theta\}|H)}{p(D|H)}. \tag{3.2}$$

[3] Indeed even the definition of a 'thing' in the probabilistic sense is vague. If a particle only has a probability of being in a given state, then is the particle itself 'something' until one or other of the states is realised?

$p(D|\{\theta\}, H)$ is known as the 'likelihood' (of the data given a set of parameters). $p(\{\theta\}|D, H)$ is the 'posterior' probability, the state of knowledge given the data. $p(\{\theta\}|H)$ is the 'prior' and represents what is known about parameter values before an experiment, a 'flat' prior is usually assumed $p(\{\theta\}|H) =$ constant which represents a complete lack of knowledge about any parameter values. $p(D|H)$ is the 'evidence' which can be used to determine how likely competing hypotheses are given the data see Saini et al. (2004). The evidence is ignored as a constant when the likelihood of different parameter values is needed since it does not depend on the parameter values themselves. So for a flat prior Bayes' theorem can be written

$$p(\{\theta\}|D) \propto L(D|\{\theta\}) \tag{3.3}$$

where a hypothesis underpinning the parameters used is implicit and the likelihood is written $L(D|\{\theta\})$. When using this technique the relative peak in the probability distribution is usually found and used as the estimate of the parameters, this is known as the **maximum likelihood**.

3.2 The Fisher Matrix Formalism

The Fisher matrix (occasionally referred to as the information matrix) (Tegmark, Taylor & Heavens, 1997; Jungman et al., 1996; Fisher, 1935) allows one to answer the question: how well will a particular experiment measure any given parameter? That is a theoretically robust, and realistic, value for the expected performance of any experiment can be determined. The power of this technique lies in its relative simplicity (as opposed to mock-catalogue or Monte-Carlo type approaches) which is manifested in the relatively small computational expense used in making predictions, and in its sound mathematical basis.

The following Section follows Tegmark, Taylor & Heavens (1997) closely. In the Fisher matrix formalism a set of data D (from now on represented by a data vector $\mathbf{x}$) is conceptualised as a random variable with some probability distribution $L(\mathbf{x}|\boldsymbol{\theta})$, which depends in some known way on a set of parameters $\boldsymbol{\theta}$ now represented by a vector of parameter values. $\boldsymbol{\theta}_0$ represent the 'true' parameter values and $\boldsymbol{\theta}$ refers to the estimate of the values which is a function of the data $\mathbf{x}$ and so is itself a random variable. For the estimate to be a 'good' estimate, that is representative of the true values, it is desired to be unbiased

$$\langle \boldsymbol{\theta} \rangle = \boldsymbol{\theta}_0, \tag{3.4}$$

and the error on the estimate to be small as possible i.e.

$$\Delta\theta_i \equiv \left(\langle\theta_i^2\rangle - \langle\theta_i\rangle^2\right)^{1/2}, \tag{3.5}$$

where θ_i is the $i^{\rm th}$ value of the parameter set. An estimate that satisfies both of these requirements is the 'Best Unbiased Estimate' (BUE).

If all model parameters and all data vectors have equal prior probability then Bayes' theorem equates the posterior probability and the likelihood $L(\mathbf{x}|\boldsymbol{\theta}) = L(\boldsymbol{\theta}|\mathbf{x})$. The **Fisher matrix** is defined as the curvature of the log-likelihood surface about it maximum, defined as:

$$\mathbf{F}_{ij} \equiv \left\langle \frac{\partial^2\mathcal{L}}{\partial\theta_i\partial\theta_j} \right\rangle, \tag{3.6}$$

where $\mathcal{L} = -\ln L$. Defining the maximum likelihood estimator (ML estimator) $\boldsymbol{\theta}_{ML}$ as the parameter vector that maximises $L(\boldsymbol{\theta}|\mathbf{x})$, and expanding the log-likelihood using a Taylor expansion about this maximum, gives

$$\ln L(\boldsymbol{\theta}|\mathbf{x}) \approx \ln L(\boldsymbol{\theta}_{ML}|\mathbf{x}) + \sum_i \Delta\theta_i \frac{\partial}{\partial\theta_i}\ln L(\boldsymbol{\theta}_{ML}|\mathbf{x}) + \sum_{ij}\frac{1}{2}\Delta\theta_i\Delta\theta_j\frac{\partial^2}{\partial\theta_i\partial\theta_j}\ln L(\boldsymbol{\theta}_{ML}|\mathbf{x}). \tag{3.7}$$

At the maximum likelihood point the gradient of the likelihood is zero and so the second term is zero, it is assumed that the log-likelihood surface drops away from its maxima sharp enough so that third order terms are not important as is the case in high precision cosmological applications where the predicted errors are small. By taking the exponential of both sides it can be seen that the likelihood is described by a multi-variate Gaussian in parameter space with a covariance equal to the inverse Hessian matrix:

$$\mathbf{T}_{ij}^{-1} \equiv \frac{\partial^2\mathcal{L}}{\partial\theta_i\partial\theta_j}. \tag{3.8}$$

The Fisher matrix is equal to the expectation value of this matrix at the BUE point (if the ML estimator is unbiased this corresponds with the ML point on average) equivalent to taking an ensemble average (for example over many Monte-Carlo simulations of the data).

A number of theorems have been proved which underpin the Fisher matrices usefulness.

- For any unbiased estimator, $\Delta\theta_i \geq 1/(\mathbf{F}_{ii})^{1/2}$.
- If the exists a BUE then it is equal to the ML estimator, or a function of the ML estimator.
- The ML estimator is asymptotically the BUE estimator.

The first theorem is known as the Cramér-Rao inequality and can be used to predict the **conditional error** estimate on a given parameter; that is the lower error limit on a parameter measurement if all other parameters are known exactly (zero error). The **marginal error** is defined as the error attainable on a parameter given that there are errors on all other parameters within the model, it takes into account these other errors, and can be estimated by generalising the Cramér-Rao inequality to $\Delta\theta_i \geq (\mathbf{F}_{ii}^{-1})^{1/2}$. By using the marginal error all correlations between parameters are taken into account, the amount of correlation can be quantitatively estimated from the Fisher matrix by defining the correlation matrix, or **degeneracy matrix**, as

$$\mathbf{D}_{ij} = \frac{\mathbf{F}_{ij}^{-1}}{\sqrt{\mathbf{F}_{ii}^{-1}\mathbf{F}_{jj}^{-1}}}. \tag{3.9}$$

So that if $0 < \mathbf{D}_{ij} \leq 1$ parameters are correlated ($\mathbf{D}_{ij} = 1$ parameters are totally correlated), and if $-1 \leq \mathbf{D}_{ij} < 0$ parameters are anti-correlated ($\mathbf{D}_{ij} = -1$ parameters are totally anti-correlated). The second theorem confirms that the if there is a best method of parameter estimation then the ML method is the one. The third theorem shows that in a practical circumstance when a large data set is used the ML estimate is the best estimate (for which the Cramér-Rao inequality becomes an equality).

If the probability distribution is a multivariate Gaussian of N variables then

$$L(\mathbf{x}|\boldsymbol{\theta}) = \frac{1}{(2\pi)^{N/2}\sqrt{\det \mathbf{C}}} \exp[-\frac{1}{2}(\mathbf{x}-\mu)\mathbf{C}^{-1}(\mathbf{x}-\mu)^T], \tag{3.10}$$

where μ is a vector of mean values, and $\mathbf{C}$ is the $N \times N$ covariance matrix. Then Fisher matrix can be expressed simply in terms of the covariance matrix and the mean

$$\mathbf{F}_{ij} = \frac{1}{2}\mathrm{Tr}[\left(\mathbf{C}^{-1}\mathbf{C}_{,i}\mathbf{C}^{-1}\mathbf{C}_{,j}\right) + \mu_{,i}\,\mathbf{C}^{-1}\mu_{,j}^T + \mu_{,j}\,\mathbf{C}^{-1}\mu_{,i}^T], \tag{3.11}$$

where a comma represents a derivative with respect to a given parameter.

Equation (3.11) is central to the work of this thesis, it allows, via the Cramér-Rao inequality, to forecast the parameter errors achievable by a given experiment using a physically justified, and readily calculable, model for the covariance matrix of a given experiment. This allows future experimental performance to be tested in terms of the scientific return it will give (how small will the errors be on a particular cosmological parameter be?) and allows for the optimisation of future experimental strategies. For example, given a certain number of nights on a given telescope what is the best survey design if your goal is to measure the equation of state of dark energy? It is questions like these which this thesis will answer within the context of 3D weak lensing.

Having introduced the Fisher matrix the remainder of this Chapter will introduce, and discuss in detail, the shear-ratio geometric test.

3.3 Introduction to the Geometric Test

Gravitational lensing can probe dark energy using both the geometry of the Universe, via the observer-lens-source distances, and the growth of structure which will lens distant galaxies. Gravitational lensing is an integral effect and so for a given line of sight these effects are degenerate with each other and other parameters. In order to disentangle these effects redshift information is required for the source images. It has already been shown that such information can be used to reconstruct the 3D distribution of dark matter (Taylor, 2001; Taylor et al., 2004). For large-scale imaging surveys, the most practical way to get redshifts for each image is from multi-band photometric redshift surveys. The COMBO-17 imaging and photometric survey (Wolf et al., 2003) has already shown the power of combining lensing with photometric redshifts (Brown et al., 2003; Taylor et al., 2004; Gray et al., 2004; Bacon et al., 2005).

Constraints on the parameters of the dark energy equation of state can be extracted from weak gravitational shear measurements by taking correlations of galaxy ellipticities at different redshifts (e.g. Bacon et al., 2005; Hu & Jain, 2003; Heavens, 2003; Semboloni, 2006), where the expansion history enters both the lens geometry and the dark matter evolution rate. Jain & Taylor (2003) proposed an alternative approach, taking the ratio of the galaxy-shear correlation functions at different redshifts. In this case the mass of the lens dropped out leaving behind a purely geometric quantity useful for measuring cosmological parameters. This had the advantages of allowing the analysis to extend into the nonlinear clustering régimes where modelling the nonlinear matter power spectrum can be inaccurate, and where the shear signal will also be stronger, i.e. in the vicinity of galaxy clusters. In addition, as this relies upon the correlation between galaxies and shear, many systematic effects will be averaged over, as in galaxy-galaxy lensing. Following this a number of papers have suggested variations on this theme (Bernstein & Jain, 2003; Hu & Jain, 2004; Zhang, Hui & Stebbins, 2005).

Geometric tests of dark energy not only complement other methods based on the clustering of matter, but directly probe the global evolution of the Universe via the redshift-distance relation, $r(z)$. Other methods measure the combined effect of the growth rate of perturbations and the global geometry. Comparison of the two can be used to test the Einstein-Hilbert action, and

extensions and modifications of GR such as extra dimensions.

While the main focus of the Jain & Taylor (2003) paper was a statistic given by the ratio of galaxy-shear correlations (or equivalently power spectra), they illustrated their method with the analysis of a single cluster. In this Chapter the Jain & Taylor idea is developed further and focuses on applying the geometric test behind individual galaxy clusters. The main difference between this and the original Jain & Taylor approach that one does not need to first generate galaxy-shear cross-correlation functions, or cross-power spectra, which require large data-sets. Rather the ratios used are just of the shears behind a given cluster at fixed redshifts. This allows the test to be applied to noisy data, since estimates of the correlation functions are not needed before applying the geometric test. This is similar to the approach of Bernstein & Jain (2004), who considered a "template matching" approach, cross-correlating a foreground galaxy template with the background shear pattern. The geometric test is different in that the galaxies are used to identify the positions of lensing haloes, and then the shear ratios are taken. Doing so focuses on the dark matter haloes generating the signal, allowing a halo decomposition of the matter distribution. This allows an investigation into how to maximise the signal with respect to galaxy cluster size and abundance. The price that is payed for this approach is that it becomes susceptible to a sampling variance due to lensing by other large-scale structure along the line of sight, which can be beaten down using multiple lines of sight. In addition these methods are generalised to non-flat cosmological models.

Zhang, Hui & Stebbins (2005) have proposed a different geometric test, which allows them to extend the correlation/power spectrum method to galaxy-galaxy and shear-shear correlations as well as galaxy-shear cross-correlations. They also point out some inaccuracies with the analysis of Jain & Taylor (2003) and Bernstein & Jain (2003), which are corrected here.

3.4 The Dark Energy Shear-Ratio Geometric Test

3.4.1 Background Cosmology

Here is a brief review of the background cosmology used in the remainder of this Chapter.

The metric used is given by equation (1.21). $r(z)$ is here defined as the the comoving distance

given by, see equation (1.51),

$$r(z) = \int_0^z \frac{dz'}{H(z')}, \tag{3.12}$$

and

$$S_k(r) = \begin{cases} r_0 \sin(r/r_0) & \text{(k=1)} \\ r & \text{(k=0)} \\ r_0 \sinh(r/r_0) & \text{(k=-1)}, \end{cases} \tag{3.13}$$

is the angular distance, where $r_0 = 1/\sqrt{|\Omega_k|}H_0$ is the radius of curvature of the Universe and H_0 is the current value of the Hubble parameter, see equation (1.22). The time-variation of the Hubble parameter, see Section 1.3.1, with the cosmic scale factor, $H(a)$, is given by

$$\frac{H(a)}{H_0} = \left(\Omega_m a^{-3} + \Omega_k a^{-2} + \Omega_{de} e^{-3\int_1^a d\ln a'[1+w(a')]}\right)^{1/2}, \tag{3.14}$$

which is a function of the dark energy equation of state, $w(a)$, and the present-day density parameters; the matter density, Ω_m, dark energy density, Ω_{de}, and the energy-density associated with the curvature, $\Omega_k = 1 - \Omega_m - \Omega_{de}$. A useful expansion of the time-dependence of the equation of state in terms of the expansion parameter, a, is (Chevallier and Polarski, 2001; Linder 2002)

$$w(a) = w_0 + w_a(1-a), \tag{3.15}$$

which evolves from $w = w_0 + w_a$ at high redshift to $w = w_0$ at low redshift, with the transition around $z = 1$, see Section 1.8.5. In this case the time-dependence of the Hubble parameter is given by

$$\frac{H(a)}{H_0} = [\Omega_m a^{-3} + \Omega_k a^{-2} + \Omega_{de} a^{-3(1+w_0+w_a)} e^{-3w_a(1-a)}]^{1/2}. \tag{3.16}$$

3.4.2 Weak Shear

A galaxy cluster at a redshift z_l will induce a shear pattern on the background galaxies, which can be expressed in complex notation as, see equation (2.23),

$$\gamma(\boldsymbol{\theta}) = \gamma_1(\boldsymbol{\theta}) + i\gamma_2(\boldsymbol{\theta}), \tag{3.17}$$

where γ_1 and γ_2 are orthogonal components of the shear field at an angle of $\boldsymbol{\theta}$. Around lensing clusters it is convenient to use the shear tangential around the cluster centre, see Section 2.2.2. This can be projected out from the total shear by

$$\gamma_t = -[\gamma_1 \cos(2\varphi) + \gamma_2 \sin(2\varphi)], \tag{3.18}$$

where φ is an azimuthal angle around the centre of the cluster.

Using equations (2.52) and (2.65) and assuming that the 3D comoving potential of a lensing cluster is a delta function in redshift, the amplitude of the induced tangential shear distortion behind a cluster at redshift z_l will grow with redshift as

$$\gamma_t(z) = \gamma_{t,\infty} \frac{S_k[r(z) - r(z_l)]}{S_k[r(z)]}, \qquad z_l < z \tag{3.19}$$

where $\gamma_{t,\infty}$ is the tangential shear induced on a galaxy at infinite redshift. If the ratio of the shear values at two different background redshifts, z_i and z_j is taken, (Jain & Taylor, 2003) then

$$R_{ij} = \frac{\gamma_{t,i}}{\gamma_{t,j}} = \frac{S_k[r(z_j)]S_k[r(z_i) - r(z_l)]}{S_k[r(z_i)]S_k[r(z_j) - r(z_l)]}, \quad z_l < z_i < z_j. \tag{3.20}$$

This is the key equation describing the geometric test. In the last term the mass and structure of the cluster has dropped out.

In the real Universe galaxy clusters are not isolated, and additional large-scale structure along the line of sight between the lens and the background source galaxies will contribute to the observed shear in both backgrounds. If we assume that the large-scale structure is uncorrelated with the cluster then this effect will average out over independent clusters. Defining

$$D_{ij} = \frac{\gamma_{t,i}}{\gamma_{t,j}} \tag{3.21}$$

as the observed ratio of the tangential shear between two redshifts, on average for a given cluster

$$\langle D_{ij} \rangle = R_{ij} \equiv \frac{S_k[r(z_j)]S_k[r(z_i) - r(z_l)]}{S_k[r(z_i)]S_k[r(z_j) - r(z_l)]}, \quad z_l < z_i < z_j. \tag{3.22}$$

3.4.3 Response of Shear Ratios to Cosmological Parameters

The intrinsic sensitivity of the shear ratio, R_{ij}, to a cosmological parameter, θ, can be estimated from its logarithmic response,

$$\frac{\Delta R_{ij}}{R_{ij}} = \left(\frac{\partial \ln R_{ij}}{\partial \ln \theta_i} \right) \frac{\Delta \theta}{\theta}. \tag{3.23}$$

Figure 3.1 shows the response of the shear ratio, R, to each of the cosmological parameters that fix the geometry of the Universe, for a lens at $z_l = 0.2$ with backgrounds at $z_1 = z$

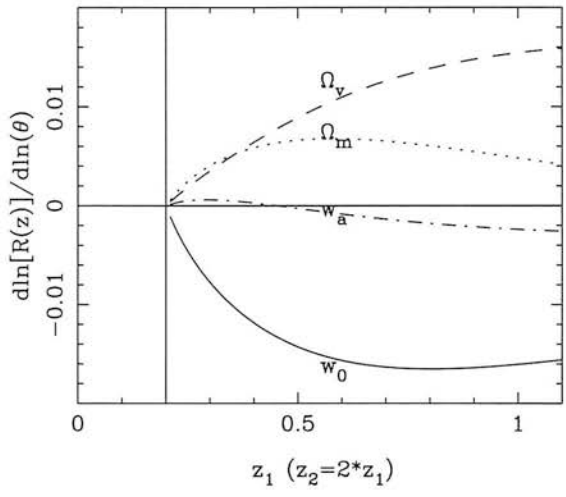

Figure 3.1: The response of the shear ratio, R, to each of the four cosmological parameters, Ω_m, Ω_{de} (where $\Omega_k = 1 - \Omega_m - \Omega_{de}$), w_0 and w_a as a function of source redshift. The line for w_a has been rescaled by a factor $1/w_a$ to make it finite, so that $\partial \ln R / \partial\, w_a$ is plotted. Here $z_2 = 2z_1$ is set. The assumed fiducial model is $\Omega_m = 0.27$, $\Omega_{de} = 0.73$, $w_0 = -1.0$ and $w_a = 0.0$. Note in this Figure and throughout this Chapter $\Omega_v = \Omega_{de}$ for clarity.

and $z_2 = 2z$. From this it can be seen that the response of the shear ratio to cosmological parameters is weak, scaling roughly as

$$R \propto |w_0|^{-0.02} \Omega_{de}^{0.01} \Omega_m^{0.002} e^{-0.001 w_a}, \tag{3.24}$$

for sources at $z_1 = 1$ and $z_2 = 2$. This weak dependence calls for high accuracy in the shear measurements. The control of systematics is discussed in Section 3.11.

The similarity of the responses of the shear ratio to different cosmological parameters in Figure 3.1 also indicates their strong degeneracies. It should be expected that w_0 will be correlated with Ω_{de} and Ω_m, whilst the Ω_{de}–Ω_m and w_0–w_a combinations will be anti-correlated with each other. The similarity of the responses of w_0 and Ω_m suggest these parameters will be highly degenerate, while the differences between w_0 and Ω_{de} at low redshift suggest these should be less correlated. The response of R to w_0 peaks at around $z = 0.8$, when the dark energy begins to dominate the energy-density of the Universe. Interestingly, although weak, the geometric test is most sensitive to w_0. As the dark energy equation of state is parameterised as $w(z) = w_0 + w_a[z/(1+z)]$ a change in w_0 affects the amplitude of $w(z)$ at all redshifts and hence affects the shape of the tangential shear as a function of redshift at all redshifts. At low redshift w_a only changes the slope of $w(z)$ and its amplitude at higher redshift where the effect of dark energy is less significant.

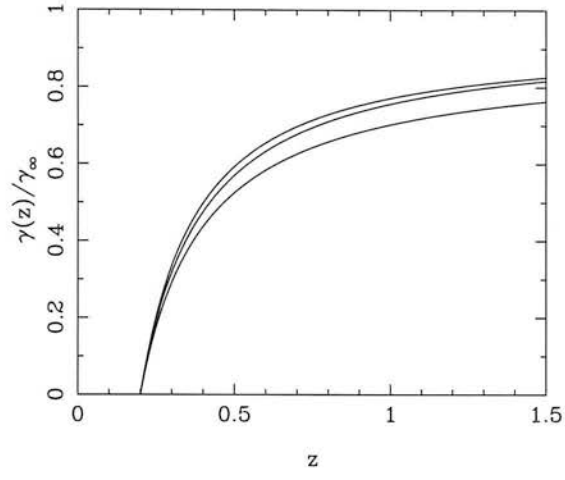

Figure 3.2: The tangential shear profile as a function of w_0 for a lens at $z = 0.2$ normalised relative to $\gamma(z = \infty)$, showing the effect of any shape changes. The lines are, from lowest to highest are for $w_0 = -1.5, -1.0, -0.5$.

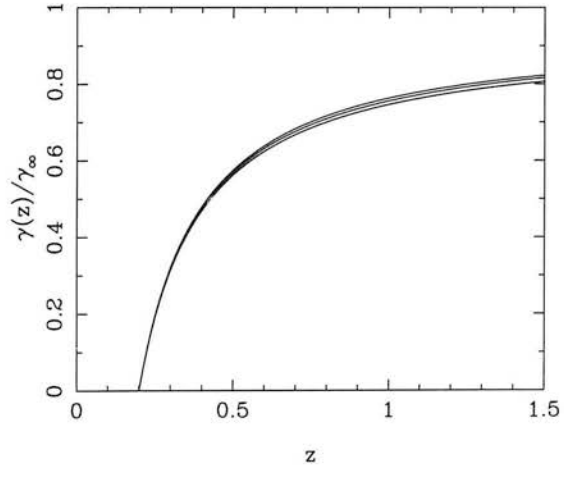

Figure 3.3: The tangential shear profile as a function of w_a for a lens at $z = 0.2$ normalised relative to $\gamma(z = \infty)$, showing the effect of any shape changes. The lines are from lowest to highest are for $w_a = -0.5, 0.0, 0.5$.

Since in this method shear ratios are taken, the method is only sensitive to changes in the shape of the shear-redshift relation. Figure 3.2 and 3.3 show the shear as a function of z normalised to unity at $z = \infty$ using equation (3.19) for different w_0 and w_a. This shows the effect that changes in w_0 and w_a have on the shape of the tangential shear. Varying both w_0 and w_a by ± 0.5. It can be seen that w_0 has a much larger effect than w_a on the shape of the shear as a function of redshift.

3.5 Statistical Properties

In this Section I present a maximum likelihood approach to measuring the geometry of the Universe from shear ratios around individual clusters and galaxy groups. This analysis considers shot-noise, from galaxy discreteness and intrinsic galaxy ellipticities, the effect of lensing by large-scale structure between the lens and the background source galaxies, which will act as an addition source of correlated and uncorrelated noise, and photometric redshift errors.

3.5.1 Likelihood Analysis

Compressing the notation for a pair of background galaxies as $\mu = (i, j)$ and $\nu = (m, n)$ the covariance matrix for shear ratios can be written as

$$\boldsymbol{C}_{\mu\nu}^{RR} \equiv \langle \Delta R_\mu \Delta R_\nu \rangle. \tag{3.25}$$

The log-likelihood function for the four cosmological parameters estimated from a single cluster is then

$$-2 \ln L_c(\Omega_{de}, \Omega_m, w_0, w_a | \boldsymbol{D}) = \sum_{\mu,\nu} (R_\mu - D_\mu)[\boldsymbol{C}_{\mu\nu}^{RR}]^{-1}(R_\nu - D_\nu). \tag{3.26}$$

Here it has been further assumed that the scatter between R_ν and D_ν, due to shot-noise, photometric redshift errors and cosmic shear from large-scale structure, is Gaussian distributed. It does not need need to be assumed that the lensing signal from the clusters itself is Gaussian.

If a survey contains multiple independent clusters, the total log-likelihood is just the sum of the log-likelihoods for the individual clusters;

$$\ln L_{\rm TOT}(\Omega_{de}, \Omega_m, w_0, w_a) = \sum_{c=1}^{N_{\rm cl}} \ln L_c(\Omega_{de}, \Omega_m, w_0, w_a | \boldsymbol{D}), \tag{3.27}$$

where $N_{\rm cl}$ is the number of independent clusters in the survey.

3.5.2 The Covariance of R

The covariance matrix of shear ratios, $\boldsymbol{C}_{\mu\nu}^{RR}$, is given by

$$\langle \Delta R_{ij} \Delta R_{mn} \rangle = \langle \Delta R_{ij} \Delta R_{mn} \rangle_{\rm sn} + \langle \Delta R_{ij} \Delta R_{mn} \rangle_{\rm lss}, \tag{3.28}$$

which can be decomposed into a shot-noise term due to the intrinsic dispersion in galaxy ellipticities, and a term due to cosmic shear induced by the intervening large-scale structure between the lens and the two background sources.

To avoid double counting and taking ratios of the same redshift bins, the indices in equation (3.28) are restricted to $i < j$ and $m < n$. Finally, there is a remaining degeneracy between the shear ratios, since the ratios between any three galaxies at redshift z_i, z_j and z_k obey the relation

$$R_{ij} = R_{ik} R_{kj}. \tag{3.29}$$

This reduces the total number of permutations of usable pairs of galaxies to $(N_g - 1)$, where N_g is the total number of galaxies. In practice the data will be binned in redshift, in which case this also applies to bins.

Shot-Noise Covariance

The first term in equation (3.28) is due to shot-noise, arising from the discrete nature of galaxies and the intrinsic dispersion in galaxy ellipticities;

$$\frac{\langle \Delta R_{ij} \Delta R_{mn} \rangle_{\rm sn}}{R_{ij} R_{mn}} = \left(\frac{\Delta \gamma_i}{\gamma_i} \right)^2 \left(\delta_{im}^K - \delta_{in}^K \right) + \left(\frac{\Delta \gamma_j}{\gamma_j} \right)^2 \left(\delta_{jn}^K - \delta_{jm}^K \right). \tag{3.30}$$

Where δ_{ij}^K is the Kronecker delta-function and, see equation (2.49),

$$\left(\frac{\Delta \gamma_i}{\gamma_i} \right)^2 = \frac{\sigma_e^2}{2\gamma_i^2} \tag{3.31}$$

is the fractional variance in the tangential shear due to the intrinsic dispersion in background galaxy ellipticity σ_e and $\gamma_i = \gamma(z_i)$ is the expected tangential shear signal from the cluster for a background galaxy at redshift z_i. Here it is assumed that $\sigma_e = 0.3$, for a ground-based survey, as measured from the COMBO-17 survey (Brown et al., 2003).

There is a subtlety in determining the distribution of the fractional variance for the ratio of two ellipticity measurements. If it is assumed that the observed ellipticities have zero mean, and

that the distribution of intrinsic galaxy ellipticities is Gaussian, the resulting distribution of the ratio of ellipticities has a Cauchy/Lorentzian distribution, and so an infinite variance. Around a lensing cluster, the mean ellipticity of the background galaxies is non-zero, and if it is assumed that the mean signal is always greater than the dispersion in the mean due to intrinsic galaxy ellipticities the variance is finite and Gaussian errors can be assumed. This is certainly the case when averaging the shear both tangentially around a cluster and in redshift bins. Hence, instead of working with individual galaxies binned galaxies will be considered. The fractional variance in the shear is now

$$\left(\frac{\Delta\gamma_i}{\gamma_i}\right)^2 = \frac{\sigma_e^2}{2N_i\gamma_i^2} \tag{3.32}$$

per redshift bin, where N_i is the number of galaxies in the i^{th} redshift bin. From hereon, the indices i and j will refer to bin number, rather than individual galaxies.

Photometric Redshift Errors

In current and future weak lensing surveys photometric redshifts will also be available as an estimate of galaxy distances (see, e.g. COMBO-17, Wolf et al, 2001; CFHTLS, Semboloni et al., 2006). Here the effect of photometric redshift uncertainty on shear ratios is characterised.

The effect of errors on the photometric estimates of galaxy redshifts is to dilute the shear signal in each redshift bin by randomly moving galaxies in and out of any particular bin. If it is assumed that the distribution of redshift errors is a Gaussian with width $\sigma_z(z_g)$ which depends on the true redshift of the galaxy, z_g, and has a bias in the mean of the distribution $z_{\rm bias}$, then

$$p(z|z_g,\sigma_z) = \frac{1}{\sqrt{2\pi}\sigma_z(z_g)} e^{-(z-z_g+z_{\rm bias})^2/2\sigma_z^2(z_g)}. \tag{3.33}$$

It will be assumed that $z_{\rm bias} = 0$ for all experiments, its effect on the marginal error of $w(z)$ will be discussed in Section 3.6.3, where the effect of a change in the variance $\sigma_z(z) \rightarrow \sqrt{[\sigma_z^2(z) + \Delta\sigma_z^2(z)]}$ is also discussed. I discuss the specific form for $\sigma_z(z)$ for photometric redshift surveys in Section 3.6.2.

The expected shear in a redshift bin of width Δz and centred on z_i is the average shear given by integrating over all redshifts weighted at each redshift by the expected number density $n(z)$ and the probability of finding a galaxy in the redshift bin in question

$$\langle\gamma_{t,i}\rangle = \gamma_{t,\infty}\int_{z_l}^{\infty} dz\, \frac{S_k[r(z)-r(z_l)]}{S_k[r(z)]} n(z)W(z) \int_{z_i-\frac{\Delta z}{2}}^{z_i+\frac{\Delta z}{2}} dz'\, p(z-z'|\sigma_z), \tag{3.34}$$

where $W(z)$ is a weighting function. The second z' integral in equation (3.34) can be solved for a Gaussian probability distribution so that

$$\langle\gamma_{t,i}\rangle = \gamma_{t,\infty}\int_{z_l}^{\infty} dz\, n(z)\frac{S_k[r(z)-r(z_l)]}{S_k[r(z)]}W(z)P_{\Delta z}[z_i - z|\sigma_z(z_i)], \tag{3.35}$$

where (e.g., Ma et al., 2006)

$$P_{\Delta z}[z|\sigma_z] = \frac{1}{2}\left[\mathrm{erf}\left(\frac{z+z_{\rm bias}+\Delta z/2}{\sqrt{2}\sigma_z}\right)\right] - \frac{1}{2}\left[\mathrm{erf}\left(\frac{z+z_{\rm bias}-\Delta z/2}{\sqrt{2}\sigma_z}\right)\right] \tag{3.36}$$

is the part of the redshift error distribution which lies in a redshift bin of width Δz centred on z, and $\mathrm{erf}(x)$ is the error function. The estimated shear is weighted by the number of galaxies scattered from one redshift to another, given by the galaxy redshift distribution, $n(z)$. The weighting function is given by

$$W(z) = \frac{\tilde{w}(z)}{\int_0^\infty dz'\tilde{w}(z')n(z')P_{\Delta z}[z-z'|\sigma_z(z)]} \tag{3.37}$$

where $\tilde{w}(z)$ is some arbitrary weighting function of the shears in redshift, which will be taken as $\tilde{w}(z) = 1$ for the remainder of this thesis except in Section 3.9.4 where its effect will be investigated.

Cosmic Shear Covariance

The second term in equation (3.28), due to the cosmic tangential shear induced by large-scale structure between the lens and the source planes, is given by

$$\begin{aligned}\frac{\langle\Delta R_{ij}\Delta R_{mn}\rangle_{\rm lss}}{R_{ij}R_{mn}} = &\frac{C^{\gamma_t\gamma_t}_{1,im}}{\gamma_{t,i}\gamma_{t,m}} + \frac{C^{\gamma_t\gamma_t}_{1,jn}}{\gamma_{t,j}\gamma_{t,n}} - \frac{C^{\gamma_t\gamma_t}_{1,in}}{\gamma_{t,i}\gamma_{t,n}} - \frac{C^{\gamma_t\gamma_t}_{1,jm}}{\gamma_{t,j}\gamma_{t,m}} \\ &+ \frac{C^{\gamma_t\gamma_t}_{2,i,\min(j,n)}}{\gamma^2_{t,j}}\delta^K_{im} + \frac{C^{\gamma_t\gamma_t}_{2,\max(i,m),j}}{\gamma^2_{t,j}}\delta^K_{jn},\end{aligned} \tag{3.38}$$

with the same restriction on indices as for the shot-noise term. C_1 and C_2 are defined in equations (3.40), (3.41) and (3.42). The first four terms in equation (3.38) are due to the correlated distortions induced on both background galaxy images by matter lying in front of the nearest source plane. The last two terms arise from matter lying between the background source planes and can be regarded as an extra noise term on the ellipticities of the furthest background source galaxies. The covariance of the induced tangential shear for background galaxies at redshifts z_i and z_j due to large-scale structure between the observer and the background source

galaxies and averaged over an aperture of area A and radius θ is

$$\begin{aligned}
C^{\gamma_t\gamma_t}(\theta) &= \frac{1}{A^2}\int d^2\theta \int d^2\theta' \,\langle\gamma_t(\boldsymbol{\theta})\gamma_t(\boldsymbol{\theta}')\rangle \\
&= \frac{1}{A^2}\int d^2\theta \int d^2\theta' \,\left(\langle\gamma_1(\boldsymbol{\theta})\gamma_1(\boldsymbol{\theta}')\rangle\cos 2\varphi\cos 2\varphi' + \langle\gamma_2(\boldsymbol{\theta})\gamma_2(\boldsymbol{\theta}')\rangle\sin 2\varphi\sin 2\varphi'\right) \\
&= \frac{1}{A^2}\int d^2\theta \int d^2\theta' \\
&\quad \left[\int \frac{d^2\ell}{(2\pi)^2}\, C_\ell^{\gamma\gamma}(\cos^2 2\varphi_\ell\cos 2\varphi\cos 2\varphi' + \sin^2 2\varphi_\ell\sin 2\varphi\sin 2\varphi')e^{i\boldsymbol{\ell}.(\boldsymbol{\theta}-\boldsymbol{\theta}')}\right] \\
&= \int \frac{d^2\ell}{(2\pi)^2}\, C_\ell^{\gamma\gamma}\cos^2 2\varphi_\ell\left(\frac{1}{A}\int d^2\theta e^{i\boldsymbol{\ell}.\boldsymbol{\theta}}\cos 2\varphi\right)^2 \\
&= \int_0^\infty \frac{\ell d\ell}{\pi}\, C_\ell^{\gamma\gamma}\left\{\frac{2[1-j_0(\ell\theta)]}{\ell^2\theta^2} - \frac{j_1(\ell\theta)}{\ell\theta}\right\}^2
\end{aligned} \tag{3.39}$$

where $\cos\varphi_\ell = \hat{\boldsymbol{\ell}}.\hat{\boldsymbol{\theta}}_1$ and $\hat{\boldsymbol{\theta}}_1$ is the unit vector along one axis. So that I define

$$C^{\gamma_t\gamma_t}_{\alpha,ij}(\theta) = \int_0^\infty \frac{\ell d\ell}{\pi}\, C^{\gamma\gamma,\alpha}_{\ell,ij}\left\{\frac{2[1-j_0(\ell\theta)]}{\ell^2\theta^2} - \frac{j_1(\ell\theta)}{\ell\theta}\right\}^2, \tag{3.40}$$

where $\alpha = (1,2)$.

Here j_n is the $n^{\rm th}$ order Bessel function, and the angular shear-shear power spectrum for the two source galaxies is, see equation (2.60),

$$C^{\gamma\gamma,1}_{\ell,ij} = \frac{9}{4}\Omega_m^2 H_0^4 \int_0^{r_i<r_j} dr\, P_\delta[\ell/S_k(r), r]\mathcal{W}[r, r_i]\mathcal{W}[r, r_j]W[z(r)], \tag{3.41}$$

and

$$C^{\gamma\gamma,2}_{\ell,ij} = \frac{9}{4}\Omega_m^2 H_0^4 \int_{r_i}^{r_j} dr\, P_\delta[\ell/S_k(r), r]\mathcal{W}^2[r, r_j]W[z(r)] \tag{3.42}$$

for sources at redshifts z_i and z_j, and $r_i = r(z_i)$. I have used a nonlinear matter power spectrum, $P_\delta(k,r)$, with a ΛCDM model with concordance parameter values, $\Omega_m = 0.27$, $\Omega_{de} = 0.73$, $h = 0.71$, using the functional form of Eisenstein & Hu (1999) for the linear power spectrum. The linear power spectrum is mapped to the nonlinear régime using the fitting functions of Smith et al. (2003). The lensing weighting function in equations (3.41) and (3.42) is given by

$$\mathcal{W}[r, r_i] = \frac{S_k(r_i - r)}{S_k(r_i)a(r)}. \tag{3.43}$$

In the case of binned data with photometric redshift errors, averaging over the bin width with in a similar way to equation (3.34), this becomes

$$\overline{\mathcal{W}}(r, r_i) = \int_{z_l}^\infty dz\, n(z)P_{\Delta z}[z_i - z|\sigma_z(z_i)]\mathcal{W}[r, r(z)]. \tag{3.44}$$

$W(z)$ is defined in equation (3.37).

3.5.3 Parameter Covariances

This likelihood analysis can be used to extract cosmological parameter error estimations. The parameter covariance matrix can be calculated from the inverse of the Fisher matrix,

$$\langle \Delta\theta_i \Delta\theta_j \rangle = \boldsymbol{F}_{ij}^{-1}, \tag{3.45}$$

where, see equation (3.6),

$$\boldsymbol{F}_{ij} = -\left\langle \frac{\partial^2 \ln L}{\partial\theta_i \partial\theta_j} \right\rangle \tag{3.46}$$

is the Fisher matrix and $\boldsymbol{\theta} = (\Omega_{de}, \Omega_m, w_0, w_a)$ is a vector containing the cosmological parameters (see Tegmark, Taylor & Heavens, 1997).

For a Gaussian likelihood function with parameters in the mean, such as equation (3.26) the Fisher matrix for the geometric test reduces to

$$\boldsymbol{F}_{ij} = \frac{1}{2} \sum_{\mu,\nu} \left[\partial_i R_\mu (\boldsymbol{C}_{\mu\nu}^{RR})^{-1} \partial_j R_\nu + \partial_j R_\mu (\boldsymbol{C}_{\mu\nu}^{RR})^{-1} \partial_i R_\nu \right],$$

where ∂_i denotes differentiation in parameter space, and the summation in μ and ν denotes summing over all non-degenerate source configurations (see Section 3.5.2). Throughout I will quote marginalized errors. Results on parameter accuracies are presented in Section 3.10.

3.6 Survey Design Formalism

To understand the contribution to the geometric test signal from clusters of differing mass and redshift, I use a halo decomposition of the matter density distribution (Peacock & Smith, 2000; Smith et al., 2003; Seljak, 2000). The full signal then comes from integrating over all halo masses, lens redshifts and background sources, but with the halo decomposition information can be extracted about which halo mass range contributes most to the signal. This will help to determine optimal survey strategies.

In this Section a more detailed model for photometric redshift errors will also be discussed, based on studies of photometric redshift accuracies from the COMBO-17 survey (Wolf et al., 2003), and the limits of ground-based measurements of galaxy ellipticities. These elements are then factored into the optimisation of a weak lensing survey in Sections 3.7 and 3.9.

3.6.1 Halo Decomposition of the Matter Density Field

So far this thesis has only considered the shear signal from a single cluster. In practice one would want to sum over many galaxy clusters in a weak lensing survey. In this case the abundance of clusters is modelled as a function of mass and redshift, $\mathcal{N}(M, z)$. To apply this a relation between mass and shear needs to be found. For simplicity I will use the Singular Isothermal Sphere (SIS) model, see Section 2.1.7.

The mean tangential shear signal inside a circular aperture of angular radius θ for a SIS, and a source with virial mass M at infinity, using equation (2.38) and (2.50), is

$$\overline{\gamma}_{t,\infty}(<\theta, M) = \frac{\theta_\infty(M)}{\theta}, \tag{3.47}$$

where, using equation (2.37),

$$\theta_\infty(M) = \frac{4\pi\sigma_v^2}{c^2} = \left(\frac{M}{M_0}\right)^{2/3} \tag{3.48}$$

is the Einstein radius for a source at infinity. The difference of a factor of two between equations (2.38) and (3.47) is due to the averaging over an aperture. Equation (3.48) has made use of the constant virial velocity of the SIS,

$$\sigma_v^2 = \frac{3GM}{2r_v}, \tag{3.49}$$

where the virial mass, M, is the mass enclosed by the virial radius, r_v;

$$M = \frac{4\pi}{3} r_v^3 \overline{\rho}_m \delta_v. \tag{3.50}$$

Here $\overline{\rho}_m$ is the mean mass-density of the Universe, $\delta_v = 340$ (Eke et al. 1996) is the virial overdensity for a ΛCDM universe, and

$$M_0 = \frac{c^3}{\pi^2\sqrt{288 G^3 \overline{\rho}_m \delta_v}} \tag{3.51}$$

is a characteristic mass. Equation (3.50) defines the virial radius, r_v, in terms of the virial mass, M, and is given by

$$r_v = 0.24 \left(\frac{M}{10^{13} M_\odot}\right)^{1/3} (\Omega_m h^2)^{-1/3} \mathrm{Mpc}. \tag{3.52}$$

Substituting this into the expression for the velocity dispersion, σ_v, in equation (3.49) and then into the expression for θ_∞ (equation 3.48) it can be seen that the shear signal scales as $\gamma_t \propto M^{2/3}$. As more massive clusters are larger their surface mass-density, and hence mean shear, scales more slowly than in proportion to the mass, as would be expected for fixed sized haloes.

The shot-noise term in the shear covariance matrix for sources at infinity is

$$\frac{\Delta\gamma^2}{\overline{\gamma}^2_{t,\infty}} = \frac{\sigma_e^2}{n_z(>z_l)\pi\theta_\infty^2}, \tag{3.53}$$

where $n_z(>z_l)$ is the surface density of galaxies that lie at a redshift greater than the lens at z_l. The angular radius, θ, drops out of this expression since the signal-to-noise ratio for the mean shear of a SIS is a constant for a uniformly distribution of background sources. Hence the Fisher matrix will scale as $\boldsymbol{F}_{ij} \propto \theta_\infty^2 \propto M^{4/3}$.

The Fisher matrix for the halo geometric test, integrating over lensing cluster mass, M, and lens redshift, z_l, is

$$\boldsymbol{F}_{ij} = \int_0^\infty \frac{dz_l}{H(z_l)} \left[\int_{M_-(z_l)}^\infty dM\, \mathcal{N}(M,z) \left(\frac{M}{M_0}\right)^{4/3} \right] \boldsymbol{F}_{ij}(M_0, z_l), \tag{3.54}$$

where the mass-dependency of the Fisher matrix has factored out, and set $\theta_\infty = 1$ in $\boldsymbol{F}_{ij}(M_0, z_l)$ for a single halo. In this expression $\mathcal{N}(M, z_l)$ is the number density of clusters per $[h^{-1}\mathrm{Mpc}]^3$ with mass M at redshift z_l. The lower mass cut-off in the integral over mass, $M_-(z_l)$, is set by the condition that a cluster shear must be measurable with a signal-to-noise of

$$\frac{\gamma}{\Delta\gamma} > \mu, \tag{3.55}$$

which, using equation (3.48), sets

$$M_-(z_l) = M_0 \left[\frac{\sigma_e \mu}{\sqrt{n_z(>z_l)\pi}} \right]^{3/2}. \tag{3.56}$$

It will be assumed that $\mu = 1$ from hereon. Note that although there is is a low signal-to-noise threshold for measuring the shear signal from a given halo, it is assumed that the detection of a halo is based on the detection of galaxies in the halo, and therefore has a high signal-to-noise.

There are many cluster detection techniques that could be employed in such a survey either by using the optical data itself or relying on different wavelength observations and observing in the same area of sky. Proven cluster detection techniques are the matched filter technique in optical (e.g. Kepner & Kim, 2000), X-ray cluster searches (e.g. Land et al., 2004) and Sunyaev-Zel'dovich (SZ) surveys of the CMB (e.g. Vale & White, 2006). Weak lensing itself can detect clusters, see Taylor et al. (2004), indeed the detection of clusters by weak lensing can be used to constrain cosmological parameters, in particular dark energy parameters (see Marian & Bernstein, 2006) although such techniques could not be used in conjunction with

the geometric test as the shear information cannot be used to extract cosmological information twice.

The halo number density is a function of mass, M, and redshift, z, given by

$$\mathcal{N}(M,z) = \frac{\overline{\rho}_m}{M} f(M,z), \tag{3.57}$$

where fraction of matter, $f(M,z)$, in haloes of mass M at redshift z, can be written in the universal Sheth-Tormen form (Sheth & Tormen, 1999),

$$\nu f(\nu) = B\left(1+\nu/\sqrt{2}\right)^{-0.3}(\nu/\sqrt{2})^{1/2}e^{-\nu/2\sqrt{2}}, \tag{3.58}$$

where B is a constant of normalisation so that

$$\int_0^\infty d\nu\, f(\nu) = 1, \tag{3.59}$$

and

$$\nu = \frac{\delta_c^2}{\sigma^2(M,z)}. \tag{3.60}$$

The form of equation (3.58) finds justification from the ellipsoidal collapse model of haloes (Sheth & Tormen, 2001). The collapse threshold for linear matter overdensities, $\delta_c = \delta\rho/\overline{\rho}$, is $\delta_c = 1.686$. The variance of overdensities in spheres of radius $R(M)$ is

$$\sigma^2(M,z) = \int_0^\infty \frac{d^3k}{(2\pi)^3} P_{\rm lin}(k,z) j_0^2[kR(M)], \tag{3.61}$$

where

$$P_{\rm lin}(k,z) = D^2(z) P_{\rm lin}(k,z=0) \tag{3.62}$$

is the linear matter power spectrum. This can be split into a linear growth factor,

$$D(z) = H(z)\int_z^\infty \frac{(1+z')dz'}{H(z')^3}, \tag{3.63}$$

(see Heath, 1977; Carroll, Press & Turner, 1992; Linder, 2003) where $H(z)$ is given by equation (3.14), and the present-day linear matter power spectrum, $P_{\rm lin}(k,z=0)$. This equation is only valid for $w_0 = \{-1, -1/3, 0\}$, see Section 1.5.2. I use it here as ΛCDM is the assumed fiducial cosmology. The spherical Bessel function, $j_0(x) = \sin(x)/x$ is the transform of a sphere. The radius of the sphere, $R(M)$, is the linearised radius of a cluster halo of mass M, which will collapse down to a nonlinear virial radius, r_v, and is given by

$$R(M) = (1+z)\delta_{\rm v}^{1/3} r_v(M). \tag{3.64}$$

Where $R(M)$ is the radius within which the density is $\delta_{\rm v}$ times the mean density of the Universe at a redshift z. The the cumulative number count of dark matter haloes per square degree as a

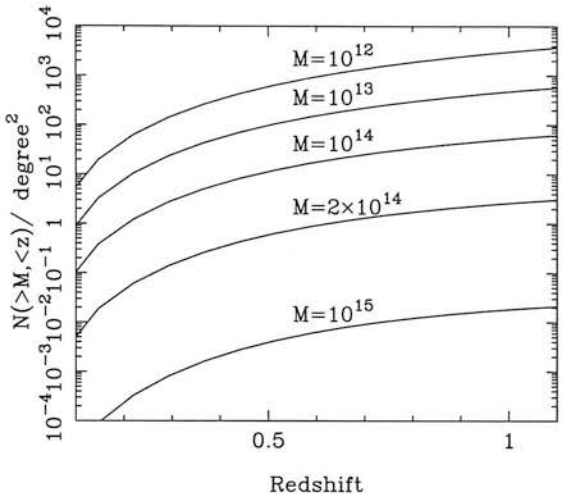

Figure 3.4: The cumulative number count of dark matter haloes per square degree, $\mathcal{N}(> M, < z)$, as a function of redshift, for the mass range $M = 10^{12} M_{\odot}$ to $M = 10^{15} M_{\odot}$.

function of redshift is plotted, for a range of halo masses in Figure 3.4. Typically, for $10^{12} M_{\odot}$ haloes one should expect 10^{3} haloes per square degree, while for $10^{15} M_{\odot}$ haloes 10^{-2} haloes per square degree should be expected.

Figure 3.5 shows the expected cumulative number count of dark matter haloes for a range of median redshifts, z_m, $\mathcal{N}(> M, z_m)$ per square degree. The dotted lines represent various upper redshift limits with no signal-to-noise limit on cluster detection for $z_m = 0.7$. The solid lines are for a detection threshold of clusters with signal-to-noise of unity, see equation (3.56), for various median redshifts and a maximum redshift of $z_{\max} = 1.5$.

In assuming a SIS model for the lensing clusters the average shear around a cluster may be systematically underestimated. A more reliable model is the Navarro-Frenk-White (NFW) profile, although the density profile form would yield a more complex relation for the shot noise term than the SIS profile. There is, however, an approximate scaling relation which relates $\bar{\gamma}_{SIS}$ to $\bar{\gamma}_{NFW}$ outlined in Wright & Brainerd (2000) which, since I take the average tangential shear in an aperture, should be adequate. Adopting the techniques outlined in Wright & Brainerd (2000), the concentration parameter depends on the mass, redshift and fiducial cosmology. I use the concentration parameter from Dolag et al. (2004), so that the overall scaling from $\bar{\gamma}_{NFW}$ to $\bar{\gamma}_{SIS}$ depends on the dark energy fiducial model, mass and redshift of the cluster. I will use this scaling to correct the shear signal expected from the halo model. Note that this only affects the noise properties since the shear ratio only depends on the redshift-distance relation. Figure 3.6 shows how the scaling depends on mass and the fiducial dark

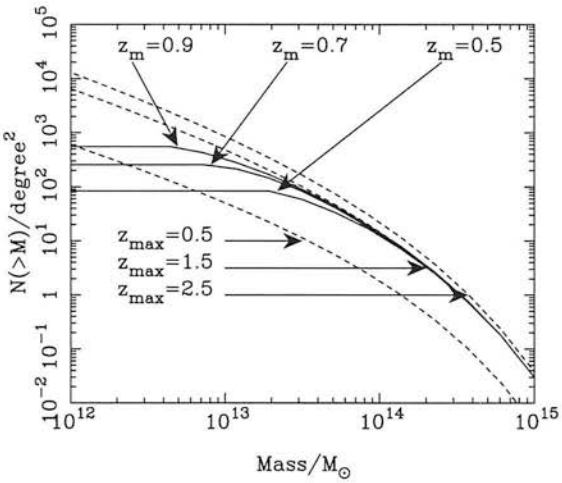

Figure 3.5: The cumulative number count of dark matter haloes for a range of median redshift distributions, $\mathcal{N}(> M, z_m)$, per square degree. The solid lines assume a maximum redshift in the halo population of $z_{\rm max} = 1.5$, while the upper dotted line assumes $z_{\rm max} = 2.5$, and lower dotted line $z_{\rm max} = 0.5$. The cut-offs in halo numbers for the $z_{\rm max} = 1.5$ (solid) lines are for different median redshifts with a shear signal-to-noise limit $\mu > 1$.

energy models (discussed in Section 3.10.6) for clusters at a redshift of $z_c = 0.1$.

If the haloes are assumed to be randomly distributed over the sky, and their physical size is taken to be the virial radius, the effect of overlapping haloes projected onto the sky is negligible. For instance, using equation (3.52), a $M = 10^{15} M_\odot$ halo has a virial radius of $r = 1.11$ Mpc and a number density of $n \approx 10^{-2}$ per square degree, while a $M = 10^{13} M_\odot$ halo has a virial radius of $r = 0.24$ Mpc and a number density of $n \approx 10^{2}$ per square degree. At $z = 0.2$, the physical distances 1.11 Mpc and 0.24 Mpc subtend ~ 0.10 degrees and ~ 0.022 degrees respectively. Hence I will assume that halo overlaps are not important.

3.6.2 Photometric Redshift Uncertainty

In Section 3.5.2 the effects of including photometric redshifts on the lensing measurements were introduced. Here the estimate of the photometric redshift errors used will be detailed.

The uncertainty on the photometric redshift error on an individual galaxy with redshift z and magnitude R for a multi-band survey is well fitted by (Wolf et al. 2004);

$$\sigma_z(z, R) = A(1+z)\left[1 + 10^{B(R-R_*)}\right]^{1/2}, \tag{3.65}$$

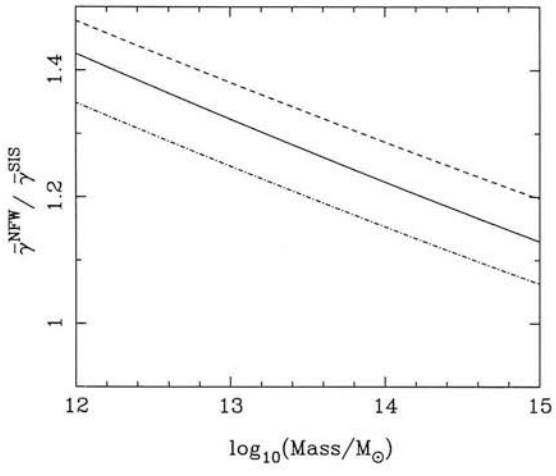

Figure 3.6: The ratio of mean shears for an SIS and NFW haloes of varying mass for haloes at a redshift of $z_c = 0.1$. The solid line is for a ΛCDM fiducial cosmology, the dashed line is for a SUGRA fiducial model and the dot-dashed for a Phatom model, see Section 3.10.6 for details.

where $A = 0.035$, $B = 0.8$ and $R_* = 23.0$ for galaxies in a 5-band survey, and $A = 0.007$, $B = 0.8$ and $R_* = 21.6$ in a 17-band, COMBO-17-type survey (Wolf, private communications). This shows that the redshift errors are well constrained at bright magnitudes but poorly constrained at faint magnitudes. The $(1 + z)$ scaling is standard in that the fixed wavelength resolution of filter set translates into an error that scales as $(1 + z)$. The first parameter, A, characterises the best performance achievable in the bright domain, where photon noise is irrelevant and spectral resolution limits the redshift estimate. The second parameter, B, describes how a decrease in photon signal propagates into the redshift signal. This is measured as 0.8 if all galaxies are considered from COMBO-17 (Wolf et al., 2004), but can be made smaller by filtering out galaxies with outlying redshift errors. The final parameter, R_*, determines the magnitude where there is a sharp rise in the redshift error function. This occurs when the spectral-resolution limited régime at bright magnitudes changes into the régime where photon noise drives the redshift noise by a factor of ≈ 2.5 per magnitude, under the assumption of a locally linear transformation from colour-space into redshift-space.

The average redshift error in a bin at redshift z is given by averaging over all observable galaxies below a limiting absolute magnitude in that bin,

$$\overline{\sigma}_z(z) = \frac{\int_{-\infty}^{\mathcal{M}_{\rm lim}(z_m)} dM\ \Psi(M)\sigma_z(z, M)}{\int_{-\infty}^{\mathcal{M}_{\rm lim}(z)} dM\ \Psi(M)}. \tag{3.66}$$

Here $\Psi(M)$ is a sum of Schechter functions $\Phi_{\rm red}$ and $\Phi_{\rm blue}$ (see Wolf et al, 2003 for details of the COMBO-17 luminosity functions) for a red and blue sample of galaxies. The luminosity

functions are defined for a colour, c, as

$$\Phi_c(M)dM = 0.4\ln 10\,\phi_c^* X_c^{\alpha}(M)e^{-X(M)}dM, \tag{3.67}$$

where

$$X(M) = 10^{-0.4(M-M_c^*)}, \tag{3.68}$$

and

$$\phi^*_{\rm red}(z) = (2.0-z)\times 10^{-3}[h^{-1}{\rm Mpc}]^{-3}, \tag{3.69}$$
$$\phi^*_{\rm blue}(z) = 3.0\times 10^{-3}[h^{-1}{\rm Mpc}]^{-3}, \tag{3.70}$$

valid for $z < 2$, are the characteristic space-densities of galaxies. The slope of the luminosity functions are

$$\alpha_{\rm red} = -0.5, \tag{3.71}$$
$$\alpha_{\rm blue} = -1.3, \tag{3.72}$$

and

$$M^*_{\rm red}(z) = -20.18 - 1.04z, \tag{3.73}$$
$$M^*_{\rm blue}(z) = -20.09 - 1.28z, \tag{3.74}$$

are the characteristic magnitudes of red and blue galaxies in the COMBO-17 survey. $M_{\rm lim}(z_m)$ is the limiting apparent magnitude of survey with median redshift z_m given by (see Brown et al. 2003, and equation (3.92) in Section 3.6.5)

$$M_{\rm lim} = 20.8 + z_m/0.23 \tag{3.75}$$

for an optical survey, which can then be transformed to the absolute limiting magnitude;

$$\mathcal{M}_{\rm lim} = M_{\rm lim} - 5\log_{10}\{(1+z)S_k[r(z)]\} + K(z). \tag{3.76}$$

The K-correction, $K(z)$, is;

$$K(z) = 2.5(\alpha-1)\log_{10}(1+z), \tag{3.77}$$

where α is the spectral slope of galaxies. I take this to be $\alpha = +1$, making the K-correction zero. Figure 3.7 shows the increase in mean photometric redshift uncertainty for a 5-band and a 17-band survey with median redshift $z_m = 0.7$, based on the galaxy luminosity functions. As the magnitude of a galaxy depends on its redshift, the scaling of the photometric redshift

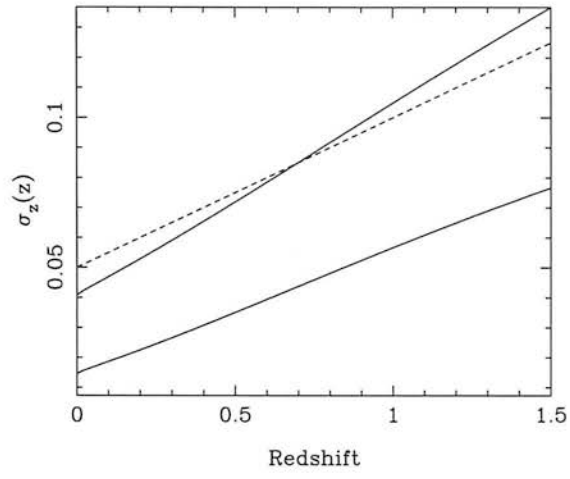

Figure 3.7: Variation of $\sigma_z(z)$ with redshift for a 5-band (upper solid line) and a 17-band (lower solid line) photometric redshift survey, averaging over galaxy luminosities, for a survey with median redshift $z_m = 0.7$ (solid line). Galaxy properties are from COMBO-17 and described in the text. Also shown is a standard 5-band photometric redshift model with $\sigma_z(z) = 0.05(1+z)$ (dashed line).

noise is more complicated than the simple $(1 + z)$ scaling commonly used. Brodwin et al. (2004) find $\sigma_z(z) \approx 0.05(1 + z)$ for a 5-band survey, which is plotted as the dashed line in Figure 3.7. The estimate of the redshift error presented here for a 5-band survey predicts a higher error for $z \gtrsim 0.7$, and a lower error for $z \lesssim 0.7$. These formulae have been extrapolated to $z = 1.5$ though this extrapolation may be optimistic as photometric redshift estimates can increases dramatically at $z \approx 1$ if IR data is not available.

For an intermediate 9-band optical survey I linearly interpolate between the 5-band and 17-band lines, assuming that at each redshift the relationship between bands is linear. Over all redshifts there is no simple linear scaling relation with $(1+z)$. However there are approximate fitting formula for a 5-band survey,

$$\sigma_z(z) \approx 0.063(0.64 + z), \tag{3.78}$$

and for a 17-band survey,

$$\sigma_z(z) \approx 0.041(0.37 + z). \tag{3.79}$$

Figure 3.8 shows the effect of a 5-band photometric redshift error, given by equation (3.35), for a photometric galaxy survey parameterised the same as the COMBO-17 survey, with median redshift $z_m = 0.7$ and limiting magnitude $R = 23.8$, on the measured tangential shear distribution behind a $M = 10^{15} M_\odot$ halo at $z = 0.2$. The main effect is a suppression of the

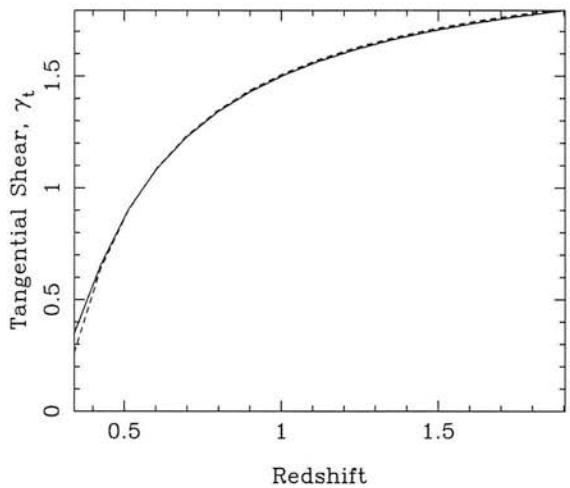

Figure 3.8: The effect of photometric redshift errors on the tangential shear behind a lensing cluster of mass $10^{15} M_{\odot}$ at a redshift of 0.2, assuming 5 bands. The solid line is the true shear response, while the dashed line is the shear with photometric redshift errors from a 5-band survey, using equation (3.35).

shear signal at low redshift, where the shear is rapidly changing. This is due to the scattering of unlensed galaxies in front of the lensing halo into bins just behind the halo.

The photometric redshift error fit from COMBO-17, given by equation (3.66), is per galaxy. In practice the photometric redshifts produced by any multi-band analysis will also provide an individual redshift error for every galaxy which will also depend on redshift and magnitude. In this current analysis photometric redshifts are averaged over all galaxy types and magnitudes. In practice one would like to weight the data optimally to minimise the effect of both shear and photometric redshift errors. Given the redshift dependence of the shear signal for redshifts just behind a lens, it is likely that both errors in the shear signal and photometric redshift errors will degrade the measurement of parameters. While at redshifts far from the lens, shear errors will dominate. This implies that there is an optimal weighting scheme which is a function of galaxy redshift and magnitude for weak shear analysis using photometric redshifts. In Section 3.9.4 I will examine the effect of some simple weighting schemes.

3.6.3 Bias in the Photometric Redshifts

In addition to the uncertainty on photometric redshifts, it is also important to know the effect of a bias in the photometric redshifts, leading to an off-set in their calibration. This effect can

be modelled by considering the first-order effect of such a bias on the measurable parameters.

Here I will show that for a Gaussian distributed likelihood function, the linear bias in a parameter, which I will call $\delta\theta_i$, due to a bias in a fixed model parameter (i.e., one whose value, it is assumed, is not being measured), which I will call $\delta\psi_j$, is given by (Knox, Scoccimarro and Dodelson, 1998; Kim et al., 2004)

$$\delta\theta_i = -(\boldsymbol{F}^{\theta\theta})^{-1}_{ik}\boldsymbol{F}^{\theta\psi}_{kj}\delta\psi_j, \tag{3.80}$$

where $\boldsymbol{F}^{\theta\theta}$ is the parameter Fisher matrix defined in equation (3.11) and $\boldsymbol{F}^{\theta\psi}$ is a matrix of derivatives with respect to parameters which are assumed fixed (ψ) and those to be determined (θ) defined as

$$\boldsymbol{F}^{\theta\psi}_{ij} = \frac{1}{2}\mathrm{Tr}(\boldsymbol{C}^{-1}\partial^{\theta}_i\boldsymbol{C}\boldsymbol{C}^{-1}\partial^{\psi}_j\boldsymbol{C} + \partial^{\theta}_i\boldsymbol{\mu}\boldsymbol{C}^{-1}\partial^{\psi}_j\boldsymbol{\mu}^T + \partial^{\psi}_i\boldsymbol{\mu}\boldsymbol{C}^{-1}\partial^{\theta}_j\boldsymbol{\mu}^T) \tag{3.81}$$

which I will refer to as a pseudo-Fisher matrix between measured and assumed parameters.

Beginning with a likelihood function, $\ln L(\boldsymbol{\theta}|\boldsymbol{\psi})$, which depends on a set of free parameters to be determined by the data, $\boldsymbol{\theta}$, and a set of fixed parameters which are assumed to be known, $\boldsymbol{\psi}$. If the $\boldsymbol{\theta}$ are at their maximum likelihood values, $\boldsymbol{\theta}_0$, then

$$\langle\partial_i \ln L(\boldsymbol{\theta}_0|\boldsymbol{\psi})\rangle = 0 \tag{3.82}$$

where the derivative is in parameter space, and I have used an ensemble averaged over all possible data.

One can now ask; what is the effect of displacing the fixed parameters? Expanding both $\boldsymbol{\psi}$ and $\boldsymbol{\theta}$ to first-order results in

$$\ln L(\boldsymbol{\theta}|\boldsymbol{\psi}) = \ln L(\boldsymbol{\theta}_0|\boldsymbol{\psi}_0) + \delta\theta_i\partial_i \ln L(\boldsymbol{\theta}_0|\boldsymbol{\psi}_0) + \delta\psi_j\partial_{\psi,j} \ln L(\boldsymbol{\theta}_0|\boldsymbol{\psi}_0), \tag{3.83}$$

were $\partial_{\psi,i}$ is the i^{th} derivative in the $\boldsymbol{\psi}$-parameter space. This displaced likelihood now maximises when

$$\langle\partial_i \ln L(\boldsymbol{\theta}|\boldsymbol{\psi})\rangle = \langle\partial_i \ln L(\boldsymbol{\theta}_0|\boldsymbol{\psi}_0)\rangle + \delta\theta_j\langle\partial_i\partial_j \ln L(\boldsymbol{\theta}_0|\boldsymbol{\psi}_0)\rangle + \delta\psi_j\langle\partial_i\partial_{\psi,j} \ln L(\boldsymbol{\theta}_0|\boldsymbol{\psi}_0)\rangle = 0. \tag{3.84}$$

The unperturbed likelihood peaks at the maximum likelihood values, and so by inspection it can be seen that the averaged second derivatives of the likelihood are the Fisher matrices. Hence

$$\delta\theta_j\langle\partial_i\partial_j \ln L(\boldsymbol{\theta}_0|\boldsymbol{\psi}_0)\rangle = -\delta\psi_j\langle\partial_i\partial_{\psi,j} \ln L(\boldsymbol{\theta}_0|\boldsymbol{\psi}_0)\rangle \tag{3.85}$$

which with the definition of the Fisher matrix, see equation (3.6), yields equation (3.80).

Assuming there is a possible bias in the mean of the photometric redshifts of the survey, $z_{\rm bias}$, (see Section 3.5.2) due to poor calibration of the photometric redshifts with spectroscopic redshifts, and marginalizing over all other cosmological parameters, I find that the induced bias in w_0 due to the bias in galaxy redshifts is

$$\delta w_0 = -C_{\rm bias}\,\delta z_{\rm bias}, \tag{3.86}$$

where $C_{\rm bias}$ is a constant. If the bias in the mean of the photometric redshifts arises from an overall bias in the photometric redshift calibration, the calibration error will be

$$\sigma(z_{\rm bias}) = \frac{\sigma(z)}{\sqrt{N_{\rm spec}}}, \tag{3.87}$$

where $N_{\rm spec}$ is the number of galaxies with a spectroscopic redshift. Setting $\delta z_{\rm bias} = \sigma(z_{\rm bias})$ and a requirement that the bias in w_0 is half of the error, $\delta w_0 = 0.5\Delta w_0$, then the number of galaxies with spectroscopic redshifts required is

$$N_{\rm spec} = \left[\frac{C_{\rm bias}\sigma(z)}{\delta w_0}\right]^2. \tag{3.88}$$

I have found that $C_{\rm bias} \approx 9.0$ for the geometric test. If it is assumed that $\sigma(z) \approx 0.1$ and $\Delta w_0 \approx 0.01$ then $N_{\rm spec} \approx 3 \times 10^4$ are required. The number of spectroscopic redshifts needed to calibrate the geometric test suggests that a large spectroscopic survey, such as that proposed for the Wide-Field Multi-Object Spectrometer (WFMOS; Bassett et al., 2005), would be required and combined with a large-scale weak lensing survey.

I have also investigated the effect of an offset in the variance of the photometric redshift errors $\sigma_z(z) \rightarrow \sqrt{[\sigma_z^2(z) + \Delta\sigma_z^2(z)]}$. I find that this effect is negligible for the geometric test, so that the total bias due to photometric redshift errors is only dependent on the bias in the offset of the mean. However in the pseudo-Fisher analysis the variation about the mean of $\Delta\sigma_z(z)$ is ± 0.05, and one would expect there to be an effect at some level if the variation was large enough. Exploring fully marginalizing over nuisance parameters in a full Fisher analysis is left for future work, see Section 7.1.

3.6.4 Limits on the Measurement of Galaxy Ellipticity

Ground-based Ellipticity Measurements

For ground-based weak lensing observations estimates of galaxy ellipticities are limited by atmospheric seeing. The angular sizes of typical galaxies in the GOODS fields scale with redshift by (Ferguson et al., 2002)

$$\theta_g = 0.8z^{-1} \text{ arcseconds.} \tag{3.89}$$

If θ_s is the typical seeing during weak lensing observations, the post-seeing galaxy image will be

$$\theta'_g = \sqrt{\theta_g^2 + \theta_s^2}. \tag{3.90}$$

This will tend to decrease the ellipticity of galaxy images. Much effort is put into weak lensing to correct this effect. However, once the seeing disc exceeds the galaxy image and $\theta_g \ll \theta_s$, this correction fails. Typically, galaxy sizes are about $\theta_g = 0.8$ arcseconds at redshift $z = 1$. If the groundbased seeing for weak lensing is typically $\theta_s \approx 0.7$ arcseconds then by a redshift of $z = 1.5$, where the galaxy sizes have dropped to $\theta_g = 0.5$ arcseconds, galaxy ellipticities cannot be recovered without the use of adaptive optics.

Another limitation which could potentially come into play is when the galaxy image is too faint to properly measure the galaxy shape against the sky background. However, Bacon et al. (2001) find that the dispersion on the measured galaxy ellipticities is very insensitive to the galaxy magnitude, and seems only limited by the detection threshold for galaxy detection. For 5-σ detected galaxies, ellipticities can be measured down to the limiting magnitude of the survey, with $\sigma_e = 0.3$.

Given these two results I will assume that shapes cannot be measured beyond $z = 1.5$ from the ground due to being unable to recover the pre-seeing ellipticity.

Space-based Ellipticity Measurements

Rhodes et al. (2003) find no dependence on ellipticity dispersion as a function of redshift for space-based data. Réfrégier et al. (2003) and Massey et al. (2004) find that $\sigma_e = 0.2$ is a reasonable measure for the ellipticity dispersion for a space-based weak lensing survey.

They also find a maximum redshift bound for space-based surveys can be set at $z = 2.0$ corresponding to a deep magnitude cut of $R = 29.1$.

3.6.5 Optical Surveys

This Section outlines how to parameterise a weak lensing and photometric redshift survey, and how these will scale for different telescopes. A reasonable way to compare between potential survey designs is to consider equal-time observations. Hence one can compare dark energy results both for a single telescope class, and across telescope classes. The time taken for an imaging survey on a given telescope scales as (cf equation 3.100)

$$T \propto z_m^4 f_{\rm sky} D^{-2} \left({\rm fov}/1^{\Box}\right)^{-1}, \tag{3.91}$$

where D is the diameter of the primary mirror of the telescope and fov is its field of view. The timescale of a survey can be normalised for 5-bands (g', u, r', i', z') using the CFHT survey, where $T = 162$ nights for $z_m = 1.17$ ($R = 25.9$), $f_{\rm sky} = 4.25 \times 10^{-3}$, $D = 3.6$m and fov $= 1$ square degree. The median redshift for an R-band survey is (Brown et al., 2003)

$$z_m = 0.23(R - 20.6), \tag{3.92}$$

where the projected surface number count density of galaxies in the COMBO-17 survey scales with the median redshift as

$$n_2(z_m) = 30\, z_m^{3.4} \ \text{ galaxies per square arcmin.} \tag{3.93}$$

A functional form for the galaxy redshift distribution also needs to be assumed which I will take to be (see e.g. Baugh and Efstathiou, 1993)

$$p(z|z_m) \propto z^2 \exp\left[- \left(z/z^*\right)^{1.5}\right], \tag{3.94}$$

where $z^* = z_m/1.412$ and

$$\int_0^\infty dz\, p(z|z_m) = 1. \tag{3.95}$$

The space density of galaxies as a function of galaxy redshift, z, and survey median redshift, z_m, is then

$$n_3(z|z_m) = n_2(z_m) p(z|z_m). \tag{3.96}$$

The 3D galaxy redshift distribution, $n(z) = n_3(z|z_m)$, is used in equations (3.35) and (3.44) when calculating the effects of photometric redshift errors, for calculating the number of galaxies in redshift bin N_i, for the shot-noise and for finding the cumulative surface density of galaxies above a halo redshift, $n_2(> z)$, in equation (3.54).

The number of redshift bins used in the background to the lenses, N_B, is determined by the photometric redshift uncertainty (Section 3.6.2) by assigning a bin width at particular redshift to be the average photometric uncertainty, $\sigma_z(z)$, at that redshift. The bins exhaustively fill the available redshift range.

3.7 Survey Design Strategy

Having formulated the basic method for estimating dark energy parameters from shear ratios, I will now consider the problem of what type of survey would be optimal for measuring the properties of the dark energy from the shear ratio geometric test. For instance, should one construct a wide area, but shallow, multi-band survey, or a narrow and deep multi-band survey with a survey-class telescope, such as the VST, the Dark Energy Survey on the CTIO (Wester, 2005), darkCAM (Taylor, 2005) or Pan-STARRS (Kaiser et al., 2005)? Or should one instead take snap-shots of galaxy clusters with a large but small field-of-view telescope such as SUBARU, the VLT or the Keck Telescope? I will compare these different strategies by minimizing the marginalized uncertainty on w_0 for fixed-time observations.

Broadly there are two possible observing strategies available: targeted observations at individual clusters or a general wide-field survey. In the former, one would use a large telescope with small field-of-view to take rapid observations of each cluster, while in the latter a large telescope with a wide field-of-view would make a general wide-field survey from which one would extract haloes. With a halo decomposition analysis of the matter distribution an investigation can be made into where most of the signal will come from for a dark energy analysis using the geometric test. It can then by seen which strategy would be most effective in terms of telescope time. I will begin with targeted observations of clusters.

3.7.1 Targeted Observation Mode

Here it will be assumed that a large telescope with a small field-of-view is available which could target pre-selected galaxy clusters from a pre-existing galaxy cluster catalogue. The survey would start by imaging the largest clusters on the sky, and then move on to subsequently smaller haloes. I will assume that the telescope has some fraction of the sky available to it, and will shall ignore scheduling issues.

Figure 3.9 shows the accuracy on w_0, marginalized over Ω_m, Ω_{de} and w_a, which can be achieved by a targeted survey as a function of the number of clusters in decreasing mass. I have assumed half the sky (20,000 square degrees) is available, and combined the lensing result with a 4-year *WMAP* prior (see Section 3.8). The time taken for such a survey is just the time taken to image down to the median redshift for a given telescope, multiplied by the number of clusters. Note that the cumulative total number of haloes, $\mathcal{N}(> M, z_m)$, depends on the median redshift of the survey, z_m; the upper scale on Figure 3.9 assumes $z_m = 0.7$ and $z_{\rm max} = 1.5$. However, comparing with Figure 3.10 it can be seen that varying z_m has only a small effect in the number of haloes above $M = 10^{13} M_\odot$, but does change the total number for masses below this.

Figure 3.9 implies that by imaging only 60 of the most massive clusters ($10^{15} M_\odot$) in a hemisphere to $z_m = 0.9$ ($R = 24.7$) in five bands and combining with the 4-year *WMAP*, one could reach an accuracy of $\Delta w_0 = 0.50$, after marginalizing over all other parameters, including w_a. This seems a viable strategy, a factor of 2 improvement on 4-year *WMAP* constraints given a marginalization over w_a. If w_a is fixed at $w_a = 0$ then the marginal error on w_0 reduces to $\Delta w_0 \approx 0.20$, a factor of 2.5 improvement on 4-year *WMAP*, marginalizing over other parameters. To rapidly image each halo in five bands with an 8-metre class telescope with a 0.025 square degree field-of-view, such as with SuprimeCam on the Subaru telescope (see Broadhurst et al., 2005, for the use of Subaru in a lensing analysis) would take 10 to 20 nights.

Beyond this accuracy, there are diminishing returns for a pointed survey from the geometric test. To reach an accuracy of $\Delta w_0 \approx 0.07$, one would have to image around 10^6 haloes, with the number of galaxies scaling roughly as

$$N \approx 10^{0.35/\Delta w_0}. \tag{3.97}$$

For a targeted survey, this seems an unfeasible task. The weakness in this relation is due to the fact that haloes have been ranked by mass, and while the number of haloes is increasing the mass per cluster, and hence lensing signal, is falling. By the time the $M < 10^{13} M_\odot$ haloes are being imaged, the shear signal is so weak as to no longer contribute to a significant measurement of dark energy.

These curves scale with the survey median redshift roughly as

$$\Delta w_0(> M, z_m) = \Delta w_0(> M, z_m = 0.7) \left(\frac{z_m}{0.7}\right)^{-1}, \tag{3.98}$$

where the increase in accuracy arises due to the increase in number of background galaxies

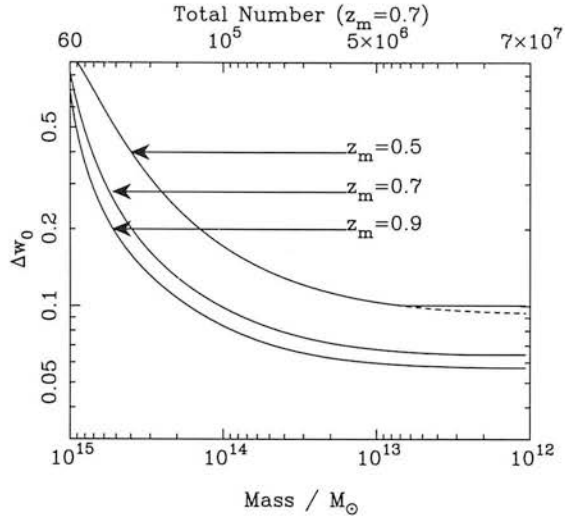

Figure 3.9: Variation of marginal error on w_0 with the mass of lensing cluster for a pointed survey with 20,000 square degrees accessible, for $z_m = 0.5$, 0.7 and 0.9. The dashed lines have no S/N threshold, the solid lines have a threshold condition set by equation (3.56). A *WMAP* 4-year prior has been assumed. Note that the cumulative total number of galaxies depends on the median redshift, z_m, (see Figure 3.10), here it is calculated for $z_m = 0.7$.

reducing the shot-noise, and the increase in available clusters reducing clustering variance. This approximation fails for the most massive clusters, where imaging deeper does not help as one is clustering-limited.

3.7.2 Time-Limited Survey Mode

In contrast to a targeted observation mode, one could also use a large survey telescope with a wide field-of-view to construct a general wide-field survey, and extract haloes from this for the shear ratio analysis. In this case it makes sense to restrict the amount of telescope time one can allocate to such a survey. In the next Section the optimisation of such a survey is discussed. Here the optimum survey parameters will be assumed and the distribution of signal across the mass spectrum of haloes will be investigated.

Figure 3.10 shows the cumulative gain in accuracy on w_0 as haloes of decreasing mass are added to the analysis. The remaining parameters $(\Omega_m, \Omega_{de}, w_a)$ have been marginalized over, and the Fisher matrix calculated using the analysis of Section 3.5.3. A fixed-time survey has been assumed with median redshifts of $z_m = 0.5$, $z_m = 0.7$ and $z_m = 0.9$ (limiting magnitudes

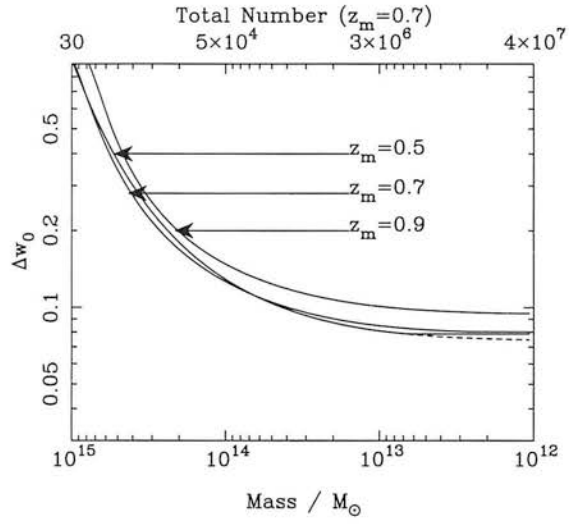

Figure 3.10: Variation of marginal error on w_0 with the mass of lensing cluster for a 10,000 square degree survey to $z_m = 0.7$, $z_m = 0.5$ and $z_m = 0.9$ with areas of $10,000(0.7/z_m)^4$. The dashed lines have no S/N threshold, the solid lines have a threshold condition set by equation (3.56). A *WMAP* 4-year prior has been assumed.

of $R = 23$, $R = 23.8$ and $R = 24.7$, respectively), combined with a 4-year *WMAP* prior (see Section 3.8). The lines for $z_m = 0.5$ and $z_m = 0.7$ cross at approximately $4 \times 10^{14} M_\odot$ this is interpreted as for a fixed time survey the optimal median redshift varies slightly with the mass range of clusters used. As clusters of lower mass are included the optimal median redshift behaviour converges so that $z_m = 0.7$ yields the lowest error, note Figure 3.10 includes a 4-year *WMAP* prior. The area of each survey is 38,400 square degrees, 10,000 square degrees and 3,660 square degrees, respectively, appropriate for a survey with one, or more, 4-metre telescopes with a 2 square degree field-of-view (more than one would be needed for a $z_m = 0.5$, $A = 38,400$ square degree survey). Note again that the upper scale (Total Number) for number of haloes depends on median redshift which is here assumed to be $z_m = 0.7$. The cumulative number of haloes is half of that for a given mass than for Figure 3.9 as the total area probed is half for a $z_m = 0.7$ survey.

Again I find that the largest haloes provide the largest contribution to the measurement of w_0, with an error of $\Delta w_0 = 0.6$ from the largest 30 haloes. The error has flattened off from 60 to 30 haloes, as shown in Figure 3.11. As with the targeted survey mode, the increase in accuracy from including smaller haloes has diminishing returns. However, given these haloes will already be in a survey of this type, the limitation here is processing time, rather than telescope time. A 10,000 square degree survey to $z_m = 0.7$ ($R = 23.8$) can achieve an

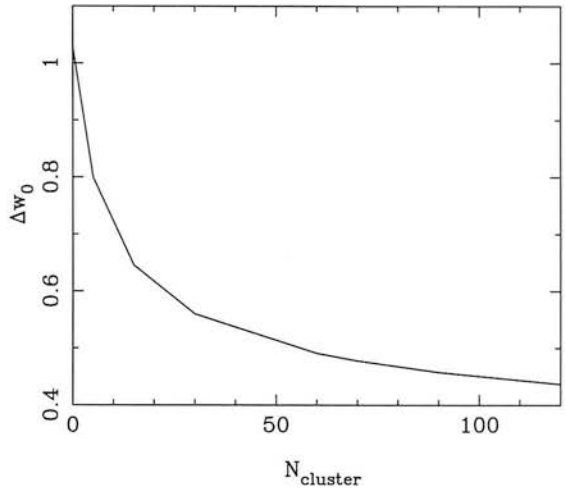

Figure 3.11: Variation in the marginal error in w_0 as a function of the number of $M = 10^{15} M_\odot$ clusters with a redshift of $z_{\rm cluster} = 0.3$, for a targeting strategy, see Section 3.7.1.

accuracy of $\Delta w_0 = 0.08$ from the analysis of $N = 3 \times 10^6$ haloes, down to haloes with $M > 10^{13} M_\odot$. The majority of the signal (the steepest gradient in Figure 3.10) comes from the relatively numerous intermediate mass haloes with $M \sim 10^{14} M_\odot$. Beyond this the signal-to-noise per cluster is too small to contribute to a measurement of w_0.

For a time-limited survey, it is useful to parameterise how the uncertainty on w_0 scales with different telescopes and surveys by scaling the error with the fractional survey sky coverage, $f_{\rm sky} = A/40,000$ square degrees, where A is the survey area, so that

$$\Delta w_0 = \Delta w_0(f_{\rm sky} = 0.25) \left(\frac{f_{\rm sky}}{0.25} \right)^{-1/2}, \tag{3.99}$$

where

$$f_{\rm sky} = 0.25 \left(\frac{T}{600\,{\rm nights}} \right) \left(\frac{z_m}{0.7} \right)^{-4} \left(\frac{\rm fov}{1^\square} \right) \left(\frac{D^2}{4{\rm m}^2} \right). \tag{3.100}$$

Hence one can trade off telescope size and field-of-view (fov) with the survey time-limit, T, and the median depth, z_m.

To summarise Sections 3.7.1 and 3.7.2, while a reasonable sized pointed survey of around 60 of the largest clusters in a hemisphere combined with the 4-year *WMAP* results could rapidly measure w_0 to around $\Delta w_0 = 0.5$ in a short space of time, to improve the accuracy to a few percent would require an unfeasible amount of telescope time. However, a time-limited wide-field 5-band photometric redshift survey could push the accuracy down to a few percent accuracy. For example $\Delta w_0 = 0.08$ for a 10,000 square degree survey to $z_m = 0.7$ in 5 bands, with the analysis of the millions of medium sized clusters and groups ($M > 10^{13} M_\odot$).

Time-limited survey designs and their optimisation in measuring $w(z)$ are considered in further detail in Section 3.9.

3.7.3 Area-limited Survey Mode

A further distinct class of experiments, such as the LSST (see Tyson et al., 2002) and Pan-STARRS (Kaiser, 2005), will repeatedly image an entire hemisphere ($20,000$ to $30,000$ square degrees) to a given limiting magnitude; this is proposed to be done by stacking multiple images. In these cases the limiting factors are the amount of sky available to a given telescope and time, allowing a given median redshift to be reached. Figure 3.9 shows that the marginal error on w_0 will vary as the median redshift of the survey as

$$\Delta w_0 = 0.07 \left(\frac{z_m}{0.7}\right)^{-1} \left(\frac{f_{\rm sky}}{0.5}\right)^{-1/2} \tag{3.101}$$

and that a $z_m = 0.7$, $A = 20,000$ square degree survey could image approximately 7×10^7 clusters between 10^{12} and $10^{15}\ M_\odot$, and achieve a marginal error of $\Delta w_0 = 0.05$. A survey of this type is a viable alternative to a time-limited wide-field survey.

3.8 Predicted Priors

As well as gravitational lensing, there are other experiments which can probe dark energy, notably the CMB, Baryon Acoustic Oscillations (BAO) in the galaxy power spectrum, and the supernova Type Ia Hubble diagram. Individually each of these can probe dark energy, but suffer from degeneracies between w_0 and w_a, and with other parameters. These degeneracies can be lifted by combining methods. Since there are a number of different probes, these experiments can generate a number of combinations which can be compared for consistency and as a test for systematics. In addition, dark energy probes can be divided into methods that probe just the geometric properties of the Universe, and those that combine the evolution of mass clustering and geometry. These may respond differently depending on whether the apparent dark energy is vacuum energy, modelled as a fluid with a negative equation of state, or a change in gravity on large scales. Again, with a combination of methods these possibilities can be explored. In this thesis I will only address the combination of methods under the assumption that the dark energy can be modelled by a negative-pressure equation of state. Finally, I will not consider

the Integrated Sachs-Wolfe (ISW) effect directly, via cross-correlating galaxy surveys with the CMB, although this too can probe dark energy.

The error analysis of a combination of independent experiments can simply be accounted for by summing over each Fisher matrix. Including a non-flat prior, and using Bayes' theorem the likelihood can be written, see equation (3.2), $L(\boldsymbol{\theta}|\mathbf{x}) = L(\mathbf{x}|\boldsymbol{\theta})p(\boldsymbol{\theta})$. Substituting this into equation (3.6) in can be seen that in order to predict the combined constraints from multiple experiments one simply sums the relevant Fisher matrices

$$\mathbf{F}^{TOTAL} = \sum_i \mathbf{F}^i \tag{3.102}$$

where i refers to various different experiments.

I examine three additional different dark energy probes, motivated by experiments which will be contemporary with any experiment that could use the geometric test to constrain $w(z)$ to the percent level. The fiducial cosmological model used in the Fisher calculations for these CMB, BAO and SNIa experiments are: $\Omega_m = 0.27$, $\Omega_{de} = 0.73$, $h = 0.71$, $\sigma_8 = 0.80$, $\Omega_b = 0.04$, $w_0 = -1.0$, $w_a = 0.0$, the scalar spectral index $n_s = 1.0$, optical depth to the surface of last scattering $\tau = 0.09$, the running of the spectral index,

$$\alpha_n = \frac{dn(k)}{d\ln k}, \tag{3.103}$$

with $\alpha_n = 0.0$, the tensor to scalar ratio $r = T/S$ with $r = 0.01$ and the galaxy bias factor, b, which I set to a constant $b = 1.2$.

3.8.1 WMAP and Planck Surveyor CMB Experiments

Here I consider both a 4-year *WMAP* experiment and a 14-month *Planck* experiment (Lamarre et al., 2003), with predictions calculated using `CMBfast` (version 4.5.1, Seljak & Zaldarriaga, 1996). The procedure used is similar to that outlined in Hu (2002) and Eisenstein et al. (1999). The Fisher matrix for a CMB experiment is

$$\boldsymbol{F}_{ij}^{CMB} = \sum_{\ell_{\min}}^{\ell_{\max}} \sum_{X,Y} \frac{\partial \boldsymbol{C}_{X\ell}}{\partial\theta_i} (\mathrm{Cov}_\ell)^{-1}_{XY} \frac{\partial \boldsymbol{C}_{Y\ell}}{\partial\theta_j} \tag{3.104}$$

where $\boldsymbol{C}_{X\ell}$ is the power for $X = T, E, TE$ or B (Temperature, E channel polarisation, Temperature-E channel cross correlation and B channel polarisation) in the ℓ^{th} multipole.

The elements of the symmetric covariance matrix are given in Eisenstein et al. (1999). For example the TT element of the covariance matrix is given by:

$$\mathrm{Cov}_{\ell TT} = \frac{2}{(2\ell+1)f_{sky}} \left(\boldsymbol{C}_{T\ell} + w_T^{-1} B_\ell^{-2} \right) \tag{3.105}$$

where B_ℓ^2 is a Gaussian beam window function $B_\ell^2 = \exp[-\ell(\ell+1)\theta^2_{\mathrm{beam}}/8\ln 2]$ and θ_{beam} is the full-width, half-maximum (FWHM) of the beam in radians. The inverse square of the detector noise level on a steradian patch for temperature and polarisation is given by $w_i = (\theta_{\mathrm{beam}}\sigma_i)^{-2}$ where $i = T, P$. The sensitivity in μK per FWHM beam ($\Delta T/T$ or $\Delta P/T$) is $\sigma_i = \sigma^i_{pix}$.

For multiple channels the quantity wB_ℓ^2 is replaced by the sum of this quantity for each channel. The values for θ_{beam} and σ_i for the various experiments were taken from Hu (2002) (Table I), the *Planck* parameters are shown in Table 3.1. I have used a maximum $\ell_{\mathrm{max}} = 2000$ and minimum $\ell_{\mathrm{min}} = 10$ in the summation over wavenumber. f_{sky} is set to 0.66 to simulate a typical galactic cut.

The 11-parameter CMB cosmological parameter set is (Ω_m, Ω_{de}, h, σ_8, Ω_b, w_0, w_a, n_s, τ, α_n, $r = T/S$). I have not included a marginalization over calibration of the CMB instrument.

3.8.2 Baryon Acoustic Oscillations Experiments

I have modelled the errors on cosmological parameters for a BAO WFMOS-type experiment. Following Seo & Eisenstein (2003), Blake and Glazebrook (2003) and Wang (2006), the Fisher matrix for a BAO experiment can be approximated by

$$\boldsymbol{F}_{ij}^{BAO} = \sum_{k,z} \left[\Delta \ln P(k,z)\right]^{-2} \frac{\partial \ln P(k_{\mathrm{eff}},z)}{\partial\theta_i} \frac{\partial \ln P(k_{\mathrm{eff}},z)}{\partial\theta_j} \tag{3.106}$$

where $P(k_{\mathrm{eff}}, z)$ is the linear matter power spectrum (see Eisenstein & Hu, 1998) at a redshift z including growth factors for an arbitrary dark energy cosmology (see Linder, 2003). The summation is over redshift bins, z, and wavenumber k. k_{eff} is an approximation to the observable wavenumber averaged over both radial and angular directions and is given by

$$k_{\mathrm{eff}} = k \left[\frac{r(z) H_{\mathrm{fid}}(z)}{r_{\mathrm{fid}}(z) H(z)} \right]^{1/3} \tag{3.107}$$

where the subscript fid refers to the comoving distance $r(z)$ and Hubble parameter $H(z)$ at the fiducial cosmology. The fractional uncertainty on the measurement of the power spectrum is

Lensing			
Area/sq degrees	z_m	$z_{\rm max}$	$N_{\rm Bands}$
10,000	0.70	1.5	5
Planck			
Band/GHz	$\theta_{\rm beam}$	$\sigma_T/10^{-6}$	$\sigma_P/10^{-6}$
44	$23'$	2.4	3.4
70	$14'$	3.6	5.1
143	$8.0'$	2.0	3.7
217	$5.5'$	4.3	8.9
WFMOS			
Area/sq degrees	$z_{\rm bin}$	$k_{\rm max}/h{\rm Mpc}^{-1}$	Bias
2000	1.0	0.15	1.25
300	1.0	0.15	1.25
SNAP			
$z_{\rm max}$	$N_{\rm bin}$	N_{SN1A}	σ_m
1.5	17	2000	0.15

Table 3.1: The main default values parameterising the Lensing, CMB, BAO and SN1A experiments considered in this paper. For further details of the surveys see Section 3.8 and Table 3.4.

given by

$$\Delta \ln P(k,z) = 2\pi \sqrt{\frac{1}{Vk^2\Delta k}} \left[1 + \frac{1}{nP(k,z)}\right] \tag{3.108}$$

where V is the volume of the survey. I assume $nP = 1$ for all surveys (see Seo & Eisenstein, 2003).

The proposed WFMOS BAO survey has two redshift slices centred on $z = 1.0$ ($0.5 < z < 1.3$) covering 2000 square degrees and $z = 3.0$ ($2.3 < z < 3.5$) covering 300 square degrees. The volume is calculated assuming the area and redshift ranges at the fiducial cosmology.

I have also calculated the BAO prediction for a survey with an area of 10000 square degrees with a median redshift of $z_m = 0.7$, using five redshifts bins with ranges centred upon $z = 0.4$ ($0.3 < z < 0.5$), $z = 0.6$ ($0.5 < z < 0.7$), $z = 0.8$ ($0.7 < z < 0.9$), $z = 1.0$ ($0.9 < z < 1.1$) and $z = 1.2$ ($1.1 < z < 1.3$). To include the effect of photometric redshift uncertainty a radial

damping term is added (see Zhan, Hui & Stebbins, 2005)

$$P(k_{\rm eff}, z) \rightarrow P(k_{\rm eff}, z) e^{-c^2 \sigma_z^2(z) k_{\rm eff}^2 / H_{\rm fid}^2(z)} \tag{3.109}$$

where $\sigma_z(z)$ is given by equation (3.66).

Alternatively, in an effort to reduce the photometric redshift error, the matter distribution could be estimated by grouping galaxies into clusters each containing $n_{\rm percluster}$ galaxies (Angulo et al., 2005). This would have the combined effects of decreasing the effective number density $n \rightarrow n/n_{\rm percluster}$ and decreasing the redshift error for the group $\sigma_z(z) \rightarrow \sigma_z(z)/\sqrt{n_{\rm percluster}}$. I found for $n_{\rm percluster} > 1$ the marginal errors on w_0 and w_a increase, since the effect of decreasing number density increases the fractional error on the power spectrum by more than the decrease in the photometric redshift error can compensate. Hence I find that using clusters for the BAO experiment here is not an optimal strategy for measuring the dark energy equation of state, combining with the expected *Planck* results the errors are not improved.

To ensure only the linear régime is used the maximum wavenumber used in all the surveys is $k = 0.15\ h{\rm Mpc}^{-1}$, and I use $\Delta k = 5 \times 10^{-3}\ h{\rm Mpc}^{-1}$. The full parameter set used is (Ω_m, Ω_{de}, h, $b\sigma_8$, Ω_b, w_0, w_a, n_s, α_n) where b is a bias factor parameterising the mapping of the dark matter distribution to the galaxy distribution.

An important assumption is that the bias is a constant on the scales probed, this assumption may be optimistic in light of the results from Croton et al. (2006) who find a scale and luminosity dependant bias from the SDSS data (they parameterise this using $b = (1 + Qk^2)/(1 + Ak)$ where Q and A are nuisance parameters) and Simon et al. (2006) who find a scale dependant bias using the CFHTLS data. Allowing a scale, redshift, luminosity and environment dependent bias has the potential to further increase the predicted marginal errors through the degeneracy of the other cosmological parameters with the bias parameter. Indeed, if the bias cannot be entirely understood the value of BAO cosmological constraints could be seriously jeopardized.

3.8.3 SNIa Experiments

I have calculated errors on parameters for SNIa experiments for the proposed SuperNova Acceleration Probe (*SNAP*; Aldering, 2005) supernovae experiment using a prescription similar to that outlined in Ishak (2005) and Yèche et al. (2006). The Fisher matrix, defined by Tegmark

et al. (1998) and Huterer & Turner (2001), is:

$$\boldsymbol{F}_{ij}^{SNIa} = \sum_{z}^{N_z} \frac{1}{[\Delta m(z)]^2} \frac{\partial m(z)}{\partial \theta_i} \frac{\partial m(z)}{\partial \theta_j} \tag{3.110}$$

where $m(z)$ is the apparent magnitude of a supernova at a given redshift and N_z is the number of supernova bins in redshift. The apparent magnitude is related to the luminosity distance by $m(z) = \mathcal{M} + 5\log_{10} D_L(z)$ where $D_L(z) \equiv (H_0/c)(1+z)r(z)$ is the H_0-independent luminosity distance. The normalisation parameter is $\mathcal{M} \equiv M - 5\log_{10}(H_0/c) + \text{constant}$, where M is the absolute magnitude of a SNIa.

The effective magnitude uncertainty in a given bin at a particular redshift, taking into account luminosity evolution, gravitational lensing, dust and the effect of peculiar velocity uncertainty is given by (Kim et al., 2004)

$$\Delta m(z) = \sqrt{\sigma_m^2 + \left(\frac{5\sigma_\nu}{cz \ln 10}\right)^2 + N_{\text{bin}}\delta_m^2} \tag{3.111}$$

where the scatter in peculiar velocities of $\sigma_\nu = 500\ \text{kms}^{-1}$ is assumed, and the systematic limit is $\delta_m = 0.02$ (for a space-based experiment). I have used the standard set of 2000 simulated *SNAP* supernova distributed in 16 redshift bins of width $\Delta z = 0.2$ between redshifts $0.0 \leq z \leq 1.8$ the number per bin taken to be the simulated sample from Yèche et al. (2006) and Virey et al. (2004). To include an additional source of error due to photometric redshift errors the uncertainty in the redshift can be simply added in quadrature to the magnitude uncertainty. The full SNIa parameter set is (Ω_m, Ω_{de}, w_0, w_a, h).

3.9 Optimisation for a Wide-Field Cluster Lensing Survey

Having investigated the source of the lensing signal which contributes to the measurement of w_0, I have shown that a time-limited, wide-field survey can reach high-accuracy measurements of w_0. I will now proceed to optimise such a weak lensing and photometric redshift survey for a fixed time observation to measure the properties of dark energy using the geometric test.

3.9.1 A Simplified Error Model

Before considering the full problem of optimising a weak lensing survey for the geometric test, it is useful to consider a simplified estimate of the parameter uncertainty, so that the more

complex results can be understood in terms of simple relations between competing effects. The uncertainty on w_0 is roughly given by

$$\frac{\Delta w_0}{w_0} \approx \frac{2}{\gamma\sqrt{N_{\rm B}N_{\rm cl}}}\left(\frac{\partial \ln R}{\partial \ln w_0}\right)^{-1}\left(\frac{\sigma_e^2}{N_i}+\boldsymbol{C}^{\gamma\gamma}\right)^{1/2}, \tag{3.112}$$

where

$$N_{\rm cl} \approx A/{\rm fov} \tag{3.113}$$

is the number of independent clusters or fields in the analysis,

$$N_{\rm B} \approx z_m/\Delta z \tag{3.114}$$

is the number of redshift bins behind the lens, where z_m is the median redshift of the survey and Δz is the typical redshift error at that depth. The factor of 2 in equation (3.112) comes from the fact that $R = \gamma_j/\gamma_i$, in transforming from a response in R to a response in γ both redshift slices contribute equally in this simplified model. The typical number of galaxies per bin is

$$N_i \approx f_l N_{\rm tot}/N_B N_{\rm cl}, \tag{3.115}$$

where f_l is the fraction of galaxies in the field behind the cluster, and $N_{\rm tot}$ is the total number of galaxies in the survey. The terms in equation (3.112) arise from two sources. The first, proportional to σ_e, is the intrinsic uncertainty per shear mode due to galaxy ellipticities, and can be beaten down by increasing the number of galaxies per redshift bin, or by averaging over more bins, or more clusters. The second term, proportional to $\boldsymbol{C}^{\gamma\gamma}$, is due to lensing by large-scale structure in between the lens and the source bins, and can be reduced by increasing the number of redshift bins (with the approximation that each lensing bin is independent) and by averaging over independent clusters. The number of clusters in the sample scales with median survey redshift as

$$N_{\rm cl}(M \geq 10^{14}M_\odot) = 10 z_m^{3.4} \tag{3.116}$$

clusters per square degree, where the cluster sample has been cut off at $10^{14}M_\odot$, where I find the signal contributing to the measurement of w_0 reduces (see Section 3.7). This scaling was taken from Figure 3.5.

In general this thesis will be concerned in fixed-time surveys, where the survey time scales roughly as

$$T = T_0 z_m^4 f_{\rm sky}, \tag{3.117}$$

where $f_{\rm sky}$ is the fraction of the sky covered by the survey, z_m is the median redshift of the survey, and T_0 is a time constant, the time to observe the whole sky to a median redshift

$z_m = 1$ (i.e. to a limiting magnitude of 25 in the r-band; see equation 3.75), set by the telescope specifications and number of observed bands. The time scales as the fourth power of the median redshift due to cosmological dimming effects and the need to detect the object against the sky background. As a concrete example I will use the Canada-France-Hawaii Telescope (CFHT; Semboloni et al., 2006; Tereno et al., 2004), which is a 3.6m telescope with a 1 square degree field of view, integrating over 5 bands, for which $T = 500$ nights and (using equation (3.117) and Table 3.2) $T_0 = 6.2 \times 10^4$ nights (the number of nights CFHT would take for an all sky survey to a depth of $z_m = 1.0$). I will also assume a projected number density on the sky which scales with the median redshift of the sample as

$$n_2(< z) = 30 z_m^{3.4} \text{ galaxies per square arcmin}, \tag{3.118}$$

and an angle averaged shear-shear correlation function,

$$C^{\gamma\gamma} \approx 10^{-5} z_m^{1.6}, \tag{3.119}$$

both measured from the COMBO-17 survey. I will use an intrinsic ellipticity dispersion of $\sigma_e = 0.3$. With this simplified error model, I find the fractional error on w_0 scales as

$$\frac{\Delta w_0}{w_0} = 0.062 z_m^{-1.35} (1 + 24.1 z_m^4 \Delta z)^{1/2}. \tag{3.120}$$

The leading term here is due to shot-noise, while the second term in quadrature is due to large-scale sampling variance. Assuming there are ten redshift bins, so that $\Delta z = 0.07$ is typical of the photometric redshift error, equation (3.120) minimises at $z_m \approx 1.0$ with a conditional error of $\Delta w_0 \approx 0.1$ for lensing alone. For a fixed-time survey I find that for a shallow, low-z, wide area survey, the error on w_0 is dominated by shot-noise. Here the signal is not very large, and the number of background galaxies (and therefore combinations of background source planes) is too low. For a deep survey this becomes dominated by large-scale structure clustering. This occurs because the survey area has to be smaller to compensate for the depth, with a fixed time available, hence there are fewer clusters to average over and reduce the clustering noise.

3.9.2 Survey Optimisation

The optimisations discussed in the following Sections only include a CMB 14-month *Planck* experiment, the combination with further experiments is discussed in Section 3.10. For a weak lensing and photometric redshift survey on a given telescope for a set amount of observing time, the survey itself is characterised by the area, the median redshift z_m of the survey in the band

used for weak lensing (usually the r or i-band) and the number of bands used for photometric redshift accuracy, $N_{\rm bands}$. For a given number of bands there is only one free parameter, which I assume is the median redshift, z_m.

The procedure presented here is to vary z_m, calculating the survey area by equation (3.91). With the galaxy number distribution and number counts, the Fisher matrix can be calculated and hence the marginalized uncertainty on a measurement of w_0. Figure 3.12 shows the marginalized error on w_0 (assuming a 14-month *Planck* experiment) for a $D = 4$m class telescope with a 2 square degree field of view for a variety of numbers of photometric bands. For example a 5-band survey would be the case for the Dark Energy Survey on the CTIO Blanco telescope or the darkCAM survey for example. The results reflect the analysis of the simple analytic model. For a shallow, wide survey the lensing signal is not strong, the number of background galaxies is low and so the error on w_0 is shot-noise dominated. The error on w_0 is poor beyond $z_m \sim 0.7$, indicating that clustering noise is a strong effect. The small variation with the number of optical bands is due to the effect that, despite the marginal error of the geometric test decreasing, the intersection with the *Planck* experiment does not substantially change. This is investigated further in Section 3.9.3.

The optimal survey is a, 5-band, 18,500 square degree survey with median redshift $z_m = 0.6$, combined with a 14-month *Planck* survey. However, note that the dependence on median redshift is shallow about the minimum and that the optimal survey when considering a figure of merit (see Section 3.9.6) is a 5-band, 10,000 square degree survey with median redshift $z_m = 0.7$, so that from hereon, and in Section 3.10, I will use this as the fiducial survey design.

3.9.3 Optical and Infrared Surveys

In the last few years multi-band surveys have started to open up the high redshift Universe. Hence it is now possible to combine 5-band optical surveys with 4-band infrared surveys for 9-band photometric redshifts. The effect of varying the number of assumed additional bands available on the measurement of dark energy parameters can be studied by varying the photometric redshift error. Figure 3.13 shows the variation of the accuracy on w_0, marginalized over all the other parameters with a 14-month *Planck* experiment, as a function of varying the

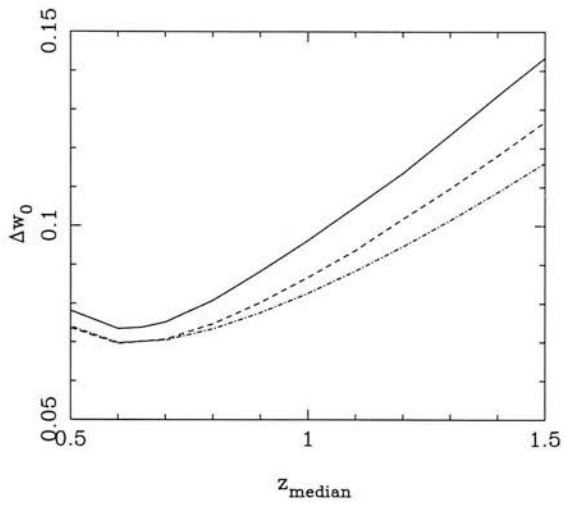

Figure 3.12: The uncertainty on w_0, marginalized over all other parameters, as a function of median redshift, z_m, for a time-limited survey, assuming a prior from a 14-month *Planck* experiment. The survey area is $A = 10,000(z_m/0.7)^{-4}$ square degrees. A lower limit of $z_m = 0.5$ has been set, which would correspond to over a hemisphere. The solid line is for 5-band photometric redshift survey, the dashed line for 9-band and the dot-dashed line for 17-band. Note that the time constraint is only on the 5-bands. Note, see Section 3.6.4, that an upper redshift limit of $z_{\max} = 1.5$ has been assumed beyond which shapes cannot be measured.

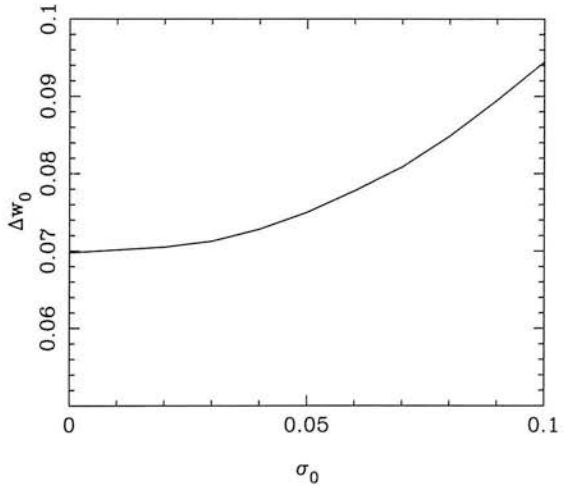

Figure 3.13: The uncertainty on w_0, marginalized over all other parameters with a 14-month *Planck* experiment, as a function of photometric redshift accuracy, parameterised by $\sigma(z) = \sigma_0(1+z)$. The normalisation, σ_0 scales roughly with the number of photometric bands as $\sigma_0 \propto N_{\rm bands}^{-1}$, where $\sigma_0 = 0.05$ for a 5-band photometric redshift survey and $\sigma_0 = 0.01$ for a 9-band (4-band infrared and 5-band optical) infrared and optical photometric redshift survey.

accuracy of the photometric redshifts. I parameterise this by defining

$$\sigma_z(z) = \sigma_0(1+z). \tag{3.121}$$

A value of $\sigma_0 = 0.05$ is approximately appropriate for a 5-band photometric redshift survey, while $\sigma_0 = 0.01$ corresponds to a 9-band (4-band infrared and 5-band optical) photometric redshift survey. For a 5-band survey ($\sigma_0 = 0.05$) I find $\Delta w_0 = 0.075$, while for a 9-band (4-band infrared and 5-band optical) photometric redshift survey ($\sigma_0 = 0.01$) I find $\Delta w_0 = 0.071$. Note this is distinct from a 9-band optical survey considered up until this point, in Section 3.9.2.

If the photometric redshifts are degraded, for instance if fewer than 5 bands are available, the accuracy of w_0 is also degraded. By the time $\sigma_0 = 0.1$ (for example 3-bands), the error has increased to $\Delta w_0 = 0.094$. Note the effect of outliers has not been consider here (see Section 3.10.8), which will degrade the signal further.

I have found that using BAO to measure dark energy from a photometric redshift survey is difficult as the damping term due to the photometric redshifts, effectively constraining the range of Fourier modes available to analyse, quickly reduces the amount of cosmological information that can be extracted. Figure 3.14 shows the variation of the error achievable using BAO from a photometric redshift survey, the error is simply the CMB error until $\sigma_0 \approx 0.02$ where the BAO constraint begins to improve the 14-month *Planck* CMB error. To constrain dark energy with a photometric redshift survey using the BAO method infrared bands are vital over the whole redshift range.

3.9.4 Weighting the Data

It has been shown that in certain cosmological methods the data can be weighted in a way which maximises the amount of information that be be extracted (e.g. Percival et al., 2004). In this Section I investigate the effect that some simple additional weighting schemes have on the marginal errors on w_0 achievable using the geometric test, this is done by assuming simple functional forms for the $\tilde{w}(z)$ factor in equation (3.37). A optimal weighting may exist but its derivation will be left for future work. Figure 3.15 shows the effect of two functional schemes on the marginal error of w_0. It can be seen that the method is largely invariant to the weighting used. The $\tilde{w}(z) = z^{\alpha}$ improves the marginal error, becoming more dominant as the power α is increased, whereas the $\tilde{w}(z) = (1+z)^{\alpha}$ has little effect on the marginal error. This can be simply understood as the dark energy effect begins to dominant at $z \sim 1$, a weighting scheme

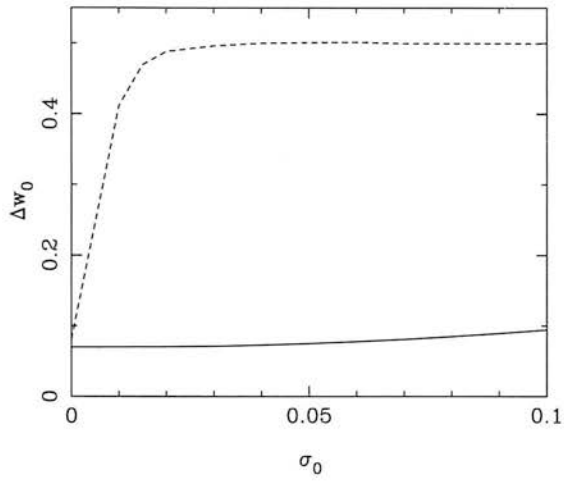

Figure 3.14: The uncertainty on w_0, marginalized over all other parameters with a 14-month *Planck* experiment, as a function of photometric redshift accuracy, parameterised by σ_0. The solid line are the geometric test constraints, the dashed line are the constraints using BAO from a $10,000$ square degree survey with $z_m = 0.7$.

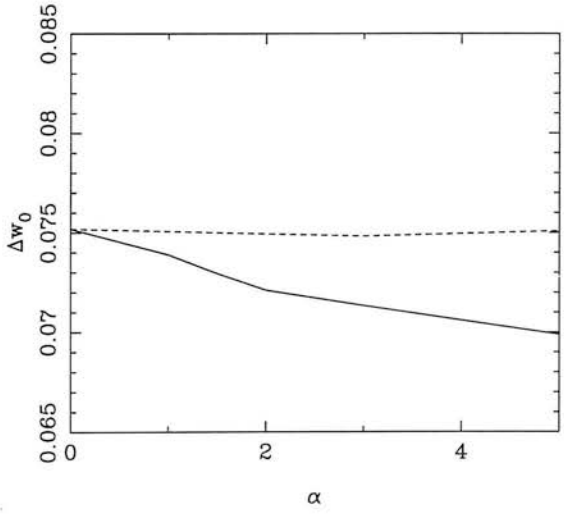

Figure 3.15: The variation in the marginal error on w_0, as the weighting scheme is varied. The solid line is for $\tilde{w}(z) = z^{\alpha}$, the dashed line is for $\tilde{w}(z) = (1+z)^{\alpha}$; α is varied.

	CFHT	COMBO-17
D(m)	3.6	2.2
fov (sq deg.)	3	1
N (bands)	5	17
z_m	1.17	0.7
Area (sq. deg.)	170	1
T (nights)	500	6

Table 3.2: Default survey parameters for the 5-band CFHT Legacy Survey and the 17-band COMBO-17 survey.

that boosts the signal at around this redshift will decrease the marginal error on the dark energy parameters. Since the survey in question probes the redshift range $0 \lesssim z \lesssim 1.5$ a z^α should slightly improve the error whereas a $(1+z)^\alpha$ weighting scheme boosts the signal at a redshift which is too high to be of use in improving the constraint of dark energy parameters.

3.9.5 Scaling Results to Other Surveys

To scale these results to other weak lensing surveys, equation (3.100) should be used with a time calibration i.e.

$$\frac{T}{T_0} = \left(\frac{z_m}{z_{m0}}\right)^4 \left(\frac{A}{A_0}\right) \left(\frac{D}{D_0}\right)^{-2} \left(\frac{\text{fov}}{\text{fov}_0}\right)^{-1}. \tag{3.122}$$

The subscript 0 refers to parameters time, median redshift and area of a survey on a telescope with certain diameter and field of view. The scaling applies between surveys with equal number of bands; for 5 bands the Canada-France-Hawaii Telescope Legacy Survey (CFHTLS) can be used, while for 17 bands COMBO-17 can be used, see Table 3.2. Although it can be naively assumed that the time for a given survey scales proportionally with the number of bands so that $T_0 \rightarrow T_0 N_{b0}/N_b$ where N_b is the number of bands in the survey.

One of two questions may arise. What is the error on w_0 (or w_a) that can be achieved given T nights on a given telescope, and freedom to choose the survey design? Or, given a survey of area A and median redshift z_m what is the constraint on w_0 (or w_a) that can be achieved? Both of these questions can be answered using the information given here.

If the field of view of the telescope is small enough so that only approximately one cluster will

be observable per pointing then a targeting strategy should be used. In this case Figure 3.9 should be used so that given P pointings on a given telescope the appropriate marginal error can be predicted. For a targeting strategy the time trade-off is determined not by the total area covered but by the number of pointings. The number of pointings achievable given T nights to a redshift z_m can be expressed, as

$$P = \left(\frac{T}{T_0}\right)\left(\frac{z_{m0}}{z_m}\right)^4\left(\frac{D}{D_0}\right)^2\frac{\mathrm{fov}_0}{A_0}. \tag{3.123}$$

The achievable marginal errors from a targeting strategy are however limited due to the large amount of clusters which need to be observed for a tight dark energy constraint.

Given the freedom to choose any wide-field surveys median redshift, the optimal median redshift of $z_m \approx 0.7$ is insensitive to the number of optical bands, when combined with a *Planck* prior (see Figure 3.12). Equation (3.122) should then be used, with the appropriate calibration (see Table 3.2), to calculate the area achievable given T nights. If the number of bands is 5, 9 or 17 the appropriate line in Figure 3.12 then scales proportionally up (and down) with decreased (or increased) areal coverage from $10,000$ square degrees, for a 5-band survey i.e. $\Delta w_0(A) = (0.075)(A/10,000)^{-1}$. If the number of bands is not shown in Figure 3.12 then Figure 3.13 can be used to find the minimum of the appropriate Δw_0 vs. z_m line (at $z_m = 0.7$). This can then be scaled for a differing areal coverage as before.

Given a fixed survey of area A and median redshift z_m Figures 3.12 and 3.13 can be used in a similar way. Given the error in Figure 3.12 for a given median redshift $\Delta w_0(z_m)$ the achievable error can be calculated using $\Delta w_0(A) = \Delta w_0(z_m)(A/10,000)^{-1}$. In scaling between bands a similar interpolation between Figure 3.12 and Figure 3.13 can be performed.

3.9.6 Constraining $w(z)$ at Higher Redshifts

Pivot Redshifts

As well as constraining the marginalized dark energy equation of state, $w(z)$, at $z = 0$ (w_0), the measured accuracy of w_0 and w_a can be combined to estimate the measured accuracy of $w(z)$ at higher redshifts. Here some information can be gained by using the degeneracy between w_0 and w_a (see Section 3.10), to find a redshift where the anti-correlation combines to minimise the error. Figure 4.13 shows the expected accuracy of $w(z) = w_0 + w_a z/(1+z)$ as a function of redshift for a 5-band, 10,000 square degree survey with median redshift $z_m = 0.7$, combined

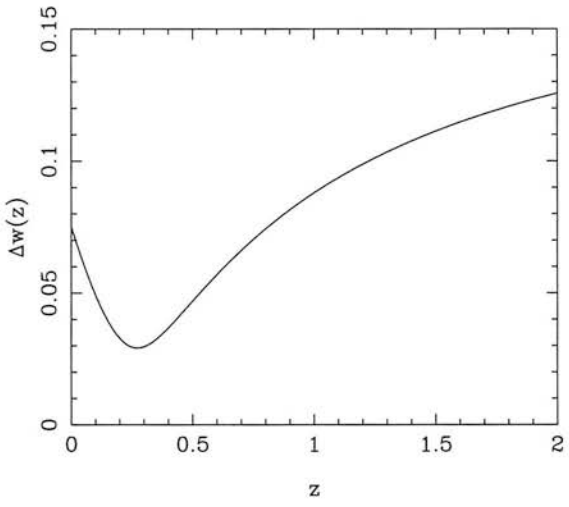

Figure 3.16: The uncertainty on $w(z)$, the dark energy equation of state measured at different redshifts, marginalized over all other parameters. For gravitational lensing combined with 14-month *Planck* experiment. This shows that the highest accuracy constraint on $w(z)$ occurs at $z = 0.27$ with $\Delta w(z = 0.27) = 0.0298$.

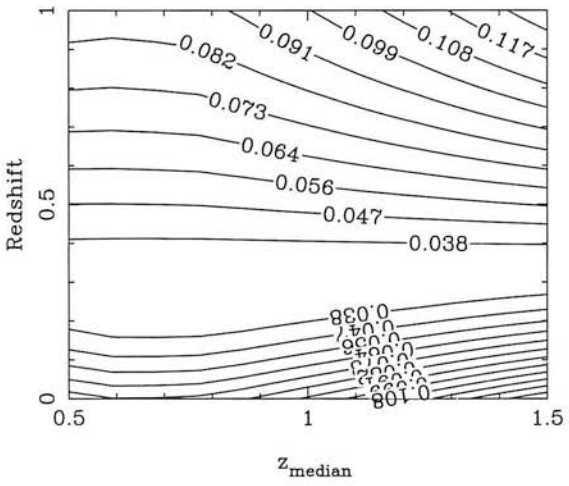

Figure 3.17: The uncertainty on $w(z)$, the dark energy equation of state measured at different redshifts, marginalized over all other parameters for gravitational lensing combined with 14-month *Planck* experiment, and its dependence on median redshift. The contours are lines of equal marginalized $w(z)$ error, the numbers on the lines being the marginal error on that line.

with a 14-month *Planck* survey. The highest accuracy measurement occurs at $z = 0.27$, where $w(z = 0.27) = 0.0298$. This low 'pivot redshift' for the geometric test is due to its insensitivity to w_a.

Figure 3.17 shows how the error on $w(z)$ varies with both redshift, z, and with median redshift of the survey, z_m, for the same time-limited survey. It can be seen that the minimisation in the error in Figure 3.12 is reproduced at the Redshift= 0 line (along the x-axis) of the plot, and Figure 4.13 is reproduced by considering the variation in the error along the $z_m = 0.7$ line. It is clear that if one is concerned with optimising a survey design to constrain the error on $w(z)$ at an optimal redshift then there is little sensitivity to the survey design. This is due to the effect of intersection that is, even though the lensing–only error may be varying, the intersection of the lensing ellipse with the 14-month *Planck* experiment ellipse does not vary considerably in width (characterising the minimum error on $w[z]$) or orientation (characterising the value of z at which the error on $w[z]$ minimises).

Figure of Merit

A useful 'figure of merit' (Linder, 2003; Linder, 2006; Dark Energy Task Force, DETF, 2006) in dark energy predictions can be constrained by considering the smallest area of parameter space constrained by a given experiment. The dark energy equation of state can be written as:

$$w(a) = w_i + w_a(a_i - a) \tag{3.124}$$

where $w_i \equiv w(a_i)$ and I have expanded around scale factor a_i. The error on $w(a)$ is:

$$\Delta w(a)^2 = \Delta w_i^2 + (a_i - a)^2 \Delta w_a^2 + 2(a_i - a)\mathrm{Cov}(w_i, w_a) \tag{3.125}$$

where $\mathrm{Cov}(w_i, w_a)$ is the covariance between w_i an w_a (equal to the corresponding inverse Fisher matrix element). By taking the derivative of this quantity the scale factor at which the error minimises can be found

$$a_{\mathrm{min}} = a_i + \frac{\mathrm{Cov}(w_i, w_a)}{\Delta w_a^2}. \tag{3.126}$$

In the standard expansion, in equations (1.113) and (3.15), $a_i = 1$ and the above expression reduces to the equation for the pivot redshift. In this formalism the pivot redshift occurs when the covariance between the w_i and w_a is zero. This is equivalent to the pivot redshift in the expansion of equation (3.15). The ellipse at the pivot redshift is then the smallest ellipse constrained

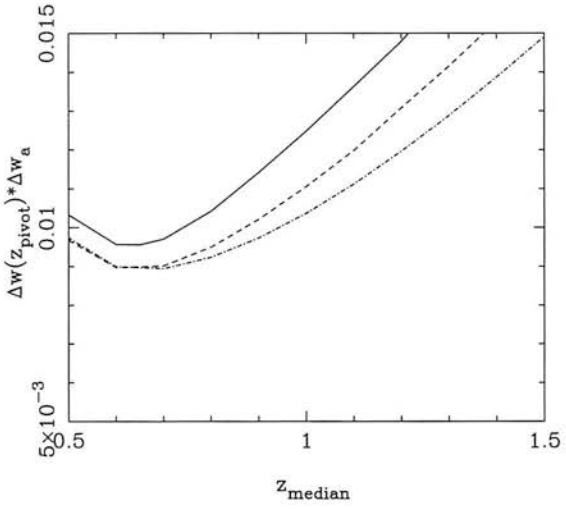

Figure 3.18: The figure of merit as a function of median redshift, z_m, for a time-limited survey, assuming a 14-month *Planck* prior. The survey area is $A = 10,000(z_m/0.7)^{-4}$ square degrees. The solid line is for 5-band photometric redshift survey, the dashed line for 9-bands and the dot-dashed line for 17-bands.

by a given experiment. Since this ellipse is de-correlated its area can be simply approximated by

$$\Delta w(z_{\rm pivot}) * \Delta w_a. \tag{3.127}$$

This is the figure of merit used to quantify the performance of any given experiment: the smaller the figure of merit the tighter the constraint on the equation of state of dark energy will be over a larger redshift range. Broadly it can visualised by comparing Figure 3.17 and Figure 3.18, the figure of merit is minimised where the lowest contour in Figure 3.17 is widest, this can be seen in Figure 3.18. It can be seen that the optimal experiment when considering the figure of merit is at a median redshift of $z_m = 0.7$ for 5 bands. The figure of merit is shown for all considered experiments in Table 3.4.

3.10 Parameter Forecasts

Having found the optimal survey strategy to measure the dark energy equation of state for a given experiment, this thesis will now investigate the constraints on the full parameter space. Throughout a 10,000 square degree 5-band photometric redshift weak lensing survey with a median redshift of $z_m = 0.7$ ($R = 23.8$) will be assumed.

In this Section dark energy parameter constraints from the geometric test alone (Section 3.10.1) will be discussed, combined with the *WMAP* 4-year and 14-month *Planck* experiments (Section 3.10.2) and combined with a WFMOS BAO experiment and *SNAP* SNIa experiment in Sections 3.10.2 and 3.10.4. The different surveys considered, and the predicted marginal errors on the dark energy parameters, are presented in Table 3.4.

Using the full Fisher matrix formalism for parameters in a consistent cosmological model the accuracy on a set of cosmological parameters for a given experiment can be estimated, taking into account marginalization over all other parameters. The details of the Fisher analysis are discussed in Section 3.8. The 11-parameter cosmological parameter set used is (Ω_m, Ω_{de}, h, σ_8, Ω_b, w_0, w_a, n_s, τ, α_n, $r = T/S$), with default values (0.27, 0.73, 0.71, 0.8, 0.04, -1.0, 0.0, 1.0, 0.09, 0.0, 0.01).

3.10.1 Parameter Forecasts for the Geometric Test Alone

On its own, the geometric test constrains a sheet in the likelihood space of (w_0, w_a, Ω_{de}, Ω_m). Figure 3.19 shows this plane in the three-space of (w_0, Ω_{de}, Ω_m), having marginalized over w_a (lighter, green plane). The surface here encloses the three-parameter, 1-σ likelihood surface. The equation of this plane in the full four-parameter space is

$$X = 0.64w_0 - 0.31w_a - 0.35\Omega_{de} - 0.67\Omega_m. \tag{3.128}$$

For model parameters of $w_0 = -1$, $\Omega_m = 0.27$, and $\Omega_{de} = 0.73$ this can be evaluated to give

$$X = -1.08, \tag{3.129}$$

which can be measured with an expected accuracy of

$$\Delta X = 0.031. \tag{3.130}$$

If $w = -1$ is fixed, it can be seen that the geometric test constrains the degenerate line $\Omega_{de} + 1.19\Omega_m = 1.26$. This can be compared with the CMB constraint on the density parameter plane of $\Omega_{de} + \Omega_m = 1$.

These constraints can be projected onto a two-parameter space, marginalizing over all other parameters. Figure 3.20 shows the two-parameter, 1-σ (68.3% confidence) likelihood contours for the parameter space of Ω_{de}, Ω_m, w_0 and w_a. The lighter (green) solid block is the constraint on parameters from the geometric test only. Here again the large degeneracies between the

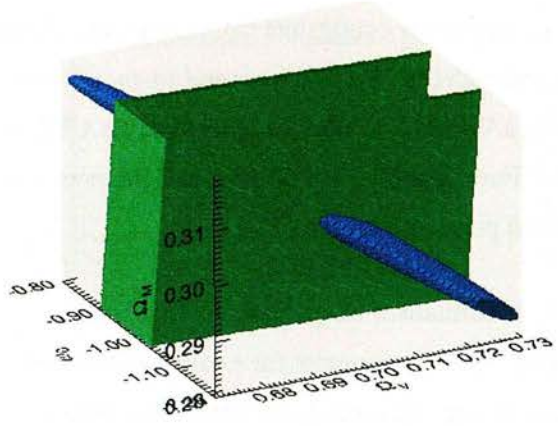

Figure 3.19: 3D parameter space for a 10,000 square degree lensing survey to a median redshift of $z_m = 0.7$ with 14-month *Planck* experiment, with no dark energy evolution. The volumes bounded by green and blue represent the three-parameter 1-σ parameter estimations for weak lensing and a 14-month *Planck* experiment respectively.

geometric parameters can be seen. In particular it is again clear that the geometric test is very insensitive to w_a (see Section 3.4.3). The one-parameter, 1-σ marginalized parameter uncertainties can be found by projecting these contours onto each axis and dividing by 2.3. These are presented in Table 3.4.

3.10.2 Comparing and Combining the Geometric Test and the CMB

To lift the degeneracies in the geometric test the predicted constraints can be combined with predicted results expected from the CMB. Here I consider combining with the expected results from the 4-year *WMAP* experiment and a 14-month experiment with the *Planck* Surveyor.

Combining with *WMAP*

The parameter forecasts for a 4-year *WMAP* survey are compared and combined with the geometric test, allowing for spatial curvature, in Figure 3.20. The lighter (green) ellipses are the geometric test alone, the darker (blue) ellipses are the marginalized parameter forecasts for *WMAP*, while the central ellipses (red), show the combined likelihood contours. In these plots I have not plotted the other parameters which are also estimated by the CMB although these are fully marginalized over. I will consider these parameters later in this Section.

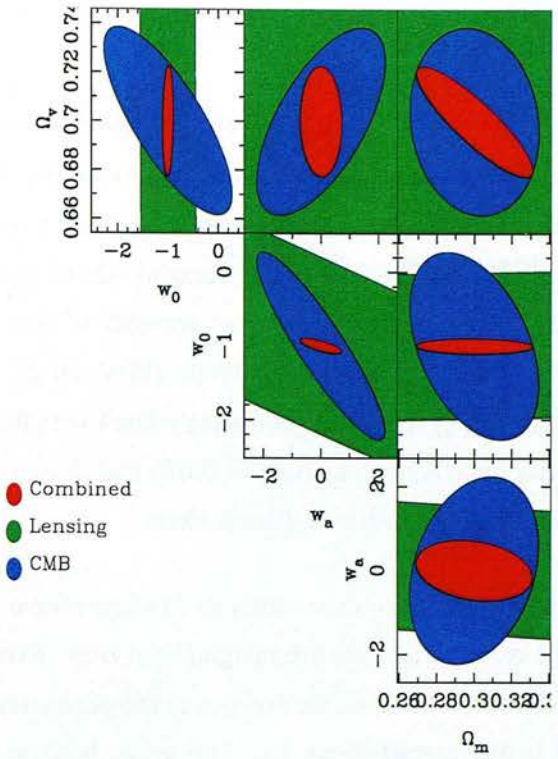

Figure 3.20: Two-parameter, 1-σ (68.3% confidence) likelihood contours for geometric parameters for a 10,000 square degree lensing survey geometric analysis to a median depth $z_m = 0.7$, compared and combined with the expected 4-year *WMAP* results.

Figure 3.20 illustrates the poor sensitivity of the CMB to w_0 and w_a, but constrains the curvature of the model by the combination $\Omega_m + \Omega_{de}$. The response of the CMB to dark energy comes mainly from the Integrated Sachs-Wolf (ISW) effect from low-ℓ modes. Combining the geometric test and the CMB, the orthogonality of the two methods reduces the error on the dark energy parameters from $\Delta w_0(\mathrm{WMAP}) = 1.268$, $\Delta w_a(\mathrm{WMAP}) = 2.225$ to $\Delta w_0(\mathrm{WMAP + GL}) = 0.089$ and $\Delta w_a(\mathrm{WMAP + GL}) = 0.714$. There is also marginal improvement in $\Delta\Omega_m$ and $\Delta\Omega_{de}$. The main improvement to the lensing analysis is the *WMAP* constraint on the curvature of the Universe in the (Ω_m, Ω_{de}) parameter plane. Note that the results presented in Spergel et al. (2006) using 3 years of *WMAP* data of $w_0 = -1.06^{+0.13}_{-0.08}$ do not include a marginalization over w_a, and are combined with 2DFGRS and SDSS data. To get a clearer picture of the orthogonality of the CMB 4-year *WMAP* and geometric test results, a 3D view of the one-parameter, 1-σ parameter surfaces are shown in Figure 3.19. This shows the (w_0, Ω_m, Ω_{de}) parameter surfaces, marginalized over all other parameters, including w_a.

Combining with *Planck* Surveyor

In this Section I will compare the information in Figure 3.20 expected from a 4-year *WMAP* experiment with that expected from a 14-month *Planck* Surveyor experiment, shown in Figure 3.21. While the *Planck* error ellipses (dark/blue) are considerably smaller than those of the 4-year *WMAP*, the degeneracy between w_0 and w_a remains. On its own *Planck* could measure w_0 to an accuracy of $\Delta w_0 = 0.502$ and on w_a to an accuracy of $\Delta w_a = 1.86$, with the main source of information from the Integrated Sachs-Wolfe (ISW) effect. Again the curvature of the model is well constrained by the CMB. Combining *Planck* with the geometric test reduces the dark energy parameter uncertainties to $\Delta w_0 = 0.075$ and $\Delta w_a = 0.326$, a factor of ~ 7 improvement in the measurement of w_0 over *Planck* alone.

The effect of the geometric tests constraints within an 11-dimensional parameter space can be seen in Figure 3.22. All other parameters are marginalized over. Even though the geometric test does not place any direct constraint on the non-geometric parameters, there is improvement in the normalisation of matter perturbations, σ_8. This arises because σ_8, measured from the CMB, is dependent on other parameters. Hu & Jain (2004) show the dependence of σ_8 on other cosmological parameters, and in particular a constant value of w. In calculating the value of σ_8 using dark energy dependent growth factors they find that the value of σ_8 depends on a combination of dark energy parameters, they find an analytic expression in the special case of a flat universe with constant w. These arguments can be generalised to w_0 and w_a using the growth factors given in Linder (2003). An alternative parameter would be to use the horizon-scale amplitude of matter perturbations, δ_ξ, which is an independent parameter. In this thesis σ_8 will be used to compare with other analysis. The improvement on CMB parameters are summarised in Table 3.3.

Comparing and Combining Lensing with CMB, BAO and SNIa Experiments

Figure 3.23 shows comparisons between the geometric lensing, CMB, SNIa and BAO experiments for the geometric tests parameter set $(\Omega_m, \Omega_{de}, w_0, w_a)$. The broad, light-grey (light blue) ellipses are for a *SNAP*-like SNIa experiment, the closed second lightest (orange) ellipses are for a WFMOS-like BAO experiment, the darker grey (green) ellipses are for the geometric test, while the dark (blue) ellipses are for a 14-month *Planck* CMB experiment. The small light-grey (red) ellipses at the centre are the combined uncertainty. It is clear that allowing for

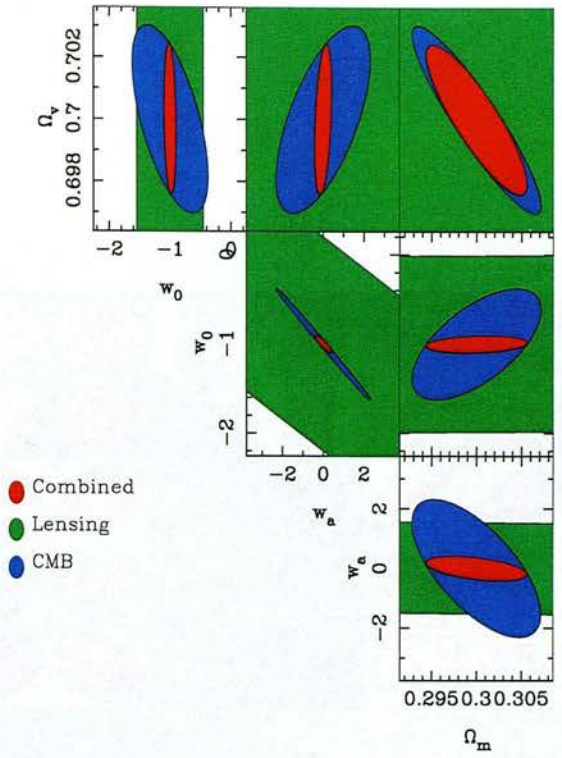

Figure 3.21: Two-parameter, 1-σ (68.3% confidence) likelihood contours for geometric parameters for a 10,000 square degree lensing survey to a median depth $z_m = 0.7$, combined with a 14-month *Planck* experiment. Note the change in the scale of the axes from Figure 3.20, from hereon the remaining Figures will use the scale introduced in this Figure.

spatial curvature and evolution of the dark energy opens up large degeneracies in many of the experiments. Because of the large-data set, and sensitivity of the CMB to parameters, the CMB provides the strongest constraints alone. It can be seen that very similar degeneracies between experiments in the (Ω_{de}, w_0) plane, while there is some orthogonality between experiments in the (w_0, w_a) plane. Combining experiments improves the constraints on all of the parameters. In particular, allowing for spatial curvature, I find $\Delta w_0 = 0.043$, and $\Delta w_a = 0.108$. The combinations of experiments will be studied in more detail in Section 3.10.4.

To illustrate further the orthogonality of the constraints from lensing, the CMB, BAO and SNIa, Figure 3.24 shows a 3-dimensional plot of the likelihood contours in the (Ω_{de}, w_0, w_a) parameter space, marginalizing over all other parameters. The one-parameter, 1-σ contours have been plotted for clarity.

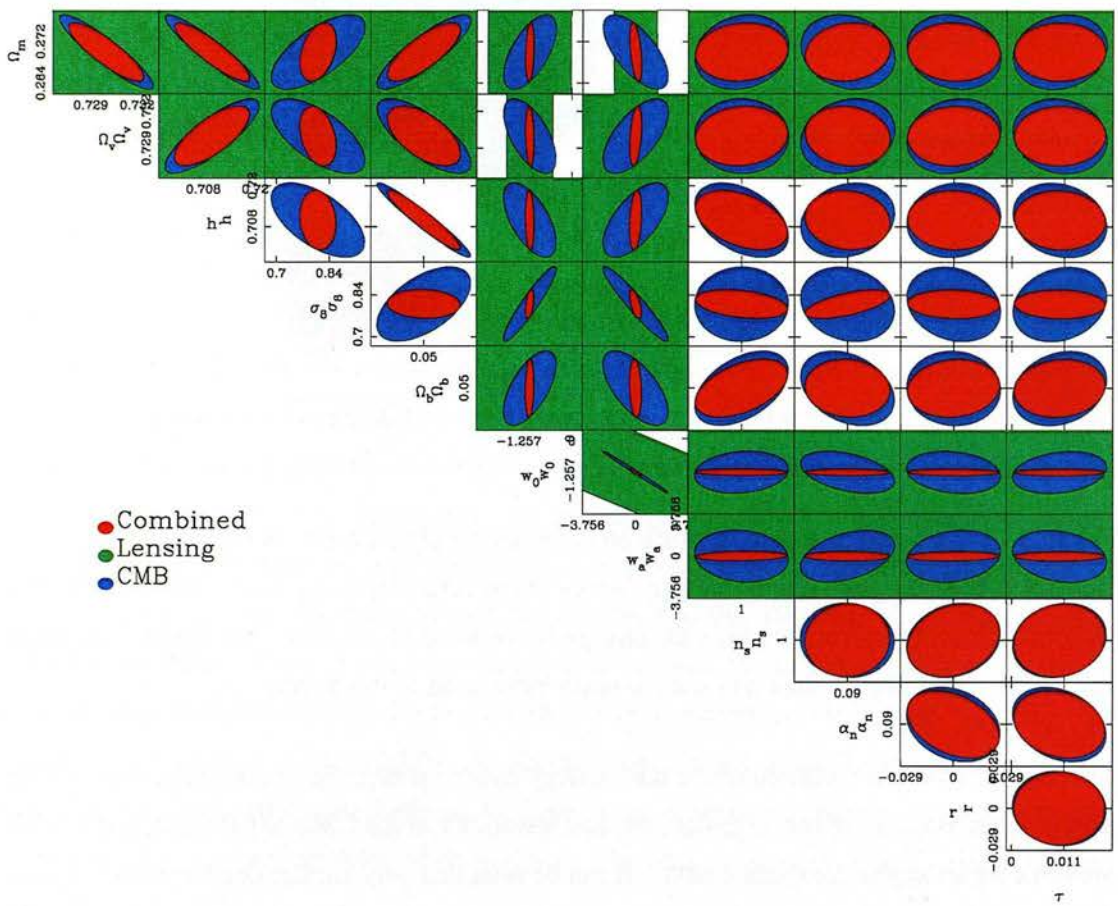

Figure 3.22: The two-parameter 1-σ (68.3% confidence) geometric constraints for a 10,000 square degree lensing survey to a median depth $z_m = 0.7$, with a 14-month *Planck* experiment in the 11-dimensional parameter space (Ω_m, Ω_{de}, h, σ_8, Ω_b, w_0, w_a, n_s, τ, α_n, r). Other parameters for the CMB calculation are marginalized over.

Parameter	*Planck* only	Lensing only	Combined
Ω_m	0.0058	11.253	0.0042
Ω_{de}	0.0024	24.501	0.0020
h	0.0088		0.0070
σ_8	0.1002		0.0383
Ω_b	0.0011		0.0008
w_0	0.5015	5.553	0.0751
w_a	1.8618	31.172	0.3256
n_s	0.0034		0.0034
α_n	0.0062		0.0056
τ	0.0208		0.0204
r	0.0079		0.0077

Table 3.3: Improvements on CMB 14-month *Planck* one-parameter 1-σ constraints by adding the geometric test from a 10,000 square degree lensing survey to a median depth of $z_m = 0.7$.

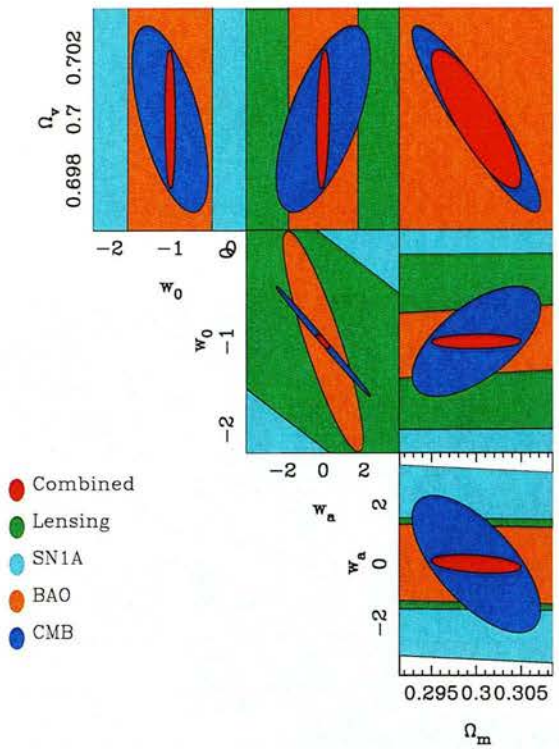

Figure 3.23: Two-parameter, 1-σ (68.3% confidence) likelihood contours for geometric parameters for a 10,000 square degree lensing survey to a median depth of $z_m = 0.7$, combined with a CMB 14-month *Planck* experiment, a BAO WFMOS experiment and a SNIa *SNAP* experiment. One-parameter marginalized results are tabulated in Table 3.4.

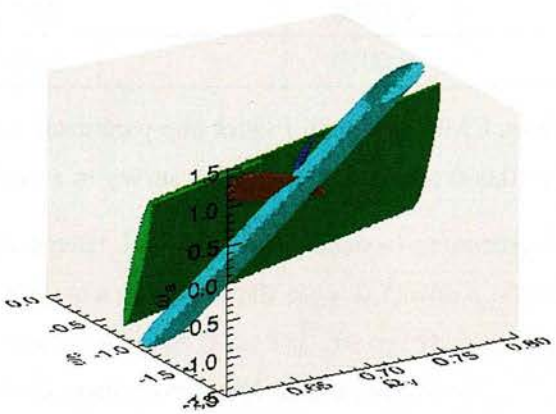

Figure 3.24: Likelihood contours in the 3-dimensional (Ω_{de}, w_0, w_a) parameter space for geometric parameters for a 10,000 square degree lensing survey to a median depth of $z_m = 0.7$, with a CMB 14-month *Planck* experiment, a BAO WFMOS experiment and a SNIa *SNAP* experiment, assuming spatial flatness, $\Omega_m + \Omega_{de} = 1$. One-parameter, 1-$\sigma$ contours are used for clarity.

Survey	Area sqdeg	z_{median}	N_{Bands}	Δw_0	Δw_a	z_{pivot}	$\Delta w(z_{pivot})$	$\Delta w(z_{pivot})\Delta w_a$
Lensing								
darkCAM	10000	0.7	5	1.254	9.384	0.15	0.218	2.0457
darkCAM + *Planck*	10000	0.7	5	0.045	0.223	0.22	0.020	0.0046
darkCAM, 9 bands + *Planck*	10000	0.7	9	0.041	0.213	0.15	0.020	0.0043
darkCAM+*Planck*+BAO+SNIa	10000	0.7	5	0.029	0.085	0.45	0.014	0.0012
darkCAM + BAO darkCAM	10000	0.7	5	0.173	1.229	0.04	0.177	0.2175
Pan-STARRS 1+*Planck*	30000	0.5	5	0.078	0.327	0.25	0.031	0.0101
Pan-STARRS 4+*Planck*	30000	1.0	9	0.026	0.161	0.18	0.013	0.0021
All-Sky Space + *Planck*	40000	1.00	9	0.037	0.184	0.19	0.013	0.0024
SNAP Lensing + SNIa + *Planck*	1000	1.38	9	0.077	0.310	0.33	0.019	0.0059
CFHTLS(Wide)+*WMAP*4	170	1.17	5	0.145	0.767	0.20	0.072	0.0552
VST-KIDS+*WMAP*4	1400	0.6	5	0.128	0.869	0.13	0.080	0.0695
CMB								
4-year *WMAP*				2.060	3.612	1.18	0.758	2.7379
14-Month *Planck*				0.501	1.873	0.367	0.035	0.0655
BAO								
BAO WFMOS+*Planck*	2000	1.0		0.070	0.154	0.78	0.019	0.0029
SNIa								
SNIa *SNAP*+*Planck*				0.142	0.513	0.37	0.028	0.0144

Table 3.4: The table gives experimental parameters and marginalized cosmological parameter error forecasts for various surveys. Note here 9 bands refers to 5 optical bands plus 4 infrared.

3.10.3 Future Lensing Surveys

There are a number of current and planned imaging surveys for weak lensing which could be analysed in 3D. The surveys vary in depth, areal coverage and number of bands. Illustrative marginal errors for these surveys using the geometric test are shown in the Table 3.4. The surveys considered are: the Canada France Hawaii Legacy Survey (CFHTLS; Semboloni et al., 2006) which is ongoing; the VST (VLT Survey Telescope) public survey KIDS; *SNAP* (Supernova/Acceleration Probe; Aldering, 2005), Pan-STARRS (1 and 4; Kaiser, 2005) which will start observing in 2007 and darkCAM on a 4-metre telescope. The errors achievable with darkCAM combined with various different experiments are shown. BAO darkCAM refers to using the photometric redshifts from darkCAM to measure BAO. VST-KIDS and CFHTLS have been combined with a 4-year *WMAP* prior as *Planck* will not be contemporary with these surveys. Here 9 bands refers to a 5-band optical survey with 4 infrared bands as discussed in Section 3.9.3.

3.10.4 Synergy of Dark Energy Experiments

It is interesting to compare the results of each of the dark energy experiments under the same conditions. In Figure 3.25 I show the dark energy equation of state parameters (w_0, w_a), marginalized over all other parameters including spatial curvature for each experiment in pair combinations.

Of all of the individual experiments considered the *Planck* CMB experiment on its own provides the strongest constraint on the (w_0, w_a) plane. However the marginalized uncertainties are still $\Delta w_0 = 0.502$ and $\Delta w_a = 1.86$. A *SNAP*-like SNIa experiment on its own provides poor constraints in the (w_0,w_a) plane, due to the large degeneracy in Ω_m and Ω_{de} in models allowing curvature. This can be seen by comparing with Figure 3.30, but note that of the experiments considered the supernova estimates are the only ones which include terms for extra systematic effects. Removing the extra systematic terms from the supernova estimates improves the constraints, when combined with a *Planck* CMB prior, by a factor of approximately 1.5 to $\Delta w_0 = 0.094$ and $\Delta w_a = 0.318$. A WFMOS-like BAO experiment provides a narrow, but highly degenerate ellipse in the (w_0, w_a) plane. This is due to the BAO experiment mainly constraining $w(z)$ at the redshift of the nearest redshift bin (in this case $z = 1.0$). Interestingly the BAO degeneracy is in a similar direction to the CMB degeneracy, presumably because a

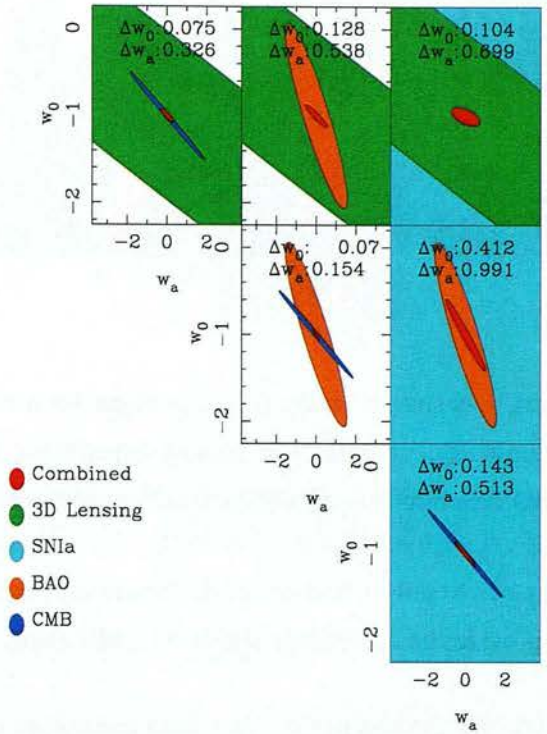

Figure 3.25: The combined marginal constraints in the (w_0, w_a) plane for two pairs of experiments. The experiments are a darkCAM lensing experiment and a CMB 14-month *Planck* experiment, a BAO WFMOS experiment and a SNIa *SNAP* experiment. Note that only the SNIa analysis contains terms for systematic effects. See Section 3.8 for details.

similar geometric effect is being measured. Finally, the geometric test has a large degeneracy in this plane, but one which is different from the other experiments. The combination of pairs of experiments is very interesting. The combination of the geometric test and CMB puts very strong constraints on the dark energy equation of state and its evolution, reducing the uncertainty to $\Delta w_0 = 0.075$ and $\Delta w_a = 0.326$. The geometric test and SNIa yields $\Delta w_0 = 0.104$ and $\Delta w_a = 0.699$ while the geometric test and BAO yields $\Delta w_0 = 0.128$ and $\Delta w_a = 0.538$. This provides three cross-checks with similar accuracy. Looking at the dependency of each method, it can be seen that both the geometric test, BAO and SNIa are all dependent on the geometry of the Universe, and so should give the same result, assuming that the w_0–w_a parameterisation is valid. The CMB combines geometry with evolution of the potential field, particularly in the ISW effect.

Looking at the other possible combinations without lensing it can be see that there is a similar sensitivity to dark energy. The CMB and BAO combination results in low marginal errors due to the high pivot redshift for the BAO experiment, which intersects with the CMB constraint.

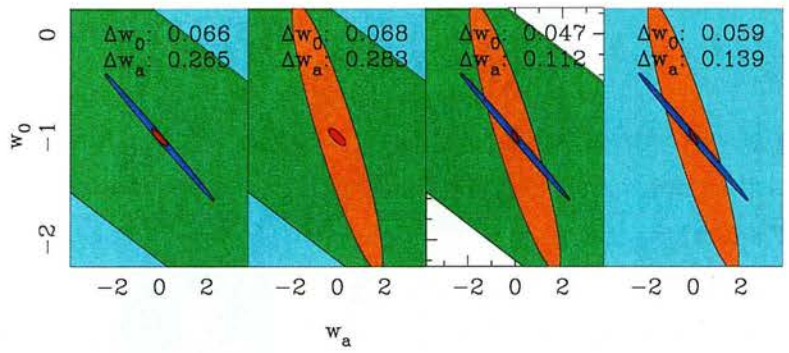

Figure 3.26: The marginal constraints in the (w_0, w_a) plane for a combination of any three of the dark energy experiments. A darkCAM lensing experiment, CMB 14-month *Planck* experiment, BAO WFMOS experiment and a SNIa *SNAP* experiment.

The similar degeneracies between the CMB and SNIa constraints result in larger uncertainties. Finally BAO and SNIa provides an uncertainly similar to CMB alone.

From this study, I conclude that the best pair combinations come from combining the geometric test with any of CMB, BAO or SNIa experiments, with $\Delta w_0 \sim 0.10$ and $\Delta w_a \sim 0.50$, and also the BAO and CMB combination. Multiple combinations will also allow a degree of cross-checking for consistency. Other combinations are a factor of up to 5 times poorer due to similar degeneracies between w_0 and w_a. Combining three experiments in Figure 3.26 it can again be seen that the strongest measurement of (w_0, w_a) comes from combining the geometric lensing analysis with any combination of two other experiments. In particular the geometric test, CMB and BAO can push the uncertainty on w_0 and w_a down to $\Delta w_0 = 0.047$ and $\Delta w_a = 0.112$. Adding the SNIa results to this makes a small difference (see Figure 3.27, but again recall that the SNIa is the only estimate to contain systematic effects).

3.10.5 Complementary Figures of Merit and Pivot Redshifts

The figure of merit and pivot redshift information can be represented as in Figure 3.28 so that both values can be seen simultaneously. The Figure shows a number of broad characteristics. As more experiments are added in combination both the pivot redshift converges to one mean value and the figure of merit decreases. The geometric test constraint forces the pivot redshift to lower values due to its unique degeneracy whilst the BAO constraint forces the pivot redshift to higher values. It is also evident that the CMB constraint is not necessary for a low figure of merit (for example LS). This Figure also shows how different combinations of surveys can

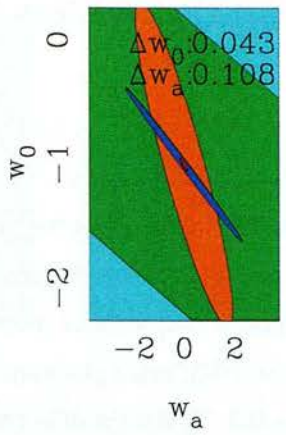

Figure 3.27: The marginal constraints in the (w_0, w_a) plane for a darkCAM lensing experiment and a CMB 14-month *Planck* experiment, a BAO WFMOS experiment and a SNIa *SNAP* experiment.

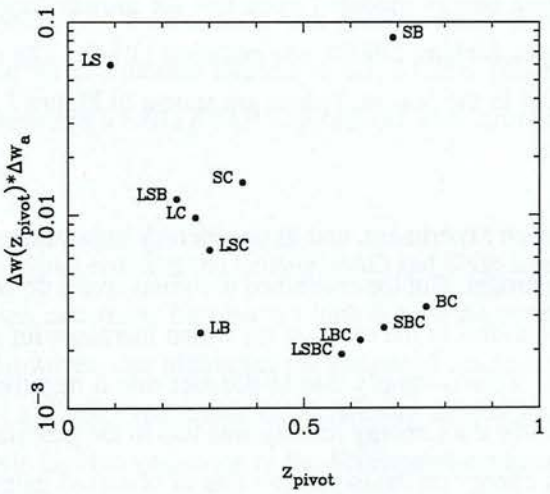

Figure 3.28: The figure of merit and pivot redshift for various experimental combinations. The combinations are labelled as L=Lensing, B=BAO, S=SNIa, C=CMB. Combinations of letters represent combinations of experiments.

probe dark energy at significantly different redshifts. For example the BC and LSC combinations both have a similar figure of merit with the BC combination $z_{\rm pivot} = 0.76$ and the LB combination $z_{\rm pivot} = 0.28$.

3.10.6 The Effect of Changing the Fiducial Dark Energy Model

The assumed fiducial cosmology has so far been a ΛCDM cosmology in which any derivatives in the Fisher matrix calculations have been about $w_0 = -1.0$ and $w_a = 0.0$ for the dark energy equation of state parameters. The effect of altering this assumption is investigated here. Here two alternative extreme dark energy models are considered which are just allowable by present constraints: a SUGRA (Super Gravity) model proposed by Weller & Albrecht (2002) represented by $w_0 = -0.8$ and $w_a = +0.3$; and a phantom model proposed by Caldwell et al. (2003) with $w_0 = -1.2$ and $w_a = -0.3$. To test the effect of changing our default dark energy model the Fisher analysis is re-run with derivatives about these parameter values.

As well as changing the point in parameter space about which the signal ratio is expanded in the Fisher matrix calculations the assumed fiducial dark energy model also affects the SIS to NFW scaling as a function of redshift and mass, as shown in Figure 3.6. It also affects the number density distribution of haloes as a function of redshift and mass given by equation (3.57), when extending to arbitrary dark energy models I exchange the growth factor in equation (3.63) to the one given in Linder & Jenkins (2003), see equation (1.84). The effects of changing the default dark energy model in the (w_0, w_a) plane are shown in Figure 3.29, fully marginalizing over all other parameters.

The marginal errors for each experiment, and its degeneracy in parameter space does indeed depend on the dark energy model. But the combined marginal errors do not significantly change. The main difference is manifest in the error on w_a which increases for all methods as its value becomes more negative. This is simply due to the fact that a negative w_a represents a dark energy scenario in which the dark energy density was less in the past (increasing in the future); so that the effect of dark energy on the expansion rate of observed galaxies (in the past) is less in these scenarios (and similarly the opposite effect for a positive w_a).

3.10.7 The Effect of Assuming Flatness

Figure 3.30 shows the same set of parameters as Figure 3.23, but this time assuming spatial flatness. Again many of the largest degeneracies in each of the experiments remain. The insensitivity of the geometric test to w_a can still be seen, rendering it nicely orthogonal to the other experiments. Comparing Figure 3.23 and Figure 3.30 it is clear that the assumption of

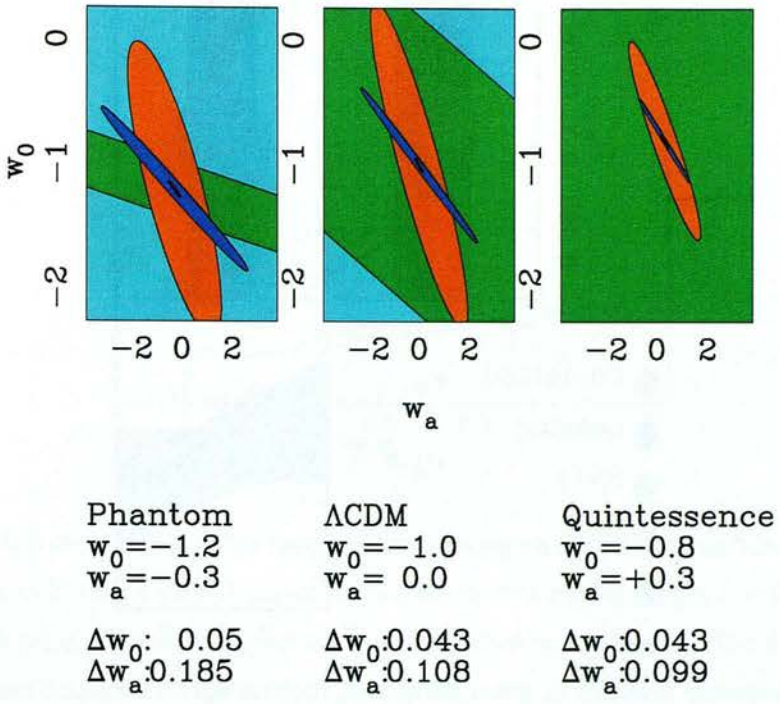

Figure 3.29: The dependence on the assumed dark energy model in the (w_0, w_a) plane, for a 10,000 square degree survey to a median depth $z = 0.7$, a CMB 14-year *Planck* experiment, a BAO WFMOS experiment and a SNIa *SNAP* experiment. The errors quoted are marginalized over all other parameters.

flatness improves the marginal errors of the lensing, BAO and SNIa significantly, however since the CMB experiment itself constrains flatness to a high degree the overall combined constraints are broadly the same. However, this highlights the danger of assuming flatness, given that the marginal errors without a CMB experiment are drastically altered by this assumption. Since some dark energy models involve variations to the Friedmann equation in non-flat geometries (e.g. Dvali & Turner, 2003) it is prudent to marginalize over spatially curved models.

3.10.8 The Effect of Photometric Redshift Outliers

In any weak lensing photometric redshift survey there will be a sample of imaged galaxies that will not have photometric redshifts assigned, usually due to several classes of objects for which determining a photometric redshift is difficult. The effect of such 'outliers' is investigated here by assuming a population within the survey $p2$ that have photometric redshifts $\sigma_z^{p2}(z) = 0.5$, that is they have practically no redshift information. There are two ways in which such a pop-

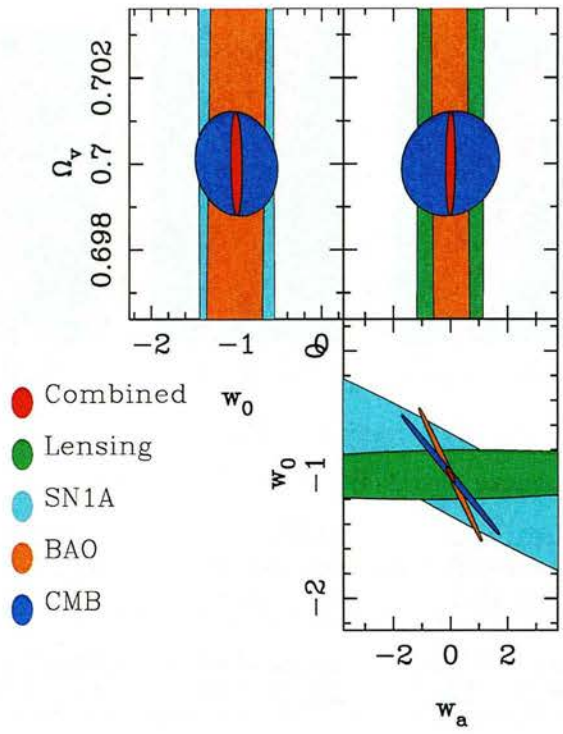

Figure 3.30: Two-parameter, 1-σ (68.3% confidence) likelihood contours for geometric parameters for a 10,000 square degree lensing survey to a median depth of $z_m = 0.7$, a CMB 14-month *Planck* experiment, a WFMOS BAO experiment and a *SNAP* SNIa experiment, assuming spatial flatness with $\Omega_m + \Omega_{de} = 1$.

ulation can be used, either they are included in the sample of galaxies analysed, or discarded.

If they are used then either they can be treated as a distinct and separate population, on which separate analysis can be performed. Or, they can be incorporated into a single population with a degraded photometric redshift, the effective redshift error distribution at a particular redshift z can be modelled by the sum of two Gaussian distributions, with errors $\sigma_z^{p1}(z)$ and $\sigma_z^{p2}(z)$, the relative amplitudes of the Gaussians constrained so that $A^{p1} + A^{p2} = 1$. Such a sum of Gaussians can be accurately modelled as an effective Gaussian, see Blake & Bridle (2005), with an effective width $\sigma_{eff} = \sqrt{A^{p1}[\sigma_z^{p1}(z)]^2 + A^{p2}[\sigma_z^{p2}(z)]^2}$. I investigated varying the relative amplitudes of two Gaussians with $\sigma_z^{p1}(z) = \sigma_z(z)$, the original photometric redshift error from equation (3.66) and $\sigma_z^{p2}(z) = 0.5$. Figure 3.31 shows the effect of varying the amplitude of the outlying sample, combined with a 14-month *Planck* prior and either using two separate populations or a single effective population.

The second possibility, that of discarding the outlying sample is investigated by simply reduc-

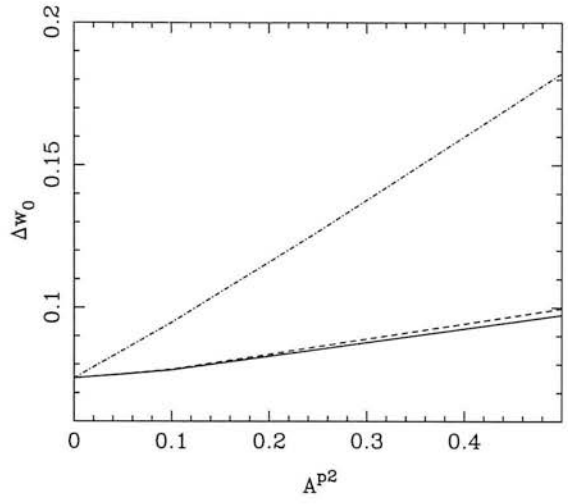

Figure 3.31: The dependence of the marginal error on w_0 on the relative abundance of outliers with a $\sigma_z^{p2}(z) = 0.5$ for a 10,000 square degree survey to a median depth $z = 0.7$, with a 14-month *Planck* prior. The solid line treats the two populations as distinct. The dot-dashed line incorporates the outliers with the original population using an effective Gaussian. The dashed line discards the outlying sample of galaxies.

ing the surface number density by $n_0 \rightarrow (1 - A^{p2})n_0$, this is also shown in Figure 3.31 as the dashed line.

All the methods for dealing with the outliers result in an increase in the marginal error on w_0. The effective Gaussian method has the effect of decreasing the number of redshift bins in the survey that can be used while retaining the surface number density, thus decreasing the signal. By discarding the outliers the number of redshift bins is retained while the surface number density is uniformly degraded. This shows that the signal is more dependent on the number of redshift bins, than the number density and that the strategy for dealing with outliers will be an important issue in future surveys. As expected using all the galaxies has the smallest effect on the marginal error, by treating the outliers as a separate population the marginal error is less than when they are discarded.

3.11 Additional Systematic Effects for Lensing

In this Section some potential systematic effects for weak lensing will be considered. To realize a $\Delta w \approx 0.01$ measurement from shear ratios not only are large enough surveys needed, but

systematics need to be controlled in a weak lensing survey to a high level. This will require controlling the systematics in the measurement of lens shear to $\Delta\gamma \sim 10^{-5}$.

3.11.1 Image Shear Analysis

The current generation of lensing surveys, with telescopes not specifically designed for lensing, induce 10% distortions, which can be corrected down to a net systematic of 0.01% ($\Delta\gamma \sim 10^{-4}$; Heymans et al., 2006). There has been extensive work into methods that can both diagnose and remove systematic errors from both intrinsic galaxy alignments (Hirata et al., 2004) and shear calibration errors. Mandelbaum et al. (2005) use a geometric test to diagnose systematic errors in the Sloan Digital Sky Survey (SDSS).

3.11.2 Strong Lensing Effects

There is a systematic effect in the strong lensing régime, where the reduced shear g_i, defined as

$$g_i = \frac{\gamma_i}{1-\kappa_i} \tag{3.131}$$

is measured from galaxy ellipticities. The ratio R_{ij} now becomes

$$R_{ij} = \frac{g_i}{g_j} = \frac{\gamma_i(1-\kappa_j)}{\gamma_j(1-\kappa_i)} \tag{3.132}$$

which, for the mildly non-linear lensing régime can be approximated as

$$R_{ij} \approx \frac{\gamma_i}{\gamma_j}(1+\kappa_i-\kappa_j) \tag{3.133}$$

Furthermore for a SIS $\kappa \approx \gamma$. This was numerically tested in the Fisher matrix calculations, using observable clusters, and the amplitude of the correction was found to be $\max(\kappa_\mathrm{i}-\kappa_\mathrm{j}) \sim 0.15$ and $\mathrm{mean}(\kappa_\mathrm{i}-\kappa_\mathrm{j}) \sim 1.5\times10^{-3}$. This numerical analysis implicitly assumes a radius of 1 arcmin from equation (3.47), which is relatively narrow: tangential shear can be measured out to radii of at least 200 arcseconds see Gray et al. 2004. The largest source of this systematic error will be from the largest clusters, those producing the largest convergence, and as shown in Section 3.7 the majority of the dark energy signal comes from clusters of intermediate mass for which this systematic effect is expected to be smaller.

Alternatively, one can construct a statistic which eliminates the mass-dependence of $\gamma/(1-\kappa)$, such as the three-point statistic suggested by Gautret, Fort & Mellier (2000). This could be

applied in the strong-lensing régime, again independent of the lens strength, and combined with the two-point geometric ratio test in the weaker lensing régime.

3.11.3 Cluster Substructure

A further potential systematic is that arising from cluster sub-structure, which I assume is averaged over. One promising avenue which may yield information on sub-structure is flexion (see Bacon et al., 2005). In the low signal-to-noise régime (low galaxy number counts or low cluster mass) in which a mass model may have to be assumed for a cosmological signal to be extracted then this systematic source of error will become important and the mass model will need to be accurately reproduced. However, in the high signal-to-noise régime where the number of available galaxies is such that ratio of the shears from the data can simply be taken this systematic source of error will not affect the analysis.

3.11.4 CMB Lensing

When combining the shear ratio analysis with CMB measurements it has been assumed that the weak lensing of the CMB by large scale structure and galaxy clusters can be ignored. Since the shear ratios do not contain any information about structure, there can be no correlation due to this. There may, however, be some correlation between lensing of the CMB and the noise term in the shear ratio method. This is left for a future investigation, see Chapter 7.

3.12 Summary

In this Chapter I have set out a new method for the analysis of 3D weak lensing information for measuring the dark energy equation of state, based on the measurement of shear ratios around individual galaxy groups and clusters. The geometric test is insensitive to the growth of structure, but sensitive to the geometry of the Universe, via the matter and dark energy density and the dark energy equation of state. This approach allows one to apply the method to individual objects, rather than requiring the measurement of some other statistic such as the galaxy-shear cross-correlation function which may be noisy for small data-sets. The down-side is that the method is now contaminated by structure along the line of sight, which can be

overcome by using many independent lines of sight.

It should be emphasised that the Fisher matrix framework used in this thesis may result in overly optimistic constraints. Since the errors are calculated by expanding about a fiducial point in parameter space any higher order effects that may change the shape of the likelihood surface cannot be taken into account. The effect of varying the fiducial dark energy model, in Section 3.10.6, demonstrates that the errors are sensitive to the choice of the fiducial model. A concrete example of higher order likelihood effects can be seen in a 3D cosmic shear analysis by comparing Fisher matrix calculations of the (σ_8, Ω_m) plane in Chapter 4 (predicting an ellipse) with the measured constraints from data in Chapter 5 which measures an extended curved constraint. These effects can be investigated by large simulations or by a Monte-Carlo type exploration of the likelihood surface, I leave such investigations for future work, see Chapter 7.

Of the parameters which govern the geometry of the Universe, or more properly the photon distance-redshift relation, the shear ratio is most sensitive to a constant dark energy equation of state, w_0, and very insensitive to evolution, parameterised here by w_a. This can be understood as due to the shear ratios being sensitive only to the change in shape of the shear signal as a function of redshift. As w_a parameterises the high-redshift effect of the dark energy equation of state, its effects are 'renormalised' away. This behaviour is very different to other probes of dark energy, and so helps to break parameter degeneracies when combined with other probes.

To account for many of the sources of uncertainty in the method, I have developed a halo decomposition analysis of the lensing dark matter distribution to model the signal from dark matter haloes over a range of mass scales and redshifts. The effects of shot-noise due to the random intrinsic orientation of each galaxy, photometric redshift errors and the contribution of large-scale structure lensing to the error budget were also included. A realistic model for the photometric redshift error was investigated in detail, based on studies of the COMBO-17 dataset, as a function of redshift, number of imaging bands and limiting magnitude. The effect of a bias in the calibration and distribution of photometric redshifts with spectroscopic redshifts was also studied, and I find that approximately 10^4 galaxies with spectroscopic redshifts are required to control calibration issues. The limitations of observing the shear signal from the ground and space are also discussed, and I argue that without adaptive optics ground-based lensing studies are seeing limited, suggesting that it will be difficult to use galaxies beyond $z = 1.5$.

The halo decomposition analysis of the dark matter lenses allowed a probe into the origin of the shear signal in different types of survey, taking a 4-metre telescope with a 2 square degree field of view as a default survey. These results can be scaled to any other telescope parameters.

For targeted observations, where the time-limitation translates into the number of clusters and groups one can observe to a given depth, I have shown that only around 60 of the largest clusters in a celestial hemisphere are required to constrain w_0 to around $\Delta w_0 \sim 0.50$, marginalizing over all other parameters, including w_a, a factor of 2 improvement on 4-year *WMAP* given a marginalization over w_a. To achieve a higher accuracy requires the imaging of an unfeasible number of haloes, and instead one should turn to a wide-field imaging and photometric redshift survey. For a 4-meter class telescope with a 2 degree field of view with a 10,000 square degree, 5-band photometric redshift survey with median redshift $z_m = 0.7$ ($R = 23.8$), one can expect to reach an accuracy of $\Delta w_0 \sim 0.07$, again marginalizing over all other parameters including w_a. These results can be easily rescaled to other telescope types, and survey strategies.

The halo decomposition allows for an investigation into where the main signal comes from in both the targeted and surveying modes. In both cases a significant fraction of the signal comes from the largest hundred clusters in each survey, reaching a sensitivity of $\Delta w_0 \sim 0.5$, however the majority of the signal comes from the numerous ($\sim 10^{5-6}$) $M > 10^{14} M_\odot$ haloes which can push the expected errors down to $\Delta w_0 \sim 0.07$.

Having determined where the majority of the dark energy signal will come from in a geometric test experiment, the optimisation of such a survey was then investigated. When combined with the expected results from the *Planck* Surveyor experiment I find that for the fiducial telescope for a fixed-time survey, going shallower ($z_m < 0.7$) over a wider area decreases the accuracy due to the drop in the number of available background sources and corresponding increase in shot-noise. Going deeper ($z_m > 0.7$) over a smaller area increases the clustering noise, since there are now fewer clusters to average over.

The effect of varying the number of imaging bands, to increase or decrease the photometric accuracy, was also studied. I find that when combined with expected 14-month *Planck* results an increase from 5, 9 or 17 optical bands makes little difference to the optimal survey. The reason for this insensitivity to higher accuracy photometric redshifts is due to the integral nature of the lensing effect, and the effects of intersection when combined with another data-set. However decreasing the number of bands is expected to have a strong effect on the accuracy of the lensing survey as redshift information is lost.

The dark energy parameters w_0 and w_a can be combined to give an uncertainty on $w(z) = w_0 + w_a z/(1+z)$, at some optimal redshift. This combination helps distinguish where the survey is most sensitive to the dark energy equation of state. In the case of our optimal lensing survey this is at $z = 0.27$ with $\Delta w(z = 0.27) = 0.0298$. Again, the reason for the low-redshift sensitivity to $w(z)$ is due to the insensitivity of the geometric test to w_a.

Having optimised the lensing survey for the geometric test in combination with the expected results from the CMB, the effect on the full set of cosmological parameters for the CMB and lensing was investigated. The geometric test constrains a narrow sheet in the $(\Omega_m, \Omega_{de}, w_0, w_a)$ parameter-space, which is nicely orthogonal to the CMB parameter constraints. Here I have shown that the CMB mainly constrains the curvature of the model, while the geometric test constrains w_0, and the combination constrain w_a.

The predicted geometric test constraints were compared and combined with the expected results from an BAO experiment, such as proposed for WFMOS, and a SNIa survey, such as that proposed for *SNAP*. Here all of the surveys (lensing, CMB, BAO and SNIa) have been put on an equal footing, using the same curved background cosmology and the same dark energy model parameterisation. I find that the degeneracies in the geometric test, in particular the insensitivity to w_a, are nicely orthogonal to all these other probes. Combining the geometric test with either CMB, BAO or SNIa will yield accuracies of a $\Delta w_0 \approx 0.10$ and $\Delta w_a \approx 0.5$, and can be compared for systematics. However, combining any other pair experiments without the geometric test can lead to a factor of 5 increase in error on w_0, and factor of 2 in w_a. An optimal combination is the geometric test, with the CMB *Planck* and BAO WFMOS experiments, yielding an expected accuracy of $\Delta w_0 = 0.047$ and $\Delta w_a = 0.11$.

Finally some of the potential systematic effects which could affect the predicted accuracy of lensing were discussed.

In summary, the prospects of accurately measuring the dark energy equation of state and its evolution to high accuracy over the next decade are very good using the geometric test.

In the next Chapter a different method for using the 3D weak lensing information will be discussed in detail, via a two-point spectral analysis (see Heavens et al., 2006 and Castro et al., 2005).

Chapter 4

The 3D Cosmic Shear Spectral Test

In this Chapter I present the 3D cosmic shear spectral test (spectral test). In particular parameter estimation forecasts for present and future 3D cosmic shear surveys. This is distinct from the geometric test in that it uses the shear and redshift information from every galaxy within a survey. This Chapter will formally introduce the method and then follow a similar layout to Chapter 3. This work is also presented in Heavens et al. (2006).

I will demonstrate in particular that, in conjunction with results from CMB experiments, the properties of dark energy can be estimated with very high precision with large-scale, fully 3D weak lensing surveys.

An optimisation of both the median redshift and photometric redshift error of an arbitrary experiment using the spectral test to measure the dark energy equation of state is presented.

In addition the spectral tests constraints will be compared and combined with the cosmological and dark energy parameters measured from planned BAO and SNIa experiments. I will also show how these results can be scaled to other telescopes and survey designs.

4.1 Introduction

As shown in Chapter 1 dark energy affects both the distance-redshift relation and the growth of structure in the Universe. The spectral test is a very attractive proposition for studying dark energy, as it is sensitive to both of these effects, and, equally importantly, the physics of weak lensing is well understood. A key part of this is that it is sensitive to the distribution of matter in the Universe, regardless of its form.

In this Chapter I will investigate analysing the shear and redshift information of galaxies as a fully 3D shear field. The statistical properties of the shear pattern are influenced by many cosmological parameters, including $w(z)$. This Chapter extends the analysis of Heavens (2003) to small-angle surveys as well as computing the expected marginal errors on w_0 and w_a, using a Fisher matrix approach, see Section 3.2. Optimisation issues such as of depth vs. area, and the number of photometric bands which should be used to determine the dark energy properties as accurately as possible are investigated. The main focus of this Chapter is in computing the expected statistical errors.

The layout of this Chapter is as follows. In Section 4.2 I will detail the transform method used and compute the covariance matrix of the transform coefficients. In Section 4.3 the method for calculating the expected statistical errors on parameters is outlined. In Section 4.4 the survey design formalism is presented, and how the results can be scale to other surveys. In Section 4.5 an optimisation of survey design is presented and the parameter error forecasts are outlined in Section 4.6 where the synergy of the spectral test with other dark energy probes and future surveys are considered.

4.2 Method

The observable quantities used are the estimates of the shear field at locations in three dimensions. The estimates of the complex shear come from the shape and orientation of galaxies, where the radial distance is obtained approximately by using photometric redshift estimates obtained from observations through several or many filters.

Heavens (2003) introduced the idea of 3D weak lensing analysis in harmonic space as a statistical tool. In Castro, Heavens and Kitching (2005), the subject was formally developed and the

power spectrum of 3D weak lensing shear was found. This Chapter will consider the flat-sky limit including the non-linear evolution of the power spectrum. I will consider a transform of the 3D shear field in spin-weight spherical harmonics and spherical Bessel functions. This is a very natural expansion for the shear field, as the complex shear γ is a spin-weight 2 object, as are the spin-weight 2 spherical harmonics: under a local rotation of the coordinate system by angle ψ, γ changes to $\gamma e^{2i\psi}$, see Section 2.2.5. The spherical harmonic transform of a spin-weight s field ${}_sf(\mathbf{r})$ is defined here by

$$ {}_sf_{\ell m}(k) \equiv \sqrt{\frac{2}{\pi}} \int d^3\mathbf{r}\, {}_sf(\mathbf{r})\, k j_\ell(kr)\, {}_sY_\ell^{m*}(\hat{\mathbf{n}}) \tag{4.1} $$

where $j_\ell(z)$ is a spherical Bessel function, ${}_sY_\ell^m$ is a spin-weight s spherical harmonic, k is a radial wavenumber, ℓ is a positive integer, $m = -\ell, \ldots \ell$ and $\hat{\mathbf{n}}$ represents the direction (θ, φ). For $s = 0$ the spin-weight spherical harmonics are the usual spherical harmonics Y_ℓ^m, and this is the appropriate spherical expansion of a scalar field. Note the presence here of a benign factor of k, to agree with the notation of Castro, Heavens and Kitching (2005). The motivation for using spherical coordinates is manyfold: firstly the selection function for a survey can often be separated into an angular (sky coverage) part and a radial component; secondly the errors in photometric redshifts introduce purely radial errors in the positions of the source galaxies; thirdly, in the Born approximation, the lensing effect is an integral effect along the (radial) line of sight. The motivation in flat space for using products of spherical Bessel functions and spherical harmonics is that, as eigenfunctions of the Laplacian operator, it is easy to relate the expansion coefficients of the gravitational potential to those of the density field. Similar considerations led Heavens and Taylor (1995) (see also Fisher et al., 1994; Tadros et al., 1999; Percival et al., 2004) to expand the large-scale structure of galaxies in spherical Bessel functions and spherical harmonics. Since cosmic shear depends on the gravitational potential, the use of this basis allows us to relate the expansion of the shear field to the expansion of the mass density field. The properties of the latter depend in a calculable way on cosmological parameters, so this opens up the possibility of using 3D weak shear to estimate these quantities.

For surveys with large opening angles on the sky, a full expansion in spherical Bessel functions and spherical harmonics is the natural choice. Such an expansion is generally applicable, but for small-angle surveys whose signal is dominated by high ℓ-modes, the spherical harmonics are cumbersome and their accurate computation can present problems. For such surveys, the spherical harmonics can be approximated as sums of exponentials, as detailed in Appendix A of Santos et al. (2003).

Here the flat-sky expansion is used, which for a scalar ($s = 0$) field reads

$$f(k, \boldsymbol{\ell}) \equiv \sqrt{\frac{2}{\pi}} \int d^3\mathbf{r} f(\mathbf{r}) k j_\ell(kr) \exp(-i\boldsymbol{\ell} \cdot \boldsymbol{\theta}), \tag{4.2}$$

where $\boldsymbol{\ell}$ is a 2D angular wavenumber and k a radial wavenumber. In the spherical Bessel function, $\ell = |\boldsymbol{\ell}|$; ℓ is necessarily an integer, but since $\ell \gg 1$ is assumed enforcing integer ℓ is a minor approximation. Note that this is a fully 3D expansion of the shear field and a flat universe is assumed except where indicated. An alternative approach, to include least some 3D information, is what is referred to as tomography, where the shear pattern of galaxies is analysed in shells, based on their photometric redshifts (Hu, 1999; Hu, 2002; Jain and Taylor, 2003; Takada and White, 2004). It is however evident that the binning process loses at least some information, and it is not necessary.

The inverse transform in the flat-sky approximation is

$$f(\mathbf{r}) = \sqrt{\frac{2}{\pi}} \int \frac{d^2\boldsymbol{\ell}}{(2\pi)^2} dk\, k j_\ell(kr) \exp(i\boldsymbol{\ell}.\boldsymbol{\theta}) f(k, \boldsymbol{\ell}). \tag{4.3}$$

The coefficients of the expansion in the two systems are related by a generalisation of equation (A13) in Santos et al. (2003):

$$f(k, \boldsymbol{\ell}) = \sqrt{\frac{2\pi}{\ell}} \sum_m i^{-m} f_{\ell m}(k) \exp(im\phi_\ell) \tag{4.4}$$

where the small angle survey is centred at the pole of the coordinate system, and the 2D transverse wavevector is $\boldsymbol{\ell} = (\ell \cos\phi_\ell, \ell \sin\phi_\ell)$. The covariances of the flat-sky coefficients are related to the power spectrum of f by

$$\langle f(k, \boldsymbol{\ell}) f^*(k', \boldsymbol{\ell}') \rangle = (2\pi)^2 P_f(k)\, \delta^D(k - k') \delta^D(\boldsymbol{\ell} - \boldsymbol{\ell}') \tag{4.5}$$

where δ^D is the Dirac delta function.

The remainder of this Section will outline how the components of the 3D shear field are transformed to produce a set of transform coefficients as a function of $(k, \boldsymbol{\ell})$. These data will depend on cosmological parameters, and can be used in a likelihood analysis to constrain those parameters.

Transformation of Shear Fields

The weak lensing shear components that are transformed are $\gamma_1(\mathbf{r})$ and $\gamma_2(\mathbf{r})$, which are related to the lensing potential $\phi(\mathbf{r})$ through (e.g. Bartelmann and Schneider, 2001)

$$\gamma_1 = \frac{1}{2}\left(\phi_{11} - \phi_{22}\right); \qquad \gamma_2 = \phi_{12} \tag{4.6}$$

where $\phi_{ij} \equiv \partial^2\phi/\partial\theta_i\partial\theta_j$. ϕ itself is dependent on cosmological parameters through its relation to the mass density field (see Section 4.2.3). I will return to this dependence later. For a large-area survey, it is a measure of the shears with respect to axes based on the spherical coordinate system, in which case the complex shear $\gamma \equiv \gamma_1 + i\gamma_2$ is the second edth derivative of ϕ, see Section 2.2.5:

$$\gamma(\mathbf{r}) = \frac{1}{2}\,\eth\,\eth\,\phi(\mathbf{r}) \tag{4.7}$$

(Castro, Heavens and Kitching, 2005). In the flat-sky limit, $\eth \rightarrow -(\partial_x + i\partial_y)$, where the $\partial_{x,y} \equiv \partial/\partial\theta_{x,y}$. Expanding the lensing potential in terms of spherical Bessel functions and exponential functions, as in equation (4.3), it can be seen that it is natural to expand the complex shear field in terms of $\eth\,\eth\exp(-i\boldsymbol{\ell}.\boldsymbol{\theta}) = \boldsymbol{\ell}^2 X_{\boldsymbol{\ell}}\exp(-i\boldsymbol{\ell}.\boldsymbol{\theta})$, where

$$X_{\boldsymbol{\ell}} \equiv \frac{(\ell_y^2 - \ell_x^2) + 2i\ell_x\ell_y}{\boldsymbol{\ell}^2}. \tag{4.8}$$

The $\boldsymbol{\ell}^2$ in the denominator is included for convenience, so the inverse transform kernel is just $\sqrt{2/\pi}k\,j_\ell(kr)X^*_{\boldsymbol{\ell}}\exp(i\boldsymbol{\ell}.\boldsymbol{\theta}_g)$.

Fiducial Cosmology

An immediate issue to address is which radial coordinate to use in the spherical Bessel function. The observed quantities are the estimated redshifts of the sources, and two things are needed: one is to translate these into radial distances; the second is to account for the error in the estimation of the redshifts. For the former, a fiducial set of cosmological parameters is chosen to define a transformation $r^0(z_p)$ from the photometric redshift estimate z_p to a radial coordinate r^0. For this thesis, the fiducial model the concordance model (Spergel et al., 2006) is chosen with $\Omega_m = 0.27$, $\Omega_b = 0.04$, $\Omega_{de} = 0.73$, $\sigma_8 = 0.8$, $h = 0.71$, $w_0 = -1$ and $w_a = 0$ where the variables are the matter, baryon, dark energy density parameters, Hubble constant in units of 100 $\mathrm{km\,s^{-1}\,Mpc^{-1}}$ and the dark energy equation of state parameters respectively. The equation of state of dark energy is modelled in terms of scale factor a by, see Section 1.8.5,

$$w(a) = w + w_a(1 - a) \tag{4.9}$$

(Chevallier and Polarski, 2001; Linder, 2003) where $a(z) = (1+z)^{-1}$ is the cosmic scale factor normalised to unity at the present epoch.

The the scalar spectral index $n_s = 1$ and its running $\alpha_n = 0$ are also included. For the CMB Fisher calculations I also include the tensor to scalar ratio $r = 0.01$ and the optical depth to the surface of last scattering $\tau = 0.09$.

4.2.1 Transformation

The lensing potential is defined everywhere, but it is only sampled at the locations of galaxies, so it is natural to make a transformation of this point process, summing over galaxies rather than integrating over space. The estimate of the transform is thus defined as

$$\hat{\gamma}(k,\boldsymbol{\ell}) = \sqrt{\frac{2}{\pi}} \sum_g \gamma(\mathbf{r}) k j_\ell(kr_g^0) \exp(-i\boldsymbol{\ell}.\boldsymbol{\theta}_g) W(r_g^0) \tag{4.10}$$

where $W(r)$ is an arbitrary weight function, and $(r_g^0, \boldsymbol{\theta}_g)$ are the coordinates of galaxy g.

Note the appearance of two distances in the transform, r and r^0 (at each galaxy g): the main application of this study is to determine cosmological parameters, which affects the $r(z)$ relation. The shear field is the shear field at the *actual* coordinate $\mathbf{r}_g$ of the galaxy, and this depends on the true cosmological parameters, whereas the expansion (and weighting) is done with the fiducial model parameters. This distinction was neglected in Heavens (2003) and leads to an underestimate of the errors on the dark energy equation of state in that paper; the error estimates for the power spectrum in that paper are unaffected by this error.

Writing the number density of source galaxies $n(\mathbf{r})$ as the sum of a set of delta functions, it can be seen that

$$\hat{\gamma}(k,\boldsymbol{\ell}) = \sqrt{\frac{2}{\pi}} \int d^3\mathbf{r}\, n(\mathbf{r}) \gamma(\mathbf{r})\, k\, j_\ell(kr^0) \exp(-i\boldsymbol{\ell}\cdot\boldsymbol{\theta}) W^0, \tag{4.11}$$

where $W^0 = W(r^0)$. Note that in the high-ℓ limit these are also the (minus) coefficients of the expansion of the convergence field κ (Castro, Heavens and Kitching, 2005). This has an expectation value which is obtained by replacing $n(\mathbf{r})$ by the mean density of the source galaxies, $\bar{n}(r)$. Here it is assumed that selection effects are uniform across the survey so there is no angular dependence. Thus the $\hat{\gamma}$ are estimators of

$$\gamma(k,\boldsymbol{\ell}) \equiv \sqrt{\frac{2}{\pi}} \int d^3\mathbf{r}\, \bar{n}(r) \gamma(\mathbf{r})\, k j_\ell(kr^0) \exp(-i\boldsymbol{\ell}.\boldsymbol{\theta}) W^0. \tag{4.12}$$

The estimates will differ because of the discrete nature of the galaxies, which leads to shot noise, the photometric redshift errors, and the source clustering. For deep surveys, and with a radial smoothing arising from the photometric redshifts, source clustering can be safely ignored. The effects of photometric errors are included, but uncertainties in the photometric redshift distribution are ignored. In terms of the observable photometric redshift distribution of sources (all sky), $\bar{n}(r)d^3\mathbf{r} = \bar{n}_z(z_p)dz_p/4\pi$,

$$\gamma(k,\boldsymbol{\ell}) \equiv \sqrt{\frac{1}{8\pi^3}} \int dz_p\, d^2\boldsymbol{\theta}\, \bar{n}_z(z_p)\gamma(\mathbf{r})\, k j_\ell(kr^0) \exp(-i\boldsymbol{\ell}\cdot\boldsymbol{\theta}) W^0. \tag{4.13}$$

4.2.2 Photometric Redshift Uncertainty

Photometric redshift errors lead to a smoothing of the distribution in the radial direction. If the probability of the photometric redshift being z_p is denoted by $p(z_p|z)$, given that the true redshift is z, the mean of the expansion coefficients will be

$$\gamma(k,\boldsymbol{\ell}) \equiv \sqrt{\frac{1}{8\pi^3}} \int dz\, dz_p d^2\boldsymbol{\theta}\, p(z_p|z)\, \bar{n}_z(z_p)\gamma(\mathbf{r})\, k j_\ell(kr^0) \exp(-i\boldsymbol{\ell}\cdot\boldsymbol{\theta}) W^0. \tag{4.14}$$

Note that $p(z_p|z)$ is arbitrary; it will generally have a dispersion which depends on redshift, and can if desired include broad wings to account for a small percentage of catastrophic failures in the photometric redshift estimates. I will assume a Gaussian, with a z-dependent dispersion:

$$p(z_p|z) = \frac{1}{\sqrt{2\pi}\sigma_z(z)} \exp\left[\frac{-(z_p - z + z_{\rm bias})^2}{2\sigma_z^2(z)}\right]. \tag{4.15}$$

$z_{\rm bias}$ is a possible bias in the photometric redshift calibration, the effect of this on dark energy parameter uncertainties is discussed in Section 4.5.4. Strictly the shear is estimated at the actual radial coordinate of the galaxy, which may differ from $r(z)$ because of peculiar velocities. These issues, whose effect is small compared with current photometric redshift errors, can safely be ignored.

4.2.3 Relationship of $\gamma(k,\boldsymbol{\ell})$ to Cosmological Parameters

Equation (4.7) can now be substituted for $\gamma(\mathbf{r})$. The lensing potential ϕ is related to the peculiar gravitational potential Φ by a radial line-of-sight integral (e.g. Bartelmann and Schneider, 2001), see equation (2.52):

$$\phi(\mathbf{r}) = \frac{2}{c^2}\int_0^r dr' F_K(r,r')\Phi(\mathbf{r}'). \tag{4.16}$$

where $F_K(r,r') \equiv \{S_k(r-r')/[S_k(r)S_k(r')]\}$, and $S_k(r)d\psi$ is the dimensionless transverse comoving separation for points separated by an angle $d\psi$. The Robertson-Walker metric is defined in equation (1.21), and $S_k(r)$ is defined in equation (1.22). For a flat universe $F_K(r,r') = (1/r' - 1/r)$.

The peculiar gravitational potential is related to the overdensity field $\delta(\mathbf{r}) \equiv [\rho(\mathbf{r}) - \bar{\rho}]/\bar{\rho}$ by the comoving Poisson's equation

$$\nabla^2\Phi = \frac{3\Omega_m H_0^2}{2a(t)}\delta, \tag{4.17}$$

where Ω_m is the present-day matter density parameter, H_0 is the present Hubble constant and $a(t) = R(t)/R_0 = 1/(1+z)$ is the scale factor, see equation (1.20).

Note that δ itself is not a homogeneous field, because it evolves with time, and hence with distance from the observer through the light travel time. The subtleties of this are circumvented by defining at each epoch a homogeneous field by referring all field measurements to that time. Thus, for example, a power spectrum can be defined which is time-dependent, and hence r-dependent. This may seem a little strange, since we have transformed from $\mathbf{r}$ space. The transforms of the homogeneous fields will be denoted by $\delta(k,\boldsymbol{\ell};r)$ etc. The $\delta(k,\ell;r)$ describe the entire homogenous field at a given time $r(z[t])$ not a shell at a given distance r.

For high ℓ, the transforms of Φ and δ (referred to epoch t or equivalently r) are related simply by

$$\Phi(k,\boldsymbol{\ell};r) = -\frac{3\Omega_m H_0^2}{2k^2a(t)}\delta(k,\boldsymbol{\ell};r). \tag{4.18}$$

Inserting these definitions in equation (4.13) for $\gamma(k,\boldsymbol{\ell})$, the relationship between $\gamma(k,\boldsymbol{\ell})$ and the transform of δ can be found:

$$\begin{aligned}\gamma(k,\boldsymbol{\ell}) \;=\; & -\frac{3\Omega_m H_0^2}{2\pi^2c^2}\int_0^\infty dz dz_p p(z_p|z) \\ & \int d^2\boldsymbol{\theta}\, k j_\ell(kr^0)W^0\,\bar{n}_z(z_p)\,\exp(-i\boldsymbol{\ell}.\boldsymbol{\theta}) \\ & \int_0^r dr' a^{-1}(r')\,F_K(r,r') \\ & \int dk'\frac{d^2\boldsymbol{\ell}'}{(2\pi)^2}\,k' j_{\ell'}(k'r')\frac{\delta(k',\boldsymbol{\ell}';r')}{k'^2}\frac{X_{\boldsymbol{\ell}'}}{2}\exp(i\boldsymbol{\ell}'.\boldsymbol{\theta}).\end{aligned} \tag{4.19}$$

The denominator for the $X_{\boldsymbol{\ell}}$ factor is a result of transforming from the potential to the shear

field, see equation 4.7. Integration over $\boldsymbol{\theta}$ gives $(2\pi)^2\delta^D(\boldsymbol{\ell}-\boldsymbol{\ell}')$, so

$$\gamma(k,\boldsymbol{\ell}) = -\frac{3X_{\boldsymbol{\ell}}\Omega_m H_0^2}{4\pi^2 c^2} \int_0^\infty dz dz_p p(z_p|z)\bar{n}_z(z_p) k j_\ell(kr^0) W^0 \int_0^r dr' F_K(r,r')(1+z') \int dk'\, k' j_\ell(k'r')\, \frac{\delta(k',\boldsymbol{\ell};r')}{k'^2}. \tag{4.20}$$

This is a fundamental result of this Chapter. It establishes the connection between the (observable) 3D shear transform coefficients, and the underlying matter density fluctuations, whose properties are calculable from theory.

4.2.4 Covariance Matrix of $\gamma(k,\boldsymbol{\ell})$

The signal part of the covariance matrix of the $\gamma(k,\boldsymbol{\ell})$ is obtained from equation (4.20). For the covariance of the overdensity field coefficients, it is algebraically convenient to use the geometric mean of the power spectra P_δ, rather than the power spectrum evaluated at epochs corresponding to r or r'. Both of these could also be justified; note also that P_δ does not depend on $\boldsymbol{\ell}$ (Castro, Heavens and Kitching, 2005)

$$\langle \delta(k,\boldsymbol{\ell};r)\delta^*(k',\boldsymbol{\ell}';r')\rangle \simeq (2\pi)^2\sqrt{P_\delta(k;r)P_\delta(k';r')}\,\delta^D(k-k')\delta^D(\boldsymbol{\ell}-\boldsymbol{\ell}'). \tag{4.21}$$

The covariance matrix for the shear expansion coefficients is then

$$\langle \gamma(k,\boldsymbol{\ell})\gamma^*(k',\boldsymbol{\ell}')\rangle_S = Q_\ell(k,k')\,\delta^D(\boldsymbol{\ell}-\boldsymbol{\ell}') \tag{4.22}$$

where $Q_\ell(k,k')$ can be written as

$$Q_\ell(k,k') = \frac{9\Omega_m^2 H_0^4 |X_{\boldsymbol{\ell}}|^2}{4\pi^2 c^4} \int \frac{d\tilde{k}}{\tilde{k}^2} G_\ell(k,\tilde{k}) G_\ell(k',\tilde{k}) \tag{4.23}$$

where

$$G_\ell(k,\tilde{k}) \equiv k \int dz\, dz_p\, \bar{n}_z(z_p) W(z_p) p(z_p|z) U_\ell(r,\tilde{k}) j_\ell(kr^0) \tag{4.24}$$

and

$$U_\ell(r,k) \equiv \int_0^r d\tilde{r}\, \frac{F_K(r,\tilde{r})}{a(\tilde{r})} \sqrt{P_\delta(k;\tilde{r})}\, j_\ell(k\tilde{r}) \tag{4.25}$$

where $r = r(z)$ etc. Equation (4.22) is the second important result of this Chapter.

Figure 4.1 demonstrates the form of the signal covariance for a given ℓ-mode, using the fiducial cosmology and survey design described in Section 4.3. The Bessel functions have zero values

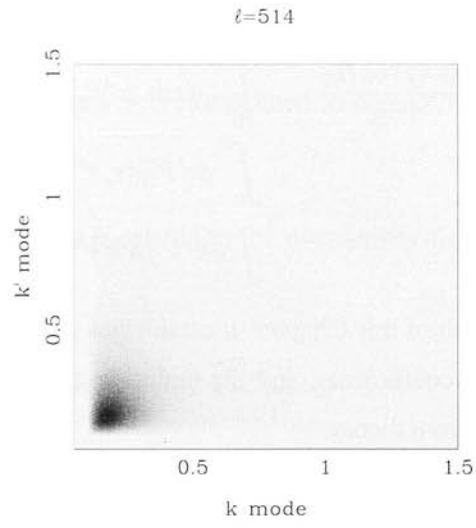

Figure 4.1: The form of the signal covariance matrix in the (k, k') plane for $\ell = 514$, using the fiducial cosmology. The survey parameters are a 5-band survey to a median redshift of $z_m = 0.7$ covering $10,000$ square degrees, see Section 4.3 for details. The k and ℓ resolutions and ranges are discussed in Section 4.4.2. Black represents the maximum value, white represents the minimum value.

for $k \lesssim \ell/r_{max}$ where r_{max} corresponds to the maximum redshift of the survey, the zero values of the signal covariance reflect this functional behaviour. Figure 4.2 shows the diagonal elements of the Q matrix for various different ℓ values for the same fiducial cosmology and survey. The overall shape can be explained by the Bessel function inequality, the $n(z)$ distribution creates the broad curve and the dampening at high-k is due to the photometric redshift error. The spikes at high-k are due to the Bessel function resolution breaking down (a tabulated Bessel function is used), and the higher frequency oscillations are due to the imposing a maximum r in the integration which formally should be to infinity. These numerical break downs have *no* effect on the cosmological parameter estimations for the values of the ranges and resolutions used, this was tested by using non-tabulated Bessel functions and increasing the maximum r limit.

4.2.5 Areal Coverage

The integration over θ in equation (4.20) assumes an all sky survey. When considering small angle surveys the integration over θ needs to be done more carefully. Starting with equation

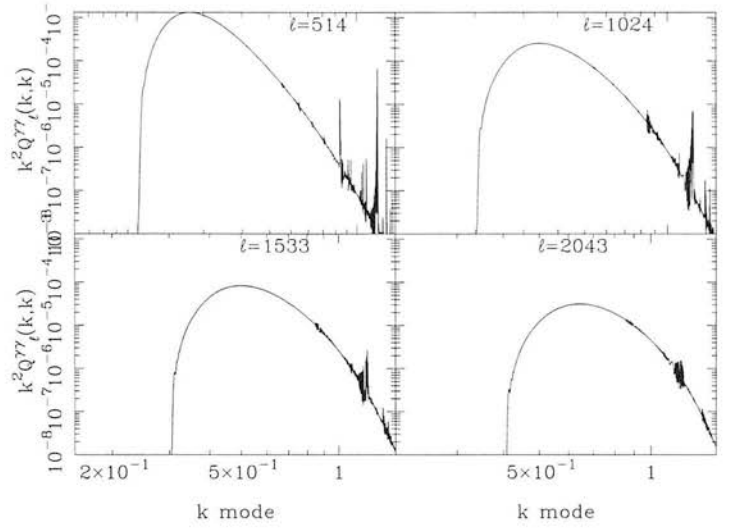

Figure 4.2: The form of the diagonal part of the signal covariance matrix for various ℓ shown in the Figure, using the fiducial cosmology. The survey parameters are a 5-band survey to a median redshift of $z_m = 0.7$ covering $10,000$ square degrees, see Section 4.3 for details. The k and ℓ resolutions and ranges are discussed in Section 4.4.2.

(4.19) the covariance of $\gamma(k,\ell)$ for a survey of size $\Delta\theta \times \Delta\theta = \Delta\Omega$ can be written as

$$\langle\gamma(k,\boldsymbol{\ell})\gamma^*(k',\boldsymbol{\ell}')\rangle_S = \int \frac{d^2\tilde{\boldsymbol{\ell}}}{(2\pi)^2} Q(\boldsymbol{\ell},\boldsymbol{\ell}',\tilde{\boldsymbol{\ell}},k,k')|X_{\tilde{\boldsymbol{\ell}}}|^2 \int_{-\Delta\theta/2}^{\Delta\theta/2} d^2\boldsymbol{\theta} \mathrm{e}^{-i(\boldsymbol{\ell}-\tilde{\boldsymbol{\ell}}).\boldsymbol{\theta}} \int_{-\Delta\theta/2}^{\Delta\theta/2} d^2\boldsymbol{\theta}' \mathrm{e}^{-i(\boldsymbol{\ell}'-\tilde{\boldsymbol{\ell}}).\boldsymbol{\theta}'} \quad (4.26)$$

where the $\boldsymbol{\ell}'$ in equation (4.20) has been replaced with $\tilde{\boldsymbol{\ell}}$. Where the Q matrix has been generalised such that

$$Q(\boldsymbol{\ell},\boldsymbol{\ell}',\tilde{\boldsymbol{\ell}},k,k') = \frac{9\Omega_m^2 H_0^4}{4\pi^2 c^4} \int \frac{d\tilde{k}}{\tilde{k}^2} G(\boldsymbol{\ell},\tilde{\boldsymbol{\ell}},k,\tilde{k}) G(\boldsymbol{\ell}',\tilde{\boldsymbol{\ell}},k',\tilde{k}) \quad (4.27)$$

where

$$G(\boldsymbol{\ell},\tilde{\boldsymbol{\ell}},k,\tilde{k}) \equiv k \int dz\, dz_p\, \bar{n}_z(z_p) W(z_p) p(z_p|z) U(\tilde{\boldsymbol{\ell}},r,\tilde{k}) j_\ell(kr^0) \quad (4.28)$$

and

$$U(\tilde{\boldsymbol{\ell}},r,\tilde{k}) \equiv \int_0^r d\tilde{r}\, \frac{F_K(r,\tilde{r})}{a(\tilde{r})} \sqrt{P_\delta(k;\tilde{r})}\, j_{\tilde{\ell}}(k\tilde{r}). \quad (4.29)$$

The integrals over $\boldsymbol{\theta}$ in equations (4.26) can be solved so that equation (4.26) can be rewritten

$$\langle\gamma(k,\boldsymbol{\ell})\gamma^*(k',\boldsymbol{\ell}')\rangle_S = \int \frac{d^2\tilde{\boldsymbol{\ell}}}{(2\pi)^2} Q(\boldsymbol{\ell},\boldsymbol{\ell}',\tilde{\boldsymbol{\ell}},k,k')|X_{\tilde{\boldsymbol{\ell}}}|^2 \mathcal{F}(\boldsymbol{\ell},\boldsymbol{\ell}',\tilde{\boldsymbol{\ell}}), \quad (4.30)$$

where

$$\mathcal{F}(\boldsymbol{\ell},\boldsymbol{\ell}',\tilde{\boldsymbol{\ell}}) \equiv \prod_{i=x,y} \frac{4}{(\tilde{\boldsymbol{\ell}}-\boldsymbol{\ell})_i (\tilde{\boldsymbol{\ell}}-\boldsymbol{\ell}')_i} \sin\left[(\tilde{\boldsymbol{\ell}}-\boldsymbol{\ell})_i \frac{\Delta\theta}{2}\right] \sin\left[(\tilde{\boldsymbol{\ell}}-\boldsymbol{\ell}')_i \frac{\Delta\theta}{2}\right], \quad (4.31)$$

$i = x, y$ represents the x and y components of a Cartesian coordinate system for a survey.

In the case where $\Delta\Omega \gg (\pi/180)^2$ the function in equation (4.31) has the limit

$$\mathcal{F}(\ell, \ell', \tilde{\ell}) \rightarrow (\Delta\theta)^2 \delta^K_{\ell\tilde{\ell}} \delta^K_{\ell'\tilde{\ell}}, \tag{4.32}$$

where δ^K is the Kroneger delta function, so that equation (4.26) becomes

$$\langle \gamma(k, \ell) \gamma^*(k', \ell') \rangle_S = Q_\ell\,(k, k') \frac{\Delta\Omega}{(2\pi)^2} \tag{4.33}$$

where Q is again defined in equation (4.23). The transformation from all sky to finite survey coverage can be simply seen by comparing equations (4.22) and (4.33), that is $\delta^D(\ell - \ell') \rightarrow \frac{\Delta\Omega}{(2\pi)^2} \delta^K_{\ell\ell'}$.

The full data vector of shear coefficients contains four terms: $\hat{\gamma}_1^R$, $\hat{\gamma}_1^I$, $\hat{\gamma}_2^R$, $\hat{\gamma}_2^I$. Which are estimated here by: $\gamma_1^R(k, \ell)$, $\gamma_1^I(k, \ell)$, $\gamma_2^R(k, \ell)$, $\gamma_2^I(k, \ell)$, superscript R represents the real part and superscript I represents the imaginary part. So far the calculations have been for a single $\gamma_\alpha(k, \ell) = \gamma_\alpha^R(k, \ell) + i\gamma_\alpha^I(k, \ell)$ estimator. As shown in Section 4.2.6 the covariance for one of the data vectors leads to a further factor of $1/2$ in the covariance, so that the signal covariance for a single data vector is

$$\langle \gamma_\alpha^A(k, \ell) \gamma_\alpha^{A*}(k', \ell') \rangle_S = Q_\ell\,(k, k') \frac{\Delta\Omega}{8\pi^2}, \tag{4.34}$$

where $A = R, I$.

4.2.6 Shot Noise

The shot noise can be calculated by making the usual assumption that the galaxies are a Poisson sampling of an underlying smooth field (see e.g. Peebles, 1980). In practice estimators of the transforms of the individual components of the shear are considered, γ_α; $\alpha = 1, 2$. In the normal way for a point process, these may be written as sums over small cells c, each of which contains $n_c = 0$ or 1 galaxy:

$$\hat{\gamma}_\alpha(k, \ell) \equiv \sqrt{\frac{2}{\pi}} \sum_{\text{cells c}} n_c \gamma_{\alpha c}(\mathbf{r}_c)\, k j_\ell(k r_c^0) \exp(-i\ell \cdot \boldsymbol{\theta}_c) W^0. \tag{4.35}$$

The variance of this involves a double sum over cells, and the averaging over cells c and d, $\langle n_c n_d \rangle$ contains shot noise terms when $c = d$, in which case $\langle n_c^2 \rangle = \langle n_c \rangle$, and the shot noise reduces to a single sum, or an integral when we move back to a continuum description. Using

the fact that the variance of the shear estimate for a single galaxy is completely dominated by the variance in the intrinsic ellipticity of the galaxy, σ_e^2, rather than by lensing, see equation (2.49),

$$\langle \gamma_\alpha \gamma_\beta^* \rangle = \frac{\sigma_\epsilon^2}{2} \delta^K_{\alpha\beta} \tag{4.36}$$

where δ^K is a Kronecker delta function, and $\sigma_\epsilon \simeq 0.3$ for a ground-based survey (Brown et al., 2003), I find an expression for the shot noise as

$$\langle \hat{\gamma}_\alpha(k,\boldsymbol{\ell}) \hat{\gamma}^*_\beta(k',\boldsymbol{\ell}') \rangle_{SN} = \sigma_\epsilon^2 \int dz\, \bar{n}_z(z) k j_\ell(kr^0) k' j_{\ell'}(k'r^0) W^2(z)\, \delta^K_{\alpha\beta}\, \delta^D(\boldsymbol{\ell} - \boldsymbol{\ell}'). \tag{4.37}$$

For a survey of size $\Delta\theta \times \Delta\theta = \Delta\Omega$ this becomes

$$\langle \hat{\gamma}_\alpha(k,\boldsymbol{\ell}) \hat{\gamma}^*_\beta(k',\boldsymbol{\ell}') \rangle_{SN} = \frac{\sigma_\epsilon^2 \Delta\Omega}{4\pi^2} \int dz\, \bar{n}_z(z) k j_\ell(kr^0) k' j_{\ell'}(k'r^0) W^2(z)\, \delta^K_{\alpha\beta} \delta^K_{\ell\ell'}. \tag{4.38}$$

As an example, for a single real data vetor $\gamma^R_\alpha(k,\boldsymbol{\ell})$ the shot noise covariance can be written

$$\begin{aligned} \langle \hat{\gamma}^R_\alpha(k,\boldsymbol{\ell}) \hat{\gamma}^R_\beta(k',\boldsymbol{\ell}') \rangle_{SN} &= \frac{2}{\pi} \sum_c \langle n_c \rangle j_\ell(kr^0_c) j_{\ell'}(k'r^0_c) kk' \\ &\quad [\cos(\boldsymbol{\ell}.\boldsymbol{\theta}) \cos(\boldsymbol{\ell}'.\boldsymbol{\theta})] W(r^0_c)^2 \langle \gamma_\alpha(r^0_c) \gamma_\beta(r^0_c) \rangle. \end{aligned} \tag{4.39}$$

Which becomes in the $\boldsymbol{\ell} = \boldsymbol{\ell}'$ limit

$$\langle \hat{\gamma}^R_\alpha(k,\boldsymbol{\ell}) \hat{\gamma}^R_\beta(k',\boldsymbol{\ell}) \rangle_{SN} = \frac{\sigma_\epsilon^2}{4\pi^2} \int dz \bar{n}(z) k k' j_\ell(kr^0) j_\ell(k'r^0) W^2(z) \delta^K_{\alpha\beta} \int_{-\Delta\theta/2}^{\Delta\theta/2} d^2\boldsymbol{\theta} \cos^2(\boldsymbol{\ell}.\boldsymbol{\theta}), \tag{4.40}$$

which should be applicable for $\Delta\Omega \gg 1$. The integration over angle can be solved so that

$$\langle \hat{\gamma}^R_\alpha(k,\boldsymbol{\ell}) \hat{\gamma}^R_\beta(k',\boldsymbol{\ell}) \rangle_{SN} = \frac{\sigma_\epsilon^2 \Delta\Omega}{8\pi^2} \int dz \bar{n}(z) k k' j_\ell(kr^0) j_\ell(k'r^0) W^2(z) \delta^K_{\alpha\beta}. \tag{4.41}$$

By comparing with equation (4.38) it can immediately be seen that each of the components of the estimator contribute equally to the covariance. A similar calculation can be performed for the imaginary data vectors and the signal part of the covariance. All off diagonal blocks (real-imaginary, $\langle \gamma^R_\alpha \gamma^I_\beta \rangle$) in the covariance are zero.

Figures 4.3 and 4.4 show the form of the shot noise part of the covariance matrix for the fiducial cosmology discussed in Section 4.3. It can be seen that the shot noise is almost diagonal in the (k, k') plane for a given ℓ and that since there are no multiplication of Bessel functions the diagonal part is fairly smooth. Since there is no photometric dampening of the shot noise part, as is the case with the signal, it does not decrease at high-k in the same way that the signal part does. In comparing the signal and the noise parts it can be seen that for a given k and ℓ the signal-to-noise is very low, highlighting the need for large surveys with many galaxies and modes to analyse.

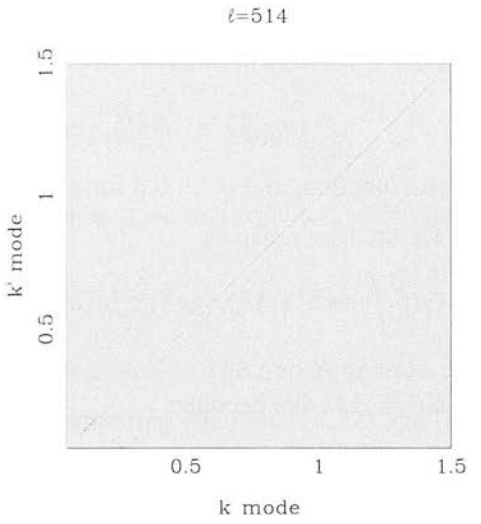

Figure 4.3: The form of the shot noise part of the covariance matrix in the (k, k') plane for $\ell = 514$, using the fiducial cosmology. The survey parameters are a 5-band survey to a median redshift of $z_m = 0.7$ covering $10,000$ square degrees, see Section 4.3 for details. The k and ℓ resolutions and ranges are discussed in Section 4.4.2. Black represents the maximum value, white represents the minimum value.

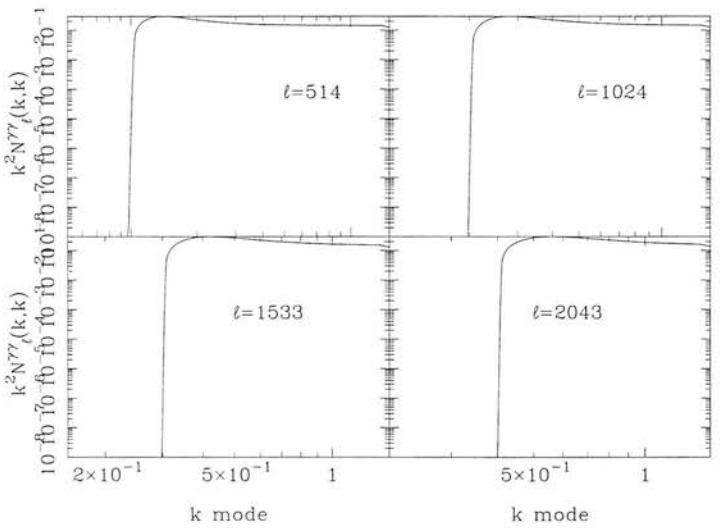

Figure 4.4: The form of the diagonal part of the shot noise part of the covariance matrix for various ℓ shown in the Figure, using the fiducial cosmology. The survey parameters are a 5-band survey to a median redshift of $z_m = 0.7$ covering $10,000$ square degrees, see Section 4.3 for details. The k and ℓ resolutions and ranges are discussed in Section 4.4.2.

4.3 Estimation of Cosmological Parameters

Cosmological parameters influence the shear transforms in a number of ways: the matter power spectrum $P_\delta(k;t)$ is dependent on Ω_m, h and the linear amplitude σ_8. The linear power spectrum is dependent on the growth rate, which also has some sensitivity to the dark energy energy equation of state parameter $w(z)$. w also affects the $r(z)$ relation and hence the angular diameter distance. These parameters ($\{\Theta_\alpha\}$) may be estimated from the data using likelihood methods. Assuming uniform priors for the parameters, the maximum a posteriori probability for the parameters is given by the maximum likelihood solution. I use a Gaussian likelihood

$$2\ln L(\mathbf{g}|\{\theta_\alpha\}) = \text{constant} - \det(\boldsymbol{C}) - \mathbf{g}\cdot\boldsymbol{C}^{-1}\cdot\mathbf{g} \tag{4.42}$$

where $\boldsymbol{C} = \mathbf{S} + \mathbf{N}$ is the covariance matrix, given by signal and noise terms equations (4.34) and (4.41). Note that the average value of $\gamma(k,\ell)$ is zero, so the information on the parameters comes from the dependence of the signal part of the covariance matrix $\boldsymbol{C}$ i.e. the parameters are adjusted until the *covariance* of the model matches that of the data. This was the approach of Heavens and Taylor (1995); Ballinger, Heavens and Taylor (1995); Tadros et al. (1999); Percival et al. (2004) in analysis of large-scale galaxy data. For many surveys useful modes of the shear transform have contributions from wavenumbers where the power spectrum is quite nonlinear. The use of a Gaussian likelihood thus needs to be justified by comparison with simulated data; this is left for future work, it is possible that a different likelihood function may be necessary in the non-linear régime.

4.3.1 Expected Errors on Cosmological Parameters

The expected errors on the parameters can be estimated with the Fisher (information) matrix (Jungman et al., 1996; Tegmark, Taylor and Heavens, 1997), see Section 3.2.

If the means of the data are fixed, the Fisher matrix can be calculated from the covariance matrix and its derivatives (Tegmark, Taylor and Heavens, 1997) by, see equation (3.11),

$$\boldsymbol{F}_{\alpha\beta} = \frac{1}{2}\mathrm{Tr}\left[\boldsymbol{C}^{-1}\boldsymbol{C}_{,\alpha}\boldsymbol{C}^{-1}\boldsymbol{C}_{,\beta}\right]. \tag{4.43}$$

For a square patch of sky, the Fourier transform leads to uncorrelated modes, provided the modes are separated by $2\pi/L$ where L is the side of the square in radians, and the Fisher

matrix is simply the sum of the Fisher matrices of each $\boldsymbol{\ell}$-mode:

$$\boldsymbol{F}_{\alpha\beta} = \frac{1}{2}\sum_{\boldsymbol{\ell}} \mathrm{Tr}\left[(\boldsymbol{C}^{\boldsymbol{\ell}})^{-1}\boldsymbol{C}^{\boldsymbol{\ell}}_{,\alpha}(\boldsymbol{C}^{\boldsymbol{\ell}})^{-1}\boldsymbol{C}^{\boldsymbol{\ell}}_{,\beta}\right], \tag{4.44}$$

where $\boldsymbol{C}^{\boldsymbol{\ell}}$ is the covariance matrix for a given $\boldsymbol{\ell}$-mode. I compute $\boldsymbol{C}^{\boldsymbol{\ell}}$ numerically from the signal and noise parts equations (4.34) and (4.41), for given $\bar{n}_z(z)$, photometric redshift error distribution, cosmology and survey area, which governs the separation of uncorrelated $\boldsymbol{\ell}$-modes.

In the calculation, in order in save computational time, the $\gamma_2^R(k, \boldsymbol{\ell})$ component is chosen as representative so that $X_{\boldsymbol{\ell}} = 2|\boldsymbol{\ell}|^2\cos(\phi_\ell)\sin(\phi_\ell)$ where ϕ_ℓ is the angle of the $\boldsymbol{\ell}$ vector in the (ℓ_x, ℓ_y) phase space. I only consider $\ell_x \geq 0$ to avoid double counting. By choosing $\phi_\ell = \pi/4$ the prefactor becomes $X_{\boldsymbol{\ell}} = |\boldsymbol{\ell}|^2$, the Fisher matrix is then integrated over all modes in a given shell using the $\gamma_2^R(k, \boldsymbol{\ell})$ component as representative

$$\boldsymbol{F}_{\alpha\beta} = g\int_{-\pi/2}^{\pi/2} d\phi_\ell \int d\ell\ell \boldsymbol{F}_{\alpha\beta}(\ell) \tag{4.45}$$

where $\boldsymbol{F}_{\alpha\beta}(\ell) = \frac{1}{2}\mathrm{Tr}\left[(\boldsymbol{C}^{\boldsymbol{\ell}})^{-1}\boldsymbol{C}^{\boldsymbol{\ell}}_{,\alpha}(\boldsymbol{C}^{\boldsymbol{\ell}})^{-1}\boldsymbol{C}^{\boldsymbol{\ell}}_{,\beta}\right]$. The density of states in ℓ-space due to the survey size is $g = \Delta\Omega/(2\pi)^2$ so that

$$\boldsymbol{F}_{\alpha\beta} = \frac{\Delta\Omega}{4\pi}\int d\ell\ell \boldsymbol{F}_{\alpha\beta}(\ell). \tag{4.46}$$

To test this approximation a full Fisher matrix calculation was done over all ϕ_ℓ where $\boldsymbol{F}_{\alpha\beta}(\ell) \rightarrow \boldsymbol{F}_{\alpha\beta}(\ell, \phi_\ell)$, for all four data vectors, the different ϕ_ℓ dependence comes from the $X_{\boldsymbol{\ell}}$ prefactor. The dark energy parameter errors were found be in agreement to within ± 0.001, since the computational time is $4 \times N_\phi$ larger for the full calculation (where N_ϕ is the total number of modes in ℓ-space) the approximation will be used for all predictions in this thesis.

In the calculations only a single data vector is considered using equations (4.34) and (4.41). To account for the imaginary modes the Fisher matrix is multiplied by two, as they are expected to contribute equally.

4.4 Survey Design Formalism

In this Section the survey design factors will be discussed. Firstly the detailed assumptions of the survey design will be discussed, as well as some details of the Fisher matrix calculation. Possible future weak lensing surveys and their effectiveness are discussed in the Section 4.5.

4.4.1 Survey Parameters

In assigning survey parameters this Chapter will use the formalism detailed in Chapter 3, Section 3.6. The assumed redshift distribution for a typical magnitude-limited survey is of the form, see equation (3.94),

$$\bar{n}(z) \propto z^2 \exp\left[-\left(\frac{z}{z_0}\right)^{1.5}\right] \tag{4.47}$$

where $z_0 = z_m/1.412$, and z_m is the median redshift of the survey (e.g. Baugh and Efstathiou, 1993). The number density of useable sources with photometric redshift and shape estimates is taken to scale as, see equation (3.93),

$$n_0 = 30 z_m^{3.4} \text{ per square arcminute.} \tag{4.48}$$

This was estimated from the COMBO-17 survey. With a maximum redshift of $z_{\max} = 1.5$ for ground-based surveys. This is due to the difficulty of measuring galaxy shape, because of the decrease in a galaxy's apparent size with increasing redshift, coupled with the seeing limit.

It is assumed that the photometric redshift errors are Gaussian, with a dispersion given by $\sigma(z) = \sigma_0(1+z)f(m,z)$, where m is the apparent magnitude of the galaxy, the function $f(m,z)$ is given in Section 3.6.2. I integrate over Schechter functions to get the average error as a function of z. The error distribution is shown for a 5-band optical survey and a 17-band optical survey in Figure 3.7. The assumption of Gaussianity of $p(z_p|z)$ can easily be relaxed: outliers can, for example, be included, I investigate this in Section 4.6.8. Again these formula have been extrapolated to $z = 1.5$, though this extrapolation may be optimistic as photometric redshift estimates can increases dramatically at $z \approx 1$ if IR data is not available.

The variables which can be varied are the area A and depth of the survey (z_m), and the number of bands. These scale with the number of nights observing T, the telescope diameter D and the field-of-view F as, equation (3.91),

$$T \propto z_m^4 A D^{-2} \text{fov}^{-1}. \tag{4.49}$$

Again the default survey is a 4-metre telescope with a 2 square degree field-of-view (fov) which could observe an area of 10,000 square degrees to $z_m = 0.7$ with 5-bands in 600 nights of observing. This could be achievable with surveys such as darkCAM (Taylor, 2005; conference proceedings of Probing the Dark Universe with Subaru and Gemini) or the Dark Energy Survey (Wester, 2005).

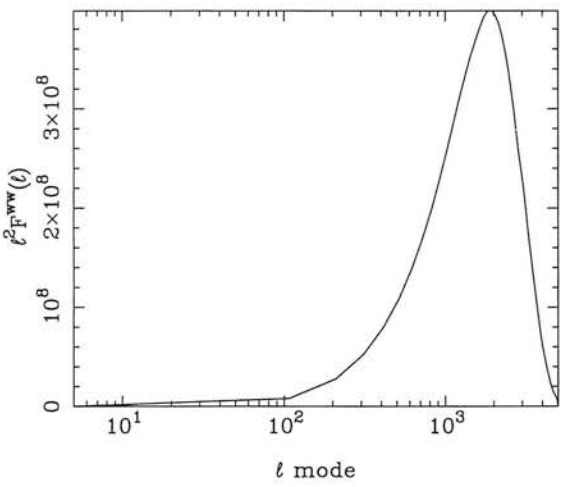

Figure 4.5: The contributions to the Fisher matrix element $\boldsymbol{F}^{ww}$ from different ranges of ℓ for a 10,000 square degree survey with $z_m = 0.70$ and 5 bands. $w = w_0$ in this Figure for clarity.

I compute the nonlinear power spectrum using the fitting formulae of Smith et al. (2003), based on linear growth rates given by Linder and Jenkins (2003). In order to avoid the high-k régime where the formulae may be unreliable, or where baryonic effects might alter the power spectrum ($k > 10h$ Mpc^{-1}; White, 2004; Zhan & Knox, 2004), I do not analyse modes with $k > 1.5$ Mpc^{-1}. Note that the non-local nature of lensing does mix modes to some degree, but these modes are sufficiently far from the uncertain highly-nonlinear régime that this is not a concern (Castro, Heavens and Kitching, 2005). In any case the results are not very sensitive to the radial k limit, since the photometric redshift errors suppress radial power at much lower k. I include angular modes as small as each survey will allow, and analyse up to $\ell_{\rm max} = 5000$. Note that the intracluster medium might affect the power spectrum on the level of a few percent for $1000 \lesssim \ell \lesssim 3000$ (Zhan & Knox, 2004). These modes will still contain useful information, but a more detailed analysis might be necessary when the method is applied. To help asses the extent of any modification to the expected accuracy, I also quote results for a more conservative limit of $\ell_{\rm max} = 2000$, this increases the predicted marginalized errors by approximately 0.01. The flat-sky approximation will break down for the low ℓ-modes, but there is little power there in any case (Figure 4.5).

I have allowed for a universe with the following parameters: Ω_m, Ω_{de}, h, σ_8, Ω_b, w_0, w_a, n_s and α_n. σ_8 represents the amplitude of the perturbations, n_s the scalar spectral index and its running α_n. $w(a)$ is parameterised by equation (1.113). Note that the assumption of this form is not critical; theoretical models with arbitrary $w(a)$ could be analysed. This form is chosen to investigate the sensitivity of these results on w_0 and w_a to time-dependence.

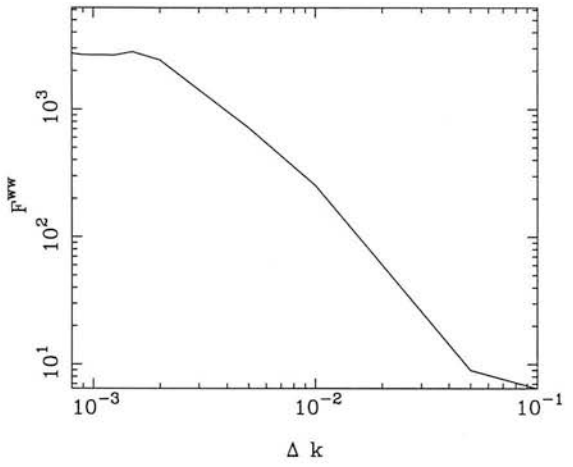

Figure 4.6: The contributions to the Fisher matrix element $\boldsymbol{F}^{ww}$ for different k resolutions for a 10,000 square degree survey with $z_m = 0.70$ and 5 bands. $w = w_0$ in this Figure for clarity. Note that $k_{\max} = 1.5$ Mpc^{-1}.

4.4.2 Numerical Convergence

Since the integrals over k, ℓ and r in equations (4.34) and (4.41) cannot be computed exactly they are approximated in the computations by a sum over the variable in question over some range, using a trapezoidal approximation. When making such a numerical approximation the resolution of the sum must be small enough that any features in the functional form of the integrand are correctly resolved and estimated, once all features are resolved any further decrease in the resolution should yield the same value. This Section shows the results of such convergence testing for the spectral test, investigating the resolution of k, ℓ and r.

Figure 4.6 shows the results of varying the k resolution keeping the ℓ and r resolutions fixed at $\Delta\ell = 100$ and $\Delta r = 1.25$ Mpc. Given that the maximum redshift allowed is $z_{\max} = 1.5$, so that the maximum r in the calculation is $r_{\max} \approx 4500$ Mpc, the k resolution at which convergence is expected to occur is $\Delta k \approx 2\pi/4500 = 1.4 \times 10^{-3}$ Mpc^{-1} at which point neighbouring k-modes begin to become correlated and no further signal is gained by increasing the resolution. It can be seen from Figure 4.6 that this is indeed the case. In the rest of the calculation a resolution of $\Delta k = 1.25 \times 10^{-3}$ Mpc^{-1} is used to ensure convergence.

Figure 4.7 shows the results of varying the ℓ resolution keeping the k and r resolutions fixed at $\Delta k = 1.25 \times 10^{-3}$ Mpc^{-1} and $\Delta r = 1.25$ Mpc. The calculations begin to converge at $\Delta\ell \approx 500$, in the rest of the calculations I will use $\Delta\ell = 100$ to ensure convergence.

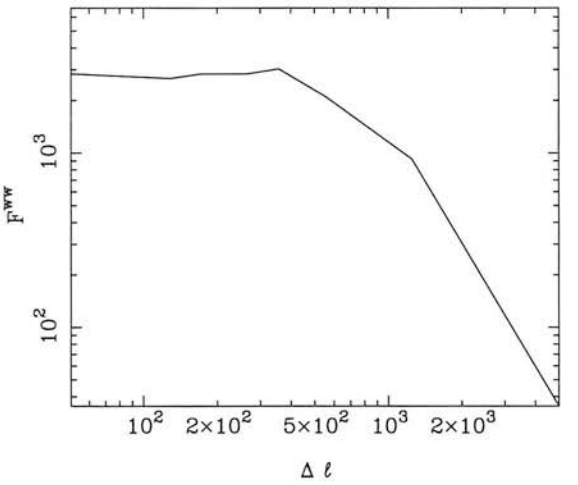

Figure 4.7: The contributions to the Fisher matrix element $\boldsymbol{F}^{ww}$ for different ℓ resolutions for a 10,000 square degree survey with $z_m = 0.70$ and 5 bands. $w = w_0$ in this Figure for clarity. Note that $\ell_{\max} = 5000$.

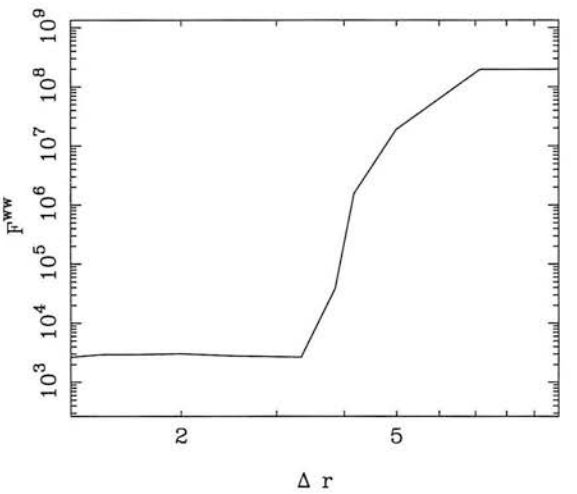

Figure 4.8: The contributions to the Fisher matrix element $\boldsymbol{F}^{ww}$ for different r resolutions for a 10,000 square degree survey with $z_m = 0.70$ and 5 bands. $w = w_0$ in this Figure for clarity.

Figure 4.8 shows the results of varying the r resolution keeping the ℓ and k resolutions fixed at $\Delta k = 1.25 \times 10^{-3}$ Mpc^{-1} and $\Delta\ell = 100$. There should be convergence in the integrals when $\Delta r \approx 2\pi/k_{\max}$ Mpc, since I have fixed $k_{\max} = 1.5$ Mpc^{-1} the r resolution should converge at $\Delta r \approx 4.2$ Mpc, and it can be seen from Figure 4.8 that this is the case. To ensure convergence I will use $\Delta r = 1.25$ Mpc in the rest of the calculations.

4.5 Optimisation for a Wide-Field Lensing Survey

Having introduced the method and the survey design formalism this Section will investigate optimising a weak lensing survey so that the marginal errors on the dark energy parameters can be minimised. I will explore the variation in the marginal error on w_0 with changes in the median depth, varying the area to preserve the total observation time, and the redshift error. Note that all of the alternative dark energy experiments, CMB 14-month *Planck*, CMB 4-year *WMAP*, BAO WFMOS and SNIa *SNAP*, are detailed in Chapter 3, Section 3.8.

4.5.1 A Simplified Error Model

Before embarking on a full optimisation of the method I will describe a simple error model so that the full, more detailed, optimisation results can be simply understood in erms of competing effects. This Section follows a similar procedure to that outlined in Section 3.9.1. The error on w_0, in this case where the mean of the data is zero and the cosmological information in extracted by varying the covariance, is minimised when the covariance is minimised. The error on w_0 (or any other cosmological parameter, by replacing w_0 with an alternative parameter) can be written simply as

$$\frac{\Delta w_0}{w_0} = \left(\frac{d\ln C}{d\ln w_0}\right)^{-1} \frac{\Delta C}{C}. \tag{4.50}$$

In this simplified error analysis I will take an average over k-modes and simply sum over ℓ-modes. The variation in the covariance can be written as $\Delta C = \Delta S + \Delta N$ where S and N are the signal and noise respectively. The full form for the signal and noise are given in equations (4.34) and (4.41), here I will simplify these substantially so that, for a given ℓ-mode

$$\begin{aligned} \Delta S &\approx \Delta\Omega n_0^2 \mathcal{S} \\ \Delta N &\approx \Delta\Omega n_0 \sigma_\epsilon^2 \mathcal{N}. \end{aligned} \tag{4.51}$$

Where $\Delta\Omega = A(\pi/180)^2$ is the area of the survey in steradians, $n_0 \approx 32 z_m^{3.4}$ per steradian is the number density of galaxies, $\mathcal{S}$ and $\mathcal{N}$ are constants for a given ℓ-mode. Using equation (4.49) for equal time the area of a survey can be written $A = (A_0 z_{m0}^4) z_m^4$ where A_0 and z_{m0} are a known achievable area and median redshift for a specific instrument. From the more complex optimisation calculations I find that $\mathcal{S} \approx 1.3 \times 10^{-3}$ and $\mathcal{N} \approx 5 \times 10^{-1}$ and that

$C \approx 4 \times 10^4$. Substituting these values in to equations (4.51) I find

$$\begin{aligned} \Delta S &\approx (1.33)(A_0 z_{m0}^4) z_m^{2.8} \\ \Delta N &\approx (16.0)(A_0 z_{m0}^4) z_m^{-0.6}. \end{aligned} \tag{4.52}$$

From the more complex optimisation Section I also find that $d\ln C / d\ln w_0 \approx 30/N_\ell$ where N_ℓ is the number of ℓ-modes in a survey. Substituting this, and equations (4.52), into equation (4.50) and assuming that the error on w_0 decreases linearly with the number of ℓ-modes the error on w_0 can be written

$$\frac{\Delta w_0}{w_0} \approx \left(\frac{A_0 z_{m0}^4}{1.2 \times 10^6} \right) (1.33 z_m^{2.8} + 16.0 z_m^{-0.6}). \tag{4.53}$$

For an instrument which could image $A_0 = 10,000$ square degrees to a median redshift of $z_{m0} = 0.7$ this becomes

$$\frac{\Delta w_0}{w_0} \approx 2.6 \times 10^{-3} z_m^{2.8} + 3.2 \times 10^{-2} z_m^{-0.6}. \tag{4.54}$$

This minimises at an optimum redshift of $z_m \sim 1.3$ with an optimal conditional error of $\Delta w_0 \sim 0.03$. The first term on the right hand side of equations (4.53) and (4.54), due to the 'cosmic variance' part of the covariance, increases with median redshift as the area decreases. The second term, due to the shot noise part of the covariance, decreases with median redshift as the shot noise increases with areal coverage. This Section will now continue with a full optimisation of the spectral test.

4.5.2 Survey Optimisation

For a given observing time, there will be an optimum depth of survey to minimise the statistical error on w_0 (or w_a). A very wide, shallow survey will yield poor cosmological constraints since the shot noise is large, whereas a very deep survey will also yield poor cosmological constraints because very little area can be covered, and the cosmic variance will be large. In addition, the distant galaxies will have shapes which are difficult to measure at high redshift. Here I explore the optimum median redshift using equation (4.48) keeping the time fixed, so that the area of the survey scales with median redshift as $A \propto z_m^{-4}$. The results are for 600 nights on a 4m survey telescope with a 2 square degree field-of-view, where $z_m = 0.70$ corresponds to $A = 10,000$ square degrees. The results are shown in Figure 4.9.

The optimal median redshift for a 5-band optical survey is $z_m = 1.0$ with an area of $A = 2400$ square degrees. The error is poor below $z_m \sim 1.0$ because shot noise increases with larger

areal coverage (lower z_m). For median redshifts above $z_m \sim 1.0$ the error is also poor as cosmic variance begins to dominate and the areal coverage becomes too small for any signal to be measured. I also investigate the effect of using 9 and 17 optical bands, keeping the median redshift and area fixed. The marginal error does not substantially decrease. This is due to the combination of the lensing and CMB, the intersection of the ellipses in parameter space, remaining similar even though the lensing marginal errors on their own decrease with increasing bands. The extra bands might well be useful in the identification of outliers which I discuss in Section 4.7.

The optimal median redshift increases with the number of optical bands, a 17-band optical survey has an optimal median redshift of $z_m = 1.1$ with an area of $A = 1640$ square degrees. Higher k-modes are accessible due to the reduced damping effect of the photometric redshift error. In order to utilise these modes, the shot noise needs to be reduced, so the optimisation favours a slightly deeper survey with higher number density. This effect increases as the redshift uncertainty decreases.

In Chapter 3 I find that the optimal survey design for the geometric test is $z_m = 0.70$ and $A = 10,000$ square degrees for a 5-band photometric redshift survey on a 4-metre telescope with a 2 square degree field-of-view. So that the results presented here can be directly comparable with the geometric test results a fiducial survey design of $z_m = 0.70$ and $A = 10,000$ square degrees in 5 bands will be adopted from hereon. It should be noted that given 600 nights on such an instrument that an optimal survey design could improve the marginal errors on w_0 and w_a using this method.

4.5.3 Optical and Infrared Surveys

By combining a 5-band optical survey with, for example, a 4-band infrared survey the photometric redshift uncertainty can decrease. Strategies such as this have the potential to be employed on future wide field surveys in an effort to improve cosmological parameter constraints. Here the redshift error is parameterised using, see equation (3.121),

$$\sigma_z(z) = \sigma_0(1+z) \tag{4.55}$$

where a 5-band optical survey can be approximately represented, see Figure 3.7, by $\sigma_0 = 0.05$. $\sigma_0 = 0.01$ corresponds to a 9-band survey comprising of 5 optical and 4 infrared bands (Wolf, private communication). Note the distinction between this and the 9-band optical (no infrared)

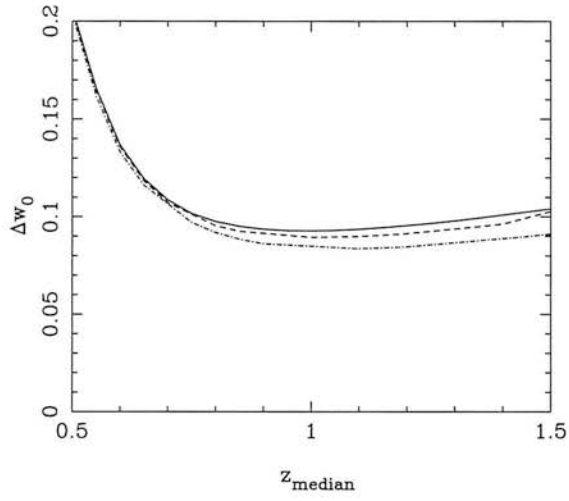

Figure 4.9: The variation in the marginal error on w_0 as the median redshift of the survey varies for a 600 night survey on a 4-metre class telescope, including a 14-month *Planck* prior. Note I assume shapes are not measurable beyond $z_{\rm max} = 1.5$. The solid line is for a 5-band survey, the dashed line for a 9-band survey and the dot-dashed line for a 17-band survey.

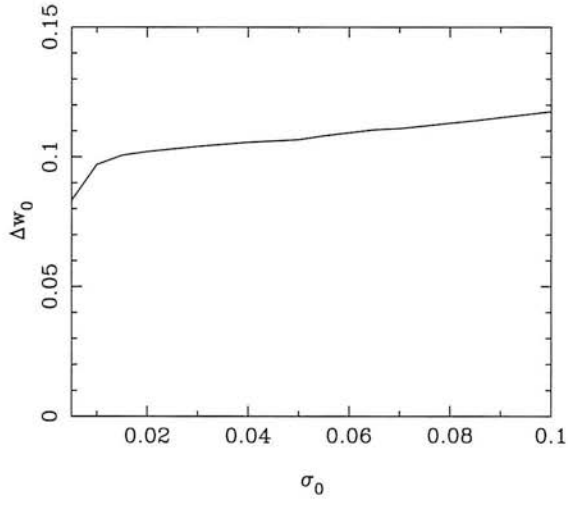

Figure 4.10: Marginal error on w_0 for different photometric redshift errors parameterised by $\sigma_z(z) = \sigma_0(1+z)$. These results include a 14-month *Planck* prior.

survey considered in Section 4.5.2.

Figure 4.10 shows how the marginal error on w_0 varies with σ_0, here the survey design has been fixed to be $z_m = 0.7$ and $A = 10,000$ square degrees. I find that the marginal error on w_0 varies slowly between $0.01 < \sigma_0 < 0.1$ and improves rapidly for $\sigma_0 < 0.01$. This turn-over corresponds to the point where the spectral tests pivot redshift error, see Section 4.5.7, becomes

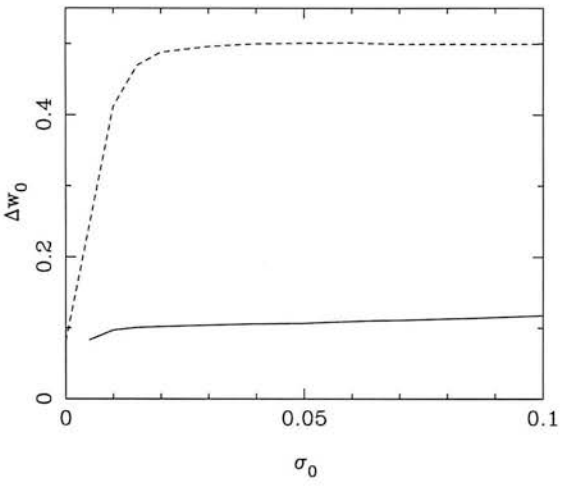

Figure 4.11: Marginal error on w_0 for different photometric redshift errors parameterised by $\sigma_z(z) = \sigma_0(1+z)$ for lensing (solid line) and a BAO experiment (dashed line) from survey of $z_m = 0.70$ and $A = 10,000$ square degrees. These results include a 14-month *Planck* prior.

comparable to the CMB pivot redshift error. So, the marginal error of the combined constraint improves at a faster rate (as σ_0 decreases) after this point since the spectral test is improving both the w_0 and w_a constraints, lifting the CMB degeneracies further. Figure 4.11 shows the marginal error from both lensing and BAO using the photometric redshifts from our fiducial survey. The treatment of a BAO experiment in a photometric redshift survey is discussed in Section 3.8. I find that for a 5-band survey lensing provides much tighter constraints on the dark energy parameters than BAO, see Section 3.9.3. The dark energy constraints from the spectral test are less affected by the photometric damping of the radial wavenumber, due to poor photometric errors, than the BAO. This is due to extra information from geometric factors via the lensing effect in the spectral test. The BAO methodology on the other hand relies on a good measurement of the power spectrum which is restricted to low wavenumbers due to the photometric redshift errors. At low σ_0 the two methods provide complementary constraints on w_0.

4.5.4 Bias in the Photometric Redshifts

As well as investigating the effect of varying the absolute values of the photometric errors, I also investigate how a bias in the photometric redshift calibration affects the dark energy parameter estimation. As shown in Section 3.6.3 the bias $\delta\psi_j$ on a fixed model parameter ψ_j is related to the marginal error on a (cosmological) parameter $\delta\theta_i$ by equation (3.80).

Again I assume that there is some bias $z_{\rm bias}$ in the mean of the photometric redshifts in a given survey (see equation 4.15) due to poor calibration of photometric redshifts with a spectroscopic training set. Marginalizing over all other parameters I find that

$$\delta w_0 = -C_{\rm bias}\delta z_{\rm bias}, \tag{4.56}$$

where $C_{\rm bias}$ is some constant. Following the arguments in Section 3.6.3 the number of galaxies requiring spectroscopic redshifts is

$$N_{\rm spec} = \left[\frac{C_{\rm bias}\sigma(z)}{\delta w_0}\right]^2, \tag{4.57}$$

where the bias on w_0 is half the error $\delta w_0 = 0.5\Delta w_0$. I find that $C_{\rm bias} \approx 1.2$ for the spectral test. If $\sigma(z) \approx 0.1$ and $\Delta w_0 \approx 0.01$ is required the number of spectroscopic redshifts needed is $N_{\rm spec} \approx 6 \times 10^2$. This number is easily achievable using the current generation of spectrometers. The number of required spectroscopic redshifts is significantly smaller than the large number required for the geometric ratio test, for which $C_{\rm bias} \approx 9.0$ (see Section 3.6.3) and tomographic methods (e.g. Hu and Jain, 2004), this difference is attributed to the binning procedure required in these methods. In binning the data any offset in the redshift estimation of a galaxy will create a discrepancy between the estimated and actual number of galaxies in a bin, and any derived quantities gained from them, for example the tangential shear behind a cluster. In this analysis any systematic offset in the galaxy population does not affect any derived quantities in this way but rather the whole shear field is offset in redshift, and galaxies are simply given a slightly increased weighting via j_ℓ. Note that I consider only a single bias parameter, rather than the more complex behaviour allowed in Ma et al. (2006). However, it is the same model as used in Chapter 3 (and Taylor et al., 2006) which shows more sensitivity to $z_{\rm bias}$.

Following the procedure outlined in Section 3.6.3 I also investigated the effect of an offset in the variance of the photometric redshift errors $\sigma_z(z) \rightarrow \sqrt{[\sigma_z(z)]^2 + [\Delta\sigma_z(z)]^2}$. I find that this effect is negligible for this analysis, so that the total bias due to photometric redshift errors is only dependent on the bias in the offset of the mean.

4.5.5 Weighting the Data

One might expect that the cosmological parameter constraints could be improved if the more distant galaxies are given higher weight. I have left a formal optimisation for future work,

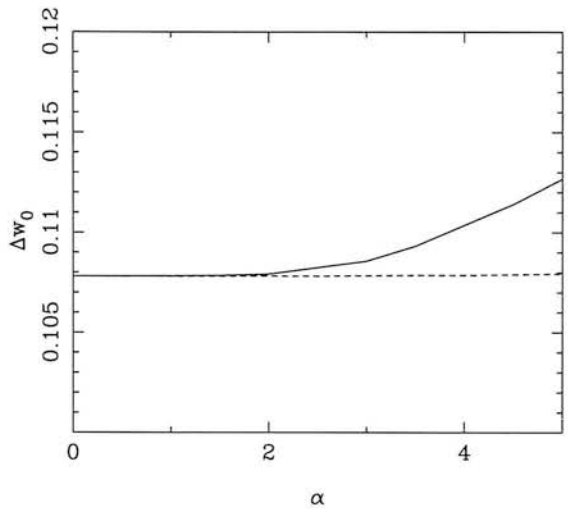

Figure 4.12: The variation in the marginal error on w_0, as the weighting scheme is varied. The solid line is for $W(z) = z^\alpha$, the dashed line is for $W(z) = (1+z)^\alpha$; α is varied.

but show some results of experimental weighting schemes. I consider two weighting schemes $W(z) = z^\alpha$ and $W(z) = (1+z)^\alpha$. Figure 4.12 shows how the error on w_0 changes as the weighting scheme is changed. The figure shows the lensing-only marginal error on w_0, combined with a 14-month *Planck* prior on all parameters. The marginal error on w_0 is fairly insensitive to the weighting scheme employed. Furthermore using equal weighting is in fact the optimal strategy for a weighting functional form of this kind. This shows that the increase in the shot noise through the weighting of high redshift galaxies counteracts any improvement in the lensing signal, used to constrain w_0.

4.5.6 Scaling Results to Other Surveys

Using the results presented in Sections 4.5.2 and 4.5.3 scaling relations can be provided in a similar way to Section 3.9.5. To scale these results to other weak lensing surveys, equation (4.49) should be used with a time calibration, see equation (3.122).

For a flexible survey design the optimal median redshift of $z_m \approx 1.0$ is approximately insensitive to the number of bands, when combined with a *Planck* prior (see Figure 4.9). If the number of bands is 5, 9 or 17 the appropriate line in Figure 4.9 then scales proportionally up (and down) with decreased (or increased) areal coverage from 2400 square degrees, for a 5-band survey i.e. $\Delta w_0(A) = (0.093)(A/2400)^{-1}$. If the number of bands is not shown in Figure 4.9 then Figure 4.10 can be used to find the minimum of the appropriate Δw_0 vs. z_m line (at $z_m = 0.7$). This

can then be scaled for a differing areal coverage as before.

For a fixed survey of area A and median redshift z_m the error, in Figure 4.9, for a given median redshift $\Delta w_0(z_m)$ can be calculated using $\Delta w_0(A) = \Delta w_0(z_m)(A/2400)^{-1}$. In scaling between bands a similar interpolation between Figure 4.9 and Figure 4.10 can be performed.

4.5.7 Constraining $w(z)$ at Higher Redshifts

Pivot Redshifts

The parameterisation used for the dark energy equation of state encodes information on both the present day value of w and its redshift evolution. By placing constraints on both w_0 and w_a a region in the w vs. redshift coordinate system is constrained. Through the anti-correlation of w_0 and w_a this constraint is minimised at a 'pivot redshift', the minimal error at this redshift being the pivot redshift error. The pivot redshift is schematically defined by the angle of the ellipse in the (w_0, w_a) plane, the error at this redshift being the width of the semi-minor axis of the ellipse.

Figure 4.13 shows the constraint on $w(z) = w_0 + w_a[z/(1+z)]$ as a function of redshift for the fiducial weak lensing survey. The highest accuracy on $w(z)$ occurs at the pivot redshift of $z = 0.373$ with $\Delta w(z = 0.373) = 0.0175$. The pivot redshift of the CMB alone is $z = 0.368$ with an error of $\Delta w(z = 0.368) = 0.0350$, the pivot redshift in this case is determined by the redshift at which the dark energy density begins to dominate over the matter density. The pivot redshift of the spectral test alone is $z = 0.208$ with an error of $\Delta w(z = 0.208) = 0.2018$ this is determined both by the redshift at which dark energy becomes dominant and the redshift at which the lensing signal is maximised.

Figure 4.14 shows how the error on $w(z)$ varies both with redshift and the median redshift of the survey. The line in Figure 4.13 can be found by tracing the $z_m = 0.70$ line in Figure 4.14, the 5-band line in Figure 4.9 can be found by tracing along the x-axis ($w(z) = w(0) = w_0$) in Figure 4.14. There is little sensitivity to the pivot redshift or the pivot redshift error on the survey design, this is due to the intersection of the spectral tests constraint with the 14-month *Planck* constraint remaining the same. This occurs because the pivot redshift of the spectral test is a property of the cosmological dependence of the method not the survey design parameters, so that despite the marginal errors on w_0 and w_a varying with the median redshift the orientation

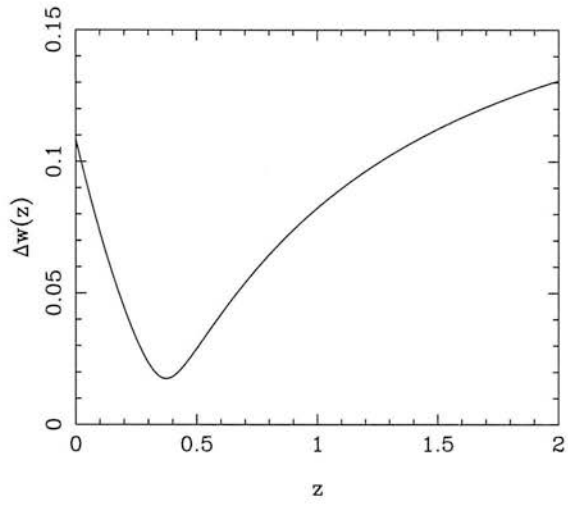

Figure 4.13: Marginal error on $w(z)$ combined with a 14-month *Planck* prior. The highest accuracy is achieved at the pivot redshift of $z = 0.373$ with an error of $\Delta w(z = 0.373) = 0.0175$.

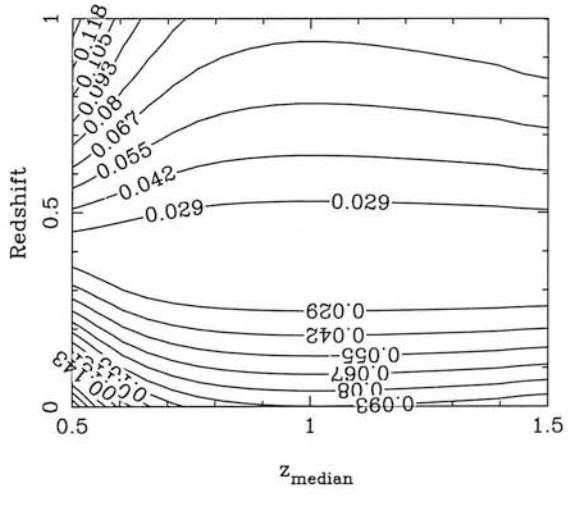

Figure 4.14: Marginal error on $w(z)$ combined with a 14-month *Planck* prior as a function of median redshift. The contours are lines of equal marginal error, the values of the contour given on the line.

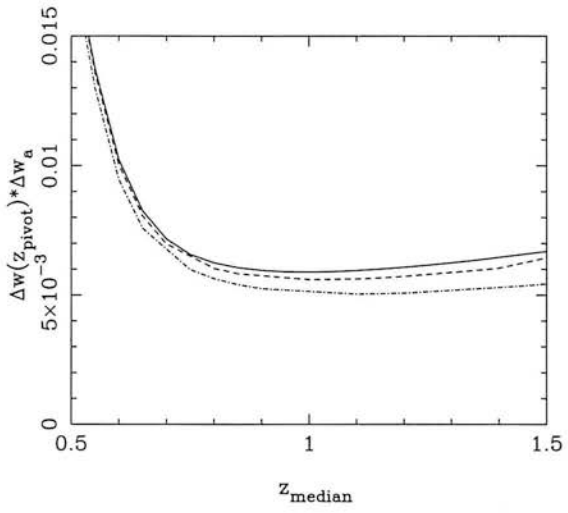

Figure 4.15: The figure of merit (product of errors in $w(z_{\rm pivot})$ and w_a) as a function of median redshift for a $z_m = 0.70$, $A = 10,000$ square degree survey including a 14-month *Planck* prior. Errors in w_0 and w_a are marginalized over all other parameters. The solid line is for 5-band photometric redshift survey, the dashed line for a 9-band survey and the dot-dashed line for 17-band survey. Note it is assumed that shapes are not measurable beyond $z_{\rm max} = 1.5$.

of the lensing ellipse, and hence its intersection with the 14-month *Planck* ellipse, remains the same.

Figure of Merit

A 'figure of merit' has recently been introduced by the Dark Energy Task Force (DETF) (2006), see Section 3.9.6, which represents the area of the decorrelated ellipse constrained by a survey at the pivot redshift see equation (3.127). In reference to Figure 4.13 the figure of merit quantifies both the pivot redshift error and the redshift range over which the error in $w(z)$ is small; a wide and deep curve in Figure 4.13 would have a small figure of merit. Figure 4.15 shows how the figure of merit for a survey consisting of 600 nights on a 4-metre telescope with a 2 square degree field-of-view varies with the median redshift of the survey. It can be seen that for a 5, 9 or 17-band optical survey the optimal median redshifts are the same as when optimising for w_0 alone, see Figure 4.9. It can be seen that the optimal median redshift in Figure 4.15 coincides with the widest point of the inner contour in Figure 4.14. The Figure of merit is shown for all considered experiments in Table 4.2.

4.6 Parameter Forecasts

This Section will present the predicted cosmological parameter error forecast for the spectral test alone, and in combination with other alternative dark energy probes. The spectral test will be exhaustively combined with predicted CMB, BAO and SNIa experiments. The various experimental combinations marginal errors will be compared as well as the combined figure of merit and pivot redshifts. The affect of assuming a fiducial dark energy model, and the affect of assuming flatness, on these parameter constraints is also investigated.

4.6.1 Parameter Forecasts for the Spectral Test Alone

The spectral test alone places constraints on all the cosmological parameters considered. In particular it places smaller independent constraints on w_0 and w_a than any other dark energy probe considered in this Section with $\Delta w_0 = 0.28$ and $\Delta w_a = 1.17$. The spectral tests pivot redshift, see Section 4.5.7 is $z_p = 0.21$ with $\Delta w(z_p) = 0.20$, this pivot redshift is symptomatic of the lensing effect maximising at around this redshift.

The 9-dimensional parameter ellipsoid constrained by the spectral test has a minimum width in a particular direction (compared with the 4-parameter geometric tests constraint, see Section 3.10.1) which can be written as an error on the parameter X where

$$\begin{aligned} X &= (-0.27)\Omega_m + (-0.37)\Omega_{de} + (0.79)h \\ &+ (-0.33)\sigma_8 + (0.036)\Omega_b + (0.20)w_0 \\ &+ (0.042)w_a + (-0.016)n_s + (-0.032)\alpha_n. \end{aligned} \tag{4.58}$$

The fiducial value of X is $X = -0.261$ with an error of

$$\Delta X = 0.032. \tag{4.59}$$

It is the multi-parameter intersection of the constrained ellipsoids that provide the combined constraints in remainder of this Section. The marginal errors for the spectral test alone are shown in Table 4.1. It can be seen that, in general, the parameter coefficients in equation (4.58) are larger for the parameters that have smaller marginal errors. It can be seen that the parameters that affect either the redshift-distance relation or the overall normalisation of the power spectrum, or both, have the smallest marginal errors and the largest affect on the combined parameter X.

4.6.2 Comparing and Combining the Spectral Test and the CMB

To help to lift degeneracies between cosmological parameters, and to retain realism in the predictions for a wide field photometric survey I consider 4-year *WMAP* and 14-month *Planck* CMB experiments. These CMB experiments will place constraints on w_0 and w_a, mainly through the large scale ISW effect, although there is a strong degeneracy between the dark energy parameters. Combining with the spectral test helps to lift this degeneracy.

Combining with WMAP

Combining the results from a 5-band photometric survey of 10,000 square degrees with a median redshift of $z_m = 0.7$ with the expected results from a 4-year *WMAP* experiment results in marginal errors of $\Delta w_0(\mathrm{WMAP} + \mathrm{GL}) = 0.231$ and $\Delta w_a(\mathrm{WMAP} + \mathrm{GL}) = 0.675$, this is a factor 9 times improvement over the *WMAP* results alone which have $\Delta w_0(\mathrm{WMAP}) = 2.05$, $\Delta w_a(\mathrm{WMAP}) = 3.61$. Note again that the results presented in Spergel et al. (2006) using 3 years of *WMAP* data of $w_0 = -1.06^{+0.13}_{-0.08}$ do not include a marginalization over w_a, and are combined with 2DFGRS and SDSS data.

Combining with Planck Surveyor

For the default survey, Figure 4.16 shows the Fisher matrix elements marginalized over all parameters. The blue (dark) areas show a 14-month *Planck* prior. The green (pale) ellipses show the two-parameter, 1-σ errors for the parameters plotted, and the red (central) ellipses show the combination. The marginal errors on w_0 and w_a are $\Delta w_0 = 0.108$ and $\Delta w_a = 0.395$ respectively, a factor of 5 improvement over the 14-month *Planck* constraints alone which could constrain w_0 and w_a to $\Delta w_0 = 0.502$ and $\Delta w_a = 1.86$.

The spectral test improves constraints on all the CMB cosmological parameters, in particular σ_8 whose constraint is improved by a factor of 14. It is already well known that weak lensing can tightly constrain the (σ_8, Ω_m) plane, using standard cosmic shear techniques (see Chapter 5; Brown et al., 2003; Semboloni et al., 2006). The spectral test constrains σ_8 in the same way by measuring the overall normalisation of the matter power spectrum. The spectral test also provides indirect (and slight) improvements on the constraints for the tensor to scalar ratio r and

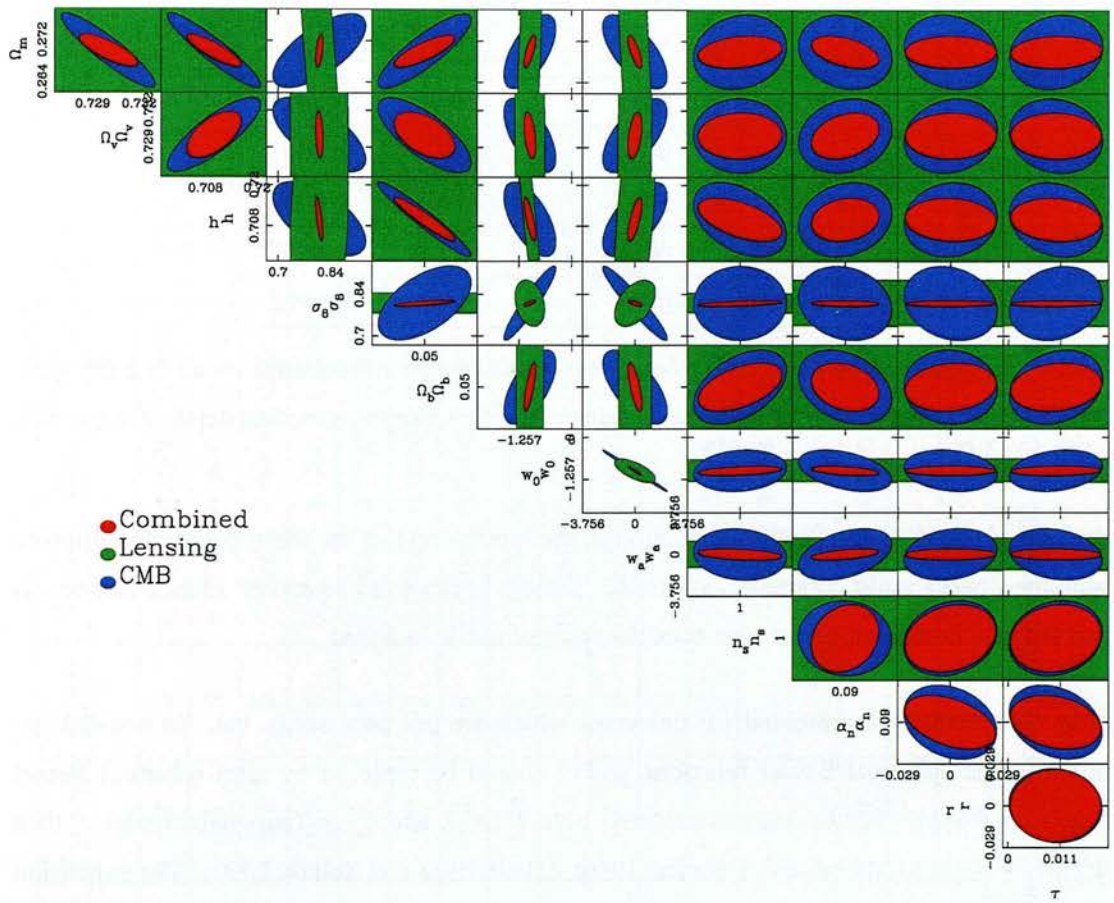

Figure 4.16: Expected marginal errors on cosmological parameters from *Planck* (dark, blue), 3D weak lensing survey using the spectral test(pale, green) and the combination (central, red). The survey covers $10,000$ square degrees to a median depth of $z_m = 0.7$ in 5 bands. Ellipses show the two-parameter 1-σ errors (68.3% confidence regions), marginalized over all other parameters. Note in this Figure and throughout this Chapter $\Omega_v = \Omega_{de}$ for clarity.

Parameter	*Planck* only	Lensing only	Combined
Ω_m	0.0058	0.0500	0.0025
Ω_{de}	0.0024	0.0795	0.0015
h	0.0088	0.0321	0.0051
σ_8	0.1002	0.0705	0.0073
Ω_b	0.0011	0.3707	0.0007
w_0	0.5015	0.2843	0.1086
w_a	1.8618	1.1792	0.3947
n_s	0.0034	0.3852	0.0031
α_n	0.0062	0.0576	0.0045
τ	0.0079		0.0077
r	0.0208		0.0203

Table 4.1: Improvements on CMB *Planck* one-parameter 1-σ, constraints by adding the spectral test constraints from a 10,000 square degree lensing survey to a median depth of $z_m = 0.7$.

the optical depth to last scattering τ through the intersection of the multi parameter ellipsoid with the CMB's multi parameter constraint. Table 4.1 shows the 14-month *Planck* constraints and the new combined constraints once the spectral test is included.

Note that results are presented for universes which are not necessarily flat. In non-flat geometries the spherical Bessel functions $j_\ell(kr)$ should be replaced by ultra-spherical Bessel functions $\Phi^\ell_\beta(y)$. For the case considered here $\ell \gg 1$ and $k \gg$ (curvature scale)$^{-1}$ then $\Phi^\ell_\beta(y) \rightarrow j_\ell(kr)$ (Abbott and Schaefer, 1986; Zaladarriaga and Seljak, 2000). The expansion used is not ideal for non-flat universes but should be an adequate approximation given current constraints on flatness, and the fact that in the Fisher matrix calculations I only consider small steps away from a fiducial flat geometry.

Survey	Area sqdeg	z_{median}	N_{bands}	Δw_0	Δw_a	$z_{\rm pivot}$	$\Delta w(z_{\rm pivot})$	$\Delta w(z_{\rm pivot})\Delta w_a$
Lensing								
darkCAM + *Planck*	10000	0.7	5	0.1082	0.3966	0.3681	0.0175	0.0069
darkCAM, 9 bands + *Planck*	10000	0.7	9	0.1072	0.3895	0.3733	0.0173	0.0067
darkCAM+*Planck*+BAO+SNIa	10000	0.7	5	0.0350	0.0944	0.5011	0.0151	0.0014
darkCAM + BAO darkCAM	10000	0.7	5	0.2764	1.1207	0.2086	0.2004	0.0418
Pan-STARRS 1+*Planck*	30000	0.5	5	0.2064	0.7127	0.4030	0.0258	0.0184
Pan-STARRS 4+*Planck*	30000	1.0	9	0.0361	0.1110	0.3619	0.0111	0.0012
All-Sky Space + *Planck*	40000	1.0	9	0.0101	0.0406	0.3047	0.0034	0.0001
SNAP Lensing + SNIa + *Planck*	1000	1.38	5	0.0579	0.2322	0.3247	0.0112	0.0026
CFHTLS(Wide)+*WMAP*4	170	1.17	5	0.2541	0.8145	0.4275	0.0711	0.0579
VST-KIDS+*WMAP*4	1400	0.6	5	0.3405	1.0818	0.4378	0.0862	0.0933
CMB								
4-year *WMAP*				2.060	3.612	1.18	0.758	2.7379
14-Month *Planck*				0.501	1.873	0.367	0.035	0.0655
BAO								
BAO WFMOS+*Planck*	2000	1.0		0.070	0.154	0.78	0.019	0.0029
SNIa								
SNIa *SNAP*+*Planck*				0.142	0.513	0.37	0.028	0.0144

Table 4.2: Expected marginal errors on cosmological parameters from proposed weak lensing surveys using the spectral test. Note here 9 bands refers to 5 optical bands plus 4 infrared.

4.6.3 Future Lensing Surveys

Here I present the predicted constraints using the spectral test for some current and planned weak lensing surveys in Table 4.2. For full details of the surveys considered see Section 3.10.3. Here 9 bands refers to a 5-band optical survey with 4 infrared bands as discussed in Section 4.5.3.

4.6.4 Synergy of Dark Energy Experiments

Here the results of comparing and combining the spectral test with other dark energy probes are presented. Combining probes, which use different cosmological effects to measure dark energy either through the growth of structure or geometric effects, will allow for cross checks to made. These cross checks may illuminate possible discrepancies between the two effects which could be important in determining the nature of dark energy. The spectral test probes both the growth of structure via the matter power spectrum, and geometry through the lensing effect and the matter power spectrum.

Comparing and Combining with CMB, BAO and SNIA Experiments

I consider the CMB, SNIa and BAO experiments as described in Section 3.8. In Figures 4.17, 4.18 and 4.19 the dark (blue) thin ellipse is the CMB constraint; the small light (green) ellipse is the lensing constraint; the darker (orange), most vertical, broad ellipse is the BAO constraint; the very broad lightest (light blue) ellipse is the SNIa constraint.

Figure 4.17 shows the combined two-parameter 1-σ (68.3%) contours for all the possible pairs of experiments considered. In comparison with the other methods the spectral tests constraint provides the smallest independent constraint. In combination the marginal errors do not vary largely between the different pairs. The BAO and CMB pair combination provides the smallest marginal errors through the unique degeneracy of the BAO ellipse providing a small intersection with the CMB. The SNIa constraint alone is poor, although in combination with the other dark energy probes does provide an improvement on the marginal errors through the intersection of the constraints. The SNIa is also a purely geometric test, so that the combination with the spectral test would provide an important cross check.

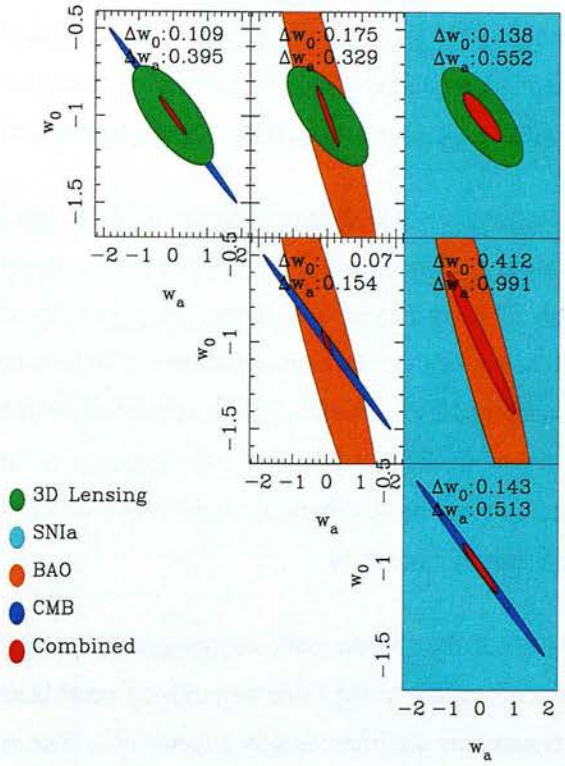

Figure 4.17: The combined marginal constraints in the (w_0, w_a) plane for individual experiments and combined in pairs. The experiments are a darkCAM lensing experiment and a CMB 14-month *Planck* experiment, a BAO WFMOS experiment and a SNIa *SNAP* experiment. The dark (blue) ellipses in the diagonal panels is the CMB constraint; the small, light (green), ellipses along the top row of panels is the spectral tests constraint; the broad darker (orange) ellipses in the top middle, right-hand middle and middle diagonal is the BAO constraint; the lightest (light blue) ellipses in the right-hand panels is the SNIa constraint. The small darker (red) central ellipses are the combined constraints.

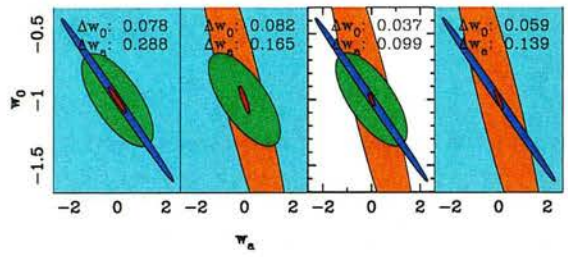

Figure 4.18: The combined marginal constraints in the (w_0, w_a) plane for three pairs of experiments. The experiments are a darkCAM lensing experiment and a CMB 14-month *Planck* experiment, a BAO WFMOS experiment and a SNIa *SNAP* experiment.

Combinations of three experiments are shown in Figure 4.18. It can be seen, by comparing with Figure 4.17, that adding further information from another experiment improves all the combined marginal errors. The largest improvements are gained by adding the spectral tests constraints, or the CMB, to the pair combinations that do not include these probes. The smallest marginal errors are achieved by combining the spectral test with the CMB and BAO. In combining the spectral test with SNIa and BAO the dark energy constraints are comparable, or better than, each pair combination that includes the CMB constraint showing that a strong CMB constraint is not absolutely necessary.

Finally the combination of all four of the dark energy probes is shown in Figure 4.19. By adding the spectral tests constraints to the three experiment combination of CMB, BAO and SNIa the marginalized constraints are improved by a factor of 2. The marginalized constraints in the combination of all four of the probes considered are

$$\begin{aligned} \Delta w_0 &= 0.035 \\ \Delta w_a &= 0.094, \end{aligned} \tag{4.60}$$

with a pivot redshift error of

$$\Delta w(z = 0.43) = 0.0147. \tag{4.61}$$

Reducing the maximum ℓ to 2000 increases these errors by approximately 0.01 to $\Delta w_0 = 0.045$ and $\Delta w_a = 0.105$.

4.6.5 Complementary Figures of Merit and Pivot Redshifts

An illustrative way to present the information of pivot redshifts and the figure of merit of a dark energy probe, or combination of different probes, is to show how the figure of merit and

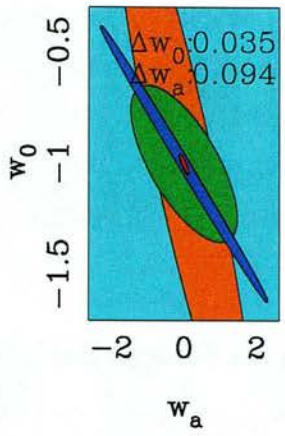

Figure 4.19: The combined marginal constraints in the (w_0, w_a) plane for all four experiments combined. The experiments are a darkCAM lensing experiment and a CMB 14-month *Planck* experiment, a BAO WFMOS experiment and a SNIa *SNAP* experiment.

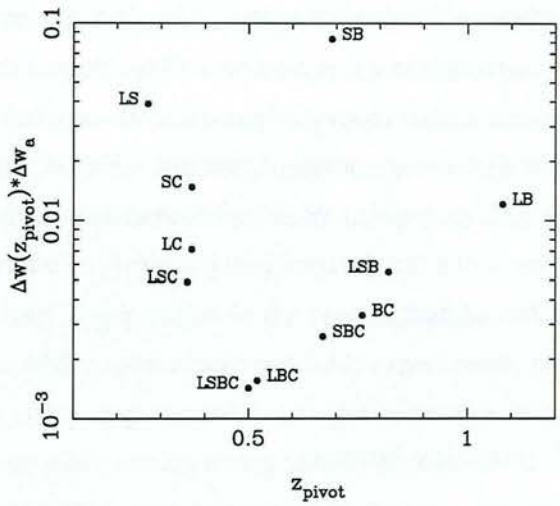

Figure 4.20: The figure of merit and pivot redshift for various experimental combinations. The combinations are labelled as L=Spectral Test, B=BAO, S=SNIa, C=CMB. Combinations of letters represent combinations of experiments.

the pivot redshift compare (see Section 3.10.5). This is shown in Figure 4.20 by plotting the figure of merit for all the possible combinations of experiments against the pivot redshift of the combined constraint. In general the more experiments that are added in combination the smaller the figure of merit becomes. As more experiments are added in combination the pivot redshift converges to a single value. In combination with other experiments the BAO constraint creates a high pivot redshift, this is due to the redshift of the nearest bin at $z = 1$. The spectral tests constraint in combination creates a low $z \approx 0.4$ pivot redshift; this is due to the lensing

pivot redshift dominating which is a symptom of the lensing signal maximising at around this redshift. It can be seen from Figure 4.20 that there exists combinations, for example SNIa with the CMB (SC) and the spectral test with BAO (LB), that have similar figures of merit but very different pivot redshifts. In using combinations such as these the $w(z)$ evolution could be constrained to a high degree over a large redshift range.

4.6.6 The Effect of Changing the Fiducial Dark Energy Model

Here the effect of the assumed fiducial dark energy cosmology on the marginal errors used in the Fisher matrix calculations is investigated in a similar way to Sections 3.10.6. The assumed fiducial cosmology has been a cosmological constant model with $w_0 = -1$ and $w_a = 0$. Figure 4.21 shows the two-parameter 1-σ (68.3%) contours for various dark energy models in the (w_0, w_a) plane fully marginalized over other parameters. Two extreme examples, just allowable from current constraints, are considered (see Section 3.10.6). Despite the marginal errors from the dark energy experiments alone changing, the combined marginal error on w_0 is largely unaffected by the assumed dark energy model. Again, the main difference occurs on the error on w_a which increases for all methods as its value becomes more negative. Here I reach the same conclusion as Section 3.10.6 that the combined marginalized errors presented here should be robust to the actual nature of dark energy.

4.6.7 The Effect of Assuming Flatness

Here the effect of assuming flatness in the parameter error estimation i.e. $\Omega_{de} = 1 - \Omega_m$, is presented. Figure 4.22 shows the two-parameter 1-σ (68.3% contour) constraints for all four dark energy probes considered, see Section 4.6.4, in the (w_0, w_a) plane with the assumption that the Universe is flat. The CMB 14-month *Planck* constraint does not considerably improve because the CMB puts a strong constraint on the overall geometry of the Universe, through the position of the first acoustic peak. The improvement in the SNIa constraint is most evident, since this dark energy probe is very sensitive to the overall geometry through the Hubble parameter (this is in agreement with Linder, 2005). The spectral test and BAO constraints also considerably improve, with the overall combined errors on the dark energy equation of state parameters being $\Delta w_0 = 0.029$ and $\Delta w_a = 0.089$, a factor of 1.2 less than the constraints considering fully open models. In assuming flatness the different dark energy probes still have

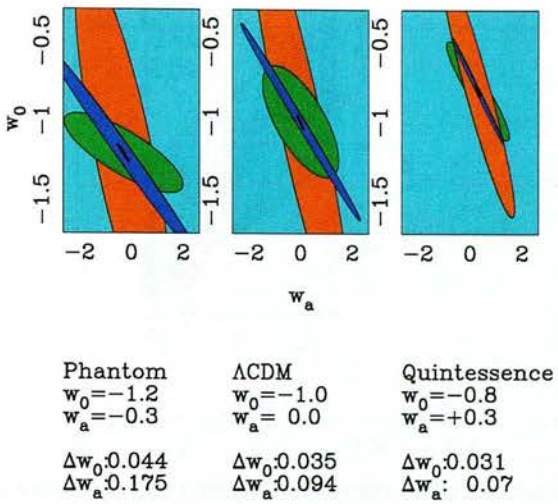

Figure 4.21: The two-parameter 1-σ (68.3%) contours for various assumed fiducial dark energy models, for a 10,000 square degree survey to a median depth $z_m = 0.7$, with a CMB 14-year *Planck* prior, a BAO WFMOS prior and a SNIa *SNAP* prior. The errors quoted are the one-parameter 1-σ marginal errors on w_0 and w_a. The dark (blue) thin ellipse is the CMB constraint; the small light (green) ellipse is the spectral tests constraint; the darker (orange), almost vertical, broad ellipse is the BAO constraint; the very broad lightest (light blue) ellipse is the SNIa constraint. The small darker (red) central ellipses are the combined constraints.

unique and complementary degeneracies in the (w_0, w_a) plane. The reduction in predicted errors, especially in the SNIa, spectral test and BAO experiments, show that the assumption of flatness can have an affect on parameter error estimation (this is in agreement with the effect of this assumption on weak lensing tomographic methods, see for example Knox, Song & Zhan, 2006). Again, given that some proposed dark energy models rely on modifications to the Friedmann equation in non-flat geometries (Dvali & Turner, 2003) it is prudent to calculate predicted parameter errors using fully open geometries.

4.6.8 The Effect of Photometric Redshift Outliers

In every photometric redshift survey there will be some galaxies in the sample for which an accurate photometric redshift cannot be assigned. To investigate the effect of these outliers on the dark energy parameter estimation I consider two galaxy populations, one with the original photometric redshift errors, see Section 4.4.1, and a second population with $\sigma_z^{p2}(z) = 0.5$. The results are shown in Figure 4.23, A^{p2} is the proportion of the total galaxy population with

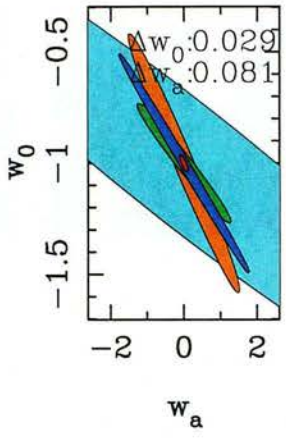

Figure 4.22: The combined marginal constraints in the (w_0, w_a) plane for all four experiments combined, with the condition $\Omega_m + \Omega_{de} = 1$ enforced. The experiments are a darkCAM lensing experiment and a CMB 14-month *Planck* experiment, a BAO WFMOS experiment and a SNIa *SNAP* experiment. The dark (blue) thin ellipse is the CMB constraint; the smaller light (green) ellipse is the spectral tests constraint; the darker (orange), almost vertical, ellipse is the BAO constraint; the broad lightest (light blue) ellipse is the SNIa constraint. The small darker (red) central ellipse is the combined constraint.

$\sigma_z^{p2} = 0.5$. I have considered three ways in which the outlying population could be dealt with, and how the effect of each of these methods varies with the proportion of the total population of outlying galaxies.

A population of outliers can either be discarded from the analysis completely or used in some way. The dashed line in Figure 4.23 shows the effect of discarding the sample, so that the surface number density of galaxies is decreased by $n_0 \rightarrow n_0(1 - A^{p2})$, but the photometric redshift error remains the same. To use the outliers either they can be treated as a separate population (solid line in Figure 4.23) or can be incorporated into a single population (dot-dashed line in Figure 4.23) in which case the overall photometric redshift is degraded to $\sigma_z(z) \rightarrow \sqrt{(1 - A^{p2})[\sigma_z(z)]^2 + A^{p2}[\sigma_z^{p2}(z)]^2}$ (see Blake & Bridle, 2005) where $\sigma_z(z)$ is the original photometric redshift error. The effect of having outliers in the sample increases the marginal error on w_0 regardless of how they are treated, though the method is relatively insensitive to this effect. As expected using the outlying galaxies, and treating them as a separate population, increases the marginal error less than discarding the galaxies completely. By incorporating the galaxies into a single population the redshift error is degraded to such a degree that for a low proportion of outliers it is optimal to discard them, note the signal-to-noise for the spectral test is proportional to n_0. For a high proportion it is optimal to include the outliers

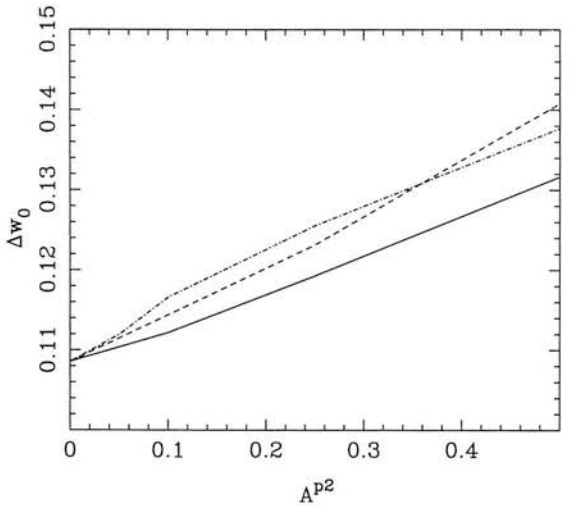

Figure 4.23: The effect of outliers with $\sigma_z^{p2}(z) = 0.5$ on the marginal error in w_0 as a function of the proportion of outliers in the survey A^{p2}. The survey is a 5-band survey of 10,000 square degrees to a median redshift of $z_m = 0.7$, with a 14-month *Planck* prior. The solid line shows the effect of treating the outliers as a separate population; the dashed line shows the effect of discarding the outliers; the dot-dashed line shows the effect of incorporating the outliers into a single galaxy population.

somehow either into a single population or as two separate populations.

4.7 Additional Systematic Effects for Lensing

In Chapter 3, Section 3.11 various potential systematic effects were considered. The discussions in Sections 3.11.1 and 3.11.4, on image shear analysis and CMB lensing, are also relevant to the spectral test; the affect of such systematics on the spectral test should be similarly small. The effects of cluster substructure and strong lensing effects should be negligible for the spectral test as all galaxies in a survey are used in the analysis and any effects on these small scales should be averaged over, furthermore the ℓ range which contributes most to the spectral tests signal corresponds to scales much larger than the scale of galaxy clusters. Any regions of very high shear could be removed, although this would yield a complicated window function; the affect of window functions is left for future study.

Errors due to the intrinsic alignment of galaxies (Heavens, Réfrégier and Heymans, 2000; Croft and Metzler, 2000; Catelan, Kamionkowski and Blandford, 2001; Crittenden et al., 2001; Jing,

2002) were not considered, as these may be reduced to a negligible level by removing pairs which are close in photometric redshifts (Heymans and Heavens, 2003; King and Schneider, 2002). This procedure has already been demonstrated in the analysis of the COMBO-17 data (Heymans et al., 2004). I have also not addressed other issues of systematics, such as optical distortions, or possible alignment of foreground galaxies with shear (Hirata and Seljak, 2004), which may be reduced using techniques such as template fitting (King, 2005).

4.8 Summary

In this Chapter I have presented a 3D weak lensing spectral method suitable for high-ℓ studies, and investigated how well 3D weak lensing surveys could determine the equation of state of dark energy. The accuracy which could be achieved if systematic errors can be controlled is impressively high, provided the surveys are analysed in 3D. Marginal statistical errors of $\Delta w_0 = 0.108$, on the current value of $w \equiv p_{de}/\rho_{de}c^2$, and its evolution w_a constrained to $\Delta w_a = 0.397$ are possible with a 10,000 square degree survey in 5 bands to a median source depth of $z_m = 0.7$. At a pivot redshift of $z = 0.37$ such an experiment could constrain $w(z)$ to $\Delta w(z = 0.37) = 0.0175$. Such a survey is possible with darkCAM or the DES, in conjunction with data from the *Planck* satellite. Even without *Planck*, the accuracy from the spectral test alone is still impressively high, and better than any other dark energy probe considered on its own. The fact that the physics of 3D weak lensing is well-understood, combined with the small statistical error forecasts, makes the spectral test a formidable prospect for advancing cosmology in the next decade. The errors on w are comparable to, but a little better than, predictions from tomography (Hu and Jain, 2004; Ishak, 2005). The constraints on $w(z)$ at the pivot redshift and the figure of merit, $\Delta w(z_{\rm pivot}) * \Delta w_a$, of the experiments considered were also discussed.

I have investigated optimising a wide field survey to measure the equation of state parameters w_0 and w_a and found an optimal survey strategy of $z_m = 1.0$ covering 2400 square degrees for a 5 optical band survey. It was found that increasing the number of optical bands to 9 or 17 makes little difference to the marginal errors when the spectral tests result is combined with a *Planck* prior. The effect of including infrared bands in a wide field survey was investigated by varying the photometric redshift error, it was found that adding 4 infrared bands to a 5-band optical survey improves the marginal constraints on w_0 slightly from $\Delta w_0 = 0.108$ to $\Delta w_0 = 0.097$.

Three alternative dark energy probes were considered: a CMB *Planck* experiment; a BAO WFMOS experiment and a SNIa *SNAP* experiment. All possible combinations of experiments were considered and the figure of merit and pivot redshifts of the combinations shown. In such a competitive environment the spectral test places strong constraints on the dark energy parameters and in combination with other experiments provides a unique degeneracy in the (w_0, w_a) plane which is manifest as a strong constraint at a particular pivot redshift.

The issues of biased photometric redshift estimates (e.g. Ma, Hu and Huterer, 2005) were addressed and it was shown that the method is relatively insensitive to this. I also investigated the effect that a sample of outliers, with poor photometric redshift estimates, would have on the predicted marginal errors. The effect of outliers on the marginal error of w_0 is small although the way in which such a sample is treated is important.

I discussed some possible systematic effects that may limit accuracy with which cosmological information can be extracted. Nevertheless, the fact that the statistical errors are small is very encouraging. Clearly to achieve the accuracies quoted here is going to be a formidable challenge for control of systematics, but at least the statistical error forecasts are small enough that the promise of accurate measurement of the equation of state of dark energy may be realized.

The two main results and themes of this thesis have now been introduced and discussed in detail. In Chapter 5 the methods presented in Chapters 3 and 4 will be applied to the COMBO-17 data with the aim of placing a conditional constraint in the (σ_8, Ω_m) plane and a conditional constraint on a constant equation of state of dark energy, w.

Chapter 5

An Application to COMBO-17

In this Chapter I will present the first application of the geometric test analysis developed in Chapter 3 and the spectral test developed in Chapter 4, to the COMBO-17 data set. The spectral test has been used to analyse galaxies with redshift estimates from two random COMBO-17 fields covering 0.52 square degrees in total, providing a conditional constraint in the (σ_8, Ω_m) plane as well as a conditional constraint on the equation of state of dark energy, parameterised by a constant $w \equiv p_{\rm de}/\rho_{\rm de}c^2$. The (σ_8, Ω_m) plane analysis constrained the relation between σ_8 and Ω_m to be $\sigma_8(\Omega_m/0.3)^{0.57\pm0.19} = 1.06^{+0.17}_{-0.16}$, in agreement with a 2D cosmic shear analysis of COMBO-17. The spectral tests conditional constraint on w using the two random fields is $w = -1.27^{+0.64}_{-0.70}$.

The geometric test has been applied to the A901/2 field, which contains three small galaxy clusters. Combining the analysis from the A901/2 field, using the geometric test, and the two random fields, using the spectral test, w is conditionally constrained to $w = -1.08^{+0.63}_{-0.58}$.

The errors presented in this Chapter are shown to agree with Fisher matrix predictions made in this thesis.

5.1 Introduction

This Chapter presents the first application of the 3D weak lensing techniques developed in this thesis to the COMBO-17 data set. This study is based on only 0.78 square degrees of data, and is essentially a proof of concept in preparation for much larger surveys which could lead to very accurate measurements of w and its redshift evolution, as shown in the previous Chapters. I will present conditional constraints on w by applying 3D weak lensing methods to the COMBO-17 survey. I will also present constraints on the amount of matter in the Universe Ω_m and the clustering of matter, parameterised by σ_8, the rms of the fractional mass density fluctuations in spheres of radius $8h^{-1}$ Mpc. Weak lensing has already proven to be a powerful probe of both Ω_m and σ_8, using 2D weak lensing techniques. I show that a fully 3D shear analysis can also place tight constraints on the matter content and clustering.

Other surveys have used weak lensing data to constrain cosmological parameters using 2D and tomographic tests. Most recently (circa 2006) Semboloni et al. (2006), Schrabback et al. (2006) and Hetterscheidt et al. (2006) have all constrained σ_8, Ω_m and Ω_{de}, though all these surveys cover a much larger area than COMBO-17 . Semboloni et al. (2006) also placed an upper bound on w, marginalizing over Ω_m, of $w < -0.8$ using the CFHTLS survey which covers 170 square degrees in 5 photometric bands. COMBO-17 has the best and most reliable photometric redshifts to date, due to the large number of bands, and so is ideal as a survey to test the 3D weak lensing constraints. COMBO-17 is then ideal for this proof of concept, however as shown in this thesis when much larger survey areas are available, a 5-band large area survey could constrain the dark energy equation of state much better than correspondingly smaller area 17-band survey.

I will apply both of the methods presented in Chapters 3 and 4 to the data available. The spectral test will be used to place conditional constraints on w, in this case assumed to be constant in redshift, and to place conditional constraints in the (σ_8, Ω_m) plane using two random COMBO-17 fields. The geometric test is applied to the A901/2 field and the clusters available are used to place a conditional constraint on w.

The results of this Chapter are a proof of method for these techniques. I have shown that in order to constrain the dark energy equation of state to $\Delta w \approx 0.01$ large and deep photometric surveys will be needed. The results in this Chapter will be compared to predictions made using the Fisher matrix formalism presented in Chapters 3 and 4. Brown et al. (2003) applied

2D weak lensing to the COMBO-17 data set to constrain the (σ_8, Ω_m) plane. The results presented in here, using the fully 3D spectral test on the same data set, should be in approximate agreement (but do slightly better than) a 2D analysis given the same data.

I will analyse the A901/2 field with the geometric test, as this test requires galaxy clusters for its analysis. I will analyse two random COMBO-17 fields using the spectral test, and neglect the A901/2 field since it contains known large over-densities which may bias the results using a cosmic shear analysis. This separation of the data allows for a combination of the two methods in the constraint of w. The A901/2 field was chosen specifically to contain a large clusters, the probability of finding these clusters in a randomly selected COMBO-17 sized field is approximately 2%, see Chapter 3, Section 3.6.1.

The structure of this Chapter is as follows: firstly the COMBO-17 data set will be introduced and discussed in Section 5.2, the application of the spectral test to the two random fields will be presented in Section 5.3, the geometric test and the results of applying the test to the A901/2 field will be presented in Section 5.4. The constraints from the A901/2 field (using the geometric ratio test) and the constraints from the two random fields (using the spectral test) will be combined in Section 5.5. A summary will be presented in Section 5.6.

5.2 The COMBO-17 Survey

The COMBO-17 survey is a 17-band photometric redshift survey with gravitational lensing quality r-band data (Wolf et al., 2001; Wolf et al., 2004). The survey consists of five fields each covering 0.26 square degrees. All of the fields were observed using the Wide-Field Imager (WFI) at the MPG/ESO 2.2m telescope on La Silla in Chile, with a 4×2 array of 2048×4096 pixel CCDs, each pixel subtending 0.238 arcseconds.

In this Chapter I will use three of the COMBO-17 fields, which were observed and reduced earlier than the remaining two, and for which there are redshift estimates and a shear catalogues available. One of the fields used, the A901/2 field, is centred on the Abell 901/2 supercluster which has previously been analysed in 2D by Gray et al (2002) and in 3D by Taylor et al. (2004). The A901/2 supercluster consists of three smaller clusters; A901a, A901b, A902, all at a redshift of $z \approx 0.16$. It should be noted that supercluster refers to a 'web of clusters', the individual clusters are much smaller $\sim 10^{14} M_{\odot}$ (see Taylor et al., 2004) than large strong

lensing clusters for example A1689. For an individual cluster the fractional error on w should decrease as the mass of the cluster increases. However in a large area survey there should be many more low and medium mass clusters than large clusters so that the constraint on w is dominated by the numerous medium mass clusters; for a detailed discussion see Chapter 3.

The COMBO-17 survey also observed a randomly selected area of sky, and a relatively empty, but well observed area. The S11 field was a randomly selected area of sky, that contains a moderately large cluster Abell 1364 at a redshift of $z \approx 0.11$. The CDFS field was chosen to overlap the Chandra Deep Field South, a relatively 'empty' region of sky containing no significant galaxy clusters. I only used galaxies with reliable photometric redshifts and with an r magnitude of $R \leq 24$.

5.2.1 Photometric Redshifts

Each of the COMBO-17 fields was observed in 17 different filters, with the intention of obtaining object classification and accurate photometric redshifts. In order to provide reliable redshifts, the filter set included five broad-band filters ($ubvri$) and 12 medium-band filters from 350 to 930 nm. This observing strategy allows simultaneous estimates of Spectral Energy Distribution (SED) classifications and photometric redshifts from empirically-based templates. Wolf et al. (2001) describe in detail the photometric redshift estimation methods used to obtain typical accuracies of $\sigma_z \approx 0.05$ for galaxies. I fit an empirical line to the data such that

$$\sigma_z(z) = 0.03(1+z)^{1.5}, \tag{5.1}$$

this $\sigma_z(z)$ is used in the likelihood analysis. It should be noted that the parameter constraints are not sensitive to the exact functional form of $\sigma_z(z)$.

5.2.2 Shear Measurements

Throughout the observing campaign the r filter was used in best seeing conditions, in order to provide a deep r-band image from which to measure the gravitational shear. Gray et al. (2002) discuss the procedure used to reduce the r-band imaging data, which totalled 21 hours for the three fields used. As described by Gray et al. (2002) and Brown et al. (2003) the 352 individual chip exposures for each field were registered using linear astrometric fits, with a 3σ rejection of bad pixels and columns.

The Kaiser, Squires & Broadhurst (1995; KSB) weak lensing measurement method was applied, using the `imcat` shear analysis package, to the reduced images (see Gray et al., 2002; Brown et al., 2003). This resulted in a catalogue of galaxies with centroids and shear estimates throughout the fields, corrected for the effects of anisotropic smearing and point spread function (PSF) circularisation. The photometric redshift estimates were appended to this catalogue for each galaxy from the standard COMBO-17 analysis of the full multicolour dataset. Of the 37,243 galaxies in the shear catalogue, 36% have a reliable photometric redshift, the remainder being fainter than the $R = 24$ reliability limit of the redshift survey. The requirement for this 3D lensing study, that the redshift of each galaxy be known, clearly results in an immediate reduction of available galaxies. It is apparent that most of the background sample is composed of galaxies that are small, and fainter than the magnitude limit of the redshift survey. These catalogues are the raw data used in this analysis. Brown et al. (2003) also include galaxies without assigned redshifts into their analysis, this can also be done in the case of 3D weak lensing however since this Chapter is a proof of concept for the 3D weak lensing methods the galaxies without redshifts will be left out of this analysis.

5.3 The 3D Spectral Test

I have applied the spectral test to the CDFS and S11 fields of COMBO-17 in order to constrain w and jointly constrain σ_8 and Ω_m. Bacon et al. (2005) analysed COMBO-17 using a real-space 3D cosmic shear method to constrain the evolution of dark matter clustering. The results presented in this Section are based on the methods outlined in Chapter 4.

5.3.1 3D Cosmic Shear Likelihood

To implement the 3D spectral test one first needs to calculate the coefficients of the devolved 3D shear field. The estimator for a given radial k-mode and angular ℓ-mode are calculated by summing over all galaxies, g each at a redshift z and position angular $\boldsymbol{\theta}$, in a given field catalogue, see equation (4.10),

$$\hat{\gamma}_i(k, \boldsymbol{\ell}) = \sqrt{\frac{2}{\pi}} \sum_g \gamma_i^g j_\ell(k r_g^0) \mathrm{e}^{-i\boldsymbol{\ell}.\boldsymbol{\theta}} W(z) \tag{5.2}$$

where subscript i denotes either the γ_1 or γ_2 component of the complex shear value ($\gamma = \gamma_1 + i\gamma_2$) for a given galaxy g or the estimator. The $j_\ell(z)$ are spherical Bessel functions. This

expansion is natural for a flat universe. Again, for non-flat universes, the appropriate functions are ultra-spherical Bessel functions $\Phi^{\ell}_{\beta}(y)$, but in the $\ell \gg 1$ and $k \gg$ (curvature scale)$^{-1}$ régime these are well approximated by ordinary Bessel functions $\Phi^{\ell}_{\beta}(y) \rightarrow j_{\ell}(kr)$ (Abbott and Schaefer, 1986; Zaladarriaga and Seljak, 2000). $W(z)$ is a weighting function which will be set to $W(z) = 1$ for the remainder of this Chapter, for an investigation of the effect of changing the weighting scheme see Section 4.5.5. r^0_g denotes the comoving distance to a galaxy calculated from the photometric redshift of the galaxy by assuming a fiducial cosmology, denoted by the superscript 0. In this case the fiducial cosmology is $\Omega_m = 0.3$, $\Omega_{de} = 0.7$, $\Omega_b = 0.04$, $h \equiv H_0/100$ kms^{-1}Mpc$^{-1} = 0.71$, $\sigma_8 = 0.8$, the equation of state of dark energy is assumed to be constant in redshift $w = -1$ i.e. $w_0 = -1$ and $w_a = 0$. I set also set the scalar spectral index to be $n_s = 1.0$ and its running $\alpha_n = 0.0$. The choice of the fiducial cosmology does not affect the results presented here, as long as the measured shear estimates and theoretical calculations use the same fiducial cosmology to calculate the transform coefficients. This fiducial cosmology simply acts, via the spherical Bessel functions, to weight the shear values in a particular way. The cosmological dependence comes from the shear values themselves γ^g_i, the cosmology dependence of the calculated covariance matrices come from modelling the shear-shear covariance. I have tested a variety of fiducial models and the results were indeed unaffected.

The whole data vector used in the likelihood analysis consists of four independent vectors at each k and $\boldsymbol{\ell}$: $\hat{\gamma}^R_1$, $\hat{\gamma}^I_1$, $\hat{\gamma}^R_2$, $\hat{\gamma}^I_2$, where the superscript R denotes the real part of the $\hat{\gamma}_i$ estimator and I the imaginary part. Note that this is for a given $\boldsymbol{\ell}$-mode.

I assume that the $\boldsymbol{\ell}$-modes are uncorrelated since I assume a periodicity in ℓ constrained by the survey geometry $\ell_i = \frac{2\pi n}{\Delta\Theta}$ where n is an integer. This is an approximation as, see equation (5.4), the power spectrum does depend on $\tilde{\boldsymbol{\ell}}$. For larger surveys this will not be an issue as the function $\mathcal{F} \rightarrow (\Delta\theta)^2 \delta^K_{\ell\tilde{\ell}} \delta^K_{\ell'\tilde{\ell}}$ for large $\Delta\theta$, see Section 4.2.5. The assumption that the $\boldsymbol{\ell}$-modes are uncorrelated may lead to slightly reduced errors though, since the $\boldsymbol{\ell}$-modes are constrained to be periodic, this assumption should be adequate as a first approximation. Also computing the full covariance would result in vast computational expense. I tested this to some degree by randomising the data, both the shear values and the angular position, and rerunning the likelihood analysis. Using the randomised data the most likely value of σ_8 was $\sigma_8 = 0$ (i.e. no cosmological information) as expected and the error on the measurement was similar to the actual data's constraint. All correlations between k-modes, for any given $\boldsymbol{\ell}$-mode are fully taken into account.

I assume then that the distribution of ℓ-modes can be represented by a multivariate Gaussian. The likelihood function for a given ℓ and set of cosmological parameters $\{\theta_\alpha\}$ is given by

$$\begin{aligned} -2\ln L_\ell(\theta_\alpha|\boldsymbol{D}) &= \sum_{A=\{R,I\}}\sum_{i=\{1,2\}} N_i^A \ln(2\pi) \\ &+ \ln(|\boldsymbol{C}_{i,\ell}(k,k')^{AA}|) \\ &+ \sum_{kk'} \hat{\gamma}^A_{i,\ell}(k)[\boldsymbol{C}^{-1}_{i,\ell}(k,k')]^{AA}\hat{\gamma}^{A,T}_{i,\ell}(k') \end{aligned} \tag{5.3}$$

where $A = \{R, I\}$ is a sum over the real and imaginary estimators and $i = \{1, 2\}$ is a sum over the γ_1 and γ_2 shear components. This log-likelihood is then summed over each independent $\boldsymbol{\ell} = (\ell_x, \ell_y)$ mode. Note that since there are four independent data vectors, two real and imaginary pairs, I only investigate the range $\ell_x \geq 0$ to avoid double counting.

Note that the average value of $\hat{\gamma}^A_i(k, \boldsymbol{\ell})$ is zero, so that information on the cosmological parameters comes from the dependence of the signal part of the covariance matrix $\boldsymbol{C}$ i.e. I adjust the parameters until the *covariance* of the model matches that of the data. This was the approach of Heavens and Taylor (1995); Ballinger, Heavens and Taylor (1995); Tadros et al. (1995); Percival et al. (2004) in analysis of large-scale galaxy data. The details of the covariance matrix derivation are given in Chapter 4, where the covariance matrix is given as the sum of signal and noise terms $\boldsymbol{C} = \mathbf{S} + \mathbf{N}$. The signal part of the covariance of $\gamma(k, \ell)$ for a survey of size $\Delta\theta \times \Delta\theta$ can be written as, see equation (4.26),

$$\langle\gamma^A_\alpha(k,\boldsymbol{\ell})\gamma^{A*}_\alpha(k',\boldsymbol{\ell}')\rangle_S = \int \frac{d^2\tilde{\boldsymbol{\ell}}}{(2\pi)^2} Q(\boldsymbol{\ell},\boldsymbol{\ell}',\tilde{\boldsymbol{\ell}},k,k')|X_{\tilde{\boldsymbol{\ell}}}|^2 \int_{-\Delta\theta/2}^{\Delta\theta/2} d^2\boldsymbol{\theta} \mathrm{e}^{-i(\boldsymbol{\ell}-\tilde{\boldsymbol{\ell}}).\boldsymbol{\theta}} \int_{-\Delta\theta/2}^{\Delta\theta/2} d^2\boldsymbol{\theta}' \mathrm{e}^{-i(\boldsymbol{\ell}'-\tilde{\boldsymbol{\ell}}).\boldsymbol{\theta}'} \tag{5.4}$$

The $X_{\boldsymbol{\ell}}$ factor comes from transforming from the potential to the shear field and is given by equation (4.8).

The Q matrix is given by equation (4.27),

$$Q(\boldsymbol{\ell},\boldsymbol{\ell}',\tilde{\boldsymbol{\ell}},k,k') = \frac{9\Omega_m^2 H_0^4}{8\pi^2 c^4}\int \frac{d\tilde{k}}{\tilde{k}^2} G(\boldsymbol{\ell},\tilde{\boldsymbol{\ell}},k,\tilde{k})G(\boldsymbol{\ell}',\tilde{\boldsymbol{\ell}},k',\tilde{k}) \tag{5.5}$$

note the extra factor of $1/2$ as here individual data vectors are used (see Section 4.2.6), where see equation (4.28),

$$G(\boldsymbol{\ell},\tilde{\boldsymbol{\ell}},k,\tilde{k}) \equiv k\int dz\, dz_p\, \bar{n}_z(z_p)W(z_p)p(z_p|z)U(\tilde{\boldsymbol{\ell}},r,\tilde{k})j_\ell(kr^0) \tag{5.6}$$

where z_p is an integral over redshift given an assumed cosmology, and the integral over z uses the cosmology to be tested. $\bar{n}_z(z)$ is the predicted number density of objects as a function of

redshift which is measured from the survey in question. $p(z_p|z)$ is a probability distribution in redshift which, by convolving with the redshift distribution, takes into account the uncertainty in redshift. I will assume a Gaussian probability distribution with the width being the measured photometric redshift as a function of redshift, see Section 5.2.1. In equation (5.6) $W(z)$ is an arbitrary weighting function of the data which I set to $W(z) = 1$ for the remainder of this Chapter.

The U matrix used in equation (5.6) is given by equation (4.29),

$$U(\tilde{\boldsymbol{\ell}}, r, \tilde{k}) \equiv \int_0^r d\tilde{r}\, \frac{F_K(r,\tilde{r})}{a(\tilde{r})} \sqrt{P_\delta(\tilde{k};\tilde{r})}\, j_{\tilde{\ell}}(\tilde{k}\tilde{r}), \tag{5.7}$$

where $P_\delta(k;r)$ is the matter power spectrum for the cosmology to be tested. I compute the nonlinear power spectrum using the fitting formulae of Smith et al. (2003), and linear growth rates given by Linder and Jenkins (2003), see Section 1.5.2. $F_K(r,r') = (1/r' - 1/r)$ for a flat universe (assumed in this Chapter) and $a(r)$ is the dimensionless scale factor, see equation (1.20).

As discussed in Section 4.2.5 the integrals over $\boldsymbol{\theta}$ in equation (5.4) can be evaluated so that

$$\langle \gamma_\alpha^A(k,\boldsymbol{\ell}) \gamma_\alpha^{A*}(k',\boldsymbol{\ell}')\rangle_S = \int \frac{d^2\tilde{\boldsymbol{\ell}}}{(2\pi)^2} Q(\boldsymbol{\ell},\boldsymbol{\ell}',\tilde{\boldsymbol{\ell}},k,k') |X_{\tilde{\boldsymbol{\ell}}}|^2 \mathcal{F}(\boldsymbol{\ell},\boldsymbol{\ell}',\tilde{\boldsymbol{\ell}}), \tag{5.8}$$

where

$$\mathcal{F}(\boldsymbol{\ell},\boldsymbol{\ell}',\tilde{\boldsymbol{\ell}}) \equiv \prod_{i=x,y} \frac{4}{(\tilde{\boldsymbol{\ell}}-\boldsymbol{\ell})_i (\tilde{\boldsymbol{\ell}}-\boldsymbol{\ell}')_i} \sin\left[(\tilde{\boldsymbol{\ell}}-\boldsymbol{\ell})_i \frac{\Delta\theta}{2}\right] \sin\left[(\tilde{\boldsymbol{\ell}}-\boldsymbol{\ell}')_i \frac{\Delta\theta}{2}\right] \tag{5.9}$$

$i = x, y$ represents the x and y components of a Cartesian coordinate system for a survey.

Section 4.2.6 derives the shot noise part of the covariance matrix to be

$$\langle \hat{\gamma}_\alpha^A(k,\boldsymbol{\ell}) \hat{\gamma}_\beta^{A*}(k',\boldsymbol{\ell}')\rangle_{SN} = \frac{\sigma_\epsilon^2 \Delta\Omega}{8\pi^2} \int dz\, \bar{n}_z(z) k j_\ell(kr^0) k' j_{\ell'}(k'r^0) W^2(z)\, \delta^K_{\alpha\beta} \delta^K_{\ell\ell'}, \tag{5.10}$$

note the extra factor of $1/2$ as here individual data vectors are used (see Section 4.2.6). σ_ϵ is measured from the data, for the CDFS field $\sigma_\epsilon = 0.19$ and for the S11 field $\sigma_\epsilon = 0.22$.

The ℓ and k ranges and resolutions used are as follows, see Section 4.4.2 for a detailed investigation into convergence issues. In integrating over $\tilde{\boldsymbol{\ell}}$ in equation (5.4) I found that the signal converges at $\Delta\tilde{\ell}_i = 100$ as shown in Figure 5.1 and for the range $(\ell_i - 1500) < \tilde{\ell}_i < (\ell_i + 1500)$ where $i = x, y$ as shown in Figure 5.2. The k resolution used was $\Delta k = 2 \times 10^{-3}$ Mpc^{-1}, as it was found that the signal part of the covariance matrix converges at $\Delta k \approx (2\pi/r_{\max}) \approx$

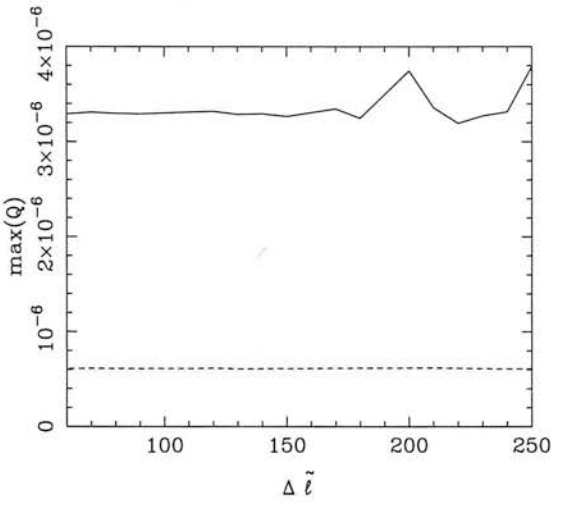

Figure 5.1: The maximum value of the signal part of the covariance matrix for the CDFS field as a function of $\Delta\tilde{\ell}$, for an $\tilde{\ell}$ range of $(\ell_i - 1500) < \tilde{\ell}_i < (\ell_i + 1500)$ where $i = x, y$. The lines shown are for the fundamental ℓ-mode $\ell_x = 671$ and $\ell_y = 0$ (solid line), and $\ell_x = 671$ and $\ell_y = 671$ ($|\boldsymbol{\ell}| = 948$; dashed line).

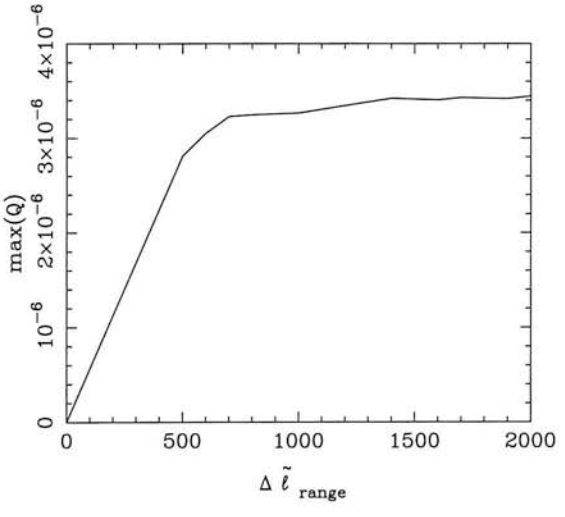

Figure 5.2: The maximum value of the signal part of the covariance matrix for the CDFS field as a function of $\Delta\tilde{\ell}_{\rm range}$, where the range is given by $(\ell_i - \Delta\tilde{\ell}_{\rm range}) < \tilde{\ell}_i < (\ell_i + \Delta\tilde{\ell}_{\rm range})$ and $i = x, y$ for a resolution of $\Delta\tilde{\ell} = 150$. The line shown is for the fundamental ℓ-mode $\ell_x = 671$ and $\ell_y = 0$.

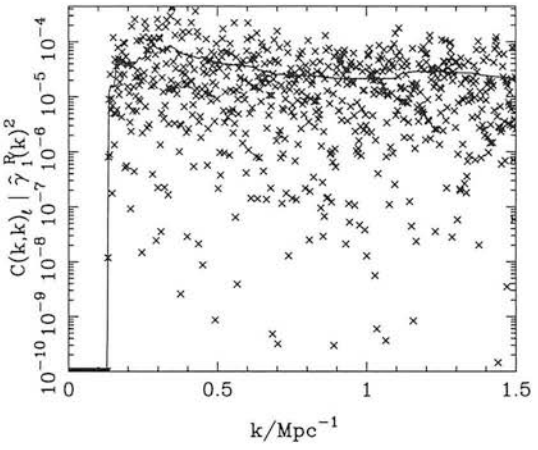

Figure 5.3: An example of the diagonal elements of the calculated covariance matrix $\boldsymbol{C}$ and the data, note this is not a fit to the data. This example shows the diagonal k-modes only, for the $\ell_x = 0$, $\ell_y = -671$ mode ($|\boldsymbol{\ell}| = 671$) for the CDFS field using the fiducial cosmology. The solid line shows the covariance matrices diagonal elements, the crosses show the measured values of the $\hat{\gamma}_1^R$ data vector squared.

2×10^{-3} Mpc^{-1} where $r_{\max}$ is the distance corresponding to a maximum redshift of $z \approx 1$. The k range used was $0.01 < k < 1.5$ Mpc^{-1}. The ℓ values available are constrained by the survey geometry, $\ell_i = \frac{2\pi n}{\Delta\Theta}$ where n is an integer. I use all modes with $|\boldsymbol{\ell}| \leq 2500$ to avoid the highly non-linear, possibly non-Gaussian, régime (Zhan & Knox, 2004; White, 2004). The very highest ℓ-modes analysed may be slightly non-Gaussian, and so slightly in error. Note that since $\boldsymbol{\ell} = (\ell_x, \ell_y)$ this corresponds to 26 independent $\boldsymbol{\ell}$-modes, the field size is actually slightly larger than $30'$ at 0.5367 degrees on a side which corresponds to a fundamental mode of $\ell_1 = 671$. I tested the lower ℓ limit and found no change in the cosmological constraints by using $\ell_1 = 700$ instead showing that these results are robust to the details of the lower ℓ range used.

The use of spherical Bessel functions in the coefficients used means that, for any given $\boldsymbol{\ell}$-mode, there is a range of k for which the signal is zero up until a particular value of $k \approx |\boldsymbol{\ell}|/r_{\max}$, see Castro et al. (2005). Figure 5.3 shows an illustrative example of this effect. These zero modes result in singular covariance matrices, however this behaviour can be taken into account using the prescription given in Section 5.3.2.

5.3.2 Removal of Singular Modes

In this Section I will describe how any singular $(k,\, \ell)$ modes can be removed from the covariance matrices used in the spectral tests likelihood analysis.

I begin with a square covariance matrix $\boldsymbol{C}$ which can be decomposed using a standard singular value decomposition (SVD) into

$$\boldsymbol{C} = \boldsymbol{U}\boldsymbol{W}\boldsymbol{V}^T, \tag{5.11}$$

where $\boldsymbol{W}$ is a diagonal matrix that contains the singular values. Note that $\boldsymbol{U}$ and $\boldsymbol{V}$ are eigenvector matrices of $\boldsymbol{C}\boldsymbol{C}^T$ and that $\boldsymbol{U}^{-1} = \boldsymbol{U}^T$ and $\boldsymbol{V}^{-1} = \boldsymbol{V}^T$. The covariance matrices are symmetric so that $\boldsymbol{U} = \boldsymbol{V}$ in this case. Now consider one of the data vectors $\hat{\gamma}_i^A(k, \boldsymbol{\ell})$ represented by $\boldsymbol{x}$ which can be transformed to a new data vector $\boldsymbol{y}$ via

$$\boldsymbol{y} = \mathbf{B}\boldsymbol{x} \tag{5.12}$$

where $\mathbf{B}$ can be any, not necessarily square, transformation matrix. A new covariance can then be defined

$$\boldsymbol{C}'_{ij} \equiv \langle \boldsymbol{y}_i \boldsymbol{y}_j \rangle = \langle \mathbf{B}_{ik}\boldsymbol{x}_k \mathbf{B}_{jl}\boldsymbol{x}_l \rangle = \mathbf{B}_{ik}\mathbf{B}_{jl}\boldsymbol{C}_{kl}, \tag{5.13}$$

which implies that

$$\boldsymbol{C}' = \mathbf{B}\boldsymbol{C}\mathbf{B}^T. \tag{5.14}$$

The choice of transformation, in this case, is motivated by decomposing $\boldsymbol{C}$ using a Cholesky decomposition which yields $\boldsymbol{C} = \boldsymbol{U}\boldsymbol{W}\boldsymbol{U}^T = \mathbf{L}\mathbf{L}^T$, where $\mathbf{L} = \boldsymbol{U}\boldsymbol{W}^{1/2}$. So I use $\mathbf{B} = \tilde{\boldsymbol{W}}^{-1/2}\boldsymbol{U}^{-1}$ where $\tilde{\boldsymbol{W}}^{-1/2} = \boldsymbol{W}^{-1/2}$ except that the elements of the inverse $\boldsymbol{W}$ matrix $1/w_i$ have been replaced with zero if $(1/w_i) \leq$(threshold) where the threshold represents machine precision (see Numerical Recipes; Press, 2002). The matrix $\mathbf{B}$ now contains a band of values below which zeros remove any singular modes from either the data vector or the covariance matrix via equations (5.12) and (5.14).

The transformation is performed using a fiducial cosmology (the choice of this does not affect the results) to yield a transformation matrix $\mathbf{B}$ which is then used throughout. $\boldsymbol{y}$ and $\boldsymbol{C}'$ replace $\boldsymbol{x}$ and $\boldsymbol{C}$ in the likelihood analysis.

5.3.3 3D Cosmic Shear Results

This Section presents the result of applying the spectral test to the CDFS and S11 fields. The results will be compared with the Fisher matrix analysis detailed in Chapter 4 and with the 2D cosmic shear analysis of Brown et al. (2003). Unless otherwise stated the fiducial cosmology that will be assumed throughout this Section is $\Omega_m = 0.3, \Omega_{de} = 0.7, \Omega_b = 0.04, h = 0.71, \sigma_8 = 0.8, w = -1.0, n_s = 1.0, \alpha_n = 0.0$, any constraints for particular parameters are conditional on these values.

Figure 5.4 shows the two-parameter 1-σ contours from applying the spectral test to the CDFS and S11 fields only. The dashed line in Figure 5.4 shows the two-parameter 1-σ contours from Brown et al. (2003) where a traditional 2D cosmic shear analysis was performed on all three COMBO fields, CDFS, S11 and A901/2 using only galaxies with accurate redshifts. It can be seen that the 3D spectral test constrains a very similar area in the (σ_8, Ω_m) plane, particularly at the concordance values of σ_8 and Ω_m using less than two thirds the number of galaxies used in the 2D analysis (since the A901/2 field contains more galaxies than the CDFS and S11 only 63% of the galaxies used in the 2D analysis have been analysed).

Note that the contours drawn in all the likelihood plots assume a Gaussian likelihood surface. The one-parameter 1-σ constraints are then $\ln(L) - \ln(L_{\max}) = -0.5$ and for the two-parameter 1-σ contours this is $\ln(L) - \ln(L_{\max}) = -1.15$. This approximation should be valid for the one-parameter case as the likelihood surfaces are approximately Gaussian, although it may yield incorrect contours in the two-parameter case.

A common way to express the constraint in the (σ_8, Ω_m) plane is to constrain the parameterisation $\sigma_8(\Omega_m/0.3)^\beta = \alpha$, where β expresses the curvature of the constraint and α the normalisation of the curve. Figure 5.5 shows the two-parameter 1-σ constraints on these two parameters. The spectral test constrains the parameters to be

$$\begin{aligned} \alpha &= 1.06^{+0.17}_{-0.16} \\ \beta &= 0.57^{+0.19}_{-0.19} \end{aligned} \tag{5.15}$$

whereas the 2D analysis constrains the values to be $\alpha = 1.08^{+0.13}_{-0.13}$ and $\beta = 0.62^{+0.12}_{-0.14}$. The constraints using the 3D and 2D analysis are consistent. These results agree with Brown et al. (2003) when we include the same sort of data. Also note that Brown et al. (2003) use approximately 4 times the number of ℓ-modes, going upto a maximum of $\ell \approx 10,000$. The main result of $\sigma_8(\Omega_m/0.3)^{0.49} = 0.72^{+0.08}_{-0.09}$ in Brown et al. (2003) included galaxies with

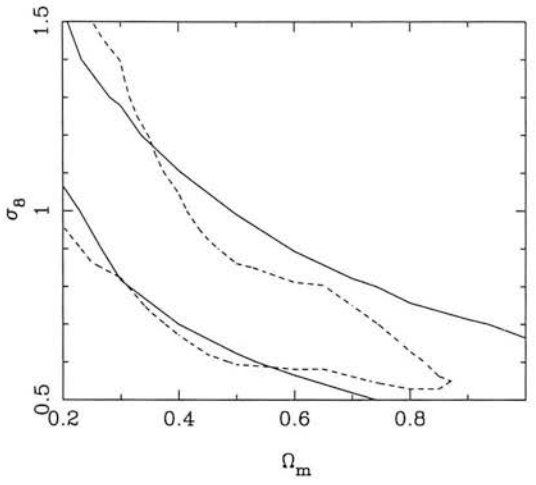

Figure 5.4: The solid lines show the two-parameter 1-σ conditional constraints in the (σ_8, Ω_m) plane from applying the spectral test to the CDFS and S11 fields only. The dashed contours show the two-parameter 1-σ conditional constraints from the Brown et al. (2003) analysis using 50% more fields: CDFS, S11 and A901/2.

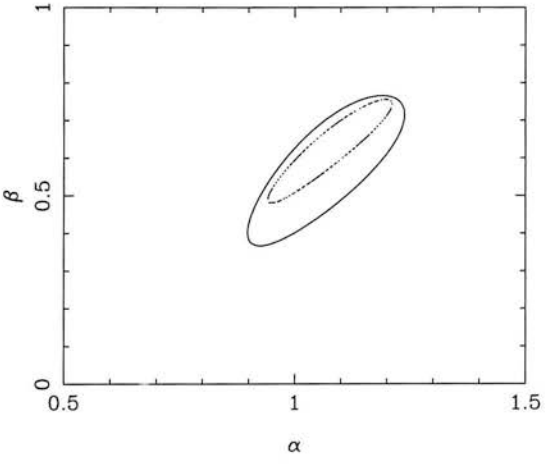

Figure 5.5: Constraining the parameters α and β in the functional fit $\sigma_8(\Omega_m/0.3)^\beta = \alpha$. The solid lines show the two-parameter 1-σ constraints in the (α, β) plane from applying the spectral test to the CDFS and S11 fields only. The dashed contours show the two-parameter 1-σ constraints from the Brown et al. (2003) analysis using the CDFS, S11 and A901/2 fields.

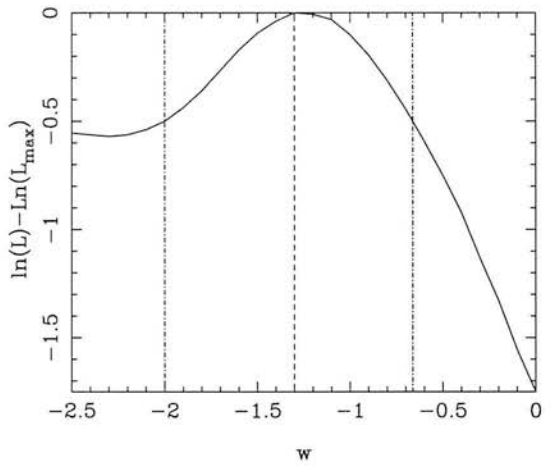

Figure 5.6: The one-parameter maximum likelihood constraint on w from the CDFS and S11 fields using the spectral test. The dashed line shows the most likely value and the dot-dashed show the one-parameter 1-σ constraints.

unknown redshifts, the result shown here is their result when considering galaxies with only reliable redshift estimates. Since this Chapter is a proof of concept for the 3D weak lensing methods I only used galaxies with reliable redshifts, however galaxies with unknown redshifts could also be included in this analysis.

The Fisher matrix calculations in Chapter 4 can be used to predict the estimated uncertainties from this analysis. Fisher matrix predictions, by construction, predict Gaussian likelihood surfaces, the curved constraint shown here highlights one limitation of the Fisher matrix technique to predict uncertainties when the errors are so large. However, using the techniques outlined in Chapter 4 I predict, for two COMBO-17 fields, a conditional constraint of $\Delta\sigma_8 = 0.19$ (assuming $\Omega_m = 0.3$). This is in agreement with the measured conditional error of $\sigma_8(\Omega_m = 0.3) = 1.05 \pm 0.20$, highlighting that the predictions made in this thesis are reliable. The values used in the Fisher matrix calculation were an area of $A = 0.52$ square degrees, to a median redshift of $z_{\rm median} = 0.8$ using the photometric redshift error given in equation (5.1).

Figure 5.6 shows the conditional constraint on w from the CDFS and S11 field only using the spectral test. The constraint is asymmetric in that the range $w < -1$ is more likely than $w > -1$. This is due to the fact that values of $w < -1$ represent dark energy scenarios in which the dark energy density is less in the past, so it is more difficult to constrain its equation of state. Semboloni et al. (2006) also found a similar asymmetric constraint when using weak

lensing tomography applied to the CFHTLS survey. The conditional constraint on w is

$$w = -1.27^{+0.64}_{-0.70}. \tag{5.16}$$

This result is consistent with other observations (for example Spergel et al., 2006) and with a cosmological constant model for dark energy. The Fisher matrix calculations presented in Chapter 4 predict a conditional error on w from two COMBO-17 fields to be $\Delta w = 0.62$ which is in agreement with the constraints presented here.

Typical reduced χ^2 values for a given ℓ-mode in the CDFS and S11 fields analysis are $\chi^2_{CDFS} \approx 1.01$ and $\chi^2_{S11} \approx 0.98$, the number of degrees of freedom for a given ℓ-mode are the corresponding number of non-singular k-modes used in the analysis, typically ~ 600 for an average ℓ-mode. The range of χ^2 values are consistent with a good fit to the data.

5.4 The Geometric Ratio Test

I will now apply the geometric test to the A901/2 field of the COMBO-17 survey in order to constrain w, and compare the measured constraint with the predicted constraint from a Fisher matrix calculation. The results presented in this Section are an extension and use of the methods outlined in Chapter 3. I will briefly review the main points of the geometric test with the objective of applying the method to data being foremost.

5.4.1 Geometric Ratio Likelihood

To implement the geometric test, I have first selected the peaks in the convergence field of the three clusters, A901a, A901b and A902. Taylor et al. (2004) have shown that there is a fourth cluster, CB1, in this field, which lies behind A902 at a redshift of $z = 0.42$. Here I will ignore the contribution of this cluster, although this will in principle bias the results slightly. To estimate the effect of the bias the CB1 cluster increases the tangential shear, at $z \gtrsim 0.4$, by $\delta\gamma_t \lesssim 0.02$ (see Taylor et al, 2004). Using the simple error formula from Chapter 3 this increase in tangential shear may bias the value of w by $\delta w \lesssim +0.03$.

Having found the centre of each cluster I averaged the tangential shear in annuli around each cluster in a series of redshift bins, following Taylor et al. (2004; see Figure 3), the width of the

redshift bins is equal to the photometric redshift at the redshift of the bin. Using the result from Section 5.2.1 I take a constant bin width of $\Delta z = 0.05$. The error on the tangential shear at each radius, given by equation (2.51), for a given redshift bin, was estimated by the orthogonal radial shear signal, equation (2.51). The tangential shear in each angular and redshift bin was then fitted with a least-square fit to a singular isothermal sphere (SIS) profile, see Section 2.1.7;

$$\gamma_{t,\mathrm{SIS}}(\theta, z) = \frac{1}{2\theta}\theta_E(z) \tag{5.17}$$

where $\theta_E(z)$ is the Einstein ring radius which parameterises the amplitude of the tangential shear as a function of source redshift, see below for a detailed description of this method. Here D denotes data and R is the theoretical estimate for the shear ratio, dependent on cosmology. The theoretical ratio of shears, R_{ij} for a pair of redshift bins can be estimated by

$$R_{ij} = \frac{\theta_E(z_i)}{\theta_E(z_j)} = \frac{(r_{\mathrm{lens}} - r_i)/r_i}{(r_{\mathrm{lens}} - r_j)/r_j} \tag{5.18}$$

where r is the predicted comoving distance for a given cosmology. The data is simply the ratio of measured tangential shears

$$D_{ij} = \frac{\gamma_t(z_i)}{\gamma_t(z_j)}. \tag{5.19}$$

The measured ratio D_{ij} and the calculated ratio R_{ij} are then used in the likelihood function, summing over all pair-pair configurations given by

$$-2\ln L_c(\Omega_{de}, \Omega_m, w, w_a|\boldsymbol{D}) = \sum_{\mu,\nu}(R_\mu - D_\mu)[\boldsymbol{C}^{RR}_{\mu\nu}]^{-1}(R_\nu - D_\nu), \tag{5.20}$$

for a given cluster. The notation for a pair of background bins has been compressed as $\mu = (i, j)$ and $\nu = (m, n)$, and all degenerate pair-pair combinations have been accounted for. The likelihood functions for multiple clusters are multiplied. Two examples of ways to create all non degenerate pair-pair combinations are: for N redshift bins, either $\gamma(z_1)/\gamma(z_i)$ for all $1 < i \leq N$; or $\gamma(z_i)/\gamma(z_{i+1})$ for all $i \leq N$.

The covariance matrix for shear ratios is written as

$$\boldsymbol{C}^{RR}_{\nu\mu} \equiv \langle \Delta R_\nu \Delta R_\mu \rangle. \tag{5.21}$$

The full covariance matrix includes shot noise and cosmic shear terms. For a full description see Chapter 3, Section 3.5.2.

In the case of the likelihood function given in equation (5.20) the mean in the likelihood is varied as a function of cosmology, the noise (covariance weighting) is measured directly from

the data. This is done by fitting an isothermal profile to the tangential shear with one free parameter γ_0 where $\gamma_t(\theta, z) = \gamma_0(z)/\theta$. By minimising using a least squares fitting the most likely value of γ_0 is

$$\gamma_0(z) = \frac{\sum_i \frac{\gamma_i}{\sigma_i^2 \theta_i}}{\sum_i \frac{1}{\sigma_i^2 \theta_i}} \tag{5.22}$$

where i is a sum over radial annuli at an angle θ_i at a particular redshift. γ_i is the average tangential shear in the radial and redshift bin i. σ_i is the cross-component shear in the same angular and redshift bin. The error on this value of γ_0 is given by

$$\sigma^2_{\gamma_0} = \left[\sum_i (\sigma_i^2 \theta_i) \right]^{-1} . \tag{5.23}$$

Following the methodology of Gray et al. (2004) (who used the `etprofile` tool from the `imcat` shear analysis package) I take logarithmically spaced bins with a logarithmic width of $\Delta \ln r = 0.25$ around the clusters centre from $50''$ to $200''$ at each redshift and calculate the average tangential and cross-component shear in each bin. The SIS fit and the error on this fit are then substituted into the covariance matrix, see equation (3.30),

$$\frac{\langle \Delta R_{ij} \Delta R_{mn} \rangle}{R_{ij} R_{mn}} = \left(\frac{\sigma_{\gamma_{0i}}}{\gamma_i} \right)^2 \left(\delta^K_{im} - \delta^K_{in} \right) + \left(\frac{\sigma_{\gamma_{0j}}}{\gamma_j} \right)^2 \left(\delta^K_{jn} - \delta^K_{jm} \right) , \tag{5.24}$$

where $\gamma_i = \gamma_0(z_i)$ and $\gamma_j = \gamma_0(z_j)$. The error on the SIS fit in a given redshift bin z_i is $\sigma_{\gamma_{0i}}$. The measured ratio is $D_{ij} = \gamma_0(z_i)/\gamma_0(z_j)$.

Note that the assumption of a SIS is not necessary, in the case of a large data set the average tangential shear in an aperture could be measured directly, and the cross-component shear for the error with no assumption on the radial tangential shear profile made. Since this data set consists of only three small clusters the SIS was adopted so that a signal could be measured, and for the radii from the centre of the clusters probed should be an adequate approximation. This assumption may however slightly decrease the errors for these results.

5.4.2 Geometric Ratio Results

The results are shown as a 1D likelihood plot in Figure 5.7. The result is conditional on $\Omega_m = 0.30$, $\Omega_{de} = 0.70$ and $w_a = 0.0$. The dashed line the most likely value, the dot-dashed lines are the one-parameter 1-σ (68%) confidence limits. The geometric tests constraint on w from the A901/2 field is:

$$w = -0.11^{+1.05}_{-1.29}. \tag{5.25}$$

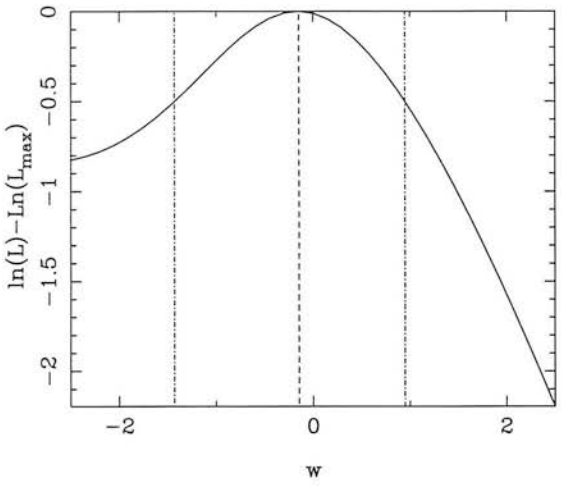

Figure 5.7: The dark energy geometric test applied to the supercluster Abell A901/2. The dashed line marks the maximum likelihood value, the dot-dashed lines show the one-parameter 1-σ limits. Note that the x-axis scale has been extended relative to Figures 5.6 and 5.9 to encompass the confidence limits of this analysis.

The constraint again shows an asymmetry between the $w < -1$ and $w > -1$ regions for the same reason given in the spectral tests constraint, that $w < -1$ represents a lower dark energy density in the past. The minimum χ^2 value is $\chi^2_{\rm min} = 122$ which is consistent with the number of degrees of freedom in the experiment. Given that $z_{\rm max} \approx 2.0$ and $\Delta z \approx 0.05$ and I have analysed $N_{\rm cluster} = 3$ clusters the predicted $\chi^2_{\rm min} = (z_{\rm max}/\Delta z)N_{\rm cluster} \approx 120$ so that $\chi^2_{\rm reduced} = 1.01$ and should be $\chi^2_{\rm reduced} = 1 \pm 0.12$. Figure 5.8 shows the shear ratio measured from the A901a cluster as a function of redshift using the $\gamma(z_i)/\gamma(z_{i+1})$ pair-pair combination, and the theoretical curve for the fiducial cosmology (note this is not a fit to the data).

The result is consistent with other constraints on w, and the confidence limits allow for most dark energy models. It should be emphasised that this constraint comes from only three small clusters.

The Fisher matrix calculations presented in Chapter 3 predict a conditional constraint on w of $\Delta w = 1.10$ for COMBO-17 which was created by assuming only three clusters at $z = 0.16$ with $\mathrm{M_{cluster}} = 10^{14}\mathrm{M}_\odot$. The predicted conditional constraint is approximately the same as the measured constraint, thus verifying the Fisher matrix methodology.

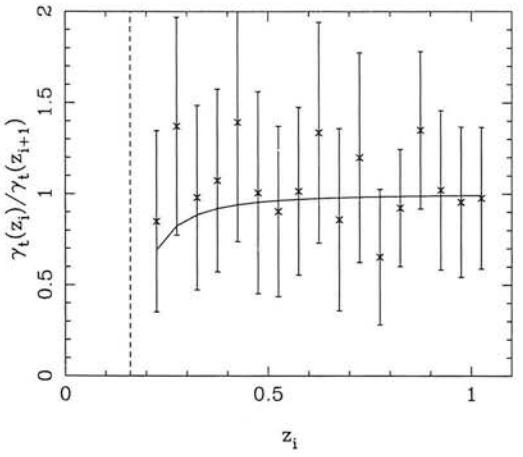

Figure 5.8: An example of the shear-ratio data from the A901/2 field, the crosses with error bars shown as measured from the data. The solid curve shows the expected shear-ratio for the fiducial cosmology assumed in this Chapter. The dashed line is the redshift of the cluster.

5.5 A Combined Constraint on w

Since the A901/2 field was analysed separately from the CDFS and S11 fields the geometric tests constraint can be combined with the constraint from the spectral test. Figure 5.9 shows the result of combining the constraints shown in Figure 5.6 and 5.7 from the CDFS and S11 fields and the A901/2 field respectively. The resulting conditional constraint on w is

$$w = -1.08^{+0.63}_{-0.58}. \tag{5.26}$$

This result demonstrates the value of combining the two techniques that can analyse distinct parts of the data. A region of particularly high density such as the A901/2 field would raise issues of cosmic variance in a cosmic shear/spectral approach, however the geometric test necessarily needs such areas. The effect on the spectral tests constraint of including the geometric constraint results in the most likely value being more positive, and a slight decrease in the error. The most likely value of $w = -1.08$ is in complete agreement with other observations (for example Semboloni et al, 2006; Spergel et al., 2006) and is close to the value of w expected if dark energy is a cosmological constant. The caveat on this conclusion is that it is conditional on the other cosmological parameters being fixed, and the error on w is still fairly large.

The second method used was the geometric test, which takes the ratio of the tangential shear around galaxy clusters at different redshifts. I applied this analysis to the A901/2 field which contains three small clusters conditionally constraining $w = -0.11^{+1.05}_{-1.29}$.

Combining the constraint on w from the geometric tests application to the A901/2 field and the spectral tests constraint from CDFS and S11 I conditionally constrain $w = -1.08^{+0.63}_{-0.58}$. For discussions on the relative merit of the two methods and varying observing strategies see Chapters 3 and 4. These Chapters also discuss the effects of systematics, number of observing bands used and the effects of the assumed fiducial cosmology.

The constraints presented here do not improve much on our cosmological understanding, they are however in agreement with the currently accepted concordance model. The constraint on w from such a small data set is encouraging and, with the warning and caveat that it is a conditional error, it is *a forteriori* consistent with dark energy being a cosmological constant.

In order for these results to become more complete I could marginalize over an increasingly large cosmological parameter set. However this would rapidly result in a loss of any constraint, for such a small survey area, due to degeneracies between the parameters as shown in Chapters 3 and 4. The result errors agree with the Fisher matrix predictions and are a very reliable proof of concept for these methods.

The agreement of the results presented here with the Fisher matrix predictions using the methods presented in Chapters 3 and 4 are a validation of the Fisher matrix framework and an encouraging sign that the predictions made in this thesis are robust and accurate.

The remaining Chapters will begin to conclude the work presented in this thesis. Chapter 6 will address some subjective questions that cosmologists are faced with when studying dark energy, and attempt to forecast the future of dark energy prediction. I will discuss future dark energy experiments and produce a timeline covering the next 15 years detailing how our state of dark energy knowledge could dramatically improve using the techniques presented in this thesis.

Chapter 6

Future Dark Energy Constraints

The cosmological parameter predictions made in this thesis, via the Fisher matrix framework, allow the marginal errors for any given 3D weak lensing, CMB, BAO or SNIa experiment to be predicted. Since the determination of the nature of dark energy is of such importance to cosmology, and indeed our understanding of particle physics, there exists a menagerie of proposed and existing experiments all designed to answer the dark energy question to some degree by placing a new, and tighter, constraint on the dark energy equation of state. These experiments, necessarily 3D (either spectroscopically or photometrically), will use a variety of cosmological probes, including 3D weak lensing in isolation or in combination with other probes. This Chapter will briefly discuss the current and future prospects for the determining the equation of state of dark energy. The issues of how accurate must it be determined, which probes are most promising and which experiments will provide the tightest constraints will be discussed. All of the calculations used in this Chapter are based on Fisher matrix calculations detailed in Chapters 3 and 4.

6.1 Introduction

This Chapter will discuss the future prospects for determining the nature of dark energy. This will be done by highlighting proposed experiments and using the Fisher matrix framework of this thesis to predict future constraints. CMB, BAO and SNIa experiments will be considered as well as 3D weak lensing. The methods themselves, as well as the experiments which propose to use the methods, will be discussed in terms of their relative merit.

The Dark Energy Task Force (DETF) report considers the same future scenario, and comes to similar conclusions. The report highlights four stages of development which they define as: Stage I representing what is currently known; Stage II are currently on going experiments that, once completed, will provide new constraints on dark energy; Stage III are near-term projects which are currently proposed; Stage IV are next-generation all sky, or near all sky, photometric surveys with median redshifts of $z_m \approx 1$. I will adopt this categorisation in this Chapter for clarity, as it provides a simple way to gauge the expected return relative to our current state of knowledge. The DETF also introduce optimistic and pessimistic, predictions for Stage IV projects, as the performance of such ambitious missions is subject to systematics. I introduce a further Stage V category which I define as a depth limited survey, of the type that is inconceivable given currently planned or proposed instruments. The results from a Stage V project may represent the limit of what we can know, given current methods, about the dark energy equation of state.

The structure of this Chapter is as follows. Section 6.2 will discuss some issues concerning the determination of the equation of state. Section 6.3 will present some current, proposed and next-generation dark energy experiments and Section 6.4 will present the predictions for these future experiments.

6.2 Dark Energy Issues

How accurately must the equation of state of dark energy be known before it is considered conclusive that an answer is known? It could be argued that since there is currently a plethora of dark energy models available all one could do is convincingly rule out any particular dark energy model, and that there could always be one or more models that fit the data no matter how accurately the equation of state is known. Trotta & Bower (2006) use Bayesian model selection

to argue that in order to distinguish dark energy models that represent small departures from a cosmological constant the equation of state needs to be known to $\Delta(w) \approx 4 \times 10^{-4}$. However, in order to rule out fluid-like dark energy models a more modest $\Delta(w) \approx 3 \times 10^{-2}$ is required. Linder & Miquel (2004) define a bound of $|w_a| \lesssim 2$ in which the rate of change of w is of the order of the change in the Hubble parameter and argue that a value outside this bound would be strong evidence for a non-cosmological constant. In this case a measurement of $\Delta w_a = 0.67$ would represent a 3σ significance of detecting a cosmological constant-like term, or not. However in the absence of any compelling theory arguments such as these seem inadequate, and one is tempted to answer the question posed in this paragraph with: "as accurately as possible".

The question of the nature of dark energy can be sub-divided into two potentially more answerable questions: is dark energy a cosmological constant? If a cosmological constant is ruled out then: what is dark energy? The first of these questions should be the primary goal of the community, and indeed will be as an answer to this question requires less accuracy. As an example a result of $w(z_p) = -0.8 \pm 0.06$ where z_p is *any* pivot redshift would represent a 3σ deviation from a cosmological constant model. Of course the equation of state may be constrained at many different pivot redshifts, as shown by this thesis, potentially yielding many 3σ results. However a result such a this would not reveal what dark energy is and a higher accuracy over a much larger redshift range would be required to illuminate the nature of dark energy.

Another way to test for a cosmological constant, and to address the first dark energy question, is to compare methods that independently measure the dark energy effect on the geometry and the growth of structure. Within the context of general relativity (GR) there should be a one-to-one relation between the comoving distance relations $D(z)$ and the growth factor $G(z)$. An inconsistency between these two values could imply a deviation from GR on large scales, potentially related to dark energy. As an example if the geometric test and a SNIa experiments joint constraints were inconsistent with the combined spectral test and CMB constraints this would highlight an underlying problem with GR. Indeed since GR and quantum mechanics (QM) are in such manifest disagreement, GR assumes a classically deterministic dynamical field whereas QM shows that all fields have quantum properties, GR must be incorrect on some level, as has long been known.

There have been theoretical advances in dark energy, although it is clear that there is no, outstanding, favourite theory, see Frampton (2004), Livio (2004) and Peebles & Ratra (2003). There have been some arguments (e.g. Shanks, 2004 and Shanks, 2006) that dark energy is so

poorly understood theoretically that this may be symptomatic of an underlying problem with the ΛCDM paradigm. This point however seems moot for two reasons. Firstly the overwhelming evidence for existence of something like a cosmological constant from so many varying and independent sources, quite the opposite from being in a ether-type situation (in which there was no theory, until the advent of relativity, which could explain the Michelson-Morley experiments). ΛCDM is in agreement with the vast majority of observations. Secondly even if we are in an epicyclic situation (in which, in analogy with epicycles, we have a workable theory but one which is not necessarily representative of reality) the only way to make advances is to continue to do experiments which test the current paradigm until convincing evidence against it arises.

6.3 Dark Energy Experiments

For a comprehensive review of the range of current and future experiments that propose using each of the dark energy probes considered in this thesis see the DETF report (DETF, 2006). Notable exceptions in the DETF report are detailed below.

Stage II projects.

- **FastSound** is a a BAO experiment using FMOS covering 300 square degrees between $0.7 \leq z \leq 1.7$, using the new FMOS instrument. Results are expected between 2008 and 2009.

- The **WiggleZ** project is a BAO experiment using the AAΩ instrument that will measure the spectra of 400,000 galaxies between $0.5 < z < 1$ covering 1000 square degrees. The results are expected between 2008 and 2009.

Stage III projects.

- **darkCAM**, a proposed 10,000 square degree survey to a median redshift of $z_m = 0.7$ that will use weak lensing, SNIa and photometric BAO to constrain dark energy, this has been examined in detail in this thesis.

- There is a proposed survey using the **HyperSuprimeCAM** on the Subaru telescope, the

Stage	Area/square degrees	z_{median}	N_{bands}
IIp	1680	1.0	4
IIIp	4000	1.0	5
IVp	20,000	1.0	9
IVSpace	4000	1.5	9
V	40,000	2.0	–

Table 6.1: The survey parameters for future weak lensing surveys

proposed survey is a 5000 square degrees to a median redshift of $z_m = 0.8$ that proposes to use weak lensing, SNIa and photometric BAO to constrain dark energy.

Stage IV projects.

- The Dark UNiverse Experiment, ***DUNE*** (Réfrégier et al., 2006), is a proposed European space-based experiment that, with support form a 5-band optical ground based survey will cover 20,000 square degrees to a median redshift of $z_m = 0.85$ in 9 bands.

Section 6.4 will present constraints for anonymous Stage II, III, IV and V experiments that are detailed here; though there should be some explicit similarities between these and actual proposed experiments. The CMB constraints, currently from *WMAP* (a Stage I experiment), are not expected to improve significantly beyond the *Planck* experiment (a Stage III experiment) and in comparison to the other methods proposed there does not exist a large number of competing projects whose primary aim is to measure the dark energy equation of state. There are many polarisation CMB experiments for example QUest (Bowden et al., 2004), Boomerang (MacTavish et al., 2006), CBI (Contaldi et al., 2002), Pique (Barkats et al., 2005) and CLOVER (Taylor et al., 2004) whose aim is to probe Inflationary scenarios; and small angular scale experiments using ground-based surveys including CBI, VSAE (Battye et al., 2004) and ACBAR (Runyan et al., 2003). Potential next generation CMB probes are *The Inflation Probe* (see Delabrouille et al., 2004) and *BPOL* both of which aim to measure CMB polarisation to the sensitivity of, for example, QUest over the whole sky.

The different experiments considered are detailed in Tables 6.1, 6.2 and 6.3, in naming of the experiments s and p denote spectroscopic and photometric ground-based surveys respectively.

Stage	Area/square degrees	$z_{\rm bin}$	$N_{\rm bands}$
IIIp	4000	0.5–1.4	5
IIIs	2000	0.5–1.3	–
	300	2.3–3.3	–
IVp	20,000	0.2–3.5	9
IVs	20,000	0.1–1.5	–
IVSpace	10,000	0.5–2.0	–
V	40,000	0.0–2.0	–

Table 6.2: The survey parameters for future BAO surveys

Stage	$N_{\rm SNIa}$	z range	$N_{\rm bands}$
IIs	700	0.1–1.0	–
IIIp	2000	0.1–1.0	5
IIIs	2000	0.1–1.0	–
IVp	300,000	0.1–1.7	9
IVSpace	2000	0.1–1.7	–
V	80,000	0.0–2.0	–

Table 6.3: The survey parameters for future SNIa surveys

The Stage V project I consider is an all sky, space-based survey of every galaxy, optically and spectroscopically, to a median redshift of $z_m = 2$.

6.4 Future Constraints

This Section will present the predicted constraints for each of the future experiments considered. All results in this Section will be combined with the expected 14-month *Planck* prior, and all predictions will be for open models, with the full cosmological parameter set used being $\Omega_m, \Omega_{de}, \Omega_b, \sigma_8, w_0, w_a, n_s, \alpha_n, \tau, r$. The combination with *Planck* is for two reasons, firstly in actuality all future experiments will be combined with a some prior in order to break degeneracies between cosmological parameters, I will combine all Stages with the same *Planck* prior as this will provide directly comparable results between the various stages. Secondly, for some proposed methods, for example the geometric test and SNIa, the constraints from the

experiments alone are poor though this disguises the ability of these experiments to constrain dark energy in combination with other probes. However this thesis has shown that a strong CMB prior, such as *Planck*, is not essential for small errors on dark energy parameters, see Sections 3.10.5 and 4.6.5.

6.4.1 Relative Future Constraints

These results will not be directly comparable with the tabulated results in the DETF report as they do not combine with any prior, and assume a flat universe for the SNIa constraints, though the conclusions drawn from these two analyses are largely similar.

For the weak lensing constraints I will consider the geometric and spectral test separately, denoted G and S respectively, and in combination. The direct combination of the methods should be valid as a first approximation, as the geometric test is only correlated with the spectral test via the noise terms in the geometric test covariance matrix, also the two methods gain the majority of their signal from different scales (the geometric test from small scale clusters, the spectral test from degree-scale ℓ-modes). However the direct combination of these two probes may yield optimistic constraints, and a correct covariance between the methods needs to be calculated; this is left for future work, see Chapter 7. Similarly the direct combination of 3D weak lensing with BAO constraints could be overly optimistic, and a full covariance between the methods needs to be calculated.

The results for the individual experiments are shown in Table 6.4, this table shows the inverse of the figure of merit considered so far, see Section 3.9.6 and 4.5.7, as this is the figure of merit used in the DETF report. In a similar vein to the DETF report the rightmost column shows the inverse figure of merit normalised to the SNIa Stage II constraint which approximates the current state of knowledge.

As demonstrated in Chapters 3 and 4, Table 6.4 clearly shows that 3D weak lensing has the potential to place the most stringent constraints on the dark energy equation of state using both near-term and future experiments. It is the wide and slightly shallower surveys which provide the tightest constraints using 3D weak lensing, as shown in Sections 3.9 and 4.5. The best constraints for an individual method come from the Stage III geometric test, through its unique degeneracy in the $(w_0,\ w_a)$ plane. It should be noted that weak lensing, whilst placing the tightest constraints on dark energy also requires the most stringent control of systematics.

Method	Stage	Δw_0	$z_{\rm pivot}$	$\Delta w(z_{\rm pivot})$	FOM	FOM^{-1}	Normalised FOM^{-1}
WL:G	IIp	0.06	0.26	0.0235	0.0068	146.6	5.25
WL:G	IIIp	0.04	0.23	0.0176	0.0037	267.9	9.66
WL:G	IVp	0.02	0.19	0.0091	0.0009	1049	37.6
WL:G	IVSpace	0.03	0.23	0.0107	0.0014	714.6	25.6
WL:G	V	0.007	0.16	0.0050	0.0002	4599	165
WL:S	IIp	0.10	0.37	0.0178	0.0067	148.6	5.33
WL:S	IIIp	0.07	0.36	0.0167	0.0047	212.2	7.61
WL:S	IVp	0.04	0.36	0.0124	0.0017	600.5	21.5
WL:S	IVSpace	0.04	0.36	0.0109	0.0018	541.1	19.4
WL:S	V	0.007	0.31	0.0018	0.00005	18397	659
WL:G+S	IIp	0.05	0.32	0.0149	0.0031	321.8	11.5
WL:G+S	IIIp	0.04	0.29	0.0121	0.0018	554.5	19.9
WL:G+S	IVp	0.02	0.25	0.0005	0.0005	2114	75.8
WL:G+S	IVSpace	0.02	0.28	0.0069	0.0007	1500	53.8
WL:G+S	V	0.006	0.26	0.0024	0.00004	26681	956
BAO	IIIp	0.15	0.33	0.0350	0.0199	50.17	1.80
BAO	IIIs	0.07	0.35	0.0072	0.0019	519.6	18.6
BAO	IVp	0.06	0.33	0.0113	0.0028	357.3	12.8
BAO	IVs	0.04	0.32	0.0169	0.0026	392.7	14.1
BAO	IVSpace	0.07	0.30	0.0256	0.0075	133.4	4.78
BAO	V	0.01	0.38	0.0041	0.0002	5264	189
SNIA	IIs	0.31	0.35	0.0301	0.0358	27.9	1.00
SNIA	IIIp	0.30	0.35	0.0290	0.0347	28.81	1.03
SNIA	IIIs	0.30	0.35	0.0290	0.0346	28.87	1.03
SNIA	IVp	0.21	0.37	0.0283	0.0225	44.30	1.59
SNIA	IVSpace	0.13	0.39	0.0262	0.0123	81.21	2.91
SNIA	V	0.10	0.38	0.0257	0.0090	110.9	3.97

Table 6.4: A table of expected constraints using varying dark energy probes for different stages of experimental development. The Figure Of Merit (FOM= $\Delta w_a \times \Delta w[z_{\rm pivot}]$) is shown as well as the FOM^{-1} (the statistic used by the DETF) and the normalisation relative to approximate current dark energy constraints, SNIa Stage IIs.

Table 6.4 also shows the constraints predicted by combining both the 3D weak lensing methods. This combination, a simple addition of Fisher matrices may be optimistic though, as shown in the table, the potential constraints resulting from the combination are very small.

The best BAO constraints comes from the Stage IIIs, this can be understood in terms of the deeper redshift bin providing an extra constraint in the (w_0, w_a) plane which intersects with the constraint from the lower redshift bin providing a smaller overall constraint. Comparing spectroscopic and photometric constraints for smaller areas the spectroscopic surveys can do a factor of 10 better. For large area surveys where the spectroscopic redshifts are over a smaller redshift range as a corresponding photometric survey the constraints are similar. However BAO constraints also suffer from systematic effects, most importantly from the galaxy bias which may vary both with scale and luminosity, see Section 3.8.2.

The SNIa performs worse than the other methods, due to the degeneracy between Ω_m and Ω_{de}. There is no significant improvement over current constraints until Stage IV when deeper SNIa will be imaged. I emphasise that all these methods have been considered using the same assumptions; they are all considered on an entirely even basis.

6.4.2 A Dark Energy Timeline

Before embarking on this Section it must be emphasised that the predictions made here are simplistic in that they assume that there will be no 'unforeseen' circumstances limiting the construction of the projects discussed and in the analysis of the data they will produce. Also, since the history of cosmology is rife with surprises, not least the discovery of dark energy, such predictions must be read with a degree of caution. Also note that the combination of the different methods may yield optimistic predictions until a full covariance between the methods is calculated. Since I am only considering the combination of all experiments given a survey, not the multitude of two and three experimental combinations discussed in Chapters 3 and 4, any potential gain in performing such an analysis, for example distinguishing dark energy from modified gravity, will be masked.

Here I will use the existing the methodology to predict the constraints for 3D weak lensing, BAO and SNIa for experiments and plot the figure of merit for the given experiments against the date that results are expected, thus producing a dark energy timeline. For each experiment all the methods that an experiment could utilise are included in the constraint: the geometric

test, the spectral test, spectroscopic or photometric BAO and spectroscopic or photometric SNIa. A *Planck* prior is combined with all the experiments so that all experiments can be considered on an equal basis. Experimental constraints which will be produced before the proposed *Planck* mission could be retrospectively combined with *Planck* constraints once the results are produced.

Table 6.5 shows the survey parameters used in the Fisher matrix calculations. I have chosen a range of experiments covering the different DETF stages and different construction dates. CFHTLS (Semboloni et al., 2006) is a currently on going 5-band photometric survey that is currently producing interesting results and will finish in 2008, KIDS (KIDS, 2006) and Pan-STARRS-1 (Kaiser et al., 2005) are proposed surveys, with very different observing strategies, that will begin observations in approximately 2010. CFHTLS, KIDS and Pan-STARRS-1 are all Stage II projects. WFMOS (Basset et al., 2005) is a proposed wide-field spectroscopic survey whose primary aim is to measure BAO's to constrain dark energy, darkCAM (Taylor, 2005) and the Dark Energy Survey (DES; Wester, 2005) are both proposed surveys which use wide-field cameras on 4m-class telescopes. WFMOS, darkCAM and DES are Stage III projects. The Stage IV projects considered are the Joint Efficient Dark-energy Investigation (*JEDI*; Wang et al., 2006) which is a space-based optical, IR and X-Ray instrument, the Large Synoptic Survey Telescope (LSST; Albrecht et al., 2005) and Pan-STARRS-4 (an extension of Pan-STARRS-1) are both all-sky ground-based optical surveys. There exists many more proposed dark energy experiments though a study of this kind cannot consider the entire raft of possibilities, however the experiments discussed here should be representative of the type proposed.

Figure 6.1 shows the predicted figure of merit for a range of on-going and proposed experiments projected over the next 15 years. Figure 6.1 shows that our knowledge of the dark energy equation of state will improve approximately exponentially with time. Fitting a straight line to the points yields the approximate formula

$$(\Delta w(z_{\rm pivot})\Delta w_a) \approx 0.02 \exp\left[0.31(2006 - \text{Date})\right], \tag{6.1}$$

which has a characteristic e-fold timescale of $\sim$ 3 years[1], shown in Figure 6.1 as the dashed line. It can be seen that the Stage II, III and IV experiments are clustered in both the figure of merit that they could achieve and the date at which they are proposed. This clustering of the Stages is not coincidental as the competitive market of constraining the dark energy equation of

[1] Coincidentally the time taken to complete a PhD or Postdoc!

Survey	Area/square degrees	$z_{\rm median}$	$N_{\rm bands}$	G/S	Methods
CFHTLS	170	1.17	5	G	WL,BAOp,SN
darkCAM | DES	5000	0.8	5	G	WL,BAOp,SN
KIDS	1400	0.6	5	G	WL,BAOp,SN
JEDI	20,000	1.0	9	S	WL,BAOp,SN
LSST	40,000	1.0	5	G	WL,BAOp,SN
Pan-STARRS-1	30,000	0.5	5	G	WL,BAOp,SN
Pan-STARRS-4	30,000	1.0	9	G	WL,BAOp,SN
WFMOS	2000	1.0	–	G	BAOs
	300	3.0	–	G	BAOs
Stage V	40,000	2.0	–	S	WL,BAOs,SN

Table 6.5: The survey parameters used in the timeline Fisher matrix calculations. The Methods column refers to which of the dark energy tests were used in combination for each given survey; WL=the geometric and spectral tests, BAOp=photometric BAO, BAOs=spectroscopic BAO, SN=SNIa. G/S refers to the number density and intrinsic ellipticity dispersion, for Ground (G) n_0 is calculated using the formula in equation (3.93) and $\sigma_\epsilon = 0.3$, for Space (S) $n_0 = 100$ per square arcminute and $\sigma_\epsilon = 0.2$ see Réfrégier et al. (2003) and Massey et al. (2004).

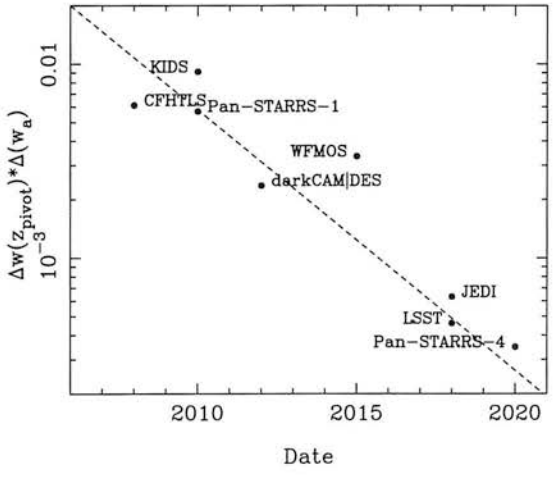

Figure 6.1: The predicted figure of merit for a variety of surveys, including all methods that could be employed using the data from each survey. The dashed line shows the fit to the points given by equation (6.1).

state has encouraged many competing proposals, the more technologically advanced inevitably taking longer to construct and fund but eventually yielding better constraints.

The constraints possible beyond the next 15 years are more uncertain. Since the Stage IV projects considered cover effectively the entire sky, in multiple wavebands, with median redshifts that are of order $z_m \gtrsim 1.0$ (the redshift range in which it thought that dark energy effects dominate), it is difficult to envisage any survey that would out-perform these experiments by an order of magnitude; representing a new DETF 'Stage'. I have defined a space-based imaging and spectroscopic survey of every galaxy to $z_m \gtrsim 2.0$ to be a type of Stage V project. I expect then, that after the Stage IV projects are completed, our state of knowledge will remain approximately fixed until such Stage V projects are feasible or new data analysis methods are created.

It is not certain when a Stage V project would be feasible, if at all. With current technologies, for example a 4m-class telescope with a 2 degree field of view (the type that could be used for the DES and darkCAM), such a survey would take 438 years, using equation (3.122), not to mention the spectroscopic requirements and the fact that this survey is assumed to be space-based. Proposed Extremely Large Telescopes (ELT's) for example the 100m Overwhelmingly Large Telescope (OWL; see for example Monnet et al., 2006) have a large diameter but very small fields of view, the OWL design has a 0.03 square degree field of view. A Stage V optical survey on the OWL would take 47 years. In order to complete a survey of this kind in a reasonable time period (say 600 nights) one would need an ELT of diameter 533 metres if the field of few is fixed at 0.03 square degrees (this reduces to 65 metres if the field of view is 2 square degrees) with space-based image quality. A discussion regarding the technological aspects of such instruments is beyond the scope of this thesis.

Assuming an optimistic timescale of 50 years for the completion of a Stage V project Figure 6.2 shows the figure of merit for such a survey in comparison with the results from Figure 6.1. It can clearly be seen that the gain in constraining the dark energy equation of state has significantly flattened off after the Stage IV projects. The Stage V constraint may represent the lower limit on the knowable accuracy of the equation of state given current methods. Since the pivot redshift of the constraints has not changed significantly, due to the dark energy effect being a $z \lesssim 1$ phenomenon, and the pivot redshift being a feature of the method not the survey design, this limit may represent what can be known about dark energy. If this limit is not good enough to distinguish between different dark energy models then this highlights the need to develop new dark energy and cosmological probes. It also illuminates the next 15-20 years as

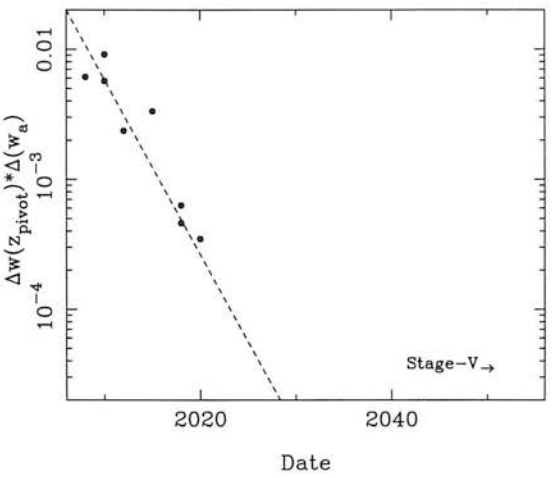

Figure 6.2: The predicted figure of merit for a Stage V survey, including all current methods that could be employed using the survey. The dashed line shows the fit to the points given by equation (6.1), the points shown are the points labelled in Figure 6.1.

potentially being the most important in terms of increasing our relative understanding of dark energy.

6.5 Summary

In this Chapter I have presented a *précis* of the future direction of dark energy constraints. Within the context of the DETF Stages I have demonstrated that 3D weak lensing is very competitive, with the caveat that future weak lensing surveys will need stringent controls of systematics. As well as 3D weak lensing I have presented results for BAO and SNIa experiments. I define a new experimental Stage V survey whose constraints may represent the limiting accuracy with which the dark energy equation of state can be known.

This Chapter presented a tentative dark energy timeline based on currently proposed future surveys by combining the Fisher matrix matrix analysis for all the probes considered in this thesis. The timeline shows that, as hoped, our knowledge of dark energy should increase with time; the constraint on $w(z)$ should decrease. Given that such future surveys are completed, this increase in knowledge should occur approximately exponentially over the next 15–20 years and then flatten off. The prospects for determining the nature of dark energy using 3D weak lensing are very promising.

Chapter 7

Conclusion

This Chapter will conclude this thesis by summarising the critical advances made, and the main results presented. The Chapter will begin by discussing the future direction of 3D weak lensing and dark energy parameter estimation by summarising some outstanding problems and challenges.

7.1 The Future of 3D Weak Lensing

This Section will summarise some outstanding issues and highlight what still needs to be done to fully utilise, understand and exploit the two exciting new methods developed in this thesis. These are presented in no particular order of importance or chronology.

7.1.1 Combining the Geometric and Spectral Tests

In Chapter 6 the geometric and spectral tests were simply added to produce a combined constraint. In detail however this addition is naive. Even though the signal used in the geometric test should be uncorrelated with the spectral tests signal, the tangential shear produced by a cluster does not depend on the large scale structure (cosmic) shear, the noise properties of the geometric test will be correlated to some degree. One way of dealing with the two methods would be to divide the survey into separate parts, using the areas around clusters for the geometric test and the open fields for the spectral test. However not only would this produce a very complex window function for the spectral test but would intentionally leave areas of high overdensity out of a wide-field survey potentially biasing the results. So, the full covariance between the two methods needs to be calculated so that both can be used in any given survey.

7.1.2 Covariance with BAO

In a similar vein to the previous discussion on combining the geometric and spectral tests there should be some correlation between the BAO signal, a measure of the matter power spectrum, and 3D weak lensing. The geometric tests noise properties may be correlated in some way, aswell as the spectral test's signal both of which depend on LSS and so the matter power spectrum in some way. Also the number counts on large scales are affected by weak lensing: see Bartelmann & Schnieder (2001). The correlation with a BAO power spectrum measurement has already been done in the case of weak lensing tomography by Zhan (2006).

7.1.3 Covariance with the CMB

The final covariance that needs to be taken into account is between the CMB and 3D weak lensing. Since the CMB photons should be lensed by LSS along the line of sight there should be a correlation again with the geometric test's noise properties and the spectral test's signal. Since the source redshift of the CMB photons is much greater that the source redshift of a background galaxy in weak lensing this effect should be small. The redshift over which the lensing LSS is the same for each source is small compared to the redshift of last scattering. However, for a full and robust combination of the distinct methods the covariance between the two should be taken into account.

7.1.4 Marginalising over Systematic and Nuisance Parameters

This thesis has taken the approach of investigating systematic and nuisance parameters (for example bias in photometric redshifts, uncertainty in the photometric redshift errors, uncertainty in shape measurement etc.) in the following way. I have predicted cosmological errors without taking these effects into account and then shown that the systematics are small independently of these constraints. This justifies that the systematics in question should have little effect on the cosmological constraints. However a more robust way to include such parameters is to add them as parameters in the Fisher matrix analysis and fully marginalize over them. This alternative approach is the one taken by Zhan (2006), Hu & Jain (2004), Munshi & Valageas (2005), Bernstein & Jain (2004), Ma et al. (2005) and Hu (2002) (amongst many others) in tomographic and other weak lensing tests. For the 3D weak lensing predictions to become even more credible such a full parameter analysis should be done.

As a concrete example of the type of nuisance parameters which may affect 3D weak lensing constraints the effect of photometric redshift bias has been investigated by Ma et al. (2005), Zhan (2006). Edmondson et al. (2006) have developed a Bayesian photometric redshift estimator and investigated the effect of this estimator on weak lensing, the effect on 3D weak lensing of such photometric redshift techniques also needs to be investigated.

7.1.5 Beyond Dark Energy

If the framework of general relativity is correct on large scales then there should be a differential relationship between the Hubble parameter and the growth rate of large scale structure. For a dark energy without couplings to other components, then deviations in the Hubble parameter – growth rate relation may be indicative of modified gravity on large scales. There exists cosmological probes that can probe either the expansion rate evolution vias luminosity or angular diameter distances (so called geometric probes) and those that can probes both the growth of structure and the expansion rate combined. A discrepancy in the dark energy constraints between the geometric and growth probes would highlight the need for a modified gravity on large scales. The approach of Ishak et al. (2006) was to use a Markov Chain Monte-Carlo (MCMC) mock survey type approach and they showed that using SNIa as a geometric probe and weak lensing tomography to probe the growth of structure one could distinguish between a dark energy and a DGP (Dvali-Gadabadze-Porrati, a model inspired by higher-dimensional physics) model, see Section 1.8.4.

Since the geometric test and the spectral test probe the geometry and growth of structure respectively there exists the possibility of combining these probes to test for modified gravity on large scales.

7.1.6 Extra Parameters

3D weak lensing has the potential to constrain extra cosmological parameters beyond those considered in this thesis. As a concrete example the mass of neutrinos and the number of neutrino families is predicted to have an effect on the matter power spectrum at small scales, as the free-streaming of neutrinos damps any power on these scales, see Eisenstein & Hu (1999). Takada et al. (2006) show that a high redshift galaxy survey could constrain the neutrino parameters. Takada (2006) also shows that a galaxy redshift survey may be able to place constraints on dark energy clustering. In as similar way the spectral test should be able to constrain these extra parameters.

7.1.7 Ray Tracing Simulations

The effect of weak lensing has been studied using N-Body simulations to investigate systematics and contaminations, see Heymans et al. (2006) for an example. 3D weak lensing has yet to be investigated in a such a way. Ray-tracing simulations have the potential to allow the effect of complex systematics on 3D weak lensing to be investigated. Also the analysis of a large simulated survey will allow any pitfalls and difficulties encountered to be addressed before a real survey is completed. Simulations also allow other effects to be investigated, Ishak et al. (2006) use an N-Body simulation to investigate the weak lensing constraints on modified gravity, see Section 7.1.5.

Also for large surveys it may be necessary to have many realistic mock surveys in order to accuratelt calculate the covariance matrices.

7.1.8 Data

This thesis has shown that 3D weak lensing has the potential to vastly increase our understanding of cosmology if large scale multi-band surveys are completed. The problems which such large data sets create has not been addressed in this thesis and warrants much more investigation. The analysis of COMBO-17, a very small field of view and a very limited cosmological parameter space, was computationally very expensive (for the spectral tests analysis). I anticipate that new techniques will need to be developed to analyse the new data sets in analogy with pseudo-C_ℓ methods used in CMB analysis (Brown et al., 2005).

7.1.9 Beyond the Fisher Matrix

The Fisher matrix formalism has both advantages and disadvantages as discussed in this thesis. Its primary advantage is that it allows for parameter errors to be estimated accurately and quickly, the covariance of only two points in parameter space need to be calculated for every parameter considered. The concern is that it is bound to predict Gaussian errors. As shown in Chapter 5 some constraints are manifestly non-Gaussian. At the other extreme are approaches that calculate the likelihood at every point in parameter space; very computationally expensive but guaranteed to exactly reproduce the correct constraint. A compromise is the MCMC ap-

proach which is widely used in the determination of cosmological parameters from data (see for example Verde et al., 2003). MCMC approaches can also be used in parameter prediction to predict the correct shape of likelihood surfaces, one such technique uses the statistical measure of entropy (Taylor, private communication).

7.1.10 More Dark Energy Probes

Finally there are some dark energy probes that this thesis has not considered that also propose to measure the dark energy equation of state. Since dark energy is thought to dominate at only $z \lesssim 1.0$ it is only methods that probe this redshift range that will be of discussed here. Most notably I have not considered weak lensing tomography (Hu, 1999; Hu, 2002; Jain and Taylor, 2003; Takada and White, 2004), that performs a 2D analysis of weak lensing data in multiple redshift bins. Most recently Jain et al. (2006) have developed 'colour tomography' a method of using the colour from surveys with very few photometric bands to do weak lensing tomography. All these appear to be a promising techniques but, given that a fully 3D method could be used instead and would provide tighter dark energy constraints, its consideration in this thesis would be redundant. Most promising is the cluster counts method (Hu, 2003) that proposes to detect the number of clusters as a function of mass and redshift out to high redshifts, as shown in Chapter 3 this statistic depends on both geometric and growth of structure effects. Cluster surveys propose using a variety of observing strategies including optical, IR and X-ray (e.g. Kepner & Kim, 2000; Land et al., 2004; Vale & White, 2006) imaging. I have also not directly considered the Integrated Sachs-Wolfe (ISW) effect via the cross-correlation of large scale structure and CMB maps. This appears to be a promising probe of the growth of structure and has the potential to provide a valuable cross-check for purely geometric tests, though it is not very sensitive to dark energy parameters compared with other probes. In the BAO analysis I have not taken in account redshift space distortions, in a galaxy redshift survey these distortions (caused by the peculiar velocity of the galaxies in a group) can also be used to constrain the dark energy equation of state via the Alcock-Paczynski test (Lin & Norman, 2002). As well as SNIa other standard candle techniques have been proposed including using γ-ray bursts (Hooper & Dodelson, 2005) or gravitational waves from coalescing binaries (Dalal et al., 2006).

There have also been proposals to measure dark energy 'in the laboratory', as opposed to the astrophysical means discussed so far. Dark energy may be due to the energy of the vacuum,

if this is the case there should be a cut-off in the observed frequency of random quantum fluctuations (noise). Koch et al. (1980, 1982) attempted to measure this cut-off, and Beck & Mackay (2005) suggest that it may be possible to place interesting constraints on dark energy in the laboratory. There have also been investigations into wether the effect of dark energy may be seen in the motion of solar system planets (e.g. Dumin, 2005), though the measurement of such effects would be very difficult achieve.

7.2 Summary

This thesis begun by summarising the current state of cosmology. From its foundation in general relativity through to the current advances, the main aspects of cosmology used in this thesis were reviewed. The startling fact that $\sim 95\%$ of the Universe is unaccounted for, and that this 'dark sector' can be subdivided into dark matter and dark energy, was introduced. Dark matter is a matter-like component, accounting for $\sim 30\%$ of the mass-energy of the Universe, that interacts only via its gravitational effect. The current paradigm is that dark matter is cold (sub-relativistic) and weakly interacting.

Dark energy is far more mysterious. The Universe is currently undergoing a phase of accelerated expansion, this acceleration can be attributed to a cosmological component with a negative equation of state that accounts for $\sim 70\%$ of the mass-energy budget of the Universe: dark energy. There exists a profusion of theories that claim to explain dark energy, although they can be generally bisected into two main categorisations. Either dark energy is a modification of gravity on the largest scales, most simply explained by a cosmological constant, higher-dimensional brane-world theories also fall into this camp. Or dark energy can be attributed to a scalar field (or fields) of some kind, whose potential has evolved in such a way that it (they) currently exert a negative pressure. Dark energy can also be attributed to the latent energy of the vacuum, although the vacuum energy predicted by the standard model of particle physics is either 0, or 10^{120} orders of magnitude larger than the observed cosmological value. Fortunately each of the proposed explanations of dark energy have a different predicted equation of state $w = p_{\rm de}/\rho_{\rm de}c^2$, the proposals vary in both the present day value w_0 and the redshift evolution predicted. Throughout this thesis I have used the parameterisation of Chevallier & Polarski (2001) and Linder (2003), $w(a) = w_0 + w_a(1-a)$. There are many questions that dark energy raises, the two commonly cited dark energy questions are: what is dark energy? and, why has it only begun to affect the expansion rate now? Although it may be that an answer to the first

question may solve the second one, so that the two can really be compressed into the first question: what is dark energy? It is the answer to this question that has the potential to illuminate our physical understanding of the Universe in such a profound way. It is this question with which this thesis has been primarily concerned.

I have presented two new cosmological probes, which both use shear and redshift information from weakly lensed galaxies, that have the potential to constrain the dark energy equation of state to an unprecedented degree. These new methods were then applied to data for the first time using the COMBO-17 survey. Using the Fisher matrix framework predictions for future experiments and a potential future direction of dark energy parameter estimation were presented.

7.2.1 The Geometric Test

The geometric test uses weakly sheared galaxies around galaxy clusters. By taking the ratio of the tangential components of weakly lensed galaxies at two different redshifts

$$R_{ij} = \frac{\gamma_t(z_i)}{\gamma_t(z_j)} = \frac{S_k[r(z_j)]S_k[r(z_i) - r(z_l)]}{S_k[r(z_i)]S_k[r(z_j) - r(z_l)]}, \tag{7.1}$$

any dependence of the signal on the mass or shape dependence of the lensing cluster is canceled, leaving a statistic that probes the redshift-distance relation only: a geometric test. The signal depends on Ω_m, Ω_{de}, w_0 and w_a where I have allowed for fully open cosmological models. A covariance of the shear-ratio statistic was calculated including noise terms from shot noise and large scale structure. An accurate photometric redshift error formula was introduced, adapting the formulae from Wolf et al. (2003). The ratio is of tangential shears in redshift bins with widths determined by the photometric redshift. A dark matter halo decomposition was performed using the approach of Sheth & Tormen (1999) so that the geometric tests signal from all clusters of any given mass and redshift within a survey could be modelled. A Fisher matrix analysis, using the shear-ratio covariance and the cluster abundance, allowed for parameter error estimations to be made for an arbitrary survey. These parameter estimations were then compared and combined with other predicted dark energy constraints from the following future experiments: 4-year *WMAP* and a 14-month *Planck* experiments using the CMB, WFMOS using BAO's and *SNAP* using SNIa.

This thesis has shown that a targeted survey of 60 of the largest clusters in 5 bands could achieve marginal error of $\Delta w_0 = 0.50$, a factor of 3 improvement over a 4-year *WMAP* experiment.

However to constrain dark energy further wide-field multiband surveys covering large areas are needed. Using an instrument such as darkCAM the optimal survey design, given 600 nights observing is a 10,000 square degree survey to a median redshift of $z_m = 0.7$ in 5 bands. Such a survey could yield marginal constraints of $\Delta w_0 \sim 0.07$, combining with expected results from *Planck*, constraining $w(z)$ at an intermediate redshift of $z_p = 0.27$ to $\Delta w(z_p) \sim 0.03$. The halo decomposition shows that the majority of the signal comes from the numerous $\sim 10^{14}\mathrm{M}_{\odot}$ haloes. I also investigated the effects that the number of photometric redshift bands, bias in the photometric redshift errors, weighting of the data and the assumptions of flatness and fiducial dark energy model have on the parameter error estimation.

Comparing with other dark energy tests it is clear that the geometric test has the potential to become a powerful cosmological probe. Due to its poor sensitivity to the w_a parameter, that effectively represents a normalisation of γ_t at high redshift, the geometric test has a unique degeneracy in the (w_0, w_a) plane. In combination with any of the CMB, BAO and SNIa constraints the geometric test is a competitive alternative to any other experiment. In combining any three experiments the optimal combination is the geometric test combined with the CMB and BAO constraints which could yield a marginal error of $\Delta w(z_p) = 0.02$ at a redshift of $z_p = 0.61$.

This thesis concludes that, with the caveat that some systematic errors can be minimised, future surveys using the geometric test have the potential to constrain the dark energy equation of state to the percent level. The geometric test has the potential to be an important and unique cosmological probe.

7.2.2 The Spectral Test

The second cosmological probe developed in this thesis is the 3D weak lensing spectral test. The spectral test uses each and every galaxy within a survey as an estimator of the 3D shear field, which is directly affected by both the underlying 3D dark matter distribution and the lensing effect of large scale structure. To analyse the 3D shear field I devolve the shear field using spherical harmonics. The coefficients of spherical harmonic expansion $\hat{\gamma}(k, \boldsymbol{\ell})$ are the signal used in this cosmological probe

$$\hat{\gamma}(k, \boldsymbol{\ell}) = \sqrt{\frac{2}{\pi}} \sum_g \gamma(\mathbf{r}) k j_\ell(k r_g^0) \exp(-i\boldsymbol{\ell}.\boldsymbol{\theta}_g) W(r_g^0). \tag{7.2}$$

A full spectral test covariance matrix was calculated which included a shot noise contribution. Photometric redshift errors were included by convolving the signal with a Gaussian error distribution with the photometric redshift error based on the error formulae adapted from Wolf et al. (2003). Using the covariance matrix a Fisher matrix framework was introduced and used to predict estimated parameter uncertainties for a variety of surveys.

This thesis has shown that with a $10,000$ square degree survey to a median redshift of $z_m = 0.7$ in 5 bands the spectral test could constrain the dark energy equation of state parameters to $\Delta w_0 \sim 0.11$ and $\Delta w_a \sim 0.40$ when combined with expected results from *Planck*, with a tighter constraint of $\Delta w(z_p) = 0.02$ at $z_p = 0.37$. The effects of the number of photometric redshift bands, bias in the photometric redshift errors, weighting of the data and the assumptions of flatness and fiducial dark energy model were also investigated.

By comparing the spectral test with predicted constraints from CMB, BAO and SNIa experiments it is clear that the spectral test, more than any other probe, independently constrains the smallest area in the (w_0, w_a) plane. In combination the spectral test is a very competitive probe of dark energy, and indeed of other cosmological parameters particularly σ_8. By combining the spectral test with expected constraints from the CMB and BAO's a marginal error of $\Delta w(z_p) = 0.01$ at $z_p = 0.50$ could be achieved.

This thesis concludes that, again given the caveat of systematic error reduction, the spectral test will prove to be one of the most important cosmological probes of dark energy. By employing this method in future surveys the dark energy equation of state could be constrained to the percent level.

7.2.3 An Application to COMBO-17

The two methods presented in the thesis, the geometric and spectral tests, have been applied to data for the first time. The survey used was COMBO-17, which is a 17-band optical survey with exceptional image quality. Of the five COMBO-17 fields three were used in this analysis, as they contain galaxies with reliable photometric redshift estimates and good image quality, each field covers an area of $30' \times 30'$. The A901/2 field contains the clusters A901a, A901b and A902. The CDFS field is centered on the Chandra Deep Field South, a relatively empty region of sky, and the S11 field was a randomly chosen field that contains a moderately large cluster, A1364.

The A901/2 field is ideal for the geometric test, which requires clusters of galaxies, and was used to place a conditional constraint on w, which was assumed to be constant in this analysis (i.e. $w = w_0$). The constraint from the three small clusters is

$$w = -0.11^{+1.05}_{-1.29}. \tag{7.3}$$

Which encompasses most potential dark energy models. The errors are in agreement with the Fisher matrix predictions made in this thesis, which predict a conditional error of $\Delta w_0 = 1.10$ for three clusters representing A901 and A902.

The spectral test was applied to the CDFS and S11 fields, neglecting the A901/2 field since it was chosen to contain a large overdensity. The spectral test was used to provide a conditional constraint in the (σ_8, Ω_m) plane. The constraint in the (σ_8, Ω_m) plane was compared to that gained from the 2D lensing analysis, using 50% more data, from Brown et al. (2003) and shown to be in good agreement. The spectral test constrained the functional parameters in $\sigma_8(\Omega_m/0.3)^{\beta} = \alpha$ to

$$\begin{aligned} \alpha &= 1.06^{+0.17}_{-0.16} \\ \beta &= 0.57^{+0.19}_{-0.19} \end{aligned} \tag{7.4}$$

which is similar to the constraint from the analysis of Brown et al. (2003) which yields $\alpha = 1.08^{+0.13}_{-0.13}$ and $\beta = 0.62^{+0.12}_{-0.14}$. The spectral test was also used to provide a conditional constraint on w from the CDFS and S11 fields. The conditional constraint on w from these two small fields is

$$w = -1.27^{+0.64}_{-0.70}, \tag{7.5}$$

which again is in agreement with a Fisher matrix prediction of $\Delta w = 0.62$.

By combining the constraints on w from the A901/2 field (using the geometric test) and the CDFS and S11 fields (using the spectral test) I place a conditional constraint on w of

$$w = -1.08^{+0.63}_{-0.58}. \tag{7.6}$$

This is a remarkably small error from such a small survey and is in complete agreement with the current concordance model. The results presented here, whilst not improving our cosmological understanding a great deal, are a validation of the methods and the Fisher matrix predictions made in this thesis and highlight the extraordinary potential that these two methods have to the constrain cosmological parameters.

7.2.4 The Future of Dark Energy

This thesis has also played the role of a prognosticator. By using the Fisher matrix framework the estimated parameter uncertainties for any arbitrary experiment can be calculated.

By predicting constraints from planned future surveys a dark energy timeline was created which showed that during the next 15–20 years there could be an exponential growth in our knowledge of dark energy. Which may flatten over the next 50 years.

By adopting the categorisation of the Dark Energy Task Force (DETF, 2006) I have shown that in a realistic future scenario 3D weak lensing, using either the geometric or spectral tests, has the potential to out-perform BAO or SNIa probes in the near, and far future, providing strong and alternative probes dark energy.

7.3 Conclusion

This thesis has presented two very different ways to use 3D weak lensing information to constrain cosmological parameters, particularly the dark energy equation of state. The two methods are complementary in that they both have the potential to place similar constraints on cosmological parameters. There are many competing cosmological probes that one could use to understand dark energy but it appears that of all of them 3D weak lensing has the potential to be the most potent, with the caveat that systematic effects can be understood and controlled. Not only is it the most promising probe but it is based on extremely well understood physics.

The future of dark energy is bright, this thesis has shown that using 3D weak lensing the nature of dark energy has the potential to be understood.

The elegance and beauty of the methods presented lies in the feature that from such a small statistical effect the nature of the Cosmos on the largest scales can be deduced.

Bibliography

Abbott, L. F. and Schaefer, R. K.: 1986, ApJ **308**, 546

Albrecht, A., Zhan, H., Knox, L., Song, Y.-S., Tyson, J. A., and Wittman, D.: 2005, *Bulletin of the American Astronomical Society* **37**, 1202

Alcock, C., Allsman, R. A., Alves, D. R., Axelrod, T. S., Becker, A. C., Bennett, D. P., Cook, K. H., Drake, A. J., Freeman, K. C., Geha, M., Griest, K., Keller, S. C., Lehner, M. J., Marshall, S. L., Minniti, D., Nelson, C. A., Peterson, B. A., Popowski, P., Pratt, M. R., Quinn, P. J., Stubbs, C. W., Sutherland, W., Tomaney, A. B., Vandehei, T., and Welch, D.: 2001, Nature **414**, 617

Aldering, G.: 2005, *New Astronomy Review* **49**, 346

Angulo, R., Baugh, C. M., Frenk, C. S., Bower, R. G., Jenkins, A., and Morris, S. L.: 2005, MNRAS **362**, L25

Bacon, D. J., Goldberg, D. M., Rowe, B. T. P., and Taylor, A. N.: 2006, MNRAS **365**, 414

Bacon, D. J., Refregier, A., Clowe, D., and Ellis, R. S.: 2001, MNRAS **325**, 1065

Bacon, D. J. and Taylor, A. N.: 2003, MNRAS **344**, 1307

Bacon, D. J., Taylor, A. N., Brown, M. L., Gray, M. E., Wolf, C., Meisenheimer, K., Dye, S., Wisotzki, L., Borch, A., and Kleinheinrich, M.: 2005, MNRAS **363**, 723

Ballinger, W. E., Heavens, A. F., and Taylor, A. N.: 1995, MNRAS **276**, L59

Bardeen, J. M.: 1980, Phys. Rev. D **22**, 1882

Barkats, D., Bischoff, C., Farese, P., Gaier, T., Gundersen, J. O., Hedman, M. M., Hyatt, L., McMahon, J. J., Samtleben, D., Staggs, S. T., Stefanescu, E., Vanderlinde, K., and Winstein, B.: 2005, ApJS **159**, 1

Barnes, L. A., Francis, M. J., Berian James, J., and Lewis, G. F.: 2006, *ArXiv Astrophysics e-prints*

Bartelmann, M.: 1996, in *Astro-Particle Physics*, pp 348–+

Bartelmann, M. and Schneider, P.: 2001, Phys. Rep. **340**, 291

Bassett, B. A., Nichol, B., and Eisenstein, D. J.: 2005, *Astronomy and Geophysics* **46**, 26

Battye, R. A. and the VSA Collaboration: 2004, *ArXiv Astrophysics e-prints*

Baugh, C. M. and Efstathiou, G.: 1993, MNRAS **265**, 145

Beacom, J. F. and Vogel, P.: 1999, *Physical Review Letters* **83**, 5222

Beck, C. and Mackey, M. C.: 2005, *Physics Letters B* **605**, 295

Bento, M. C., Bertolami, O., and Sen, A. A.: 2002, Phys. Rev. D **66(4)**, 043507

Bernabei, R., Belli, P., Cappella, F., Cerulli, R., Montecchia, F., Nozzoli, F., Incicchitti, A., Prosperi, D., Dai, C. J., Kuang, H. H., Ma, J. M., and Ye, Z. P.: 2003, *Dark Matter search*

Bernstein, G. and Jain, B.: 2004, ApJ **600**, 17

Blake, C. and Bridle, S.: 2005, MNRAS **363**, 1329

Blake, C. and Glazebrook, K.: 2003, ApJ **594**, 665

Bond, J. R., Contaldi, C. R., Lewis, A. M., and Pogosyan, D.: 2004, *ArXiv Astrophysics e-prints*

Bowden, M., Taylor, A. N., Ganga, K. M., Ade, P. A., Bock, J. J., Cahill, G. A., Carlstrom, J. E., Church, S. E., Gear, W. K., Hinderks, J. R., Hu, W., Keating, B. G., Kovac, J., Lange, A. E., Leitch, E. M., Maffei, B., Mallie, O., Melhuish, S. J., Murphy, J. A., Pisano, G., Piccirillo, L., Pryke, C., Rusholme, B. A., O'Sullivan, C. M., Thompson, K. L., and Zemcov, M.: 2004, in J. M. Oschmann, Jr. (ed.), *Proceedings of the SPIE, Volume 5489, pp. 84-94 (2004).*, pp 84–94

Bridle, S. L., Lahav, O., Ostriker, J. P., and Steinhardt, P. J.: 2003, *Science* **299**, 1532

Broadhurst, T., Takada, M., Umetsu, K., Kong, X., Arimoto, N., Chiba, M., and Futamase, T.: 2005, ApJ **619**, L143

Brodwin, M., Lilly, S. J., Porciani, C., McCracken, H. J., Le Fevre, O., Crampton, D., Foucaud, S., Eisenhardt, P. R., and Stern, D.: 2004, *Bulletin of the American Astronomical Society* **36**, 1477

Brown, M. L., Castro, P. G., and Taylor, A. N.: 2005, MNRAS **360**, 1262

Brown, M. L., Taylor, A. N., Bacon, D. J., Gray, M. E., Dye, S., Meisenheimer, K., and Wolf, C.: 2003, MNRAS **341**, 100

Caldwell, R. R., Kamionkowski, M., and Weinberg, N. N.: 2003, *Physical Review Letters* **91(7)**, 071301

Capozziello, S., Cardone, V. F., and Troisi, A.: 2006, *Journal of Cosmology and Astro-Particle Physics* **8**, 1

Carroll, S. M., Press, W. H., and Turner, E. L.: 1992, ARA&A **30**, 499

Castro, P. G., Heavens, A. F., and Kitching, T. D.: 2005, Phys. Rev. D **72(2)**, 023516

Catelan, P., Kamionkowski, M., and Blandford, R. D.: 2001, MNRAS **320**, L7

CDMS: 2005, *Physical Review D* **72**, 052009

Chevallier, M. and Polarski, D.: 2001, *International Journal of Modern Physics D* **10**, 213

Chodorowski, M.: 2006, *ArXiv Astrophysics e-prints*

Cline, J. M.: 2006, *ArXiv High Energy Physics - Phenomenology e-prints*

Coles, P.: 2002, *ArXiv Astrophysics e-prints*

Contaldi, C. R., Bond, J. R., Pogosyan, D., Mason, B. S., Myers, S. T., Pearson, T. J., Pen, U. L., Prunet, S., Readhead, A. C., Ruetalo, M. I., Sievers, J. L., Wadsley, J. W., and Zhang, P. J.: 2002, *ArXiv Astrophysics e-prints*

Copeland, E. J., Sami, M., and Tsujikawa, S.: 2006, *ArXiv High Energy Physics - Theory e-prints*

Crittenden, R. G., Natarajan, P., Pen, U.-L., and Theuns, T.: 2001, ApJ **559**, 552

Croft, R. A. C. and Metzler, C. A.: 2000, ApJ **545**, 561

Croton, D. J., Gao, L., and White, S. D. M.: 2006, *ArXiv Astrophysics e-prints*

Dalal, N., Holz, D. E., Hughes, S. A., and Jain, B.: 2006, *ArXiv Astrophysics e-prints*

Dark Energy Task Force Report: 2006, http://www.nsf.gov/mps/ast/detf.jsp

Delabrouille, J., Kaplan, J., Piat, M., and Rosset, C.: 2004, *ArXiv Astrophysics e-prints*

Dumin, Y. V.: 2005, *ArXiv Astrophysics e-prints*

Dvali, G., Gabadadze, G., and Porrati, M.: 2000, *Physics Letters B* **485**, 208

Dvali, G. and Turner, M. S.: 2003, *ArXiv Astrophysics e-prints*

Edmondson, E., Miller, L., and Wolf, C.: 2006, *ArXiv Astrophysics e-prints*

Einasto, J.: 2005, in A. Blanchard and M. Signore (eds.), *Frontiers of Cosmology*, pp 241–+

Einstein, A.: 1916, *The Foundation of the General Theory of Relativity*, Annalen der Physik

Eisenstein, D. J. and Hu, W.: 1999, ApJ **511**, 5

Eisenstein, D. J., Hu, W., and Tegmark, M.: 1999, ApJ **518**, 2

Eisenstein, D. J., Zehavi, I., Hogg, D. W., Scoccimarro, R., Blanton, M. R., Nichol, R. C., Scranton, R., Seo, H.-J., Tegmark, M., Zheng, Z., Anderson, S. F., Annis, J., Bahcall, N., Brinkmann, J., Burles, S., Castander, F. J., Connolly, A., Csabai, I., Doi, M., Fukugita, M., Frieman, J. A., Glazebrook, K., Gunn, J. E., Hendry, J. S., Hennessy, G., Ivezić, Z., Kent, S., Knapp, G. R., Lin, H., Loh, Y.-S., Lupton, R. H., Margon, B., McKay, T. A., Meiksin, A., Munn, J. A., Pope, A., Richmond, M. W., Schlegel, D., Schneider, D. P., Shimasaku, K., Stoughton, C., Strauss, M. A., SubbaRao, M., Szalay, A. S., Szapudi, I., Tucker, D. L., Yanny, B., and York, D. G.: 2005, ApJ **633**, 560

Fisher, K. B., Scharf, C. A., and Lahav, O.: 1994, MNRAS **266**, 219

Fisher, R. A.: 1935, *J. Roy. Stat. Soc.* **98**, 39

Frampton, P. H.: 2004, *ArXiv Astrophysics e-prints*

Gautret, L., Fort, B., and Mellier, Y.: 2000, A&A **353**, 10

Gray, M. E., Wolf, C., Meisenheimer, K., Taylor, A., Dye, S., Borch, A., and Kleinheinrich, M.: 2004, MNRAS **347**, L73

Guo, Z.-K., Piao, Y.-S., Zhang, X., and Zhang, Y.-Z.: 2005, *Physics Letters B* **608**, 177

Guth, A. H. (ed.): 1997, *The inflationary universe. The quest for a new theory of cosmic origins*

Hamana, T., Ohyama, Y., Chiba, M., and Kashikawa, N.: 2005, *ArXiv Astrophysics e-prints*

Hamilton, A. J. S., Kumar, P., Lu, E., and Matthews, A.: 1991, ApJ **374**, L1

Hawkins, E., Maddox, S., Cole, S., Lahav, O., Madgwick, D. S., Norberg, P., Peacock, J. A., Baldry, I. K., Baugh, C. M., Bland-Hawthorn, J., Bridges, T., Cannon, R., Colless, M., Collins, C., Couch, W., Dalton, G., De Propris, R., Driver, S. P., Efstathiou, G., Ellis, R. S., Frenk, C. S., Glazebrook, K., Jackson, C., Jones, B., Lewis, I., Lumsden, S., Percival, W., Peterson, B. A., Sutherland, W., and Taylor, K.: 2003, MNRAS **346**, 78

Heath, D. J.: 1977, MNRAS **179**, 351

Heavens, A.: 2003, MNRAS **343**, 1327

Heavens, A., Refregier, A., and Heymans, C.: 2000, MNRAS **319**, 649

Heavens, A. F., Kitching, T. D., and Taylor, A. N.: 2006, *ArXiv Astrophysics e-prints*

Heavens, A. F. and Taylor, A. N.: 1995, MNRAS **275**, 483

Hetterscheidt, M., Simon, P., Schirmer, M., Hildebrandt, H., Schrabback, T., Erben, T., and Schneider, P.: 2006, *ArXiv Astrophysics e-prints*

Heymans, C., Brown, M., Heavens, A., Meisenheimer, K., Taylor, A., and Wolf, C.: 2004, MNRAS **347**, 895

Heymans, C. and Heavens, A.: 2003, MNRAS **339**, 711

Heymans, C., White, M., Heavens, A., Vale, C., and Van Waerbeke, L.: 2006, MNRAS pp 817–+

Hinshaw, G., Spergel, D. N., Verde, L., Hill, R. S., Meyer, S. S., Barnes, C., Bennett, C. L., Halpern, M., Jarosik, N., Kogut, A., Komatsu, E., Limon, M., Page, L., Tucker, G. S., Weiland, J. L., Wollack, E., and Wright, E. L.: 2003, ApJS **148**, 135

Hirata, C. M. and Seljak, U.: 2003, Phys. Rev. D **67(4)**, 043001

Hirata, C. M. and Seljak, U.: 2004, Phys. Rev. D **70(6)**, 063526

Hooper, D. and Dodelson, S.: 2005, *ArXiv Astrophysics e-prints*

Hu, W.: 1999, ApJ **522**, L21

Hu, W.: 2002, Phys. Rev. D **66**, 083515

Hu, W.: 2003, Phys. Rev. D **67(8)**, 081304

Hu, W. and Jain, B.: 2004, Phys. Rev. D **70(4)**, 043009

Hubble, E.: 1929, *Proceedings of the National Academy of Science* **15**, 168

Huterer, D.: 2002, Phys. Rev. D **65**, 063001

Huterer, D. and Turner, M. S.: 2001, Phys. Rev. D **64**, 123527

Ishak, M.: 2005, *ArXiv Astrophysics e-prints*

Ishak, M., Hirata, C. M., McDonald, P., and Seljak, U.: 2004, Phys. Rev. D **69(8)**, 083514

Ishak, M., Upadhye, A., and Spergel, D. N.: 2006, Phys. Rev. D **74(4)**, 043513

Isham, C.: 1995, *Lectures on Quantum Theory*, Imperial College Press

Jain, B., Connolly, A., and Takada, M.: 2006, *ArXiv Astrophysics e-prints*

Jain, B., Mo, H. J., and White, S. D. M.: 1995, MNRAS **276**, L25

Jain, B. and Taylor, A.: 2003, *Physical Review Letters* **91**, 141302

Jassal, H. K., Bagla, J. S., and Padmanabhan, T.: 2005, MNRAS **356**, L11

Jing, Y. P.: 2002, MNRAS **335**, L89

Jungman, G., Kamionkowski, M., Kosowsky, A., and Spergel, D. N.: 1996, Phys. Rev. D **54**, 1332

Kaiser, N.: 1996, in *Gravitational dynamics*, pp 181–+

Kaiser, N.: 1998, ApJ **498**, 26

Kaiser, N. and Pan-STARRS Team: 2005, *Bulletin of the American Astronomical Society* **37**, 1409

Kaiser, N., Squires, G., and Broadhurst, T.: 1995a, ApJ **449**, 460

Kaiser, N., Squires, G., and Broadhurst, T.: 1995b, ApJ **449**, 460

Kepner, J. and Kim, R.: 2000, *ArXiv Astrophysics e-prints*

Keyton, I.: 1990, *General Relativity*, Oxford University Press

Kilbinger, M. and Schneider, P.: 2004, A&A **413**, 465

KIlo Degree Survey KIDS: 2006, http://www.strw.leidenuniv.nl/ kuijken/KIDS/

Kim, A. G., Linder, E. V., Miquel, R., and Mostek, N.: 2004, MNRAS **347**, 909

King, L. and Schneider, P.: 2002, A&A **396**, 411

King, L. J.: 2005, A&A **441**, 47

Kitching, T. D. et al.: 2006

Knop, R. A., Aldering, G., Amanullah, R., Astier, P., Blanc, G., Burns, M. S., Conley, A., Deustua, S. E., Doi, M., Ellis, R., Fabbro, S., Folatelli, G., Fruchter, A. S., Garavini, G., Garmond, S., Garton, K., Gibbons, R., Goldhaber, G., Goobar, A., Groom, D. E., Hardin, D., Hook, I., Howell, D. A., Kim, A. G., Lee, B. C., Lidman, C., Mendez, J., Nobili, S., Nugent, P. E., Pain, R., Panagia, N., Pennypacker, C. R., Perlmutter, S., Quimby, R., Raux, J., Regnault, N., Ruiz-Lapuente, P., Sainton, G., Schaefer, B., Schahmaneche, K., Smith, E., Spadafora, A. L., Stanishev, V., Sullivan, M., Walton, N. A., Wang, L., Wood-Vasey, W. M., and Yasuda, N.: 2003, ApJ **598**, 102

Knox, L., Scoccimarro, R., and Dodelson, S.: 1998, *Physical Review Letters* **81**, 2004

Knox, L., Song, Y.-S., and Zhan, H.: 2006, *ArXiv Astrophysics e-prints*

Koch, R. H., Van Harlingen, D. J., and Clarke, J.: 1980, *Phys. Rev. Lett.* **45(26)**, 2132

Koch, R. H., Van Harlingen, D. J., and Clarke, J.: 1982, *Phys. Rev. B* **26(1)**, 74

Kogut, A., Spergel, D. N., Barnes, C., Bennett, C. L., Halpern, M., Hinshaw, G., Jarosik, N., Limon, M., Meyer, S. S., Page, L., Tucker, G. S., Wollack, E., and Wright, E. L.: 2003, ApJS **148**, 161

Kolb, E. W., Matarrese, S., Notari, A., and Riotto, A.: 2005, *ArXiv High Energy Physics - Theory e-prints*

Kosowsky, A., Milosavljevic, M., and Jimenez, R.: 2002, Phys. Rev. D **66**, 063007

Krasnikov, N. V. and Matveev, V. A.: 1997, *FIZ.ELEM.CHAST.ATOM.YADRA* **28**, 1125

Lamarre, J. M., Puget, J. L., Bouchet, F., Ade, P. A. R., Benoit, A., Bernard, J. P., Bock, J., de Bernardis, P., Charra, J., Couchot, F., Delabrouille, J., Efstathiou, G., Giard, M., Guyot, G., Lange, A., Maffei, B., Murphy, A., Pajot, F., Piat, M., Ristorcelli, I., Santos, D., Sudiwala, R., Sygnet, J. F., Torre, J. P., Yurchenko, V., and Yvon, D.: 2003, *New Astronomy Review* **47**, 1017

Lampton, M. and SNAP: 2004, *Bulletin of the American Astronomical Society* **36**, 1559

Land, K. R., Nichol, R. C., Davidson, M., Sabirli, K., Romer, A. K., Liddle, A. R., Collins, C. A., Kay, S. T., Mann, R. G., Viana, P. T. P., and West, M. J.: 2004, *ArXiv Astrophysics e-prints*

Lasserre, T., Afonso, C., Albert, J. N., Andersen, J., Ansari, R., Aubourg, É., Bareyre, P., Bauer, F., Beaulieu, J. P., Blanc, G., Bouquet, A., Char, S., Charlot, X., Couchot, F., Coutures, C., Derue, F., Ferlet, R., Glicenstein, J. F., Goldman, B., Gould, A., Graff, D., Gros, M., Haissinski, J., Hamilton, J. C., Hardin, D., de Kat, J., Kim, A., Lesquoy, É., Loup, C., Magneville, C., Mansoux, B., Marquette, J. B., Maurice, É., Milsztajn, A., Moniez, M., Palanque-Delabrouille, N., Perdereau, O., Prévot, L., Regnault, N., Rich, J., Spiro, M., Vidal-Madjar, A., Vigroux, L., Zylberajch, S., and The EROS collaboration: 2000, A&A **355**, L39

Li, M.: 2004, *Physics Letters B* **603**, 1

Lifshitz, E. M.: 1946, *J. Phys. USSR, 10, 116*

Lin, W.-C. and Norman, M.: 2002, *ArXiv Astrophysics e-prints*

Linde, A. D.: 1987, *A New Inflationary Universe Scenario: A Possible Solution of the Horizon, Flatness, Homogeneity, Isotropy and Primordial Monopole Problems*, pp 149–+, Quantum Cosmology

Linder, E. V.: 2003a, *Physical Review Letters* **90(9)**, 091301

Linder, E. V.: 2003b, *ArXiv Astrophysics e-prints*

Linder, E. V.: 2004, Phys. Rev. D **70(6)**, 061302

Linder, E. V. and Huterer, D.: 2005, Phys. Rev. D **72(4)**, 043509

Linder, E. V. and Jenkins, A.: 2003, MNRAS **346**, 573

Linder, E. V. and Miquel, R.: 2004, Phys. Rev. D **70(12)**, 123516

Livio, M.: 2004, *The Dark Universe: Matter, Energy and Gravity*, The Dark Universe: Matter, Energy and Gravity Series: Space Telescope Science Institute Symposium Series (No. 15) Edited by Mario Livio. Published by Cambridge University Press, 2004. ISBN-10: 0521822270 — ISBN-13: 9780521822275

Ma, Z., Hu, W., and Huterer, D.: 2006, ApJ **636**, 21

MacTavish, C. J., Ade, P. A. R., Bock, J. J., Bond, J. R., Borrill, J., Boscaleri, A., Cabella, P., Contaldi, C. R., Crill, B. P., de Bernardis, P., De Gasperis, G., de Oliveira-Costa, A., De Troia, G., di Stefano, G., Hivon, E., Jaffe, A. H., Jones, W. C., Kisner, T. S., Lange, A. E., Lewis, A. M., Masi, S., Mauskopf, P. D., Melchiorri, A., Montroy, T. E., Natoli, P., Netterfield, C. B., Pascale, E., Piacentini, F., Pogosyan, D., Polenta, G., Prunet, S., Ricciardi, S., Romeo, G., Ruhl, J. E., Santini, P., Tegmark, M., Veneziani, M., and Vittorio, N.: 2006, ApJ **647**, 799

Mandelbaum, R., Hirata, C. M., Seljak, U., Guzik, J., Padmanabhan, N., Blake, C., Blanton, M. R., Lupton, R., and Brinkmann, J.: 2005, MNRAS **361**, 1287

Marian, L. and Bernstein, G. M.: 2006, Phys. Rev. D **73(12)**, 123525

Massey, R., Refregier, A., and Rhodes, J.: 2004, *ArXiv Astrophysics e-prints*

Meiksin, A., White, M., and Peacock, J. A.: 1999, MNRAS **304**, 851

Mellier, Y.: 1999, ARA&A **37**, 127

Monnet, G. and D'Odorico, S.: 2006, in P. Whitelock, M. Dennefeld, and B. Leibundgut (eds.), *IAU Symposium*, pp 52–59

Munshi, D. and Valageas, P.: 2005, *ArXiv Astrophysics e-prints*

Narayan, R. and Bartelmann, M.: 1999, in *Formation of Structure in the Universe*, pp 360–+

Navarro, J. F., Frenk, C. S., and White, S. D. M.: 1997, ApJ **490**, 493

Newman, E. T. and Penrose, R.: 1966, *J. Math. Phys.* 7(5)

Ostriker, J. P. and Steinhardt, P.: 2003, *Science* **300**, 1909

Peacock, J.: 1999, *Cosmological Physics*, Cambridge University Press

Peacock, J. A. and Dodds, S. J.: 1996, MNRAS **280**, L19

Peacock, J. A. and Smith, R. E.: 2000, MNRAS **318**, 1144

Peebles, P. J. and Ratra, B.: 2003, *Reviews of Modern Physics* **75**, 559

Peebles, P. J. E.: 1980, *The large-scale structure of the universe*, Research supported by the National Science Foundation. Princeton, N.J., Princeton University Press, 1980. 435 p.

Peebles, P. J. E.: 1993, *Principles of physical cosmology*, Princeton Series in Physics, Princeton, NJ: Princeton University Press, —c1993

Percival, W. J., Burkey, D., Heavens, A., Taylor, A., Cole, S., Peacock, J. A., Baugh, C. M., Bland-Hawthorn, J., Bridges, T., Cannon, R., Colless, M., Collins, C., Couch, W., Dalton, G., De Propris, R., Driver, S. P., Efstathiou, G., Ellis, R. S., Frenk, C. S., Glazebrook, K., Jackson, C., Lahav, O., Lewis, I., Lumsden, S., Maddox, S., Norberg, P., Peterson, B. A., Sutherland, W., and Taylor, K.: 2004a, MNRAS **353**, 1201

Percival, W. J., Sutherland, W., Peacock, J. A., Baugh, C. M., Bland-Hawthorn, J., Bridges, T., Cannon, R., Cole, S., Colless, M., Collins, C., Couch, W., Dalton, G., De Propris, R., Driver, S. P., Efstathiou, G., Ellis, R. S., Frenk, C. S., Glazebrook, K., Jackson, C., Lahav, O., Lewis, I., Lumsden, S., Maddox, S., Moody, S., Norberg, P., Peterson, B. A., and Taylor, K.: 2002, MNRAS **337**, 1068

Percival, W. J., Verde, L., and Peacock, J. A.: 2004b, MNRAS **347**, 645

Perlmutter, S., Turner, M. S., and White, M.: 1999, *Physical Review Letters* **83**, 670

Preskill, J. P.: 1979, *Physical Review Letters* **43**, 1365

Press, W. H.: 2002, *Numerical recipes in C++ : the art of scientific computing*, Numerical recipes in C++ : the art of scientific computing by William H. Press. xxviii, 1,002 p. : ill. ; 26 cm. Includes bibliographical references and index. ISBN : 0521750334

Refregier, A.: 2003, ARA&A **41**, 645

Refregier, A. and Bacon, D.: 2003, MNRAS **338**, 48

Réfrégier, A., Boulade, O., Mellier, Y., Milliard, B., Pain, R., Michaud, J., Safa, F., Amara, A., Astier, P., Barrelet, E., Bertin, E., Boulade, S., Cara, C., Claret, A., Georges, L., Grange, R., Guy, J., Koeck, C., Kroely, L., Magneville, C., Palanque-Delabrouille, N., Regnault, N., Smadja, G., Schimd, C., and Sun, Z.: 2006, in *Space Telescopes and Instrumentation I: Optical, Infrared, and Millimeter. Edited by Mather, John C.; MacEwen, Howard A.; de Graauw, Mattheus W. M.. Proceedings of the SPIE, Volume 6265, pp. (2006).*

Refregier, A., Ellis, R., and SNAP Weak Lensing Working Group Collaboration: 2001, *Bulletin of the American Astronomical Society* **33**, 1481

Rhodes, J. and SNAP Collaboration: 2003, *Bulletin of the American Astronomical Society* **35**, 1336

Riess, A. G., Filippenko, A. V., Challis, P., Clocchiatti, A., Diercks, A., Garnavich, P. M., Gilliland, R. L., Hogan, C. J., Jha, S., Kirshner, R. P., Leibundgut, B., Phillips, M. M., Reiss, D., Schmidt, B. P., Schommer, R. A., Smith, R. C., Spyromilio, J., Stubbs, C., Suntzeff, N. B., and Tonry, J.: 1998, AJ **116**, 1009

Rovelli, C.: 1999, *Quantum spacetime: what do we know?*

Runyan, M. C., Ade, P. A. R., Bhatia, R. S., Bock, J. J., Daub, M. D., Goldstein, J. H., Haynes, C. V., Holzapfel, W. L., Kuo, C. L., Lange, A. E., Leong, J., Lueker, M., Newcomb, M., Peterson, J. B., Reichardt, C., Ruhl, J., Sirbi, G., Torbet, E., Tucker, C., Turner, A. D., and Woolsey, D.: 2003, ApJS **149**, 265

Saini, T. D., Weller, J., and Bridle, S. L.: 2004, MNRAS **348**, 603

Sánchez, A. G., Baugh, C. M., Percival, W. J., Peacock, J. A., Padilla, N. D., Cole, S., Frenk, C. S., and Norberg, P.: 2006, MNRAS **366**, 189

Santos, M. G., Heavens, A., Balbi, A., Borrill, J., Ferreira, P. G., Hanany, S., Jaffe, A. H., Lee, A. T., Rabii, B., Richards, P. L., Smoot, G. F., Stompor, R., Winant, C. D., and Wu, J. H. P.: 2003, MNRAS **341**, 623

Schneider, P.: 2006, in G. Meylan, P. Jetzer, P. North, P. Schneider, C. S. Kochanek, and J. Wambsganss (eds.), *Saas-Fee Advanced Course 33: Gravitational Lensing: Strong, Weak and Micro*, pp 269–451

Schneider, P., Ehlers, J., and Falco, E. E.: 1992, *Gravitational Lenses*, Gravitational Lenses, XIV, 560 pp. 112 figs.. Springer-Verlag Berlin Heidelberg New York. Also Astronomy and Astrophysics Library

Schneider, P., van Waerbeke, L., and Mellier, Y.: 2002, A&A **389**, 729

Schrabback, T., Erben, T., Simon, P., Miralles, J. ., Schneider, P., Heymans, C., Eifler, T., Fosbury, R. A. E., Freudling, W., Hetterscheidt, M., Hildebrandt, H., and Pirzkal, N.: 2006, *ArXiv Astrophysics e-prints*

Seljak, U.: 2000, MNRAS **318**, 203

Seljak, U. and Zaldarriaga, M.: 1996, ApJ **469**, 437

Semboloni, E., Mellier, Y., van Waerbeke, L., Hoekstra, H., Tereno, I., Benabed, K., Gwyn, S. D. J., Fu, L., Hudson, M. J., Maoli, R., and Parker, L. C.: 2006, A&A **452**, 51

Seo, H.-J. and Eisenstein, D. J.: 2003, ApJ **598**, 720

Shanks, T.: 2005, in M. Colless, L. Staveley-Smith, and R. A. Stathakis (eds.), *IAU Symposium*, pp 398–+

Shanks, T.: 2006, *ArXiv Astrophysics e-prints*

Shapiro, I. L. and Sola, J.: 2004, *ArXiv Astrophysics e-prints*

Sheth, R. K. and Tormen, G.: 1999, MNRAS **308**, 119

Sheth, R. K. and Tormen, G.: 2002, MNRAS **329**, 61

Silk, J.: 2002, *ArXiv Astrophysics e-prints*

Simon, P., Hetterscheidt, M., Schirmer, M., Erben, T., Schneider, P., Wolf, C., and Meisenheimer, K.: 2006, *ArXiv Astrophysics e-prints*

Simon, P., King, L. J., and Schneider, P.: 2004, A&A **417**, 873

Smith, R. E., Peacock, J. A., Jenkins, A., White, S. D. M., Frenk, C. S., Pearce, F. R., Thomas, P. A., Efstathiou, G., and Couchman, H. M. P.: 2003, MNRAS **341**, 1311

Sorkin, R. D.: 1997, *International Journal of Theoretical Physics* **36**, 2759

Spergel, D. N., Bean, R., Dore', O., Nolta, M. R., Bennett, C. L., Hinshaw, G., Jarosik, N., Komatsu, E., Page, L., Peiris, H. V., Verde, L., Barnes, C., Halpern, M., Hill, R. S., Kogut, A., Limon, M., Meyer, S. S., Odegard, N., Tucker, G. S., Weiland, J. L., Wollack, E., and Wright, E. L.: 2006, *ArXiv Astrophysics e-prints*

Spergel, D. N., Verde, L., Peiris, H. V., Komatsu, E., Nolta, M. R., Bennett, C. L., Halpern, M., Hinshaw, G., Jarosik, N., Kogut, A., Limon, M., Meyer, S. S., Page, L., Tucker, G. S., Weiland, J. L., Wollack, E., and Wright, E. L.: 2003, ApJS **148**, 175

Starkman, G. D. and Trotta, R.: 2006, *ArXiv Astrophysics e-prints*

Stebbins, A.: 1996, *ArXiv Astrophysics e-prints*

Steinhardt, P. J. and Turok, N.: 2005, *New Astronomy Review* **49**, 43

Susskind, L.: 2003, *The Anthropic Landscape of String Theory*

Tadros, H., Ballinger, W. E., Taylor, A. N., Heavens, A. F., Efstathiou, G., Saunders, W., Frenk, C. S., Keeble, O., McMahon, R., Maddox, S. J., Oliver, S., Rowan-Robinson, M., Sutherland, W. J., and White, S. D. M.: 1999, MNRAS **305**, 527

Takada, M.: 2006, Phys. Rev. D **74(4)**, 043505

Takada, M., Komatsu, E., and Futamase, T.: 2006, Phys. Rev. D **73(8)**, 083520

Takada, M. and White, M.: 2004, ApJ **601**, L1

Taylor, A.: 2003, in *The Davis Meeting On Cosmic Inflation. 2003 March 22-25, Davis CA., p.20*

Taylor, A.: 2005, in *Probing the Dark Universe with Subaru and Gemini*

Taylor, A. C., Challinor, A., Goldie, D., Grainge, K., Jones, M. E., Lasenby, A. N., Withington, S., Yassin, G., Gear, W. K., Piccirillo, L., Ade, P., Mauskopf, P. D., Maffei, B., and Pisano, G.: 2004a, *ArXiv Astrophysics e-prints*

Taylor, A. N.: 2001, *ArXiv Astrophysics e-prints*

Taylor, A. N., Bacon, D. J., Gray, M. E., Wolf, C., Meisenheimer, K., Dye, S., Borch, A., Kleinheinrich, M., Kovacs, Z., and Wisotzki, L.: 2004b, MNRAS **353**, 1176

Taylor, A. N., Kitching, T. D., Bacon, D. J., and Heavens, A. F.: 2006, *ArXiv Astrophysics e-prints*

Tegmark, M., Eisenstein, D. J., Hu, W., and Kron, R.: 1998, *ArXiv Astrophysics e-prints*

Tegmark, M., Strauss, M. A., Blanton, M. R., Abazajian, K., Dodelson, S., Sandvik, H., Wang, X., Weinberg, D. H., Zehavi, I., Bahcall, N. A., Hoyle, F., Schlegel, D., Scoccimarro, R., Vogeley, M. S., Berlind, A., Budavari, T., Connolly, A., Eisenstein, D. J., Finkbeiner, D., Frieman, J. A., Gunn, J. E., Hui, L., Jain, B., Johnston, D., Kent, S., Lin, H., Nakajima, R., Nichol, R. C., Ostriker, J. P., Pope, A., Scranton, R., Seljak, U., Sheth, R. K., Stebbins, A., Szalay, A. S., Szapudi, I., Xu, Y., Annis, J., Brinkmann, J., Burles, S., Castander, F. J., Csabai, I., Loveday, J., Doi, M., Fukugita, M., Gillespie, B., Hennessy, G., Hogg, D. W., Ivezić, Ž., Knapp, G. R., Lamb, D. Q., Lee, B. C., Lupton, R. H., McKay, T. A., Kunszt, P., Munn, J. A., O'Connell, L., Peoples, J., Pier, J. R., Richmond, M., Rockosi, C., Schneider, D. P., Stoughton, C., Tucker, D. L., vanden Berk, D. E., Yanny, B., and York, D. G.: 2004, Phys. Rev. D **69(10)**, 103501

Tegmark, M., Taylor, A. N., and Heavens, A. F.: 1997, ApJ **480**, 22

Tereno, I., Doré, O., van Waerbeke, L., and Mellier, Y.: 2005, A&A **429**, 383

Trotta, R. and Bower, R.: 2006, *Astronomy and Geophysics* **47**, 20

Tyson, J. A. and LSST Collaboration: 2002, *Bulletin of the American Astronomical Society* **34**, 1317

Vale, C. and White, M.: 2006, *New Astronomy* **11**, 207

Verde, L., Peiris, H. V., Spergel, D. N., Nolta, M. R., Bennett, C. L., Halpern, M., Hinshaw, G., Jarosik, N., Kogut, A., Limon, M., Meyer, S. S., Page, L., Tucker, G. S., Wollack, E., and Wright, E. L.: 2003, ApJS **148**, 195

Villumsen, J. V.: 1996, MNRAS **281**, 369

Virey, J.-M., Ealet, A., Tao, C., Tilquin, A., Bonissent, A., Fouchez, D., and Taxil, P.: 2004, Phys. Rev. D **70(12)**, 121301

Wang, Y.: 2006, ApJ **647**, 1

Wang, Y., Baron, E., Branch, D., Casertano, S., Cheng, E., Crotts, A., Dell'Antonio, I., Garnavich, P. M., Habib, S., Hamuy, M., Heitmann, K., Kutyrev, A. S., MacKenty, J. W., Moustakas, L. A., Papovich, C., Phillips, M., Priedhorsky, W. C., Silverberg, R., Springel, V., Squires, G., Tegmark, M., Wheeler, C., Wright, E. L., and JEDI Collaboration: 2005, *Bulletin of the American Astronomical Society* **37**, 1329

Wang, Y. and Freese, K.: 2004, *ArXiv Astrophysics e-prints*

Wang, Y. and Tegmark, M.: 2004, *Physical Review Letters* **92(24)**, 241302

Weinberg, N. N. and Kamionkowski, M.: 2003, MNRAS **341**, 251

Weller, J. and Albrecht, A.: 2002, Phys. Rev. D **65(10)**, 103512

Wester, W. and For The Dark Energy Survey Collaboration: 2005, in S. C. Wolff and T. R. Lauer (eds.), *ASP Conf. Ser. 339: Observing Dark Energy*, pp 152–+

White, M.: 2004, *Astroparticle Physics* **22**, 211

Wilson, R. W. and Penzias, A. A.: 1965, AJ **70**, 697

Wittman, D.: 2002, *LNP Vol. 608: Gravitational Lensing: An Astrophysical Tool* pp 55–+

Wolf, C., Meisenheimer, K., Rix, H.-W., Borch, A., Dye, S., and Kleinheinrich, M.: 2003, A&A **401**, 73

Wright, C. O. and Brainerd, T. G.: 2000, ApJ **534**, 34

Yahata, K., Suto, Y., Kayo, I., Matsubara, T., Connolly, A. J., vanden Berk, D., Sheth, R., Szapudi, I., Anderson, S. F., Bahcall, N., Brinkmann, J., Csabai, I., Fan, X., Loveday, J., Szalay, A. S., and York, D.: 2005, PASJ **57**, 529

Yèche, C., Ealet, A., Réfrégier, A., Tao, C., Tilquin, A., Virey, J.-M., and Yvon, D.: 2006, A&A **448**, 831

Zebrun, K., Soszynski, I., Wozniak, P. R., Udalski, A., Kubiak, M., Szymanski, M., Pietrzynski, G., Szewczyk, O., and Wyrzykowski, L.: 2001, *Acta Astronomica* **51**, 317

Zhan, H.: 2006, *Journal of Cosmology and Astro-Particle Physics* **8**, 8

Zhan, H. and Knox, L.: 2004, ApJ **616**, L75

Zhang, J., Hui, L., and Stebbins, A.: 2005, ApJ **635**, 806